IMAGING SINGLE-ELECTRON CHARGING IN NANOSTRUCTURES BY LOW-TEMPERATURE SCANNING FORCE MICROSCOPY

A Dissertation

Presented to the Faculty of the Graduate School

of Cornell University

in Partial Fulfillment of the Requirements for the Degree of

Doctor of Philosophy

by

Markus Brink

January 2007

This document is in the public domain.

IMAGING SINGLE-ELECTRON CHARGING IN NANOSTRUCTURES BY LOW-TEMPERATURE SCANNING FORCE MICROSCOPY

Markus Brink, Ph.D.

Cornell University 2007

In this thesis we investigate Coulomb blockade phenomena and single-electron charging effects in two nanoscale structures: Long semiconducting carbon nanotubes (CNTs) and gold nanoparticles that are linked to a CNT by an organic molecule. While gold nanoparticles naturally exhibit single-electron charging at low temperature, it is disorder that causes the formation of quantum dots in long semiconducting CNTs at low carrier density. Our instrument of choice is a low-temperature atomic force microscope (AFM) that is sensitive to electrostatic sample forces. A theory of the interactions between single-electron charging of a quantum dot and the AFM tip and cantilever is worked out in linear response.

In semiconducting CNTs we resolve single-electron charging events in the resonance frequency of the AFM cantilever. The AFM's spatial resolution allows us to locate the quantum dots and address them individually. We extract the size of the quantum dots, their gate couplings, and exemplify how to extract their charging energy from the AFM measurements. We frequently observe interaction between neighboring quantum dots and characterize their interdot coupling. The evolution of the quantum dots in CNTs with gate voltage reflects the underlying potential energy landscape for the carriers on the tube. We observe the CNT band structure and extract quantitative information about the disorder potential.

On the gold nanoparticle sample, we combine dissipation and frequency shift measurements by our AFM. In addition to the electrostatic gate couplings and the charging energy, this combination allows us to characterize the tunnel coupling between the gold nanoparticle and the CNT, which is acting as a lead.

The power of the demonstrated force probe techniques lies largely in the local nature of the measurement. Sensitive, spatially resolved information on electron transport is available even in the absence of device conduction. This advantage is apparent in the single-contact geometry of the gold nanoparticles, but also demonstrated on CNTs.

BIOGRAPHICAL SKETCH

Markus Brink was born 1974 in Forst/Lausitz, East Germany. He went to elementary and high school in his home town. After high-school he served for 15 months in the emergency medical services of the German Red Cross as a substitute for compulsory military service. He begun his undergraduate and early graduate studies in physics at Dresden University of Technology in 1994. Markus studied a year in the Fulbright exchange program at the University of Missouri in Columbia, MO in 1997/98. Before returning to Dresden, he spent a summer at the National Institute of Standards and Technologies in Gaithersburg, MD. In fall 1999 he started in the graduate program in physics at Cornell and joined the McEuen research group in spring 2001. After graduation, Markus will pursue postdoctoral research on superconducting quantum circuits in Michel Devoret's lab at Yale.

ACKNOWLEDGEMENTS

Science is a collaborative and social endeavor, and it is my pleasure to acknowledge other people's contributions to this work. There is a large number of colleagues, collaborators, and friends that I had a chance to interact and work with, and it seems impossible to credit them all. Many of the people mentioned below also stand in place of others who are not named explicitly, but had an impact on the progress of scientific projects and my personal journey through graduate school. All their help, encouragement, and support is sincerely appreciated.

My advisor, Paul McEuen, certainly had the largest impact on this research. Paul's intuitive insights and deep understanding of physics were a real inspiration throughout the years. He is an outstanding experimentalist with an incredible sense for the right direction to pursue. His confidence, trust, and experience have sustained the project during times of drought. Paul is also one of the rare kind of people who combine competence and knowledge with kindness and hippie coolness. I really hope that some of his unique qualities and skills got transferred during my time in Paul's group.

I have also been very fortunate with the members of my Special Committee: Jeevak Parpia has accompanied and helped guide my graduate studies at Cornell from my first days in Ithaca. He has always been available with valuable, personal advice on any subject that I brought to him. Piet Brouwer is probably the best teacher to learn solid state theory from. His vast knowledge in the field is not only amazing, but also useful, as he takes an honest interest in experiments. I have many times admired his patience and his ability to explain a phenomenon from yet another angle. I am also grateful to Erich Mueller for taking Piet's place at my Ph.D. defense, who is currently on a sabbatical. During the short time we have

interacted, I have already learned to appreciate his open and straight-forward style of communication.

The low-temperature atomic force microscope (LT-AFM) was bequeathed to me by Michael Woodside. After assembling the instrument together at Cornell and incorporating a new controller and software, Mike taught me all about the LT-AFM and its temper, in particular all the things not to do with it. After Mike left, the LT-AFM lab became rather quiet, but after a short solo interlude, Jun Zhu joined the project. Jun's knowledge in low-temperature experiments was invaluable for the LT-AFM project and her skills were often complementary to mine, which made for very productive team work. Both sets of experiments presented in this thesis are a result of work done in tandem with Jun.

I am also indebted to many collaborators on other projects, among them Scott Bunch, Ethan Minot, Jed Whittaker, David Tanenbaum, Rob Davis, Ali Javey, Andre Mkhoyan, and Rob Ilic. The many discussions on related and unrelated research often also left their imprint on the LT-AFM project.

The McEuen lab members have been there through thick and thin, working on various projects together, sharing experience on fabrication and equipment, bouncing thoughts around, laughing and drinking tea together, arguing global and local politics, hiking along the gorges, etc. Thanks to you all, Sami Rosenblatt, Vera Sazonova, Ethan Minot, Scott Bunch, Jiwoong Park, Michael Woodside, Ji-Yong Park, Yuval Yaish, Alex Yanson, Xinjian Zhou, Jun Zhu, Luke Donev, Lisa Larrimore, Shahal Ilani, Arend van der Zande, Zhaohui Zhong, Nathan Gabor, Patrycja Paruch, and Samantha Roberts.

Beyond the McEuen lab, there were always fellow grad students around in the basement of Clark Hall to get ideas, help, and information for research projects

or to procrastinate with outside the dungeon. Thanks to Erik Mueller, Alex Champagne, Luat Vuong, Abhay Pasupathy, Ferdinand Kümmeth, Dan Schuette, Eric Ryan, Jason Petta, Kiril Bolotin, Jack Sankey, Jacob Grose, Nathan Emley, Sean Garner, Mike and Tammie Weinberger, Craig Caylor, Alexei Kisselev, Sergey Kriminski, Marcus Collins, Jonathan Wrubel, and Gil Toombes.

Clark Hall is beautifully setup to do experimental research, and there are many people who support this work. Eric Smith is always available with invaluable advise on all aspects of low-temperature equipment and owns just the right little gizmo to diagnose the latest cryostat problem. Stan Carpenter and the people in the professional machine shop make all the things you want to have but can't buy. My own machining skills I owe to Bob Snedeker, who runs the graduate machine shop. If physics won't work out for me in the future, thanks to you I could just start a new career in my grandfather's machine shop. Among the computer and network wizards, Barry Robinson is our secret weapon and the last line of defense in the e.world. Thanks also for getting my backup hard drive back to live.

Just a block down the road is Duffield Hall and Cornell's wonderful nanofabrication cleanroom. Apart from the large number of powerful, state-of-the-art machines, the friendly and user-oriented CNF staff has been very supportive with training on the equipment and suggestions on our fabrication protocols.

Whenever university bureaucracy took overhand or a deadline was almost passed, the problem's solution was only one floor away, at Deb Hatfield's office. Judy Wilson was instrumental in figuring out the problems related to graduating in the middle of a semester. Douglas Milton was always helpful with various administrative tasks. Lisa Margosian and Rosemary French stand for the many friendly and joyful people in the physics office. All their assistance is greatly appre-

ciated. The Cornell International Students and Scholars Office certainly deserves a mention for their kind help with visa and travel documents.

Outreach has become an imperative part of doing science. Thanks to the work and dedication of many people, including Monica Plisch, David Tanenbaum, Carl Franck, and Nev Singhota, bringing science to a wider audience was well-organized and often also lots of fun.

For more than 3 years now I have lived in the science coop, where I have enjoyed the company of many great house mates and guests, among them Luat Vuong, Vera Sazonova, Karin Rebel, Larissa Smith, Anoek Backx, Sarah Stockwell, Patrycja Paruch, Mary Killilea, Sylvie Doutriaux, Jef Leroy, Lalo Carrillo-Rubio, Jon Klapwyk, Tony David, Faisal Ahmad, and Jahan Dawlaty. It's been great spending time with all of you.

Ithaca will also remain memorable for many fun hours spent recreationally over non-science matters: Raphael Kapfer and I went on two bike tours around Cayuga Lake. Unfortunately, it couldn't become an annual habit as planned. Raphael also taught me the French national card game with the unfortunate name 'Tarot' and got me into badminton. More recently, Erik Mueller and Alex Champagne have been great challenges on the badminton court. Ultimate frisbee with the physics fun team has always been a welcome diversion. Playing squash with Erik Mueller and Dan Ralph was reliably a great workout. Due to many dinner invitations after our weekly badminton matches, Jun Zhu has refined my taste for Chinese food. The summer bookclub organized by Luat Vuong and Justin Rice was something to look forward to every year. It was always worth the time listening to and discussing music with Mike Woodside. Since he left, playing piano has taken a definite dent. The Brahms project is still unfinished, but I hope to pick it up some day again.

Susan Wiser and the dogs deserve a special mention. Jake, Harpo, Sadie, Maggie, Dylan, and Duke were always a blast to hang out with.

Finally, I owe all my accomplishments to my family. My parents and my sister have shaped my personality more than anyone. Though far away, they have been a constant source of love and support. Thanks for your patience, your trust, all the wisdom and experience you continue to offer, and your guidance in this complex scheme of modern life.

Ithaca, October 2006

TABLE OF CONTENTS

LIST OF TABLES

LIST OF FIGURES

CHAPTER 1

INTRODUCTION

"Small is big!" is a characteristic slogan for the trend of technology over the past few decades. In all domains of technology – mechanical, optical, and electronic – the size of functional devices that serve a useful purpose has steadily decreased. Apart from the convenience of ever-decreasing size, typical reasons for miniaturization include better device performance (faster operation, lower power consumption), smaller production cost per unit (cheaper fabrication, less material input), and new functionality. This ubiquitous trend in technology has a parallel evolution in science. Led by the capabilities of the microelectronics industry, scientists and engineers have been able to design and fabricate ever-smaller man-made devices. New discoveries and developments in materials science and chemistry have further added to this progress.

When miniaturization leads to very small sizes, it ultimately results in rudimentary changes in the behavior of the device. There are two common mechanisms that bring such changes about:

1. **Classical vs. quantum mechanical phenomena.** As the device size shrinks from macroscopic via mesoscopic to microscopic, its proper description and governing laws cross over from classical to quantum mechanical. This results in fundamentally new behavior of the system.

2. **Reduced dimensionality and finite size effects.** If the size of some structure is continuously reduced in all dimensions, the structure ultimately always turns into a zero-dimensional (0D) dot-like object. This example illustrates the more general observation that reducing the size eventually implies

a reduction of dimensionality. Reducing the dimensionality has important consequences, as the same governing laws often manifest themselves in qualitatively different behavior depending on the the system's dimensionality. In the transition regime between two dimensionalities, these phenomena are often called finite-size effects.

Both effects are well illustrated by electron transport in conductors: Ohmic conduction in metals, as described classically by the Drude theory (Drude 1900), is fundamentally different from conduction by Cooper pairs of electrons in a superconductor[1], which is inherently quantum mechanical in nature and requires a many-body quantum description, such as the BCS theory (Bardeen et al. 1957). Universal conductance fluctuations (Altshuler 1985, Lee and Stone 1985) and the Aharanov-Bohm effect (Aharonov and Bohm 1959, Beenakker and van Houten 1991) are two more examples of quantum effects in the electron transport. On the other hand, phenomena that depend on the dimensionality of the conductor and do not occur in three-dimensional (3D) bulk metals include the integer and fractional quantum Hall effect in two-dimensional (2D) sheet-like conductors, spin-charge separation and Luttinger-liquid behavior in a one-dimensional (1D) conduction channel, quantized conductance through a quantum point contact, and Coulomb blockade and single-electron charging effects in 0D dot-like conductors, called *quantum dots*.

In parallel with the progress in miniaturization, new analytical tools and measurement techniques were developed to resolve and characterize these ever-smaller samples. Among them, a new class of imaging tools called *Scanning Probe Mi-*

[1]Even though superconductivity does not arise from small size, but occurs in specific materials at low temperature, it illustrates the effect of fundamentally different physical laws.

croscopes (SPMs) was devised. In all SPMs, a sharp tip or probe is brought near the surface of the sample. The local interaction between the tip and the sample is resolved to measure some sample property at the position of the tip. By scanning the tip over the sample surface and measuring this local property at many points, one obtains a spatial image. The first SPM invented was the *Scanning Tunneling Microscope* (STM) (Binnig et al. 1982). It measures the tunneling current between the tip and the metallic sample across the gap between them. The STM is a very sensitive, high-resolution tool, but its application is limited to conducting samples. The most widely used SPM today is the *Atomic Force Microscope* (AFM) (Binnig et al. 1986), which is sometimes also called *Scanning Force Microscope* (SFM). As the name suggests, it measures the local force between the tip and the sample. Even though the resolution of most AFMs is typically inferior to STMs, its versatility makes it broadly applicable. We discuss its principles of operation in more detail below.

In this thesis we use the capabilities of AFMs to investigate the electronic properties of two low-dimensional nanostructures: Semiconducting carbon nanotubes (CNTs) and gold nanoparticles that are tethered to a CNT by an organic molecule. We observe Coulomb blockade phenomena and single-electron charing in both samples. To resolve these phenomena, our AFM operates at cryogenic temperatures.

This thesis is organized as follows: In the remainder of this chapter, we briefly introduce carbon nanotubes and discuss their basic properties, followed by some comments on the principles of atomic force microscopy. Theoretical background on Coulomb blockade phenomena and single-electron charging effect are provided in Chap. 2. This chapter also discusses the theoretical aspects of force detection

by a cantilever and the interaction between an AFM and quantum dots. Some details and features of our specific home-built AFM are provided in Chap. 3. The fabrication procedure of our samples is outlined in Chap. 4. In Chap. 5 we discuss frequency shift measurements on semiconducting CNTs at $T = 4.2\,\mathrm{K}$. Scanning probe measurements on the gold nanoparticles are detailed in Chap. 6. The thesis finishes with some final remarks and conclusions (Chap. 7).

1.1 Carbon nanotubes

Carbon nanotubes are a family of stable crystalline forms of carbon that were discovered only 15 years ago (Iijima 1991). We distinguish between single-walled and multi-walled CNTs. A single-walled CNT can be thought of as a single sheet of graphite (called *graphene*) rolled seamlessly into a tube. There are many ways to roll up a sheet of graphite: Rolling it more or less tightly would give the tube a smaller or larger diameter. We can also roll the sheet at different angles with respect to a crystallographic direction of the graphene lattice, as illustrated in Fig. 1.1. This gives a single-walled CNT a specific chirality. The crystal structure of a single-walled CNT is fully specified by its diameter and chiral angle. Multi-walled CNTs essentially consist of several concentric single-walled CNTs. In this thesis, we are only concerned with single-walled carbon nanotubes.

CNTs have a number of amazing properties. Typically, they are only 1 to a few nanometers in diameter, but can be extremely long (Huang et al. 2003a). CNTs that are several millimeters long have been reported (Zheng et al. 2004). Their mechanical properties place them among the strongest materials synthesized to date (Treacy et al. 1996). Electronically, a single-walled CNT can be either metallic or semiconducting, depending on its diameter and chiral angle. Metallic

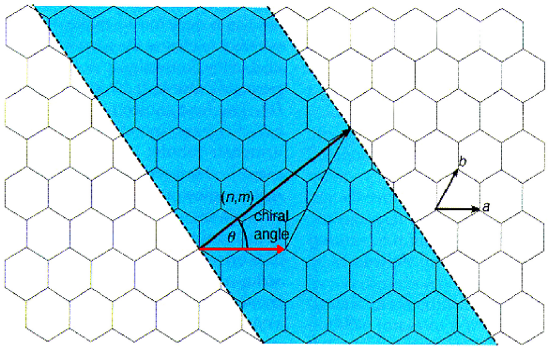

(a) Rolling graphene into a CNT.

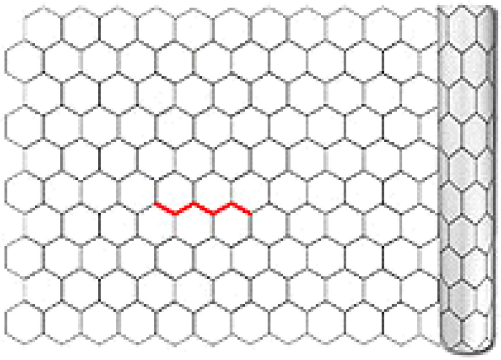

(b) Zig-zag CNT ($\theta = 0°$).

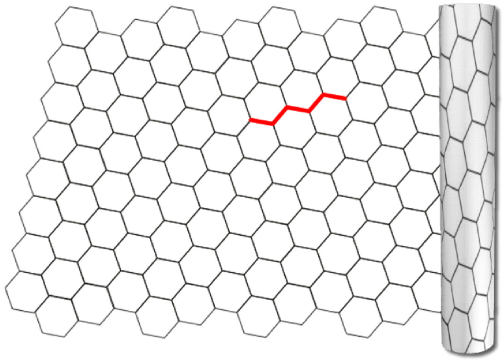

(c) Chiral CNT ($0° < \theta < 30°$).

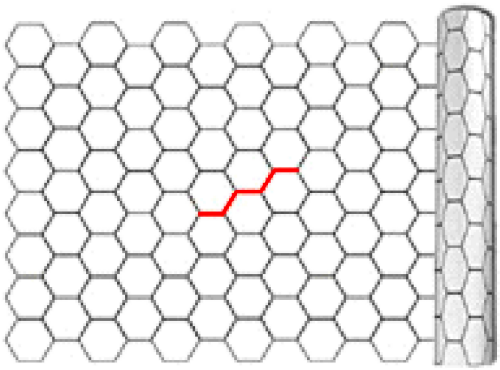

(d) Armchair CNT ($\theta = 30°$).

Figure 1.1: Chirality of single-walled carbon nanotubes. The chiral angle θ of a CNT is defined between the "zig-zag" direction of the honeycomb lattice (as indicated in red in all images) and the direction of rolling the graphene sheet (perpendicular to the CNT axis). It varies uniquely between 0° and 30°. Single-walled CNTs with a chiral angle at either extreme are called zig-zag ($\theta = 0°$) and armchair ($\theta = 30°$). The crystal structure of a single-walled CNT is fully determined by its diameter and chiral angle.

CNTs have a continuous dispersion relation, while semiconducting CNTs have a bandgap. The curvature of the rolled graphene sheet can also open a small bandgap in the continuous dispersion relation. This kind of CNT is referred to as small-bandgap tube. To measure the electronic properties of a CNT, we place the tube in a field-effect transistor (FET) geometry. In the FET device geometry, the CNT is contacted by two metal electrodes, called *source* and *drain*. A third electrode, commonly called *gate*, is brought near the CNT. In our samples, we use the degenerately doped silicon wafer as a gate electrode, which we call the *backgate*. A topographic AFM image of such a CNT device is shown in Fig. 1.2. The voltage applied to the gate influences the electrostatic potential of the CNT through their mutual capacitance. The FET geometry allows us to measure the electronic properties of a CNT. Figure 1.3 shows several transport traces of different CNT devices, where we plot the source-drain conductance as a function of the voltage applied to the backgate. The conductance of a metallic CNT is independent of the voltage on the backgate. In a semiconducting CNT, the gate voltage can turn the conductance of the nanotube on and off. In between these two transport characteristics falls the case of small-bandgap CNT, whose conductance shows a marked drop near zero gate voltage, but does not reach the off state of zero conductance at room temperature. Many more details of CNTs and their properties can be found in the literature (see Dresselhaus et al. 1996, 2001, Saito et al. 1998, Thune and Strunk 2005, for example).

Due to their small diameters, imaging carbon nanotubes requires high-resolution tools. A commonly used instrument for this purpose is the AFM, whose principles of operation are outlined below.

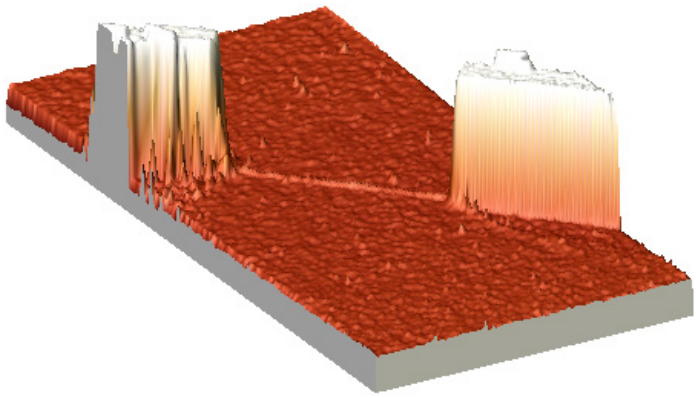

Figure 1.2: Topographic AFM image of a CNT that is contacted by two leads. This image was recorded in tapping mode at room temperature. The CNT is visible in the image as a thin line connecting the two tall metal contacts.

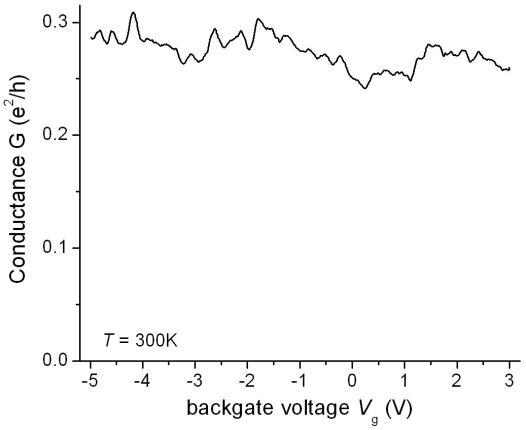

(a) Metallic CNT.

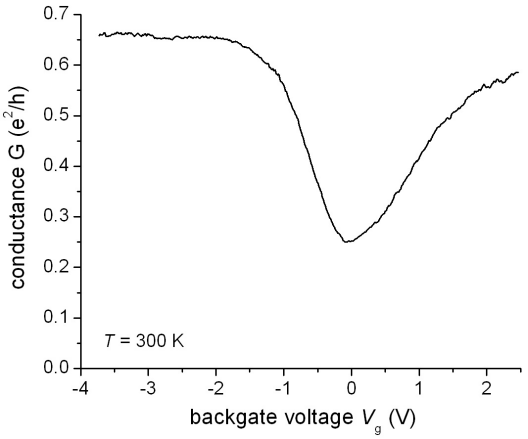

(b) Small-bandgap CNT.

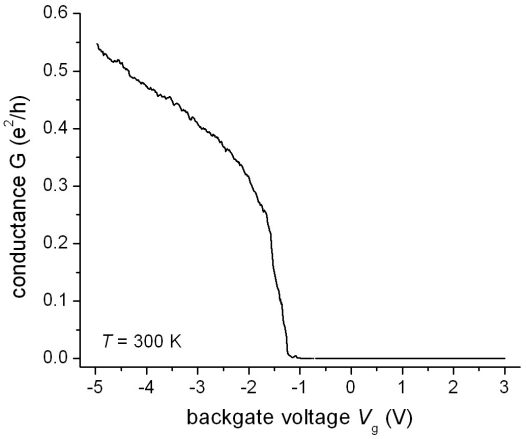

(c) Semiconducting CNT.

Figure 1.3: Transport characteristics of different CNT devices. All traces are recorded under ambient conditions at room temperature. The maximum (theoretical) conductance of a single-walled carbon nanotube is $4e^2/h \approx 155\,\mu$S, but any contact resistance between the carbon nanotube and either metal lead or non-unity transmission probability of the CNT due to electron scattering reduce the device conductance.

1.2 Scanning Force Microscopy

A scanning force microscope (SFM), which is synonymously also called atomic force microscope (AFM), is a specific kind of scanning probe microscope (SPM) that resolves local sample forces. In an AFM, a sharp tip is mounted on a flexible cantilever and brought near the sample surface. The cantilever can deflect up and down in response to a force acting on the tip. By Hooke's law, the cantilever deflection Δz resolves the force F acting on the tip,

$$F = -k\,\Delta z\ . \tag{1.1}$$

The proportionality constant k is the spring constant of the cantilever. By raster scanning the tip over the sample surface and recording the cantilever deflection point by point on a square grid, we obtain a spatial map of the forces originating from the sample – an AFM image.

In effect, the cantilever acts as a mobile, microscopic force detector on our local probe, the AFM tip. There are many different ways to operate an AFM and extract information from the cantilever deflection. For example, in the so-called *contact mode*, the tip is lightly pushed into the sample surface and then dragged over it by scanning. In this regime the interatomic repulsion between the sample and the tip is strong. This mode of operation is typically used to collect a topographic image of the sample surface. In *intermittent contact* or *tapping mode*, the tip is oscillating and makes contact with the sample surface only for part of each oscillation cycle. This reduces the shear forces on the tip, but the signal is still dominated by surface repulsion. An example of a topographic AFM image recorded in tapping mode is shown in Fig. 1.2. In any *non-contact mode* of operation, in contrast, the tip never touches the surface of the sample, and van-der-Waals, electrostatic, magnetic and

other forces can be resolved. All our low-temperature images are collected in non-contact mode.

The cantilever deflection also lends itself to extracting multiple quantities. For example, if the tip is set into oscillation, we can record the static deflection, the tip oscillation amplitude, its phase with respect to the driving force, the cantilever resonance frequency, the oscillation amplitude and phase at some harmonic, etc. Most importantly, all of these quantities are contained in the deflection signal and can be recorded simultaneously. There are further signal channels that may contain useful information about the sample. Just to give an example, in *Scanning Gate Microscopy* (SGM) the conductance of an electronic device on the sample is recorded as the biased AFM tip scans above it. The number of imaging modes devised for AFMs has become quite large, and many of them are detailed in the literature (Wiesendanger 1994, Sarid 1994, Odom et al. 2001, Morita et al. 2002).

To observe basic electronic properties of our samples, such as single-electron charging, we need to reduce the thermal energy of the carriers. Consequently, we need to operate the AFM at cryogenic temperatures. For that purpose, our home-built AFM is mounted in a ^{3}He cryostat. Some details of our low-temperature AFM are discussed in Chap. 3.

CHAPTER 2

THEORETICAL BACKGROUND

The purpose of this chapter is to summarize the known body of theory that underlies our experiments in a coherent and comprehensive manner. We introduce relevant concepts, discuss necessary conditions to observe the phenomena in our experiments, explore their various limits, and provide a set of essential equations needed to understand our observations and analyze the data.

This chapter divides into two sections: The first section, entitled *single-electron tunneling and quantum dots*, relates to our nanoscale samples and discusses phenomena observed in our experiments. Since there is a vast amount of literature available on this subject (Grabert and Devoret 1992, Sohn et al. 1997), we keep this section brief and refer to published work liberally. The second section, entitled *cantilever dynamics*, focuses on instrumentation and the particular way we measure such phenomena using an atomic force microscope (AFM). Of main concern are the interactions between a quantum dot and the biased AFM tip, particularly during single-electron charging, and how this interaction is resolved by the cantilever. To our knowledge, this particular subject is not extensively covered externally, and we offer considerable detail in some parts, including a few detailed derivations.

2.1 Single-Electron Tunneling and Quantum Dots

2.1.1 Tunnel Junctions

The essential ingredient to quantum dots and single-electron charging is the tunnel junction. A tunnel junction is a quantum mechanical circuit element, consisting

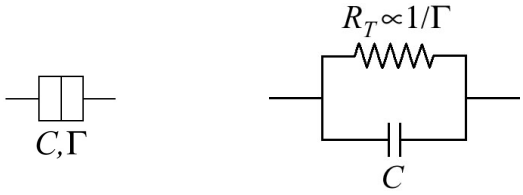

Figure 2.1: Circuit symbol and equivalent circuit of a tunnel junction.

of two conductors that are separated by a thin insulating barrier. It is macroscopically characterized by the junction capacitance C and the tunneling rate Γ (or equivalently the tunnel resistance $R_T \propto 1/\Gamma$) across the junction. A tunnel junction is different from a classical capacitor in that it permits quantum tunneling of electrons across the insulating barrier when energetically favorable. Although commonly depicted as a resistor, the tunnel resistance is fundamentally different from an ohmic resistance. The circuit symbol of a tunnel junction and its equivalent circuit are depicted in Fig. 2.1.

2.1.2 Quantum dots and Coulomb blockade

A *quantum dot* is a small conducting island that is weakly coupled to one or more charge reservoirs through tunnel barriers. Due to its small size, the Coulomb interaction between charges on the island becomes important. Simply put, electrons feel each other's presence on the dot. Before an electron can tunnel onto the dot, it has to overcome the Coulomb repulsion from the electrons already on the dot. This phenomenon is called *Coulomb blockade* and is a result of the quantization of charge. In effect, the Coulomb interaction opens an energy gap between the occupied and empty electron states on the small island. This energy gap due to

electrostatics is called the *charging energy* of the quantum dot and is given by

$$E_C = \frac{e^2}{C_{\text{dot}}} \, , \tag{2.1}$$

where $-e$ is the charge of an electron and C_{dot} is the total capacitance of the island.

Expressing these conditions quantitatively, a quantum dot must meet two requirements to exhibit Coulomb blockade:

1. As the term *quantum dot* suggests, the conductive island must be effectively 0-dimensional (0D) in size so that the Coulomb interaction between individual charges on the dot becomes relevant. This geometric size requirement is reflected by the value of the total capacitance of the quantum dot, C_{dot}. Practically, this means that the charging energy of the dot must be the largest energy scale of the system. In particular, is must be larger than the average thermal energy $k_B T$ of electrons,

$$E_C = \frac{e^2}{C_{\text{dot}}} \gg k_B T \, . \tag{2.2}$$

2. The total number of electrons on the quantum dot must be well defined. Stated differently, the amount of charge on the island must be quantized in units of e. In practice, this requirement mandates that the tunnel barrier at each junction be sufficiently large. Quantum mechanically, this condition implies that the wavefunctions of electrons on the dot are well localized within the boundaries of the dot. Correspondingly, the tunnel resistances R_T of the tunnel junctions must be large (or equivalently their tunneling rates $\Gamma \propto 1/R_T$ must be small),

$$R_T \gg \frac{h}{e^2} \approx 25.8\,\text{k}\Omega \, . \tag{2.3}$$

The Coulomb blockade can be lifted in multiple ways. Most commonly, the voltage on a nearby electrode (called *gate*) is used to change the electrostatic potential of the quantum dot[1]. Once the gate has electrostatically overcome the charging energy, a single electron can tunnel onto the quantum dot. But unless an electron tunnels off, the dot is in Coulomb blockade again, and the gating procedure starts over before another electron can join the dot. In other words, the gate induces electrons discretely on the quantum dot, one at a time. This effect is called *single-electron charging* of the quantum dot and is described in more detail in Sec. 2.1.5.

Theoretically, the dynamics of quantum dots under the two conditions above is described by the so-called *orthodox theory* (Likharev 1988, Averin and Likharev 1991, Grabert and Horner 1991, Grabert and Devoret 1992, Sohn et al. 1997). A few aspects of this theory that are relevant to this thesis are outlined below.

2.1.3 Energy scales

To further specify condition 1 above, we explore a few energy scales that are native to quantum dots:

- The most important energy scale of quantum dots is the **charging energy** $E_C = e^2/C_{\text{dot}}$. It measures the strength of Coulomb interactions between charges on the dot and is determined by the size of the quantum dot. The smaller the quantum dot, the more pronounced the Coulomb interactions between the electrons on the quantum dot and the larger the charging energy.

- The **thermal energy** of electrons, $k_B T$, is set by the electron temperature T of the sample, where $k_B = 1.38 \times 10^{-23}$ J/K is Boltzmann's constant. The

[1] Alternatively to gating, a large bias across the quantum dot or irradiation with photons of high enough energy can also lift the Coulomb blockade.

electron temperature is important as it sets the width of the Fermi-Dirac distribution (2.10) in the charge reservoirs.

- Given the small size requirement for quantum dots, quantum mechanical effects such as energy level quantization may become important, as well. The relevant energy scale here is the single-particle **energy level spacing** $\Delta E_{\mathrm{level},N} = E_N - E_{N-1}$ of the quantum system. Apart from the size of the quantum dot, material parameters influence this energy scale.

- A charge that is energetically permitted to tunnel into the leads does not do so instantaneously. It still has a non-zero life time on the quantum dot, which is related to the finite tunneling rates that characterize the tunnel junctions of the dot. The energy scale $h\Gamma$ introduced by the electron life time $\tau = 1/\Gamma$ is the **intrinsic broadening** of Coulomb oscillations. It turns out that the requirement of small intrinsic broadening is equivalent to Eq. (2.3).

There are other energy scales of quantum dots that are not listed above. For example, the exchange energy of electrons, which favors alignment of their spins, is always present. Furthermore, particular samples may have additional energy scales that are not generic to quantum dots in general. To give an example, the description of quantum dots in CNTs (Oreg et al. 2000) involves the exchange energy J between electron spins, the subband mismatch δ, and the excess Coulomb energy δU. Experimental measurements on CNTs suggest, though, that these are small (Sapmaz et al. 2005).

Our experimental apparatus – the scanning force microscope – introduces another two energy scales that may become relevant during the measurement. The energy scales set by the AFM cantilever are the total energy stored in the can-

tilever, $\frac{1}{2}kz_\omega^2$, and the energy of a single oscillation quantum, $\hbar\omega_0$. Here k is the cantilever spring constant, z_ω is the oscillation amplitude, $2\pi\hbar = 6.626 \times 10^{-34}\,\mathrm{J\,s}$ is Planck's constant, and ω_0 is the cantilever resonance frequency. The total energy in the cantilever oscillations needs to be considered for peak broadening; different ratios between the cantilever resonance frequency and the electron tunneling rate, ω_0/Γ, can affect the measurement signal due to single-electron tunneling. We will comment on them in the experimental chapters as needed.

2.1.4 The classical and the quantum limit of Coulomb blockade

The conditions for observing Coulomb blockade phenomena, which were discussed in Sec. 2.1.2, mandate that the charging energy E_C is the largest energy scale in the system and that the intrinsic broadening $h\Gamma$ is small. This hierarchy of energy scales still leaves room for comparison between the thermal energy of electrons k_BT and the quantum level spacing of single-particle states $\Delta E_{\mathrm{level}}$. As a result, we distinguish between two different regimes of Coulomb blockade:

1. **Classical limit, $E_C \gg k_BT \gg \Delta E_{\mathrm{level}}$.** If the electron temperature is larger than the single-electron level spacing, the width of the Fermi-Dirac distribution of electrons in the charge reservoir spans multiple levels and the electron density of states of the dot is effectively continuous. This situation is called the *classical regime* of Coulomb blockade. In this limit, the state of the quantum dot is well described by the total number of electrons on the dot. The occupation of electron states on the dot follows the Fermi-Dirac distribution (2.10). Quantum dots in the classical regime are sometimes referred to as *classical dots*. For example, our gold nanoparticles at $T = 77\,\mathrm{K}$, as discussed in Chap. 6, fall certainly into the classical limit.

2. **Quantum limit,** $E_C \geq \Delta E_{\text{level}} \gg k_B T$**.** The single-particle energy levels retain their individual character in a measurement if the electron temperature is small compared to the non-interacting level spacing. Under this condition, quantum dots need to be treated as quantum mechanical objects with a discrete single-particle density of states. Denoting the state of the quantum dot in this limit is slightly more tedious as the occupation of each single-particle level needs to be accounted for.

While Coulomb blockade and single-electron charging phenomena are observed in either regime, the difference in the density of states of the quantum dot has subtle consequences on some details of the single-electron charging effects.

2.1.5 Electrostatics of quantum dots

For our analysis of quantum dots in the Coulomb blockade regime, we introduce two simplifications that are known as the *constant interaction model* (Averin et al. 1991, Kouwenhoven et al. 2001). This model assumes that the charging energy E_C is independent of the number of electrons on the quantum dot. In other words, the charging energy is taken to be the same for all charging events of the quantum dot. Furthermore, the constant interaction model hypothesizes that the single-particle energy spectrum is unaffected by the electron-electron interaction.

In our analysis, we start from a general quantum dot circuit. In principle, it can have any number of tunnel coupled leads and capacitively coupled gates. Fig. 2.2 illustrates two common circuits each containing one quantum dot. The simplest useful quantum dot circuit is the *single-electron box* (Fig. 2.2(a)), where the quantum dot is coupled to a single charge reservoir (labeled 'lead') and at least one gate. The most common quantum dot circuit is the *single-electron transistor*,

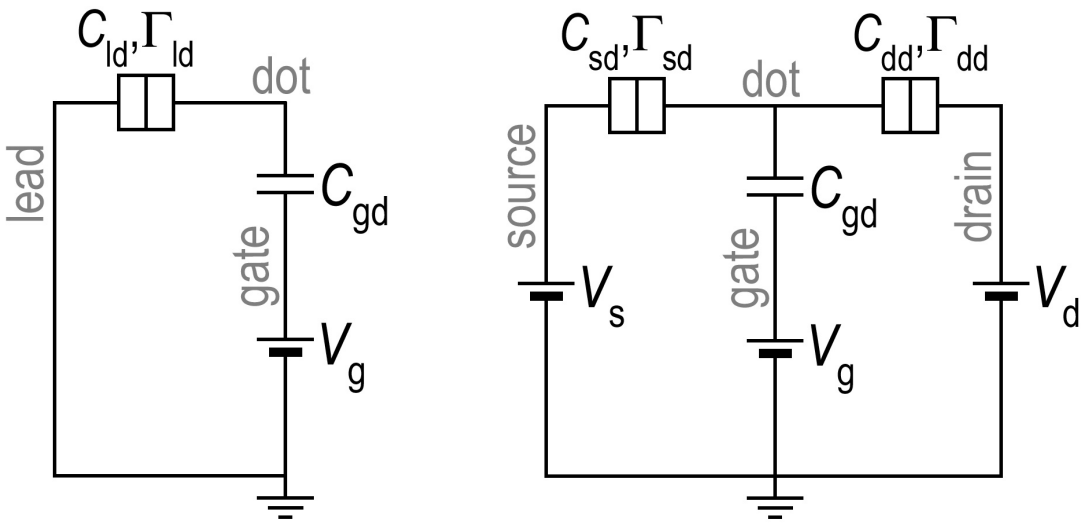

(a) Single-electron box.

(b) Single-electron transistor (SET).

Figure 2.2: Circuit diagrams of the single-electron box and the single-electron transistor, each with only one gate electrode. The different electrodes (except GND) are labeled in grey.

as shown in Fig. 2.2(b). Here the quantum dot couples to two charge reservoirs (labeled 'source' and 'drain') via tunnel barriers and has at least one gate.

To calculate the electrostatics of a quantum dot, we turn off all tunnel couplings to the quantum dot, which fixes the number of electrons on the dot and converts all tunnel barriers into capacitors. Then the circuit is easily analyzed in a total energy calculation or, more simply, in a capacitive network by Kirchhoff's laws. Assuming that there are N electrons on the dot, the electrostatic potential of the quantum dot is given by

$$\phi_{\mathrm{dot},\,N} = -(N-N_0)\,\frac{e}{C_{\mathrm{dot}}} + \sum_i \frac{C_{i\mathrm{d}}}{C_{\mathrm{dot}}}\,V_i\;. \tag{2.4}$$

The index i in the sum runs over all conductors in the system except for the quantum dot. $C_{i\mathrm{d}}$ is the mutual capacitances between the i^{th} conductor and the quantum dot, and V_i is the voltage on that conductor. N_0 is a constant that fixes the electrostatic potential of the dot when the number of electrons N on the dot and all voltages V_i are set to 0. The electrostatic potential depends on the total charge on the quantum dot, $q_{\mathrm{dot},\,N} = -(N-N_0)\,e$, and the voltages on all conductors. The latter is externally adjustable and sometimes summarized in a so-called *gate charge* or *control charge* q_{c} of the quantum dot,

$$q_{\mathrm{c}} = -\sum_i C_{i\mathrm{d}}\,V_i \qquad \Rightarrow \qquad \phi_{\mathrm{dot},\,N} = \frac{q_{\mathrm{dot},\,N} - q_{\mathrm{c}}}{C_{\mathrm{dot}}}\;. \tag{2.5}$$

The gate charge represents the charge that would like to reside on the quantum dot in the classical limit if charge wasn't quantized.

The chemical potential of the quantum dot depends on the density of single-particle states and is thereby different in the classical and quantum limit of Coulomb blockade. Correspondingly, we find different expressions for the electrochemical

potential of a quantum dot in either limit,

$$\begin{aligned} \mu_{\mathrm{cdot},\,N} &= -e\,\phi_{\mathrm{dot},\,N} = (N-N_0)\,\frac{e^2}{C_{\mathrm{dot}}} - \sum_i \frac{C_{i\mathrm{d}}}{C_{\mathrm{dot}}}\,eV_i\ , \\ \mu_{\mathrm{qdot},\,N} &= E_N - e\,\phi_{\mathrm{dot},\,N} = E_N + (N-N_0)\,\frac{e^2}{C_{\mathrm{dot}}} - \sum_i \frac{C_{i\mathrm{d}}}{C_{\mathrm{dot}}}\,eV_i\ . \end{aligned} \tag{2.6}$$

The labels 'cdot' and 'qdot' refer to the expressions in the classical and the quantum limit, respectively. E_N is the energy of the N^{th} single-particle level on the quantum dot.

We call the difference between electrochemical potentials of consecutive charge states of the quantum dot the *single-electron addition energy* E_{add}. It is given by

$$E_{\mathrm{add},\,N} = \mu_{\mathrm{dot},\,N} - \mu_{\mathrm{dot},\,N-1} \qquad \Rightarrow \qquad \begin{aligned} E^{(\mathrm{cdot})}_{\mathrm{add},\,N} &= \frac{e^2}{C_{\mathrm{dot}}} \\ E^{(\mathrm{qdot})}_{\mathrm{add},\,N} &= \Delta E_{\mathrm{level},\,N} + \frac{e^2}{C_{\mathrm{dot}}}\ , \end{aligned} \tag{2.7}$$

where $\Delta E_{\mathrm{level},\,N} = E_N - E_{N-1}$ is the single-particle level spacing, which is negligible in the classical limit. The addition energy in the classical limit is given by the charging energy (2.1) and independent of the number of electrons on the dot – at least within the constant interaction model. In the quantum limit, the addition energy is further increased by the single-particle energy level spacing.

We can ask how much change in gate voltage is needed to promote an additional electron onto the dot. This experimentally measurable quantity is called the single-electron *addition gate voltage* $\Delta V_{\mathrm{g}}^{(\mathrm{add})}$ of the gate g and determined by

$$\mu_{\mathrm{dot},\,N}(V_{\mathrm{g}} + \Delta V_{\mathrm{g}}^{(\mathrm{add})}) = \mu_{\mathrm{dot},\,N-1}(V_{\mathrm{g}}) \qquad \Rightarrow \qquad \frac{C_{\mathrm{gd}}}{C_{\mathrm{dot}}}\,e\Delta V_{\mathrm{g}}^{(\mathrm{add})} = E_{\mathrm{add}}\ . \tag{2.8}$$

Clearly, the addition gate voltage has to be scaled by the ratio between the gate-dot capacitance C_{gd} and the total dot capacitance C_{dot} in order to be converted to the generic quantum dot energy scale. We call this capacitance ratio the *gate*

efficiency of the particular gate (and dot),

$$\alpha_{\mathrm{g}} = \frac{C_{\mathrm{gd}}}{C_{\mathrm{dot}}} \ . \tag{2.9}$$

Some of the electrostatic properties of a quantum dot are plotted in Fig. **??**ore details and the derivations of the above equations can be found in the literature (Kouwenhoven et al. 1997, for example).

2.1.6 Tunneling rates

In this section we turn to the actual electron tunneling process of a quantum dot. The tunneling rate Γ of a tunnel junction is defined as the number of electrons tunneling across the barrier per time interval. Consequently, it is directly proportional to the tunneling current I. We distinguish between tunneling onto and off the quantum dot, $\Gamma_{\mathrm{on/off}} = \dfrac{I_{\mathrm{on/off}}}{-e}$. The tunneling rates depends on the properties of the tunnel junction, such as the height and width of the barrier. These properties are summarized in the tunneling resistance R_T. The tunneling rates also depend on the availability of occupied states on one side of the barrier and empty states on the other. If the impedance of the external circuit is small, as realized in the experiments, the electrons tunnel elastically across the barrier and an occupied and an empty states must align in energy. Consequently, the density of states and the occupation of these states on either side of the tunnel junction becomes relevant. We assume a constant and continuous density of states in the metal leads. The electron states in the leads are occupied according to the Fermi-Dirac distribution

$$f(\epsilon) = \frac{1}{1 + e^{\beta\epsilon}} \ , \tag{2.10}$$

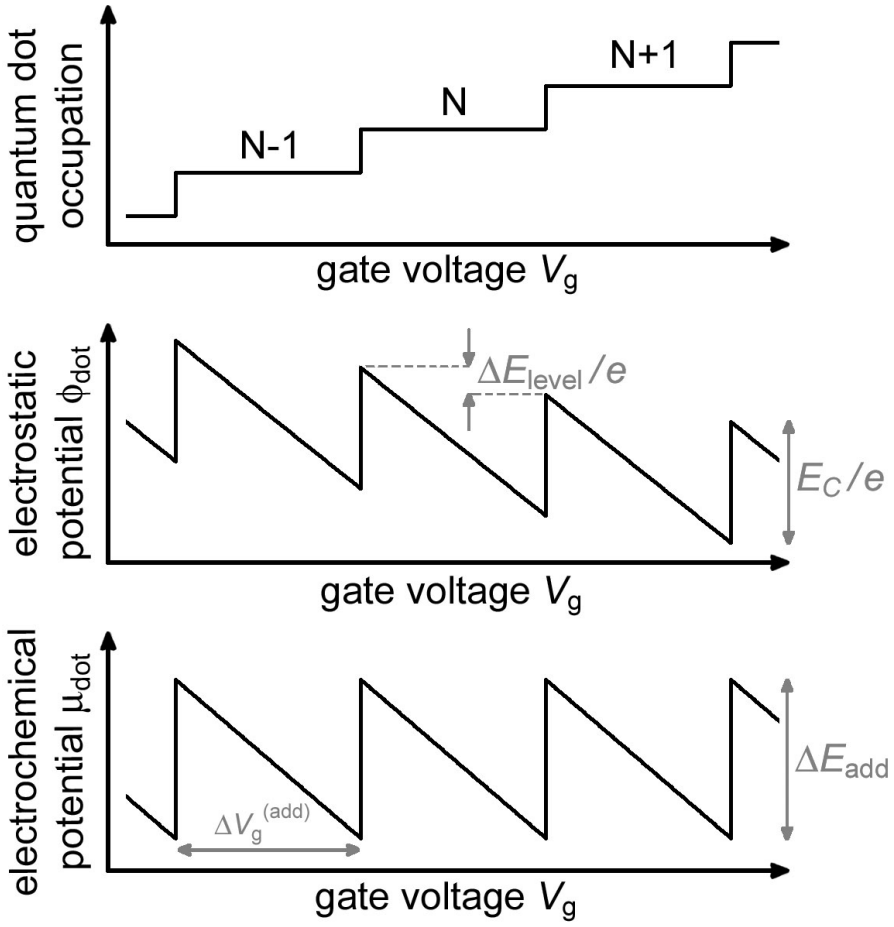

Figure 2.3: Electrostatic properties of a quantum dot at $T = 0$. The electrostatic potential and the electrochemical potential of the quantum dot are plotted from Eqs. (2.4) and (2.6). The quantum dot occupation is defined as $-q_{\mathrm{dot}}/e$. Adding another electron to the requires the addition gate voltage as calculated in Eq. (2.8). Upon tunneling of an electron, the electrostatic potential of the dot jumps by the charging energy (2.1) over the electron charge. At the same time, the addition energy jumps by addition energy (2.7).

where $\beta = 1/k_B T$ is the inverse temperature and $\epsilon = E - \mu$ is the energy E of the electron state under consideration, measured with respect to the electrochemical potential μ. On the other side of the tunnel junction, the description of the quantum dot depends on whether we are in the classical and in the quantum limit, as discussed in Sec. 2.1.4. The two limits are analyzed separately below.

Tunneling rates in the quantum limit, $\Delta E_{\rm level} \gg k_B T$. In the quantum limit, the density of states of the quantum dot reflects its discrete single-particle level structure. The state of the quantum dot is denoted by the occupation of each single-particle level. Correspondingly, tunneling occurs into and out of individual levels and we consider the tunneling process of a single quantum level first. Assuming that the level is empty, tunneling onto it occurs if the level is aligned with an occupied state in the lead. Since the electron occupation probability in the lead is distributed by the Fermi-Dirac function (2.10), the tunneling rate onto the level is given by the Fermi-Dirac distribution of the lead at the energy of the level, $f(E_{\rm level} - \mu_{\rm lead})$. Similarly, if the level is occupied, tunneling into the lead occurs if there is an empty final state available and the tunneling rate off the quantum level is given by $1 - f(E_{\rm level} - \mu_{\rm lead})$. Denoting the energy difference between the quantum level and the electrochemical potential of the lead by $\Delta E = E_{\rm level} - \mu_{\rm lead}$, we find

$$\begin{aligned} \Gamma_{\rm on}^{\rm (level)}(\Delta E) &= \Gamma_{\rm level}\, f(\Delta E) \\ \Gamma_{\rm off}^{\rm (level)}(\Delta E) &= \Gamma_{\rm level}\, [1 - f(\Delta E)] \;=\; \Gamma_{\rm level}\, f(-\Delta E)\ . \end{aligned} \tag{2.11}$$

Note that the tunneling rates obey the bias symmetry, $\Gamma_{\rm on}^{\rm (level)}(\Delta E) = \Gamma_{\rm off}^{\rm (level)}(-\Delta E)$.

The tunneling rates on and off the quantum dot are obtained by summing over the respective tunneling rates of all its single-particle levels and taking an ensemble average weighted by the grand canonical distribution function of the

quantum dot, as shown in the literature (Beenakker 1991). At low temperature the tunneling rate of a single level is sufficient for our description: Under the conditions of the quantum limit, at most one single-particle level of the quantum dot falls within the thermal width of the Fermi-Dirac distribution of the lead and potentially contributes to tunneling (van Houten et al. 1992, 2005). In the electronic ground state of the quantum dot in the quantum limit, all energy levels below the electrochemical potential of the dot are filled while all energy levels above it are empty. Correspondingly, this relevant level is located at the electrochemical potential of the quantum dot, so that $\Delta E = \mu_{\mathrm{dot}} - \mu_{\mathrm{lead}}$.

The amplitude of the tunneling rates (2.11)

$$\Gamma_{\mathrm{level}} \equiv \Gamma_{\mathrm{qdot}} = \frac{1}{e^2 R_T}\, h\nu_{\mathrm{level}} = \frac{1}{e^2 R_T}\, \Delta E_{\mathrm{level}} \tag{2.12}$$

are independent of ΔE. The quantity $\nu_{\mathrm{level}} = \frac{1}{2}\, v_F/L$ is the attempt frequency of the level, where v_F is the Fermi velocity of the particle, and L is the size of the quantum dot. Classically, the attempt frequency describes how often a particle on the level impinges on the barrier of the dot. Its relation to the single-particle energy level spacing is easily derived in the "particle in a 1D box" model (at high occupation $N \gg 1$). Notice that the sum of the two tunneling rates

$$\Gamma_{\mathrm{on}}^{(\mathrm{level})}(\Delta E) \;+\; \Gamma_{\mathrm{off}}^{(\mathrm{level})}(\Delta E) \;=\; \Gamma_{\mathrm{level}} \tag{2.13}$$

is independent of ΔE.

From Eq. (2.12) it is apparent that the condition of small intrinsic broadening, $h\Gamma_{\mathrm{level}} \ll \Delta E_{\mathrm{level}}$, is equivalent to the previously stated requirement (2.3) of large tunnel barriers for Coulomb blockade.

Tunneling rates in the classical limit, $k_B T \gg \Delta E_{\mathrm{level}}$. In the classical limit, the density of single-particle states on the quantum dot is continuous. Conse-

quently, the electron occupation on the quantum dot also follows the Fermi-Dirac distribution (2.10), just like in the lead. As a result, there are multiple single-particle states that could participated in tunneling, and we need to add up all their contributions. For example, to calculate the tunneling rate onto a classical dot, we need to evaluate the overlap between empty states on the dot, which are distributed by $1 - f(E-\mu_{\rm dot})$, and occupied electron states on the lead, which are distributed by $f(E-\mu_{\rm lead})$. Correspondingly, the tunneling rates onto and off in the classical regime are given by

$$\begin{aligned}
\Gamma_{\rm on}^{\rm (cdot)} &= \frac{1}{e^2 R_T} \int_{-\infty}^{\infty} dE\, [1 - f(E-\mu_{\rm dot})]\, f(E-\mu_{\rm lead}) = \frac{1}{e^2 R_T}\, \frac{-\Delta E}{1 - e^{\beta \Delta E}} \\
\Gamma_{\rm off}^{\rm (cdot)} &= \frac{1}{e^2 R_T} \int_{-\infty}^{\infty} dE\, f(E-\mu_{\rm dot})\, [1 - f(E-\mu_{\rm lead})] = \frac{1}{e^2 R_T}\, \frac{\Delta E}{1 - e^{-\beta \Delta E}}\ .
\end{aligned} \tag{2.14}$$

Just like in the quantum limit, ΔE is defined as the electrochemical potential difference between the dot and the lead, $\Delta E = \mu_{\rm dot} - \mu_{\rm lead}$. The calculation of the above integrals over products of Fermi-Dirac functions is detailed in the literature (Ingold and Nazarov 1992). Both tunneling rates are positive definite for all ΔE. For convenience of notation, we define the dimensionless function g as

$$g(\Delta E) = \frac{1}{2}\, \frac{-\beta\, \Delta E}{1 - e^{\beta\, \Delta E}}\ , \tag{2.15}$$

and rewrite the tunneling rates (2.14) in terms of this function as

$$\begin{aligned}
\Gamma_{\rm on}^{\rm (cdot)} &= \Gamma_{\rm cdot}\, g(\Delta E) \\
\Gamma_{\rm off}^{\rm (cdot)} &= \Gamma_{\rm cdot}\, g(-\Delta E)
\end{aligned} \qquad \text{with} \qquad \Gamma_{\rm cdot} = \frac{2\, k_B T}{e^2 R_T}\ . \tag{2.16}$$

In this notation, the tunneling rates for classical dots appear similar in structure to the ones for quantum dots, Eq. (2.11). The detailed functional form, however, is quite different. In particular, the relation equivalent to Eq. (2.13) does not hold in the classical limit. The tunneling rates (2.16) are plotted in Fig. 2.4.

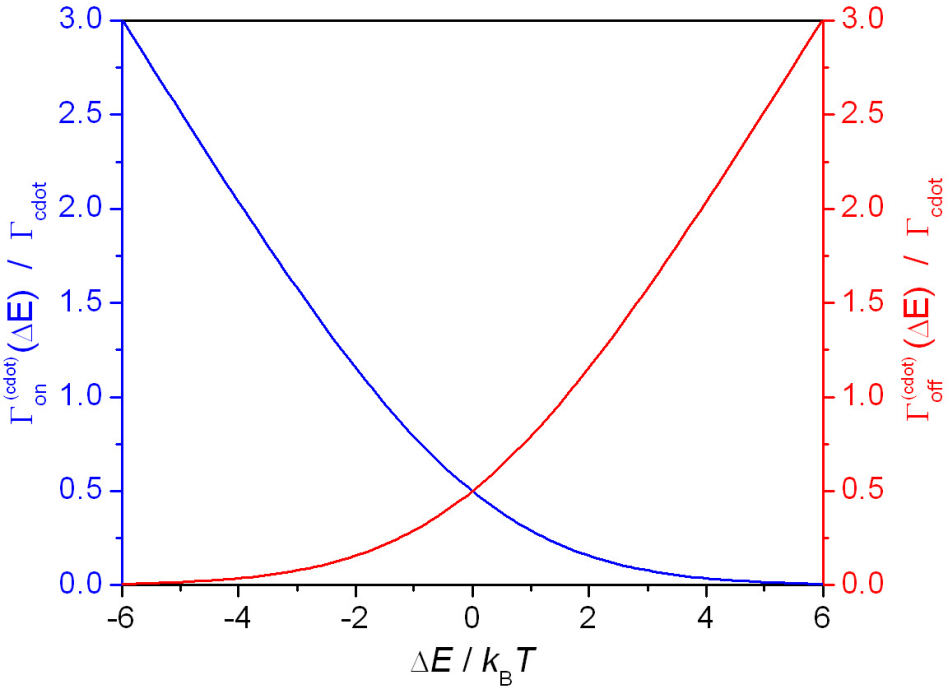

Figure 2.4: Tunneling rates $\Gamma_{\rm on}^{\rm (cdot)}(\Delta E)$ and $\Gamma_{\rm off}^{\rm (cdot)}(\Delta E)$ in the classical limit of Coulomb blockade as a function of the difference between the electrochemical potentials of the quantum dot and the lead, $\Delta E = \mu_{\rm dot} - \mu_{\rm lead}$, normalized by $k_B T$. The tunneling rates are derived in Eq. (2.16) and plotted in units of $\Gamma_{\rm cdot} = \dfrac{2\,k_B T}{e^2 R_T}$.

Given the amplitude of the tunneling rates in the classical limit, Eq. (2.16), small intrinsic broadening, $h\Gamma_{\mathrm{cdot}} \ll k_B T$, implies one of the two requirements for Coulomb blockade, Eq. (2.3).

2.1.7 Kinetic Equation for Occupation Probabilities

With the knowledge of the tunneling rates on and off the dot, we address some aspects of the state of the quantum dot and the change of state in response to changes in the environment, such as external perturbations. This description is important for experiment, as it allows us to describe the interaction between a quantum dot and our microscope. In Sec. 2.2.2, we use these results to describe the response of quantum dot to a biased AFM tip that is oscillating near the quantum dot and derive the resulting measurement signal in our local force detector.

In this section we introduce the *kinetic equation* for the state of quantum dots, which is also known as *rate equation* or *Master equation*. An underlying assumption of the kinetic equation is that any change of the state of the quantum dot can only depend on its current state. In stochastics, this "no memory" condition is called Markov property (Bharucha-Reid 1997, Papoulis and Pillai 2002). Since the state of a quantum dot is described differently in the classical and the quantum limit, we need two separate treatments in the two regimes. Fortunately, the two cases unify into one simplified description under well-fulfilled conditions.

In the following, we first discuss in some detail the solution to the kinetic equation in the classical regime, where the state of the quantum dot is described by the total number of electrons on the dot. From the kinetic equation, we derive the stationary state of the quantum dot in terms of the tunneling rates. The parallel derivation in the quantum limit is just as easy, but tedious and lengthy in

notation, because we have to account for each single-particle state and the change of it individually. For this reason, we don't detail the equations here, but comment on a simplification that is pragmatically motivated and applicable to the classical and quantum limit. This simplification is detailed at the end.

Kinetic equation in the classical regime, $k_BT \gg \Delta E_{\text{level}}$. As pointed out in Sec. 2.1.4, in the classical regime, the state of the quantum dot is specified by the total number of electrons on the dot. Denoting the probability to find the dot occupied with N electrons (and no more than N electrons) by p_N, its kinetic description follows the rate equation,

$$\frac{dp_N}{dt} = p_{N+1}\,\Gamma_{N+1\to N} + p_{N-1}\,\Gamma_{N-1\to N} - p_N(\Gamma_{N\to N+1} + \Gamma_{N\to N-1})\;. \tag{2.17}$$

Since electrons tunnel only one at a time (apart from cotunneling and other higher order processes, which we ignore here), only charge states differing by one electron are directly connected. The tunneling rate $\Gamma_{N+1\to N}$ contains the rates of all tunneling processes that change the charge state of the dot from $N{+}1$ to N electrons. Accounting for all leads i that are coupled to the dot via tunnel junctions,

$$\Gamma_{N\to N+1} = \sum_{\text{jcts}\,i} \Gamma_{\text{on},\,i,\,N} \qquad\qquad \Gamma_{N\to N-1} = \sum_{\text{jcts}\,i} \Gamma_{\text{off},\,i,\,N}\;. \tag{2.18}$$

For the equilibrium occupancy of the dot, the stationary solution $\dfrac{dp_N}{dt} = 0$ to the kinetic equation is satisfied by the *detailed balance* condition,

$$p_{N+1}\,\Gamma_{N+1\to N} = p_N\,\Gamma_{N\to N+1}\;. \tag{2.19}$$

It turns out that this is also the only non-trivial stationary solution. Essentially, the detailed balance requires that the current onto the dot is compensated by an equal

current off the dot. This recursion relation allows us to express all probabilities p_N in terms of one probability $p_{N_{\rm ref}}$ through

$$p_N = \begin{cases} p_{N_{\rm ref}} \displaystyle\prod_{n=N_{\rm ref}+1}^{N} \frac{\Gamma_{n-1\to n}}{\Gamma_{n\to n-1}} & N > N_{\rm ref} \ , \\ p_{N_{\rm ref}} \displaystyle\prod_{n=N}^{N_{\rm ref}} \frac{\Gamma_{n+1\to n}}{\Gamma_{n\to n+1}} & N < N_{\rm ref} \ . \end{cases} \tag{2.20}$$

The single remaining undetermined probability $p_{N_{\rm ref}}$ is fixed by the normalization condition

$$1 = \sum_{n=-\infty}^{\infty} p_n \ . \tag{2.21}$$

These relations (2.20) and (2.21) determine the equilibrium distribution $\{p_N\}$ of the charge states N of a quantum dot in the classical regime in terms of the tunneling rates (2.16).

Kinetic equation in the quantum limit, $k_BT \ll \Delta E_{\rm level}$. In the quantum limit, it is not enough to consider the total number of electrons on the dot to describe its state. Instead, we need to account for the possible occupation of each single-particle level. Correspondingly, tunneling into or out of each single-particle state has to be considered for the rate equation in the quantum limit, before taking an ensemble average. The kinetic equation for the change of state of the dot in the quantum limit is straight-forward, but lengthy to write down. For details, see the literature (Beenakker 1991).

Instead of detailing the full kinetic equation, we point out a pragmatic simplification: As touched upon in Sec. 2.1.6, almost all states have fixed occupation and there is realistically at most one single-particle level that participates in tunneling[2]. This is a result of the actual condition of the quantum limit, where the

[2]This conditions breaks down, of course, if a large bias is applied across the dot, if the quantum dot is irradiated with high-energy photons, etc.

separation of single particle levels is much larger than the thermal width of the Fermi-Dirac distribution of electrons in the lead. If only one single-particle state participates in tunneling, the state of the quantum dot can only change between two possible configurations: (1) The relevant state is occupied, or (2) the relevant state is empty. The kinetic equation for this binary phase space of quantum dot states is simple and easy to write down, as given in Eq. (2.25). This simplification of the kinetic equation is derived in the classical limit below, but it is also valid in the quantum limit, by virtue of the argument presented here.

Practical simplifications and unified kinetic equation. Since the charging energy is the largest energy scale in the system, different charge states of the quantum dot are well separated in energy. Consequently, under any given gating conditions, only one or at most two neighboring charge states are practically relevant for its description.

This situation implies that the tunneling rates leading away from either of the these two charge configurations are small (or equal to zero in the theoretical extreme), while the tunneling rates leading towards either charge configuration are large in comparison. Naming the two relevant charge states N and $N+1$, we formally require

$$\begin{aligned} \Gamma_{n-1\to n} &\ll \Gamma_{n\to n-1} \qquad \text{if} \quad n > N+1 \\ \Gamma_{n\to n+1} &\gg \Gamma_{n+1\to n} \qquad \text{if} \quad n < N \end{aligned} \tag{2.22}$$

as the minimum necessary conditions for the simplifications below. Indeed, looking at the tunneling rates in the classical limit, Fig. 2.4, the rates onto and off the dot are only similar near $\mu_{\rm dot} = \mu_{\rm lead}$ (denoted as $\Delta E = 0$). At $\Delta E \geq E_C \gg k_B T$ we find $\Gamma_{\rm on}^{\rm (cdot)}(\Delta E) \ll \Gamma_{\rm off}^{\rm (cdot)}(\Delta E)$ and similarly $\Gamma_{\rm on}^{\rm (cdot)}(\Delta E) \gg \Gamma_{\rm off}^{\rm (cdot)}(\Delta E)$ at $\Delta E \leq -E_C \ll -k_B T$, as needed for Eq. (2.22).

As a result of the conditions (2.22), we find (by design) for our occupation probabilities

$$p_n \approx 0 \qquad \forall n \notin \{N, N+1\} \tag{2.23}$$

from the detailed balance equation (2.19) and

$$p_N = 1 - p_{N+1} \tag{2.24}$$

by normalization (2.21). Under these conditions, the kinetic equation (2.17) for the probability of occupying the dot with $N+1$ electrons simplifies to

$$\frac{dp_{N+1}}{dt} \;=\; (1 - p_{N+1})\,\Gamma_{\text{on}} \;-\; p_{N+1}\,\Gamma_{\text{off}}\;, \tag{2.25}$$

where we have used the intuitive shorthand notation $\Gamma_{\text{on}} = \Gamma_{N\to N+1}$ and $\Gamma_{\text{off}} = \Gamma_{N+1\to N}$ for the tunneling rates between the two relevant charge states. This simplified kinetic equation is also valid in the quantum limit, as argued above.

We will use this kinetic equation in Sec. 2.2.2 to calculate the response of a quantum dot when it is driven out of equilibrium.

2.1.8 Coupled quantum dots

The unusual electronic properties of quantum dots make them interesting building blocks for circuits, where single-electron control is needed. Several quantum dots can be arranged in a network to perform a more complex function. For example, several quantum dots can be strung in series to form a turnstile or a single-electron pump (Pothier et al. 1991, Kouwenhoven et al. 1991, 1992, Keller et al. 1999). When two quantum dots are connected by a tunnel barrier, we call these two dots *coupled*. An elementary circuit of a coupled double dot system, where the gate charge of each dot can be tuned independently, is shown in Fig. 2.5. The tunnel

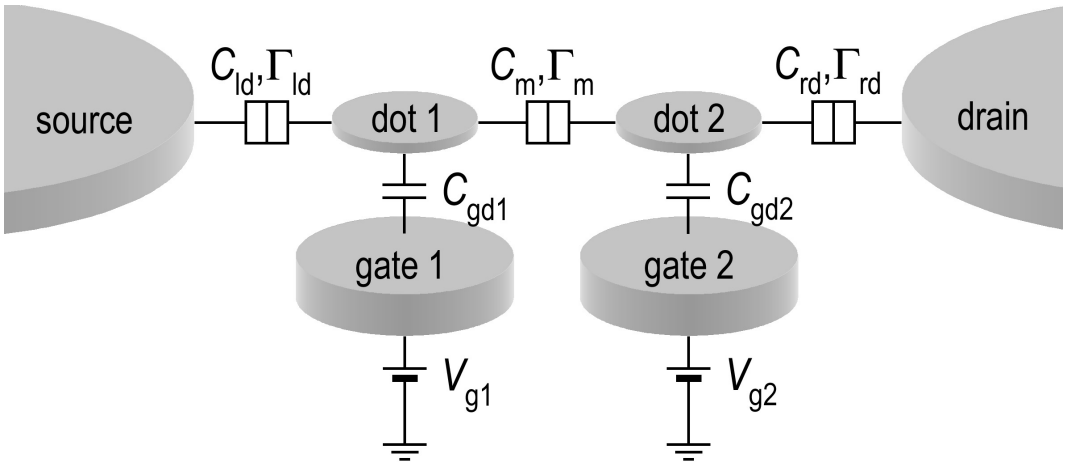

Figure 2.5: Schematic circuit layout of a typical double dot system with two independent gates, each coupling to only one quantum dot. The tunnel barrier that couples the two quantum dots is characterized by an interdot tunneling rate Γ_{m} and a mutual dot capacitance C_{m}. Each quantum dot couples to a separate charge reservoir (labeled source and drain). The charge reservoirs set the electrostatic potential reference for their respective dot and provide charges to tunnel on or off their dot as needed. For a stability diagram with sharp triple points, as shown in Fig. 2.6(a), the source and drain contacts have to be shorted (zero bias).

barrier that couples the two quantum dots is characterized by an interdot tunneling rate $\Gamma_{\rm m}$ and a mutual capacitance $C_{\rm m}$. In this circuit, each quantum dot couples to a separate charge reservoir, which sets the reference electrochemical potential for the respective dots and provides or accepts electrons to tunnel onto or off the dot. This circuit is useful to explore the basic properties of coupled quantum dots and the effects that one quantum dot has onto another.

The Stability Diagram. As the term suggests, in a coupled quantum dot system, the state of a quantum dot also depends on the state of other, coupled dots. A useful representation of the charge state of two dots in a coupled double dot system as a function of their gate voltages is the *stability diagram* (Pothier et al. 1992). Figure 2.6(a) shows a typical stability diagram of a coupled double dot system. Due to its appearance, the stability diagram is sometimes also called *honeycomb diagram*. In this plot, each dot has a separate gate that doesn't couple to the other dot, as illustrated schematically in Fig. 2.5. In the stability diagram, the stable charge state of the double dot system at any given combination of gate voltages $V_{\rm g1}$ and $V_{\rm g2}$ is labeled by (N_1, N_2), where N_1 and N_2 represent the number of electrons on dot #1 and #2, respectively. Different charge states of the double dot system are separated by single-electron charging events of either dot, as depicted by black lines. The zig-zag shape of these single-electron charging lines is due to the coupling between the dots. Figure 2.6(b) shows the same stability diagram in the absence of coupling, $\Gamma_{\rm m} \to 0$ and $C_{\rm m} \to 0$. In this case, we find quadruple points where 4 different charge states of the double dot system meet. In the presence of coupling between the two quantum dots, these quadruple points split into two separate triple points. In other words, the coupling creates an avoided crossing of the single-electron charging lines at their intersection, near the quadruple points.

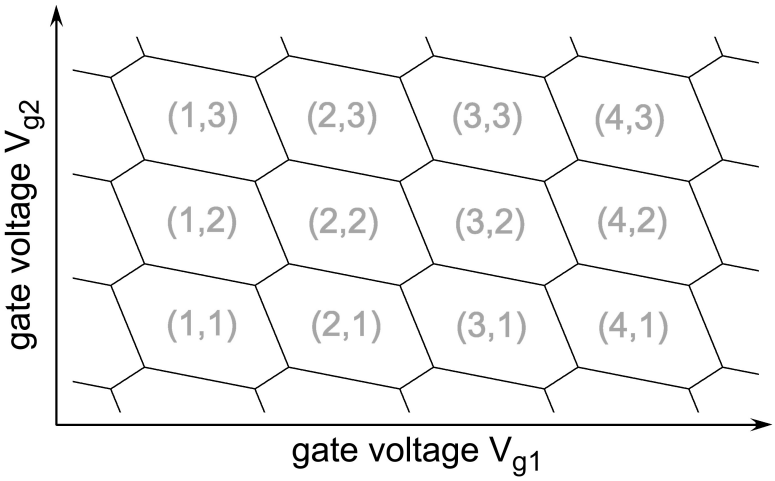

(a) Stability diagram of a coupled double dot system.

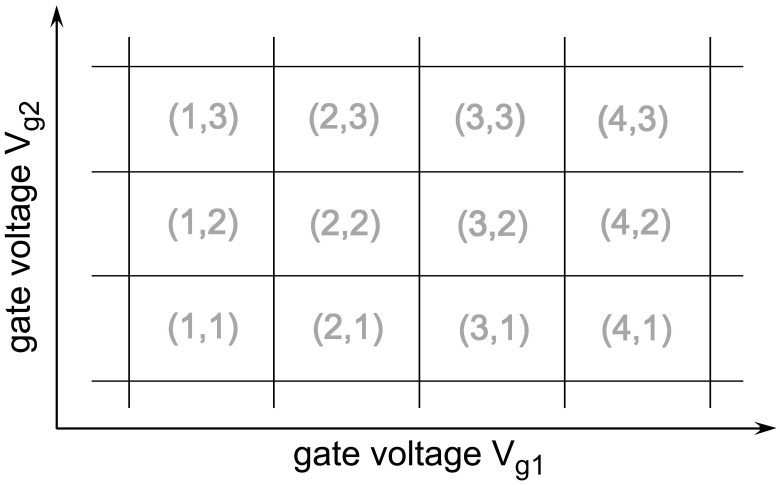

(b) Stability diagram of two non-interacting quantum dots.

Figure 2.6: Stability diagrams of a double dot system with and without coupling. Both diagrams assume that the gate voltages V_{g1} and V_{g2} couple only to their respective dots, as illustrated in Fig. 2.5. The labels (N_1, N_2) denote the equilibrium occupation of electrons on dot #1 and #2, respectively, up to an offset. The coupled dot diagram reduces to the non-interacting case in the limit of vanishing coupling, $\Gamma_m \to 0$ and $C_m \to 0$. For sharp triple points, as shown in Fig. 2.6(a), the source and drain contacts have to be at the same potential (zero bias).

Possible Origins of the Line Splitting. As discussed above, the avoided crossings in the stability diagram are a sign of interaction between the two quantum dots whose single-electron charging lines intersect. In the metaphor of artificial atoms, we could say that the two quantum dots show signs of forming a molecule. The splitting of the charging lines can be either due to an elevated interdot tunnel coupling Γ_m (covalent molecular bond) or a large mutual capacitance C_m (ionic molecular bond) between the quantum dots (Waugh et al. 1996, Livermore et al. 1996). Since the mechanism that causes the line splitting is somewhat different in either case, we comment on both possibilities separately.

Capacitively coupled double dots. Capacitively coupled quantum dots are conceptually easier to treat than tunnel-coupled dots, as it is a purely classical effect consistent with the requirements for Coulomb blockade phenomena. The splitting of single-electron charging lines due to capacitive coupling is well described within the orthodox theory. It assumes, though, that the interdot tunnel coupling is small, $\Gamma_\mathrm{m} \to 0$ or equivalently $1/\Gamma_\mathrm{m} \propto R_T^{(\mathrm{m})} \gg h/2e^2$.

The mechanism that creates the avoided crossings by means of a mutual dot capacitance works as follows[3]: When an electron tunnels onto a quantum dot, its electrostatic potential jumps by $-e/C_\mathrm{dot}$. If the dot is capacitively coupled to another dot, this change won't go unnoticed by the other. The jump in electrostatic potential induces a gate charge of $-eC_\mathrm{m}/C_\mathrm{dot}$ on the other dot. In this way the mutual dot capacitance makes the other dot part of its electrostatic environment.

[3]The detailed functional form of the three expressions in this intuitive explanation is only accurate as long as the mutual dot capacitance is not too large. There is a correction factor of $(1-\frac{C_\mathrm{m}^2}{C_1\,C_2})^{-1}$ to all three terms that becomes relevant when the coupling capacitance becomes large, $C_\mathrm{m} \to C_\mathrm{dot}$. We omit this correction in this paragraph to keep the expressions simple and short. For more details, see Appendix A.1.

Effectively, the capacitively coupled dots gate each other with an interdot gating efficiency $C_{\rm m}/C_{\rm dot}$. The induced gate charge due to the electron tunneling onto the first dot needs to be compensated for by the gate on the second dot. Consequently, this gate voltage must increase further in order to induce an electron onto the other dot. This compensative gating appears as splitting of the single-electron charging lines in the images.

Tunnel-coupled double dots. The interdot tunnel coupling $\Gamma_{\rm m}$ increases when the tunnel barrier $R_T^{(\rm m)} \propto 1/\Gamma_{\rm m}$ between the dots is lowered. As a result, the wave function of electrons may extend across the barrier onto the other dot. When the ground state energies of the two dots line up (at the intersection of two charging lines), the double dot system can lower its energy by mixing the electronic states of the two dots. This mixing or entanglement of states breaks the degeneracy and lowers the energy of the coupled double dot system compared to the sum of the isolated dot energies. This mechanism causes the single-electron charging lines to split (Waugh et al. 1995, Livermore et al. 1996). At the same time, we relax one of the two conditions for the formation of quantum dots, Eq. (2.3), and the orthodox theory breaks down.

In the extreme limit of very large tunnel coupling ($R_T^{(\rm m)} \approx h/2e^2$), the two dots join into one larger dot. Then the orthodox theory is applicable again, provided that the combined dot is well isolated. In this extreme limit, the mutual capacitance between the two dots is shorted out and has no longer any influence.

Unified description of quantum dot interactions: Coupling impedance. Before finishing the section on coupled quantum dots, we want to bring forward and briefly discuss an idea for a unified description of the two coupling mecha-

nisms discussed above. This idea is phenomenological in nature and based on the equivalent circuit model of a tunnel junction, Fig. 2.1, applied to the interdot barrier. The contributions from the tunnel coupling $\Gamma_{\rm m} \propto 1/R_T^{(\rm m)}$ and the mutual dot capacitance $C_{\rm m}$ to the line splitting could be accounted for in terms of a coupling impedance

$$Z_{\rm m} = R_T^{(\rm m)} \parallel (i\omega C_{\rm m})^{-1} = \frac{R_T^{(\rm m)}}{1 + i\omega C_{\rm m} R_T^{(\rm m)}} \; . \tag{2.26}$$

Both limiting cases of dominant interdot tunneling ($C_{\rm m} \to 0$) and purely capacitive coupling ($R_T^{(\rm m)} \to \infty$) are included in the description. This concept of a coupling impedance is most useful in the mixed coupling regime, though.

The frequency parameter appearing in the expression (2.26) should be determined by the electrostatic coupling energy, $E_{C_{\rm m}} = \hbar\omega$, which is given in Eq. (A.3) in Appendix A.1 and derived in the literature (Ruzin et al. 1992, Dixon 1998, van der Wiel et al. 2003). This results in the expression

$$\omega C_{\rm m} = -2\pi \, \frac{e^2}{h} \, \frac{1}{1 - C_1 C_2 / C_{\rm m}^2} \tag{2.27}$$

to appear in the denominator of Eq. (2.26), where C_1 and C_2 are the total capacitances of the two coupled quantum dots.

Checking the strong coupling limit, we find that in either strong coupling case[4], $R_T^{(\rm m)} \to 0$ or $C_{\rm m} \to \sqrt{C_1 C_2}$, the coupling impedance (2.26) vanishes, $Z_{\rm m} \to 0$. The fact that both weak and both strong coupling limits reproduce the expected result for the proposed coupling impedance gives us confidence in the validity of this concept of a unified, phenomenological description of the interdot coupling.

[4]Note that the interdot capacitance is constrained by the total dot capacitances, $C_{\rm m} \leq C_1$ and $C_{\rm m} \leq C_2$. Consequently, zero coupling impedance can only be achieved capacitively if $C_{\rm m} = C_1 = C_2$.

2.2 Cantilever Dynamics

In this section we turn to our measurement tool, the atomic force microscope (AFM). The cantilever is at the heart of the AFM. It is a mobile, microscopic detector that senses forces acting on the tip. Modeling the cantilever as a simple harmonic oscillator, we can treat it classically: With our cantilever parameters (Table 3.1) and a typical resonance amplitude of 1 nm, there a literally billions of harmonic oscillator quanta excited in the cantilever.

The first part of this section reviews the basic cantilever dynamics under the influence of different external forces. Since classical harmonic resonators are covered extensively in many textbooks, most results will be stated for later reference without detailed derivations. In the second part we combine the description of the AFM and quantum dots and detail a theory of interaction in linear response.

2.2.1 The Damped Harmonic Oscillator

A damped harmonic oscillator is characterized by three intrinsic parameters – its effective mass m, damping coefficient γ, and spring constant k – and follows the dynamic equation

$$m\frac{d^2z}{dt^2} + \gamma\frac{dz}{dt} + k\,(z - z_0) = F_{\text{ext}}(z,t)\;. \tag{2.28}$$

The value of the static deflection z_0 depends on the origin of the coordinate system. Experimentally, z_0 is the static tip height above the sample surface (as set by the scan tube extension). $F_{\text{ext}}(z,t)$ is an external force that may depend on both tip position z and time t. It includes any force that we deliberately apply to the tip or cantilever, for example, the actuation force to drive the cantilever on resonance, and the forces originating from the sample, which we try to resolve. The tip

deflection $\Delta z = z - z_0$ is the readout signal in the experiment, which may have a static (dc) and an oscillating (ac) component.

From an experimental point of view, the AFM cantilever is more readily described in terms of a related set of parameters – the resonance frequency of its free, undamped motion $\omega_0 = \sqrt{k/m}$, the spring constant k, and the quality factor of the resonance $Q = m\omega_0/\gamma$, whose inverse measures the full width at half power of the resonance peak, $\Delta\omega_{\mathrm{FWHP}} = \gamma/m$. In terms of these intrinsic parameters $\{\omega_0, Q, k\}$, the equation of motion reads

$$\frac{d^2z}{dt^2} + \frac{\omega_0}{Q}\frac{dz}{dt} + \omega_0^2\,(z - z_0) = \frac{\omega_0^2}{k}\,F_{\mathrm{ext}}(z,t)\ . \tag{2.29}$$

The effects of several different forces on the cantilever are discussed below.

Briefly, time-independent forces that are constant or linear in z are simple to treat. Constant forces create an equilibrium deflection and dc-force gradients change the spring constant, thus shifting the resonance frequency. In effect, they map back onto the free oscillation problem with altered parameters. Higher order dc-force terms will not be treated in this chapter. Non-linear effects and the Duffing oscillator are treated in the literature (Minorsky 1962, Hayashi 1985, Nayfeh and Mook 1979, Hagedorn and Stadler 1988). Non-linearities can be avoided experimentally by limiting the cantilever oscillations and deflections to small amplitudes.

For external forces that don't depend on the spatial coordinate z, i.e., purely time-dependent forces, the superposition principle allows us to consider each force term separately. In particular, we can Fourier decompose any time-dependent force and consider contributions from different frequencies separately. In the end, the oscillator acts like the sum of the solutions due to the individual (z-independent) forces. For high-Q cantilevers, the amplitude response is sharply peaked about the cantilever resonance, and for small force amplitudes only frequencies near reso-

nance will be relevant. Additionally, the use of filters and lock-in amplifiers in our experiments enables us to look at the response at specific frequencies and thereby permits to delineate between different frequency contributions.

Damped, free oscillations: $F_{\mathrm{ext}}(z,t) = 0$. In the absence of external forces, the cantilever motion follows

$$z(t) = z_0 + z_{\mathrm{m}}\, e^{-t/\tau} \cos(\omega_{\mathrm{res}} t + \phi_{\mathrm{m}}) \; . \tag{2.30}$$

The amplitude z_{m} and phase ϕ_{m} of the oscillation are determined by the initial conditions[5]. This so-called *homogenous solution* of the differential equation (2.28) describes resonant oscillations of the cantilever about its equilibrium deflection z_0 that decay exponentially due to damping. As the oscillations decay, the cantilever approaches the static deflection z_0. The time constant of the exponential decay, commonly also called *ring-down time*,

$$\tau = \frac{2m}{\gamma} = \frac{2Q}{\omega_0} \tag{2.31}$$

scales linearly with the quality factor. The damped free resonance frequency

$$\omega_{\mathrm{res}} = \omega_0 \sqrt{1 - \frac{1}{4Q^2}} \quad \xrightarrow{Q \gg 1} \quad \omega_0 \left(1 - \frac{1}{8Q^2}\right) \; . \tag{2.32}$$

is shifted from the undamped resonance frequency ω_0. For our cantilevers with high quality factors in vacuum, this shift in resonance frequency due to damping is extremely small, about 1 ppb (part per billion) of the undamped resonance

[5] If the initial deflection $z(0)$ and its time derivative $\dot{z}(0)$ are given at time $t = 0$, the parameters z_{m} and ϕ_{m} follow from

$$z_{\mathrm{m}} \cos(\phi_{\mathrm{m}}) = z(0) - z_0 \qquad \text{and} \qquad z_{\mathrm{m}} \sin(\phi_{\mathrm{m}}) = \frac{\tau\, \dot{z}(0) + z(0) - z_0}{\omega_{\mathrm{res}}\, \tau} \; .$$

frequency. Hence, in the following we won't differentiate between the 'damped' and 'undamped' resonance any longer and use ω_0 and $\omega_{\rm res}$ interchangeably.

The relevance of this solution to the homogeneous differential equation is that every solution[6] to Eq. (2.28) contains an additive term of the form (2.30). If the excitation force or the resonance frequency changes (as we scan across the surface or change some experimental parameter, for example), the transient towards a new stationary amplitude is described by Eq. (2.30) with a transient time (2.31). For high cantilever quality factors (as in our vacuum system) this transient time can be significant and mandates slow scan speed for amplitude images.

Time-independent external force $F_{\rm ext}(z,t) = F_{\rm dc}(z)$. Any static force that doesn't vanish at the static deflection z_0 of the cantilever, $F_{\rm dc}(z_0) \neq 0$, changes the static deflection from z_0 to a new equilibrium deflection value $z_{\rm eq}$ given by

$$z_{\rm eq} = z_0 + \frac{F_{\rm dc}(z_{\rm eq})}{k} \ . \tag{2.33}$$

Notice that this equation is implicit in $z_{\rm eq}$, as the new equilibrium deflection depends on the functional form of the static force $F_{\rm dc}(z)$.

If the cantilever oscillation is small in amplitude, non-linear terms of the force are negligible and we can expand the force about the equilibrium deflection $z_{\rm eq}$,

$$F_{\rm dc}(z) = F_{\rm dc}(z_{\rm eq}) + \left.\frac{F_{\rm dc}}{dz}\right|_{z=z_{\rm eq}} (z-z_{\rm eq}) + o(z-z_{\rm eq})^2 \ , \tag{2.34}$$

and the problem can be mapped back onto a free, damped oscillation

$$m\frac{d^2z}{dt^2} + \gamma\frac{dz}{dt} + \left(k - \left.\frac{dF_{\rm dc}}{dz}\right|_{z_{\rm eq}}\right)(z-z_{\rm eq}) = 0 \tag{2.35}$$

[6]Mathematically, this statement requires a linear differential equation and, hence, a force law that contains only constant or linear terms in $z-z_0$. Since we limit the cantilever to small oscillation amplitudes in the experiment, non-linear force terms are typically negligible and the statement remains valid.

as described in Eq. (2.28), but with a new equilibrium deflection $z_{\rm eq}$ as given in Eq. (2.33) and an effective spring constant that is shifted by the spatial force gradient,

$$k_{\rm eff} = k - \left.\frac{dF_{\rm dc}}{dz}\right|_{z=z_{\rm eq}} . \tag{2.36}$$

Correspondingly, the undamped resonance frequency shifts to a new value

$$\tilde{\omega}_0 = \sqrt{\frac{k_{\rm eff}}{m}} = \omega_0 \sqrt{\frac{k_{\rm eff}}{k}} \simeq \omega_0 \left(1 - \frac{1}{2k} \left.\frac{dF_{\rm dc}}{dz}\right|_{z_{\rm eq}}\right) . \tag{2.37}$$

This relation is compactly expressed as a relative frequency shift,

$$\frac{\Delta\omega_0}{\omega_0} \simeq -\frac{1}{2k} \left.\frac{dF_{\rm dc}}{dz}\right|_{z_{\rm eq}} , \tag{2.38}$$

where $\Delta\omega_0 = \tilde{\omega}_0 - \omega_0$ is the absolute frequency shift. The width of the resonance $\Delta\omega_{\rm FWHP} = \gamma/m$ remains unchanged, but the quality factor changes to

$$\tilde{Q} = \frac{m\tilde{\omega}_0}{\gamma} = \frac{\tilde{\omega}_0}{\Delta\omega_{\rm FWHP}} = Q\,\frac{\tilde{\omega}_0}{\omega_0} = Q\sqrt{\frac{k_{\rm eff}}{k}} . \tag{2.39}$$

It is important to note that this change in quality factor does not correspond to a change in dissipation. The quality factor is the ratio of the energy stored in the resonator to the energy dissipated in one oscillation cycle, i.e., $1/Q$ measures the fractional energy loss per cycle. While the absolute energy loss remains constant, the energy stored in the cantilever $\frac{1}{2}kz_{\rm max}^2$ changes with a shift in spring constant (2.36) due to force gradient, creating a change in the quality factor.

Periodic driving force with constant force amplitude: $F_{\rm ext}(z,t) = F_\omega \cos(\omega t)$**.** The steady state response of the damped harmonic oscillator to a harmonic driving force is to oscillate at the same frequency ω as the driving force with a phase lag,

$$z(t) = z_0 + z_\omega \cos(\omega t - \theta_\omega) . \tag{2.40}$$

The amplitude and phase of the oscillation generally depend on the driving frequency. For a constant force amplitude F_ω one finds

$$z_\omega = \frac{F_\omega}{k} \frac{\omega_0^2}{\sqrt{\left(\omega_0^2 - \omega^2\right)^2 + \left(\omega\omega_0/Q\right)^2}} \xrightarrow{\omega\to\omega_0} \frac{F_\omega}{k} Q$$
$$\tan(\theta_\omega) = \frac{1}{Q} \frac{\omega\,\omega_0}{\omega_0^2 - \omega^2} \xrightarrow{\omega\to\omega_0} \frac{1}{2Q} \frac{\omega_0}{\omega_0 - \omega} \,. \tag{2.41}$$

A plot of the oscillation amplitude z_ω as a function of the driving frequency ω is termed *resonance curve* of the oscillator (provided that $Q > \frac{1}{2}$). Figure 2.7 plots the amplitude resonance curve and the phase response of the oscillator, as given in Eq. (2.41). The resonance curve directly measures the cantilever resonance frequency ω_0 and its quality factor Q, as indicated in Fig. 2.7. From this common representation of the phase lag θ_ω, it is only incompletely determined (modulo π as opposed to 2π). The phase lag is fully specified by

$$\sin(\theta_\omega) = \frac{z_\omega \omega \gamma}{F_\omega} = \frac{1}{Q}\frac{\omega}{\omega_0}\frac{k z_\omega}{F_\omega} \qquad \text{and} \qquad \cos(\theta_\omega) = \left(1 - \frac{\omega^2}{\omega_0^2}\right)\frac{k z_\omega}{F_\omega} \tag{2.42}$$

or by giving the sign of either $\sin(\theta_\omega)$ or $\cos(\theta_\omega)$ in addition to $\tan(\theta_\omega)$. The oscillation amplitude on resonance[7]

$$z_{\omega_0} = \frac{F_{\omega_0}}{k} Q \tag{2.43}$$

[7]The true resonance frequency – defined as the maximum of the resonance curve Eq. (2.40) – is located at

$$\omega_{\max} = \omega_0 \sqrt{1 - \frac{1}{2Q^2}} \xrightarrow{Q\gg 1} \omega_0 \left(1 - \frac{1}{4Q^2}\right)$$

with an amplitude response

$$z_{\omega_{\max}} = \frac{z_{\omega_0}}{\sqrt{1 - \frac{1}{4Q^2}}} \xrightarrow{Q\gg 1} z_{\omega_0}\left(1 + \frac{1}{8Q^2}\right) \,.$$

For large quality factors as in our experiments, these corrections are extremely small, though, about 1 part per billion (see Table 3.1).

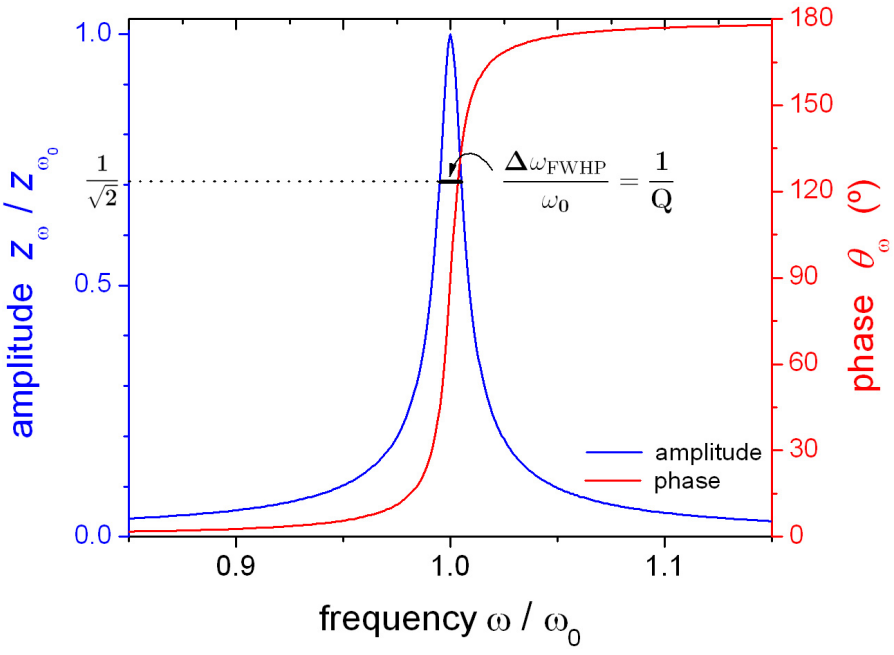

Figure 2.7: Amplitude resonance curve and phase response of a harmonic oscillator. The amplitude and phase are calculated from Eq. (2.41), assuming $Q = 100$. The location of the maximum of the resonance curve gives the resonance frequency of the oscillator. The width of the resonance frequency (at an amplitude $\frac{z_{\omega_0}}{\sqrt{2}}$) determines the inverse quality factor $1/Q$, as shown. On resonance, the oscillator responds with a 90° phase lag with respect to the driving force. The phase changes sensitively with driving frequency near resonance.

is amplified by the quality factor Q (compared to a corresponding dc deflection signal). Similarly, the phase θ_ω is most sensitive on resonance, changing from zero phase lag at low frequencies to π at high frequencies with $\theta_{\omega_0} = \pi/2$ on resonance. Most of the phase change happens within the frequency range $\omega_0 \pm \gamma/2m = \omega_0(1 \pm 1/2Q)$, and is determined by the quality factor Q, too.

Static and harmonic force: $F_{\rm ext}(z,t) = F_{\rm dc}(z) + F_\omega \cos(\omega t)$. If a static force is applied in addition to a periodic driving force with constant force amplitude, we can apply the previous two cases sequentially. First, the static force $F_{\rm dc}(z)$ changes the equilibrium tip position from z_0 to $z_{\rm eq}$ and shifts the resonance frequency to $\tilde{\omega}_0$ according to Eqs. (2.33,2.38), independently of any purely time-dependent force. Hence, the problem is mapped back to an ac-driven resonator as treated in the previous paragraph, but with different parameters $\{\tilde{\omega}_0, \tilde{Q}, k_{\rm eff}\}$ and equilibrium position $z_{\rm eq}$. In effect, the amplitude resonance curve and the phase response retain their shape, but are centered about the shifted resonance frequency $\tilde{\omega}_0$,

$$z_\omega = \frac{F_\omega}{k} \frac{\omega_0^2}{\sqrt{\left(\tilde{\omega}_0^2 - \omega^2\right)^2 + \left(\omega\omega_0/Q\right)^2}} \qquad \text{and} \qquad \tan(\theta_\omega) = \frac{1}{Q} \frac{\omega\,\omega_0}{\tilde{\omega}_0^2 - \omega^2} \tag{2.44}$$

This can be verified by substituting the shifted parameters $\{\tilde{\omega}_0,\, \tilde{Q},\, k_{\rm eff}\}$ as given in Eqs. (2.36, 2.37, 2.39) in the resonance curve (2.41) and using the invariants $k/\omega_0^2 = k_{\rm eff}/\tilde{\omega}_0^2 = m$ and $\omega_0/Q = \tilde{\omega}_0/\tilde{Q} = \gamma/m = \Delta\omega_{\rm FWHP}$.

Periodic driving force with force gradient: $F_{\rm ext}(z,t) = F_\omega(z)\cos(\omega t)$. The situation becomes more complicated if the force amplitude changes as a function of z. As usual we assume a small oscillation amplitude about the equilibrium deflection and Taylor expand the force amplitude,

$$F_\omega(z) = F_\omega(z_0) + \left.\frac{dF_\omega}{dz}\right|_{z=z_0} (z - z_0) + o(z - z_0)^2 \,. \tag{2.45}$$

The constant term in the expansion, $F_\omega(z_0)\cos(\omega t)$, excites oscillations at the drive frequency ω, as described in the previous paragraph. The force gradient term in the expansion couples in higher harmonics, as do higher order terms in the expansion. The steady state amplitude response to Eq. (2.45) is of the form

$$z(t) = z_0 + \sum_{m=1}^{\infty} z_{m\omega}\cos(m\omega t - \theta_{m\omega}) \; . \tag{2.46}$$

The amplitude and phase of the fundamental oscillation, z_ω and θ_ω, respectively, are solely due to the constant force amplitude term and were already calculated above in Eq. (2.41). From the linear term in the expansion (2.45), we obtain a recursion relation for the oscillation amplitudes of the harmonics,

$$z_{m\omega} = \frac{z_{(m-1)\omega}}{k}\left.\frac{dF_\omega}{dz}\right|_{z_0} \frac{\omega_0^2}{\sqrt{(\omega_0^2 - m^2\omega^2)^2 + (\omega_0\, m\omega/Q)^2}} \qquad \text{for } m \geq 2 \; . \tag{2.47}$$

This recursion is only useful in the linear approximation of the force amplitude, Eq. (2.45). For the full expansion, this recursion relation gives the correct amplitude only for the 1$^{\text{st}}$ harmonic, $m=2$, as the n^{th} order expansion term starts contributing at the n^{th} harmonic. Hence, for the amplitude of the 2$^{\text{nd}}$ harmonic, $z_{3\omega}$, the 2$^{\text{nd}}$ order amplitude $\left.\dfrac{d^2F_\omega}{dz^2}\right|_{z_0}$ also contributes.

It is worthwhile noting that the amplitude of every harmonic contains the amplitude of the fundamental as a prefactor, $z_{m\omega} \propto z_\omega \; \forall m \geq 1$.

Summary. Modeling the AFM cantilever as a classical damped harmonic oscillator, we have discussed the cantilever response to several external forces:

- A static force of constant amplitude changes equilibrium deflection of the tip, Eq. (2.33).
- Force gradients of a static force dF_{dc}/dz cause the spring constant and resonance frequency to shift, Eqs. (2.36) and (2.38).

- A periodic driving force of constant amplitude $F_\omega \cos(\omega t)$ sets the cantilever into oscillations about the equilibrium deflection at the driving frequency, Eq. (2.40). The amplitude response depends on the ratio of the driving frequency to the resonance frequency, ω/ω_0, and peaks on resonance, Eq. (2.41). The phase lag of the oscillations with respect to the driving force changes sensitively near resonance.

- Spatially varying amplitudes of a periodic driving force couple in higher harmonics of the driving frequency, Eq. (2.46).

- Free, damped oscillations in the absence of external forces decay exponentially with time, Eq. (2.30). The time constant for amplitude decay scales linearly with the quality factor, Eq. (2.31). This solution is relevant even in the presence of external forces, particularly for high-Q cantilevers, as it sets a time scale for any present oscillation to disappear, once it is no longer excited, for example, after a change in driving frequency.

2.2.2 The Single-Electron Tunneling Force

In this section we analyze how quantum dots interact with the microscope. In particular, we ask how single-electron charging effects are resolved. The microscope adds two important components to the system: The biased AFM tip and the cantilever. The biased AFM tip acts as a local, mobile gate on the sample. The AFM cantilever is our microscopic force detector.

The experiment is setup in the following way: We park the biased AFM tip near the quantum dot and set it mechanically into oscillation. The tip oscillations gate the quantum dot with an ac electric field. If the quantum dot is near resonance

with the Fermi energy of the lead, the oscillating AFM tip may push an electron on and off the quantum dot periodically – depending on the transparency of the tunnel barrier, up to once on and off per tip oscillation cycle. By quantum dot physics (Sec. 2.1.5), the electrostatic potential of the quantum dot (2.4) jumps by an amount $E_C = e^2/C_{\rm dot}$ each time an electron tunnels. This abrupt change in electrostatic potential is sensed by our force detector, the AFM cantilever. Stated more generally, the cantilever resolves the response of the quantum dot to the periodic perturbations created by the AFM tip.

Previewing the results briefly here, the response of the quantum dot to an ac-gate and the ensuing cantilever measurement signal show some common features of driven feedback systems. Electron tunneling on and off the quantum dot as a dynamic response to an ac-driving gate occurs at a phase lag. As one might expect intuitively, the phase lag depends on how the driving frequency compares to tunneling rate of electrons, ω/Γ. This phase lag results in an in-phase and an out-of-phase component of the force on the AFM cantilever, which is of the form

$$F \propto \frac{1 + i\omega/\Gamma}{1 + (\omega/\Gamma)^2} \tag{2.48}$$

and gives rise to a resonance frequency shift of the cantilever and additional power dissipation.

In the following we derive in detail the response of the quantum dot to the oscillating AFM tip and the resulting feedback on the cantilever that is measured. We derive these two parts in the opposite order:

- First, we examine the electrostatic force from a quantum dot due to a tunneling electron. This is a basic exercise in capacitance network theory. We derive a general expression, but keep the notation simple and exemplify the

situation on a single electron box with two gates. This example realistically models a gold nanoparticle that is linked to a carbon nanotube and gated by the AFM tip and the degenerately doped wafer (backgate), as discussed in Chap. 6.

- Second, we evaluate the dynamic response of the quantum dot to a periodically varying gate, such as the oscillating AFM tip. Here we solve the kinetic equation governing the dot occupancy when the electrochemical potential of the dot is driven into oscillations. Since the tunneling rates that enter the kinetic equation are different in the classical and quantum limits, we treat the two regimes separately.

- For later reference, we combine the findings from the two sections in a short summary and recapitulate relevant equations.

To make the derivation more tangible, we quickly introduce a simple but representative model of the experiment that exemplifies the situation discussed below: Figure 2.8 shows a quantum dot in a single-electron box geometry with two gates and its equivalent circuit. The two gates in our experiment are the AFM tip and the degenerately doped silicon wafer. The lead sets an electrochemical potential reference for the quantum dot and provides charges to tunnel on and off the dot as needed. It also serves as reference voltage and is thereby our ground plane. Including the quantum dot, there are 4 conductors in the system. From an electrostatic point of view, these conductors form a capacitive network. Accounting for the capacitance to the lead as a self-capacitance to GND, the network can be described by a 3×3 capacitance matrix and a gate charge of the quantum dot given by Eq. (5.2). The sole purpose of this model here is to provide a specific

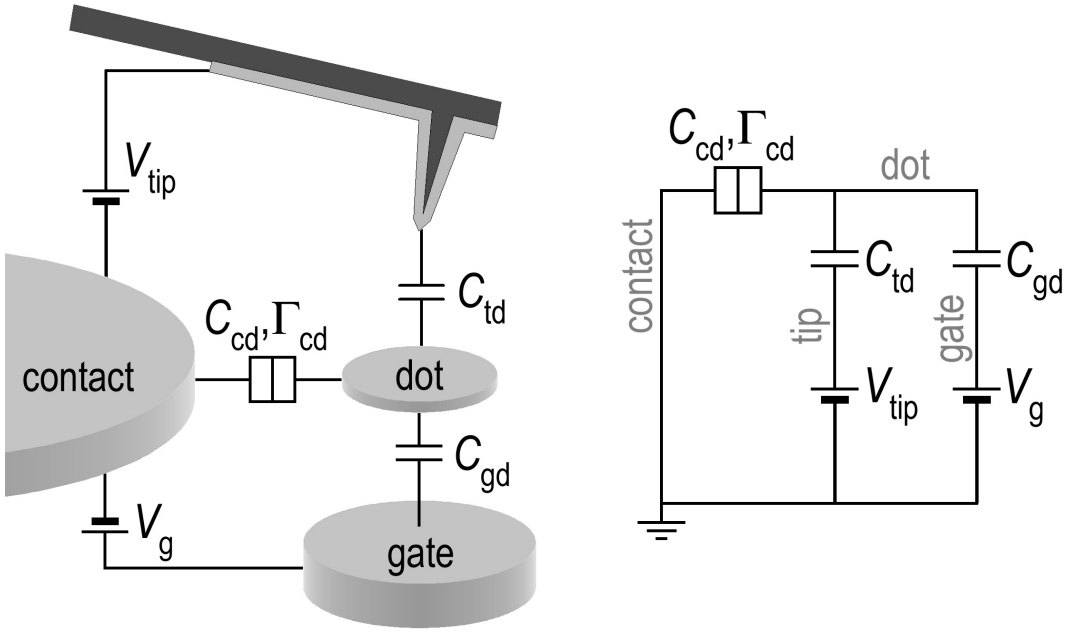

(a) Schematic of a quantum dot with tunnel contact, gate, and tip.

(b) Equivalent circuit diagram of Fig. 2.8(a).

Figure 2.8: Simple model of a quantum dot device in the AFM. The dot is shown in a single-electron box geometry with two gates, the AFM tip and the backgate.

setup that illustrates the potentially abstract derivation below.

The force due to single-electron tunneling

We start from a general quantum dot circuit that can couple to several charge leads and have multiple gates. From an electrostatic point of view, the quantum dot, the leads, and the gates are conductors that form a capacitive network (Jackson 1999, van der Wiel et al. 2003). In such a network, the electrostatic force acting on the AFM tip is capacitive and given by[8]

$$F_{\rm cap} = \sum_{i,j} \frac{1}{2} \frac{d\bar{c}_{ij}}{dz} V_i V_j = \sum_{i<j} \frac{1}{2} \frac{dC_{ij}}{dz} (V_i - V_j)^2 \,, \tag{2.49}$$

where $\bar{c}_{ij}$ are the elements of the capacitance matrix, V_i and V_j are the electrostatic potentials on the conductors i and j, and C_{ij} is their mutual capacitance. z is the vertical separation between the tip and the quantum dot.

We isolate the electrostatic force from the quantum dot on the tip by collecting all terms linear in its electrostatic potential, $V_{\rm dot}$, and obtain

$$\begin{aligned} F_{\rm cap}^{\rm (dot)} &= -\sum_{i \neq {\rm dot}} \frac{dC_{{\rm dot},i}}{dz} V_i V_{\rm dot} \\ &= \frac{dq_{\rm c}}{dz} V_{\rm dot} \,. \end{aligned} \tag{2.50}$$

In the 2nd line, we have compactly rewritten the force in terms of the *gate charge* or *control charge* of the quantum dot,

$$q_{\rm c} = -\sum_{i \neq {\rm dot}} C_{{\rm dot},i} V_i \,. \tag{2.51}$$

It represents the charge that would reside on the dot in the classical limit if charge wasn't quantized and expresses the cumulative gating effect of all conductors that are capacitively coupled to the dot.

[8] It is a subtle and remarkable fact that the force (2.49) on a conductor in a general capacitive network is independent of whether any conductor is a voltage or a charge node, or what the distribution of voltage and charge nodes is.

To evaluate the force due to single-electron tunneling, we find the electrostatic potential of the quantum dot[9] from Eq. (2.5) as

$$V_{\rm dot} = \frac{q_{\rm dot} - q_{\rm c}}{C_{\rm dot}} \ , \tag{2.52}$$

where $q_{\rm dot}$ is the charge on the dot, $q_{\rm c}$ is the gate charge (2.51), and $C_{\rm dot}$ is the total capacitance of the quantum dot,

$$C_{\rm dot} = \sum_{i \neq {\rm dot}} C_{{\rm dot},i} \ , \tag{2.53}$$

which determines the charging energy E_C of the quantum dot.

To calculate the force due to single electron tunneling, we assume that N electrons are fixed on the dot and only the $(N+1)^{\rm th}$ electron may tunnel on or off the dot. If $\wp$ is the probability that the $(N+1)^{\rm th}$ electron resides on the quantum dot, then the total charge on the dot is

$$q_{\rm dot} = -\wp\, e - (N - N_0)\, e \ , \tag{2.54}$$

where the offset N_0 was defined in Eq. (2.4) and $-e$ is the electron charge.

When combining Eqs. (2.50), (2.52), (2.54), we omit all force terms that remain constant when an electron is tunneling between the quantum dot the the lead. This way we isolate the force acting on the tip due to single-electron tunneling. It is given by

$$F_{e^-} = -\frac{dq_{\rm c}}{dz}\,\frac{e}{C_{\rm dot}}\,\wp \tag{2.55}$$

and correlates directly with the probability $\wp$ of an extra electron occupying the dot. This result is quite intuitive: $\dfrac{-e}{C_{\rm dot}}$ is the jump in electrostatic potential of the

[9] From a capacitance matrix point of view, Eq. (2.52) immediately follows from

$$q_{\rm dot} = \sum_i \bar{c}_{{\rm dot},i}\, V_i = \sum_{i \neq {\rm dot}} C_{{\rm dot},i}\,(V_{\rm dot} - V_i) = C_{\rm dot}\, V_{\rm dot} + q_{\rm c} \ .$$

.

quantum dot when an electron tunnels onto the dot, $\frac{dq_c}{dz}\frac{-e}{C_{dot}}$ is the accompanying force on the cantilever, and $\wp$ is the probability that the tunneling event happens. In the following section we evaluate exactly this probability for our experiments.

Dynamic response of a quantum dot to an oscillating gate

In this section we use the kinetic equation (2.25) to calculate the response of the quantum dot to an oscillating gate. In our experiment, we use the biased AFM tip to create this time-dependent gating. The AFM tip is an unusual gate in that it can change the gate charge of the quantum dot (2.51) in 2 different ways – by its voltage V_{tip} or by its position $\vec{r} = (x, y, z)$ via the tip-dot capacitance $C_{td}(\vec{r})$. We use the 2nd mechanism here. In our experiment, we set the biased AFM tip into oscillation nearby a quantum dot. The tip oscillations are described by (Sec. 2.2.1)

$$z(t) = z_0 + z_\omega\, e^{-i\omega t}\ . \tag{2.56}$$

As a consequence of the resonating, biased tip nearby, the electrochemical potential of the quantum dot oscillates synchronously with the tip. With respect to the electrochemical potential of the lead it is given by

$$\Delta E = \mu_{dot} - \mu_{lead} = \Delta E_{dc} + \Delta E_\omega\, e^{-i\omega t}\ , \tag{2.57}$$

where the static part, ΔE_{dc}, is set by the electrostatic environment of the dot and can be changed by dc gate voltages. The oscillating part is solely due to the tip

resonating near the dot and given by[10]

$$\Delta E_\omega = \frac{e}{C_{\rm dot}} \frac{dq_{\rm c}}{dz} z_\omega \ . \tag{2.58}$$

If the electrochemical potential of the quantum dot is near resonance with the electrochemical potential of the lead, $\Delta E_{\rm dc} < \Delta E_\omega$, then the mechanical oscillations of the tip may push an electron on and off the dot periodically. The dynamic response of the quantum dot to the changing electrochemical potential is governed by the kinetic equation (2.25),

$$\begin{aligned} \frac{d\wp}{dt} &= -\wp\,\Gamma_{\rm off} + (1-\wp)\,\Gamma_{\rm on} \\ &= -\wp\,(\Gamma_{\rm off} + \Gamma_{\rm on}) + \Gamma_{\rm on} \ , \end{aligned} \tag{2.59}$$

where $\wp$ is the probability of the extra electron residing on the dot. $\Gamma_{\rm on}$ and $\Gamma_{\rm off}$ are the tunneling rates on and off the dot, respectively. They are different in the classical and the quantum regime, as discussed in Sec. 2.1.6. We treat each regime separately below and solve the kinetic equation for $\wp$ in linear response to an oscillating gate (2.57) below.

Dynamic response of a quantum dot in the quantum limit, $\Delta E_{\rm level} \gg k_B T$. In the quantum limit, the electron tunneling rates on and off the dot are given by Eq. (2.11). Together with the relation (2.13), we find for the kinetic equation (2.59)

$$\frac{1}{\Gamma_{\rm qdot}} \frac{d\wp}{dt} = -\wp + f(\Delta E) \ , \tag{2.60}$$

where f is the Fermi-Dirac distribution, Eq. (2.10), and ΔE is the misalignment of the electrochemical potentials, $\Delta E = \mu_{\rm dot} - \mu_{\rm lead}$. From this equation we im-

[10]Note that an oscillating electrochemical potential of the quantum dot as in Eq. (2.57) can also be created by an ac voltage on a gate. In this case, Eq. (2.58) has to be replaced by $\Delta E_\omega = e C_{{\rm dot},i} V_i^{(\omega)} / C_{\rm dot}$, where $V_i^{(\omega)}$ is the peak amplitude of the ac-voltage on the gate i.

mediately see that the equilibrium occupancy, $\frac{d\wp}{dt} = 0$, of the charge state is given by the Fermi-Dirac distribution,

$$\wp_{\rm eq} = f(\Delta E) \; . \tag{2.61}$$

To evaluate to quantum dot's response to a time-varying gate, Eq. (2.57), we expand the Fermi-Dirac function about the static misalignment $\Delta E_{\rm dc}$,

$$f(\Delta E) \;\approx\; f(\Delta E_{\rm dc}) + f'(\Delta E_{\rm dc}) \cdot \Delta E_\omega \, e^{-i\omega t} \; , \tag{2.62}$$

and retain only terms up to linear order, assuming that ΔE_ω is small, $\Delta E_\omega \ll k_B T$. With this linear expansion, the kinetic equation (2.60) becomes

$$\frac{1}{\Gamma_{\rm qdot}} \frac{d\wp}{dt} = -\wp + f(\Delta E_{\rm dc}) + f'(\Delta E_{\rm dc}) \cdot \Delta E_\omega \, e^{-i\omega t} \tag{2.63}$$

in linear response and is solved[11] by the ansatz

$$\wp(t) = \wp_{\rm dc} + \wp_\omega \, e^{-i(\omega t - \phi_\omega)} \; . \tag{2.64}$$

The coefficients of the solution are given by

$$\wp_{\rm dc} = f(\Delta E_{\rm dc}) \qquad \text{and} \qquad \wp_\omega \, e^{i\phi_\omega} = \frac{f'(\Delta E_{\rm dc}) \, \Delta E_\omega}{1 - i\omega/\Gamma_{\rm qdot}} \; . \tag{2.65}$$

Rewriting Eq. (2.64) using Eq. (2.56), we can express the single-electron tunneling response in terms of the cantilever motion,

$$\wp(t) = \wp_{\rm dc} + \wp_\omega \, e^{i\phi_\omega} \; \frac{z(t) - z_0}{z_\omega} \; . \tag{2.66}$$

[11] We restrict ourselves to the steady-state solution of the linear differential equation (2.63). The full solution

$$\wp(t) = \wp_{\rm dc} + \wp_\omega e^{-i(\omega t - \phi_\omega)} + \wp_{\rm decay} \, e^{-t/\tau}$$

contains an additional transient term, which decays exponentially with a time constant $\tau = 1/\Gamma_{\rm qdot}$. The transient amplitude $\wp_{\rm decay}$ is fixed by the initial conditions. Experimentally, we find that the electrons readily tunnel on and off our CNT dots on the time scale of our cantilever oscillations, $\omega_0 < \Gamma_{\rm qdot}$. Since we average over many tip oscillations when recording data, this decay term is experimentally irrelevant, as $t_{\rm avg} \gg 2\pi/\omega_0 > 1/\Gamma_{\rm qdot} = \tau$.

For the single-electron tunneling force on the AFM cantilever, Eq. (2.55), this solution implies

$$F_{e^-}^{(\mathrm{qdot})} = -\frac{dq_\mathrm{c}}{dz}\frac{e}{C_\mathrm{dot}}\frac{f'(\Delta E_\mathrm{dc})\,\Delta E_\omega}{1-i\omega/\Gamma_\mathrm{qdot}}\,\frac{z-z_0}{z_\omega}\;, \tag{2.67}$$

where we omitted the constant term due to the average dot occupation $\wp_\mathrm{dc}$. Inserting the amplitude of oscillation of the dot's electrochemical potential, ΔE_ω, from Eq. (2.58), we obtain

$$F_{e^-}^{(\mathrm{qdot})} = -\left(\frac{dq_\mathrm{c}}{dz}\frac{e}{C_\mathrm{dot}}\right)^2\frac{f'(\Delta E_\mathrm{dc})}{1-i\omega/\Gamma_\mathrm{qdot}}\,(z-z_0)\;. \tag{2.68}$$

We analyze the experimental implications of this force further in the summary of this section (see page 59). In the meantime, we derive the dynamic single-electron tunneling force in the classical limit.

Dynamic response of a quantum dot in the classical limit, $k_BT \gg \Delta E_\mathrm{level}$. In completely parallel treatment to the quantum limit above, we start from the tunneling rates on and off a classical dot, as given in Eq. (2.14). Using their compact notation (2.16) in terms of the dimensionless function g, which is defined in Eq. (2.15), the kinetic equation (2.59) reads for classical dots

$$\frac{1}{\Gamma_\mathrm{cdot}}\frac{d\wp}{dt} = -\wp\,\{g(\Delta E)+g(-\Delta E)\}+g(\Delta E)\;. \tag{2.69}$$

Although not immediately obvious, the stationary solution, $\dfrac{d\wp}{dt}=0$, to this equation is given by the Fermi-Dirac distribution,

$$\wp_\mathrm{eq} = \frac{g(\Delta E)}{g(\Delta E)+g(-\Delta E)} \equiv f(\Delta E)\;, \tag{2.70}$$

just like in the quantum limit, Eq. (2.61).

To solve the kinetic equation (2.69) in linear response, we Taylor expand the two functions

$$\begin{aligned} g(\Delta E) &\approx g(\Delta E_{\rm dc}) + g'(\Delta E_{\rm dc}) \cdot \Delta E_\omega \, e^{-i\omega t} \\ \tilde{g}(\Delta E) = g(\Delta E) + g(-\Delta E) &\approx \tilde{g}(\Delta E_{\rm dc}) + \tilde{g}'(\Delta E_{\rm dc}) \cdot \Delta E_\omega \, e^{-i\omega t} \; . \end{aligned} \tag{2.71}$$

and use these approximations in the kinetic equation (2.69). This gives

$$\frac{1}{\Gamma_{\rm cdot}} \frac{d\wp}{dt} = -\wp \left\{ \tilde{g}_{\rm dc} + \tilde{g}_\omega \, e^{-i\omega t} \right\} + g_{\rm dc} + g_\omega \, e^{-i\omega t} \; , \tag{2.72}$$

with coefficients

$$\begin{aligned} g_{\rm dc} &= g(\Delta E_{\rm dc}) \; , \\ g_\omega &= g'(\Delta E_{\rm dc}) \, \Delta E_\omega \; , \\ \tilde{g}_{\rm dc} &= g(\Delta E_{\rm dc}) + g(-\Delta E_{\rm dc}) = \tfrac{1}{2} \, \beta \, \Delta E_{\rm dc} \, \coth \left(\tfrac{1}{2} \, \beta \, \Delta E_{\rm dc} \right) \; , \\ \tilde{g}_\omega &= \tilde{g}'(\Delta E_{\rm dc}) \, \Delta E_\omega = [g'(\Delta E_{\rm dc}) - g'(-\Delta E_{\rm dc})] \, \Delta E_\omega \; . \end{aligned} \tag{2.73}$$

Comparing the master equation for quantum dots and classical dots, Eqs. (2.63) and (2.72), respectively, classical dots have an additional, qualitatively different term $\wp \, \tilde{g}_\omega \, e^{-i\omega t}$ that arises from the absence of relation (2.13) in the classical limit. This term excites higher order harmonics of the oscillation even in linear response. The steady-state solution to Eq. (2.72) is given by

$$\wp(t) = \wp_{\rm dc} + \sum_{n=1}^{\infty} \wp_{n\omega} \, e^{-i(n\omega t - \phi_{n\omega})} \tag{2.74}$$

with amplitudes $\wp_{n\omega}$ and phases $\phi_{n\omega}$ to be determined. For the static and the fundamental term we find

$$\begin{aligned} \wp_{\rm dc} &= \frac{g_{\rm dc}}{\tilde{g}_{\rm dc}} = \frac{1}{1 + e^{\, \beta \, \Delta E_{\rm dc}}} = f(\Delta E_{\rm dc}) \\ \wp_\omega \, e^{i\phi_\omega} &= \frac{g_\omega - \tilde{g}_\omega \wp_{\rm dc}}{\tilde{g}_{\rm dc} - i\omega/\Gamma_{\rm cdot}} = \frac{f'(\Delta E_{\rm dc}) \, \Delta E_\omega}{1 - i\omega/\tilde{g}_{\rm dc}\Gamma_{\rm cdot}} \; . \end{aligned} \tag{2.75}$$

The amplitudes and phases of higher harmonics are easily extracted from Eq. (2.72), as well, but for accurate results, corresponding higher order terms in the expansion (2.71) must also be taken into account.

From the response of the quantum dot to an oscillating gate, as expressed in Eqs. (2.74) and (2.75), we can calculate the force on the cantilever due to single-electron tunneling (2.55) in the classical regime. The ω-component of the single-electron force can be written in terms of its cause, the cantilever oscillations $z - z_0 = z_\omega \, e^{-i\omega t}$, as

$$F_{e^-}^{(\mathrm{cdot})} = - \frac{dq_\mathrm{c}}{dz} \frac{e}{C_\mathrm{dot}} \frac{f'(\Delta E_\mathrm{dc}) \, \Delta E_\omega}{1 - i\omega/\tilde{g}_\mathrm{dc}\Gamma_\mathrm{cdot}} \frac{z - z_0}{z_\omega} \, . \tag{2.76}$$

Using the expression for the amplitude of the dot's electrochemical potential oscillations, Eq. (2.58), we rewrite the single-electron tunneling force as

$$F_{e^-}^{(\mathrm{cdot})} = - \left(\frac{dq_\mathrm{c}}{dz} \frac{e}{C_\mathrm{dot}} \right)^2 \frac{f'(\Delta E_\mathrm{dc})}{1 - i\omega/\tilde{g}_\mathrm{dc}\Gamma_\mathrm{cdot}} \, (z - z_0) \, . \tag{2.77}$$

The time delay between the cantilever motion and the electron tunneling response gives rise to an in-phase and out-of-phase component of the force, corresponding to a resonance frequency shift and additional energy dissipation, respectively, from single-electron tunneling. The details are discussed in the summary below.

Note in Eq. (2.76) that besides the derivative of the Fermi-Dirac distribution, the dimensionless parameter $\tilde{g}_\mathrm{dc}$ is also a function of the static misalignment between the electrochemical potentials of the dot and the lead, ΔE_dc. This misalignment is set (and changed) by the equilibrium tip position z_0, the dc gate voltages $\{V_i\}$, and the amount of charge on the dot. Limiting expansions of the functional form (2.73) show that $\tilde{g}_\mathrm{dc}$ varies quadratically at small misalignments and increases linearly at large misalignments,

$$\tilde{g}_\mathrm{dc} \quad \rightarrow \quad \begin{cases} 1 + \dfrac{(\beta \, \Delta E_\mathrm{dc})^2}{12} & \text{if} \quad |\beta \, \Delta E_\mathrm{dc}| \ll 1 \, , \\ \frac{1}{2} \, |\beta \, \Delta E_\mathrm{dc}| & \text{if} \quad |\beta \, \Delta E_\mathrm{dc}| \gg 1 \, . \end{cases} \tag{2.78}$$

Its minimum value is $\tilde{g}_\mathrm{dc} = 1$, which occurs only on resonance, $\Delta E_\mathrm{dc} = 0$.

The fact that $\tilde{g}_{\rm dc}$ only appears as a factor to $\Gamma_{\rm cdot}$ suggests the view that the effective tunneling rate in the classical limit is $\Gamma = \tilde{g}_{\rm dc}\,\Gamma_{\rm cdot}$, where $\tilde{g}_{\rm dc}$ describes the dependence on the gate voltages, tip position, and charge state of the quantum dot and $\Gamma_{\rm cdot}$ carries the inherent properties of the tunnel barrier, such as its height and width.

Summary. While the classical and the quantum limit were treated separately due to the dot's different tunneling rates in the two limits, the final expressions for the single-electron tunneling force, Eqs. (2.68) and (2.76), look very similar in both limits. Unifying both equations in one common result, the force exerted on the cantilever by single-electron tunneling is given by

$$F_{e^-} = -\left(\frac{dq_{\rm c}}{dz}\,\frac{e}{C_{\rm dot}}\right)^2 \frac{f'(\Delta E_{\rm dc})}{1 - i\omega/\Gamma}\,(z - z_0)\;, \tag{2.79}$$

The only difference between the single-electron force in the quantum and the classical limit is the tunneling rate Γ. Its formula in both limits is summarized in Table 2.1. The single-electron force (2.79) has an in-phase and out-of-phase component, which give rise to a resonance frequency shift and an additional dissipation term, respectively. This is more clearly seen after rewriting the force (2.79) in the general form

$$\begin{aligned} F_{e^-} &= -\delta k \left(1 + \frac{i\omega}{\Gamma}\right)(z - z_0) \\ &= -\delta k\,(z - z_0) \;-\; \delta\gamma\,\frac{dz}{dt}\;. \end{aligned} \tag{2.80}$$

The change in spring constant due to single-electron tunneling is given by

$$\delta k = \left(\frac{dq_{\rm c}}{dz}\,\frac{e}{C_{\rm dot}}\right)^2 \frac{f'(\Delta E_{\rm dc})}{1 + (\omega/\Gamma)^2} \tag{2.81}$$

with a corresponding resonance frequency shift and energy dissipation term

$$\frac{\delta\omega_0}{\omega_0} = \frac{\delta k}{2k} \qquad \text{and} \qquad \delta\gamma = -\frac{\delta k}{\Gamma}\;. \tag{2.82}$$

Table 2.1: Tunneling rate Γ of a quantum dot in the classical and quantum limit. In the quantum limit, Γ is independent of the gate voltage or tip position and fully described by the properties of the barrier. Inherently, this is a consequence of Eq. (2.13). In the classical limit, Γ has an explicit dependence on the gate voltages and the tip position, which is described by the dimensionless parameter $\tilde{g}_{\mathrm{dc}}$. Its formula above is a near-resonance expansion, $\Delta E_{\mathrm{dc}} \ll k_B T$, as relevant in the experiment. For the exact expression and an off-resonance expansion, see Eqs. (2.73) and (2.78). The properties of the tunnel barrier in the classical limit are encoded in Γ_{cdot}.

Coulomb blockade regime	tunneling rate Γ	
quantum limit: $k_B T \ll \Delta E_{\mathrm{level}}$	$\Gamma = \Gamma_{\mathrm{qdot}}$	$\Gamma_{\mathrm{qdot}} = \dfrac{h\nu_{\mathrm{level}}}{e^2 R_T} = \dfrac{\Delta E_{\mathrm{level}}}{e^2 R_T}$
classical limit: $k_B T \gg \Delta E_{\mathrm{level}}$	$\Gamma = \tilde{g}_{\mathrm{dc}}\, \Gamma_{\mathrm{cdot}}$	$\Gamma_{\mathrm{cdot}} = \dfrac{2\, k_B T}{e^2\, R_T}$ $\tilde{g}_{\mathrm{dc}} \approx 1 + \dfrac{1}{12}\left(\dfrac{\Delta E_{\mathrm{dc}}}{k_B T}\right)^2$

Notice that the resonance frequency always shifts towards lower values, while the dissipation only increases due to single-electron tunneling. The evolution of these two terms with drive frequency ω and tunneling rate Γ is shown in Fig. 2.9.

The quality factor Q of the cantilever, whose inverse measures the relative energy loss per oscillation cycle, has a contribution from the in-phase and the out-of-phase component of the single electron force (2.79). The in-phase component (or frequency shift) reduces the total energy stored in the cantilever; the out-of-phase component increases the amount of energy dissipated per cycle. Hence, both contributions increase the loss,

$$\begin{aligned} \delta\left(\frac{1}{Q}\right) &= \frac{\omega_0}{k}\,\delta\gamma - \frac{1}{Q}\frac{\delta\omega_0}{\omega_0} \\ &= -\frac{\delta k}{k}\left[\frac{\omega_0}{\Gamma} + \frac{1}{2Q}\right] . \end{aligned} \tag{2.83}$$

The in-phase term (due to the resonance frequency shift) is negligibly small, typically a few parts per billion (ppb), as $\delta\omega_0/\omega_0 < 10^{-4}$ due to single-electron tunneling and $1/Q < 10^{-4}$ in our experiments. The out-of-phase term depends on ω_0/Γ and can be significant.

Similarly, the tip oscillation amplitude also has a contribution from the in-phase and the out-of-phase component of the single-electron tunneling force. For a resonantly driven cantilever, Eq. (2.43), the relative change in tip amplitude due to single-electron tunneling is given by

$$\begin{aligned} \frac{\delta z_{\omega_0}}{z_{\omega_0}} &= -\frac{\delta\gamma}{\gamma} - \frac{\delta\omega_0}{\omega_0} \\ &= \frac{\delta k}{k}\left(Q\,\frac{\omega_0}{\Gamma} - \frac{1}{2}\right) , \end{aligned} \tag{2.84}$$

where we assume a constant ac-force amplitude F_ω. The first term in parentheses is the dissipation term that arises from the out-of-phase component of the single-electron force (2.79). The second term is due to the in-phase contribution. In our

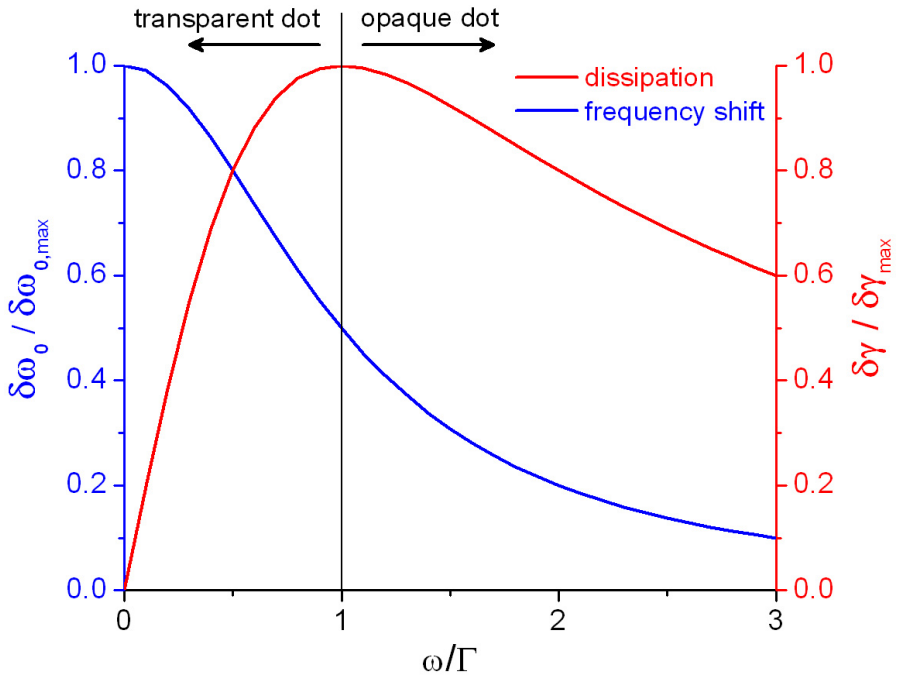

Figure 2.9: Evolution of the frequency shift and dissipation signal due to single-electron tunneling with the ratio of driving frequency ω to tunneling rate Γ. Both quantities are normalized by their maximum change. Since the cantilever resonance frequency shift is negative, we take the normalizing $\delta\omega_{0,\max}$ as its most negative value, $\delta\omega_{0,\max} \leq \delta\omega_0 \leq 0$. The frequency shift signal varies as $\delta\omega_0 \propto \dfrac{1}{1+(\omega/\Gamma)^2}$ and the dissipation signal as $\delta\gamma \propto \dfrac{\omega/\Gamma}{1+(\omega/\Gamma)^2}$.

samples, the in-phase term is too small to be observed in the amplitude signal. As a consequence, the tip oscillation amplitude resolves the dissipation due to tunneling and is complementary to the resonance frequency shift measurement, as discussed in Sec. 6.6.

2.2.3 Power dissipation due to single-electron tunneling

The previous section derived the single-electron tunneling force and described the resulting signal on the cantilever fully. In this section we derive only the dissipation signal due to single-electron tunneling on an alternative route. This path gives additional physical insight into the dissipation mechanism and explicitly evaluates some other useful quantities.

The approach in this section is based on enforcing energy conservation: If electrons dissipate energy in the tunneling process, this energy has to be supplied by some source in the system. Given the experimental setup, the only candidate in the system with a steady energy input is the AFM cantilever. Consequently, we require that the power dissipated by single-electron tunneling be exactly compensated for by the AFM cantilever. In turn, this implies that single-electron tunneling is visible as extra "damping" or "friction" on the cantilever.

This section proceeds in the following steps: First, we derive the power dissipation due to single-electron tunneling. Here we correlate the electron tunneling current on and off the quantum dot with the ac-drive signal. A phase lag between the two results in steady dissipation of energy. This part requires separate treatment in the classical and quantum limit. To avoid any repeat analysis, we heavily borrow the solution to the kinetic equation from the previous section. To balance this dissipation due to single-electron tunneling, we calculate the power

dissipation in the cantilever and how it is reflected in the cantilever parameters. In a summary we compare the two powers and confirm consistency with the results from the previous section.

Power dissipation due to single-electron tunneling. The experimental setup in this section is identical to the setup in the previous section. Briefly, a biased AFM tip is resonating near a quantum dot. The motion of the AFM tip generates an ac electric field at the quantum dot, and its electrochemical potential is oscillating in synch with the AFM tip,

$$\Delta E = \mu_{\rm dot} - \mu_{\rm lead} = \Delta E_{\rm dc} + \Delta E_\omega \, \cos(\omega t) \; . \tag{2.85}$$

As a consequence of this time-varying perturbation, an electron may tunnel on and off the quantum dot if the electrochemical potentials of the dot and the lead are close to resonance. This changes the occupation probability $\wp$ of the quantum dot over time. In solving the kinetic equation (2.59), we found in the quantum limit of Coulomb blockade a solution of the form

$$\wp(t) = \wp_{\rm dc} + \wp_\omega \, \cos(\omega t - \phi_\omega) \; . \tag{2.86}$$

The associated electron current is given by

$$I = -e \, \frac{d\wp}{dt} \qquad \Rightarrow \qquad I_\omega = e \, \wp_\omega \, \omega \, \sin(\omega t - \phi_\omega) \tag{2.87}$$

across the tunnel barrier. The energy dissipated in a tunneling event is the difference in electrochemical potential between the quantum dot and the lead at the moment of tunneling. In a circuit picture, the power dissipated by this tunneling current is determined by the "voltage" across the tunnel barrier at the time of tunneling,

$$\mathcal{P} = \langle V_{\rm jct} \cdot I \rangle_{\rm time} \; . \tag{2.88}$$

The effective voltage across the tunnel barrier is given by the misalignment between the electrochemical potentials of the dot and the lead,

$$V_{\rm jct} = \frac{\mu_{\rm dot} - \mu_{\rm lead}}{-e} = \frac{\Delta E}{-e} = \frac{\Delta E_{\rm dc} + \Delta E_\omega \, \cos(\omega t)}{-e} \; . \tag{2.89}$$

Consequently, the average[12] power dissipated by single-electron tunneling is

$$\mathcal{P}_\omega = \left\langle \frac{\Delta E}{-e} \cdot I_\omega \right\rangle_{\rm time} = \omega \, \Delta E_\omega \, \wp_\omega \, \frac{\sin(\phi_\omega)}{2} \; . \tag{2.90}$$

Clearly, any phase $0 < \phi_\omega < 180^\circ$ will cause energy to be dissipated in the tunneling process. For a perfectly transparent tunnel barrier, there is no phase lag, $\phi_\omega = 0$, and no power is dissipated, $\mathcal{P}_\omega = 0$, as predicted by Eq. (2.90).

In the classical limit, the solution to the kinetic equation (2.59) also contains higher harmonics and is of the form

$$\wp(t) = \wp_{\rm dc} + \sum_{n=1}^{\infty} \wp_{n\omega} \, \cos(n\omega t - \phi_{n\omega}) \; . \tag{2.91}$$

The associated electron tunneling current across the tunnel barrier has the higher harmonics, as well,

$$I = -e \, \frac{d\wp}{dt} = e \sum_{n=1}^{\infty} \wp_{n\omega} \, n\omega \, \sin(n\omega t - \phi_{n\omega}) = \sum_{n=1}^{\infty} I_{n\omega} \; , \tag{2.92}$$

but the dissipated power remains the same, because the electrochemical potential oscillates only at the fundamental. Restated in mathematical terms, the power $\mathcal{P}_{n\omega}$ due to the harmonic $I_{n\omega}$ in current is

$$\begin{aligned} \mathcal{P}_{n\omega} &= -\tfrac{1}{e} \, \langle \Delta E \cdot I_{n\omega} \rangle_{\rm time} \\ &= -\Delta E_\omega \, \wp_{n\omega} \, n\omega \, \langle \cos(\omega t) \, \sin(n\omega t - \phi_{n\omega}) \rangle_{\rm time} \\ &= -\Delta E_\omega \, \wp_{n\omega} \, n\omega \, \left\langle \tfrac{\sin((n+1)\omega t - \phi_{n\omega}) \, - \, \sin((n-1)\omega t - \phi_{n\omega})}{2} \right\rangle_{\rm time} \; . \end{aligned} \tag{2.93}$$

[12] Use

$$\cos(\alpha) \, \sin(\beta) = \frac{\sin(\alpha+\beta) - \sin(\alpha-\beta)}{2} \quad \text{and} \quad \langle \sin(2\omega t - \phi_\omega) \rangle_{\rm time} = 0 \; .$$

Clearly, the time average in the last line of Eq. (2.93) vanishes unless $n = \pm 1$. We conclude that the total power dissipated by single-electron tunneling is

$$\mathcal{P} = \mathcal{P}_\omega = \omega\, \Delta E_\omega\, \wp_\omega\, \frac{\sin(\phi_\omega)}{2} \tag{2.94}$$

in both the classical and quantum regime of Coulomb blockade. All that remains to do now is to evaluate $\wp_\omega\, \sin(\phi_\omega)$ in the classical and quantum limit, which we quote from Sec. 2.2.2.

Power dissipation in the quantum limit, $\Delta E_{\rm level} \gg k_B T$. From the solution of the kinetic equation in the quantum limit, Eq. (2.65), we find

$$\wp_\omega\, \sin(\phi_\omega) = f'(\Delta E_{\rm dc})\, \Delta E_\omega\, \frac{\omega/\Gamma_{\rm qdot}}{1 + (\omega/\Gamma_{\rm qdot})^2}\ . \tag{2.95}$$

From this solution we evaluate the power dissipated (2.94) to be

$$\begin{aligned} \mathcal{P}_{\rm qdot} &= -\frac{\omega\, f'(\Delta E_{\rm dc})\, \Delta E_\omega^{\,2}}{2}\, \frac{\omega/\Gamma_{\rm qdot}}{1 + (\omega/\Gamma_{\rm qdot})^2} \\ &= -\frac{1}{2}\, \omega\, z_\omega^2 \left(\frac{dq_{\rm c}}{dz}\frac{e}{C_{\rm dot}}\right)^2 f'(\Delta E_{\rm dc})\, \frac{\omega/\Gamma_{\rm qdot}}{1 + (\omega/\Gamma_{\rm qdot})^2}\ , \end{aligned} \tag{2.96}$$

where we used Eq. (2.58) to eliminate ΔE_ω in the 2$^{\rm nd}$ line. We analyze and comment on this expression further in the summary section, after we state the corresponding relation in the classical limit.

Power dissipation in the classical limit, $k_B T \gg \Delta E_{\rm level}$. In the classical limit, the solution to the kinetic equation was given by Eq. (2.75) and reads

$$\wp_\omega\, \sin(\phi_\omega) = f'(\Delta E_{\rm dc})\, \Delta E_\omega\, \frac{\omega/\tilde{g}_{\rm dc}\Gamma_{\rm cdot}}{1 + (\omega/\tilde{g}_{\rm dc}\Gamma_{\rm cdot})^2}\ . \tag{2.97}$$

This leads to a power dissipation of

$$\begin{aligned} \mathcal{P}_{\rm cdot} &= -\frac{\omega\, f'(\Delta E_{\rm dc})\, \Delta E_\omega^{\,2}}{2}\, \frac{\omega/\tilde{g}_{\rm dc}\Gamma_{\rm cdot}}{1 + (\omega/\tilde{g}_{\rm dc}\Gamma_{\rm cdot})^2} \\ &= -\frac{1}{2}\, \omega\, z_\omega^2 \left(\frac{dq_{\rm c}}{dz}\frac{e}{C_{\rm dot}}\right)^2 f'(\Delta E_{\rm dc})\, \frac{\omega/\tilde{g}_{\rm dc}\Gamma_{\rm cdot}}{1 + (\omega/\tilde{g}_{\rm dc}\Gamma_{\rm cdot})^2}\ . \end{aligned} \tag{2.98}$$

In the 2$^{\rm nd}$ line, we used Eq. (2.58) to eliminate ΔE_ω.

Power dissipation of the cantilever. If a damped harmonic oscillator is driven by a periodic force $F_{\rm ac}(t) = F_\omega \cos(\omega t)$, its power dissipation is given by

$$\begin{aligned} \mathcal{P}_{\rm cantilever}(t) &= -\frac{dz(t)}{dt} \cdot F_{\rm ac}(t) &&= \omega z_\omega \sin(\omega t + \theta_\omega) \cdot F_\omega \cos(\omega t) \\ &&&= \frac{1}{2} F_\omega z_\omega \omega \left[\sin(2\omega t + \theta_\omega) + \sin(\theta_\omega)\right] \ , \end{aligned} \tag{2.99}$$

where we used Eq. (2.40) for the motion $z(t)$ of the harmonic oscillator in response to the ac driving force. Averaging the power dissipation over one oscillation period $\tau_{\rm osc} = 2\pi/\omega$, we find

$$\begin{aligned} \langle \mathcal{P}_{\rm cantilever} \rangle_{\frac{2\pi}{\omega}} &= \int_0^{\frac{2\pi}{\omega}} \frac{dt}{2\pi/\omega} \, \mathcal{P}_{\rm cantilever}(t) \\ &= \frac{1}{2} F_\omega z_\omega \omega \, \sin(\theta_\omega) \ = \ \frac{1}{2} z_\omega^2 \, \omega^2 \, \gamma \ = \ \frac{k \, z_\omega^2}{2} \, \frac{1}{Q} \, \frac{\omega^2}{\omega_0} \ . \end{aligned} \tag{2.100}$$

Expectedly, the oscillator's average power dissipation is directly proportional to the damping coefficient γ or the inverse of the quality factor $1/Q$. In the 2nd line we used the phase relation (2.42).

The power dissipation due to different damping mechanisms adds cumulatively. Consequently, any additional damping, as reflected by a change $\delta\gamma > 0$, results in additional power dissipation,

$$\delta \mathcal{P}_{\rm cantilever} \ = \ \frac{1}{2} z_\omega^2 \, \omega^2 \, \delta\gamma \ , \tag{2.101}$$

and vice versa.

Summary. The power dissipation due to single-electron tunneling, which was derived separately in the quantum and the classical limit, Eqs. (2.96) and (2.98), can be formulated in one expression as

$$\mathcal{P} = -\frac{1}{2} \, \omega \, z_\omega^2 \left(\frac{dq_{\rm c}}{dz} \frac{e}{C_{\rm dot}} \right)^2 f'(\Delta E_{\rm dc}) \, \frac{\omega/\Gamma}{1 + (\omega/\Gamma)^2} \ . \tag{2.102}$$

The only difference between the classical and the quantum limit lies in the tunneling rate Γ, as detailed in Table 2.1. This power dissipation is solely due to the

out-of-phase component of the single-electron force, as can be verified from Eqs. (2.81) and (2.82),

$$\mathcal{P} = -\frac{1}{2} k z_\omega^2 \, \frac{\delta k}{k} \, \frac{\omega^2}{\Gamma} = \frac{1}{2} \, z_\omega^2 \, \omega^2 \, \delta\gamma \; . \tag{2.103}$$

This expression already relates the dissipation due to single-electron tunneling to experimentally accessible quantities of the coupled resonator, our AFM cantilever. The last relation verifies Eq. (2.101) and thereby confirms that the force calculation from the previous section and the power derivation in this section agree.

In the two limits of a transparent and an opaque dot we find from Eq. (2.102)

$$\begin{aligned} \mathcal{P} &\xrightarrow{\omega \ll \Gamma} -\frac{1}{2} \, z_\omega^2 \left(\frac{dq_\mathrm{c}}{dz} \frac{e}{C_\mathrm{dot}} \right)^2 f'(\Delta E_\mathrm{dc}) \, \frac{\omega^2}{\Gamma} \\ \mathcal{P} &\xrightarrow{\omega \gg \Gamma} -\frac{1}{2} \, z_\omega^2 \left(\frac{dq_\mathrm{c}}{dz} \frac{e}{C_\mathrm{dot}} \right)^2 f'(\Delta E_\mathrm{dc}) \, \Gamma \; , \end{aligned} \tag{2.104}$$

respectively. Clearly, the power dissipation ultimately approaches 0 in either limit. This is intuitively clear: In the transparent limit, the electron tunnels instantly as soon as it is energetically favorable, and no energy is dissipated in the process. In the opaque limit, the tunneling rate is so slow that the half-period of the tip oscillation, during which it is energetically favorable for an electron to tunnel, passes by and tunneling never occurs. The maximum power dissipation occurs in the intermediate regime, at $\omega = \Gamma$, where the driving frequency equals the electron tunneling rate,

$$\mathcal{P} \xrightarrow{\omega \approx \Gamma} -\frac{1}{2} \, \omega \, z_\omega^2 \left(\frac{dq_\mathrm{c}}{dz} \frac{e}{C_\mathrm{dot}} \right)^2 f'(\Delta E_\mathrm{dc}) \left[\frac{1}{2} - \frac{1}{4} \left(1 - \frac{\omega}{\Gamma} \right)^2 \right] \; . \tag{2.105}$$

This was in principle already illustrated in Fig. 2.9 in the previous section.

CHAPTER 3

INSTRUMENTATION

An *atomic force microscope* (AFM) or *scanning force microscope* is a powerful tool that was invented only 20 years ago (Binnig et al. 1986). Its principles of operation were introduced in Sec. 1.2. Today AFMs are widely used owing to several reasons. The AFM's combination of high resolution (standardly below 1 nm in z under ambient conditions) and ease of operation is difficult to match. There are many commercial table-top AFMs available that are ready to use with a minimum of training, experience, and maintenance. Since forces are ubiquitous in nature, the force sensing scheme is applicable to many samples. It provides a real-space map of the sample forces, and typically little or no post-processing of images is needed. An AFM can operate under many external conditions, including ambient, liquid, and vacuum. It is a versatile instrument that can be run in many different ways, each of which may relate to different properties of the sample. Even within a certain mode of operation, there are typically multiple signal channels that can be recorded simultaneously. Beyond imaging, it can also be (ab)used invasively to modify the sample or locally deposit certain chemicals.

Mounting an AFM into a cryostat and cooling it to cryogenic temperatures brings unique opportunities and challenges for this technique. Low temperatures often set samples in a different, more basic regime of behavior, as thermally activated processes are frozen out. Furthermore, the sensitivity of the AFM, which is often thermally limited at room temperature, increases as the thermal noise in the cantilever is reduced. Lower Johnson-Nyquist noise in cold electronic parts may contribute further to the instrument's noise performance. Cryogenic temperatures also imply vacuum operation and much higher cantilever quality factors than un-

der ambient conditions, improving the AFM's force sensitivity further. At the same time, we sacrifice some of the ease of operation and fast sample turn-around times. This is also reflected in the fact that there is no well-established and widely used commercial low-temperature AFM available yet. Lastly, some common implementations of essential AFM components are not suitable for low-temperature operation.

In this chapter we detail some aspects of our specific home-built low-temperature atomic force microscope (LT-AFM). Further information on this instrument can be found in previous graduate students' theses (McCormick 1998, Woodside 2001).

3.1 The Low-Temperature Atomic Force Microscope

Our home-built AFM head is mounted in a commercial bottom-loading one-shot ^{3}He cryostat (by Janis Research Company) with base temperature $T_{\text{base}} = 0.3\,\text{K}$ (Richardson and Smith 1988, Pobell 1996). The AFM controller (SPM 1000), high-voltage amplifiers (HVA 900), and the software interface were made by RHK Technologies. The RHK SPM 1000 unit controls the scanning and the coarse sample translation hardware. For the scan tube, we use additional high-voltage amplifiers (HVA 900), which bias the 5 piezo electrodes in the range $\pm 520\,\text{V}$.

Vibration isolation. The cryostat mounting features several stages of vibration isolation to mechanically decouple the AFM from the environment. Three massive concrete pillars stand at 120° angle with respect to each other upon 5 layers of alternating rubber and steel plates. On each pillar's top, a passive air piston lifts a corner of the triangular air table. The air table is filled with lead bricks to increase its weight. The cryostat is mounted from the air table. Within the inner vacuum

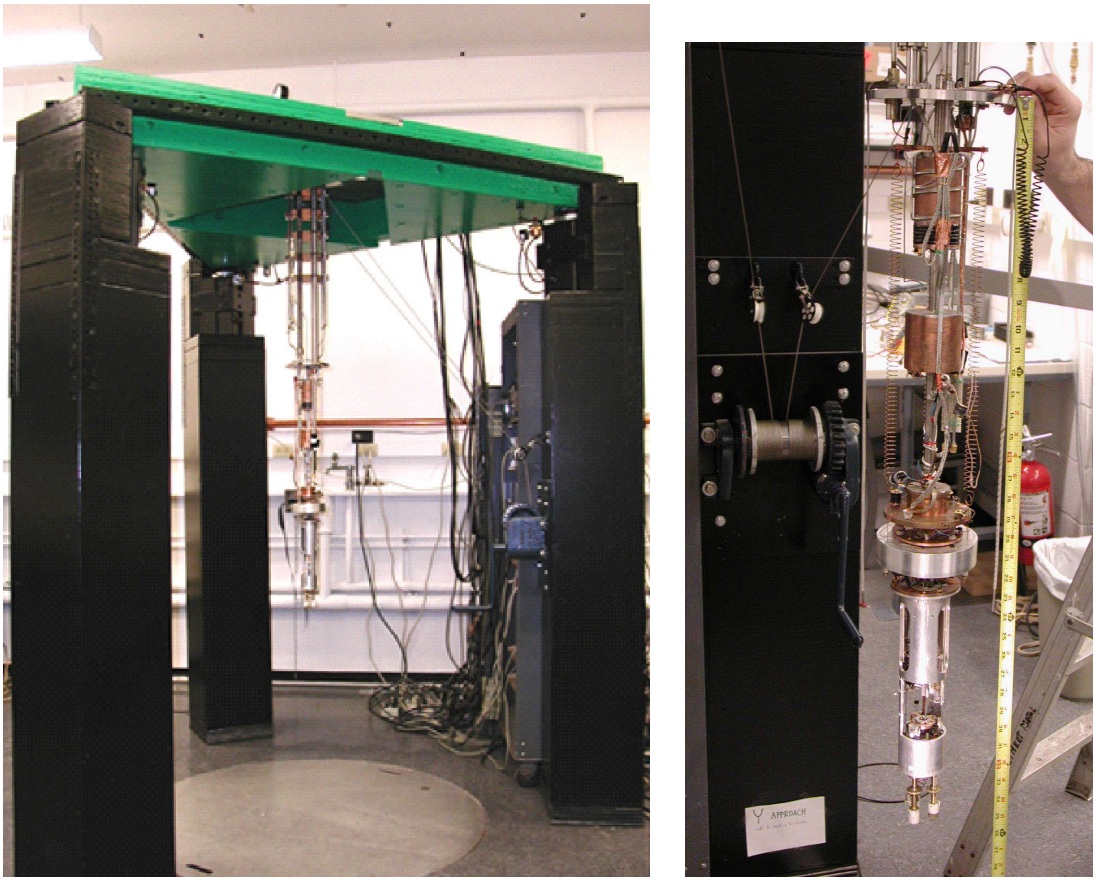

Figure 3.1: Vibration isolation stages of our low-temperature atomic force microscope. The left image shows the 3 concrete pillars (black) with air pistons that support the heavy air table (green) and the cryostat insert. The right image shows the inside of the inner vacuum chamber of the cryostat. The AFM cage (bottom center) is suspended from three long springs. The yellow tape measure in the right image gives a sense of scale.

chamber of the cryostat, the home-built AFM head is suspended from 3 long, soft springs. The photographs in Fig. 3.1 give an impression of our LT-AFM setup in the lab. The vacuum pump line is mechanically isolated from the cryostat through a bellow system.

AFM head. Our sample translation system is based on a Besocke style slip-stick walker (Besocke 1987). It enables the sample positioning underneath the tip in (x, y) and the coarse tip-sample approach in z. The walker has a translation range of 3 mm in (x, y) and a ramp size of 0.03 inches in z. It rests on 3 piezo tubes, as shown in Fig. 3.2. When walking, the piezos are biased in a saw-tooth voltage profile with a fixed time delay in between each voltage spike. The voltage on the walker piezo electrodes is limited to ± 100 V.

Three capacitance sensors allow us to monitor the sample position in the (x, y) plane. A copper band on the circumference of the sample holder is ac-voltage biased at 4 V and 4 kHz. The 3 readout plates are located at 120° angle with respect to each other. Each plate is coupled to a current amplifier followed by a lock-in amplifier chip. The electronic readout circuitry is detailed elsewhere (McCormick 1998).

We use a custom-made 4-inch long piezo tube to scan the tip above the sample surface. The 5 scan piezo electrodes are biased over a range of ± 520 V. The combination of this unusually long piezo scan tube and a very high bias voltage range allows us to maintain a large scan size even at low temperatures. At $T = 4$ K the scan size is still larger than $30\,\mu\text{m} \times 30\,\mu\text{m}$. The downside of such a long scan tube is the correspondingly long mechanical path length between tip and sample, causing the mechanical eigenmodes of the scan system to appear at lower frequencies.

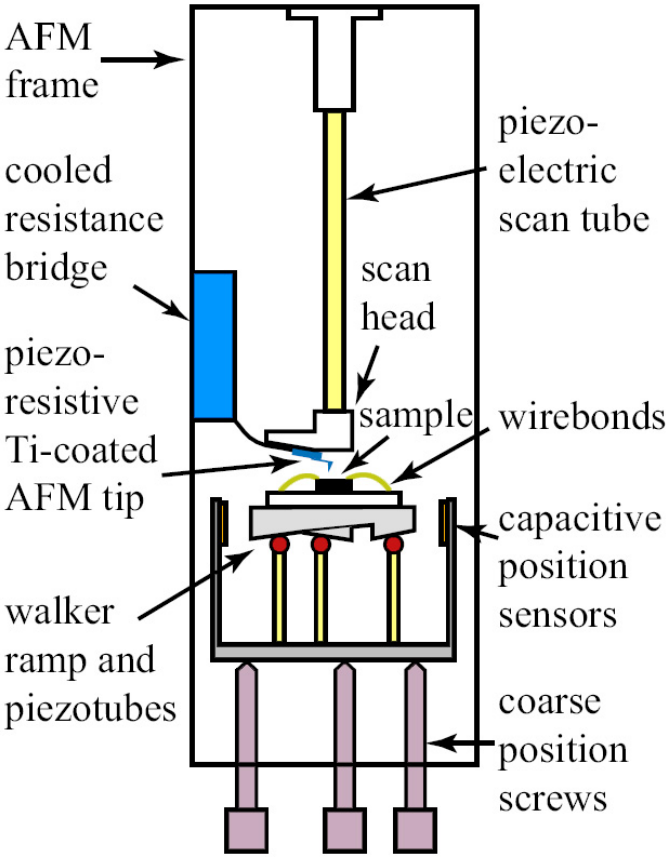

Figure 3.2: Schematic of the home-built LT-AFM head (from Woodside 2001).

The tip holder contains a piezoelectric bimorph actuator underneath the cantilever substrate. It enables us to drive the tip into oscillations at a constant ac-force amplitude, as needed for dissipation measurements (Sec. 6.4).

3.2 Piezo-resistive Cantilevers

Most room-temperature AFMs use an optical readout of forces acting on the tip. Keeping the optics aligned (either in the reflecting laser beam detection geometry or using a fiber interferometer (Rugar et al. 1988, 1989, Albrecht et al. 1992)) despite thermal contraction can be challenging in a cryogenic setup. Our force detection mechanism is all-electronic and relies on commercial piezo-resistive cantilevers (Park Scientific, ThermoMicroscopes, Veeco TM Microscopes). The cantilever has two legs of piezo-resisitve material that join at the end, where the tip is mounted, like a split diving board geometry. Some typical parameters of these cantilevers are listed in Table 3.1. The force detection scheme works as follows: A force acting on the tip causes the cantilever to flex. The resulting cantilever deflection $\Delta z = z - z_{\rm eq}$ follows from Hooke's law,

$$F = -k\,\Delta z\ . \tag{3.1}$$

In response to the mechanical deflection of the cantilever, the piezo-resistive legs of the cantilever change their resistance, $R_{\rm lever} = R_{\rm lever}(\Delta z)$. For typical tip deflections of 1 nm to a few nm, the relative change of piezo resistance is quite small (see piezo sensitivity in Table 3.1). We use a Wheatstone bridge to convert the relative resistance change of the cantilever into a differential voltage output. The Wheatstone bridge operates at cryogenic temperatures. Its schematic circuit diagram is shown in Fig. 3.3. The battery and its series resistor $R_{\rm limit}$ set the current

Table 3.1: Properties of the commercial piezo-resistive cantilevers.

Quantity	*Symbol*	*Typical Value or Range*
spring constant	k	$1-3\,\mathrm{N/m}$
resonance frequency	$\omega_0/2\pi$	$20-70\,\mathrm{kHz}$
quality factor	Q	$15,000-50,000$
resonance width	$\frac{\Delta\omega_{\mathrm{FWHP}}}{2\pi}=\frac{\omega_0}{2\pi Q}$	$0.8-1.6\,\mathrm{Hz}$
deflection sensitivity	$\frac{\Delta R/R}{\Delta z}$	$2\times10^{-6}/\mathrm{nm}$ $(T=4.2\,\mathrm{K})$
piezo resistance	R_{lever}	$2\,\mathrm{k\Omega}$
tip angle near apex	ϕ_{tip}	$\pm12^\circ$

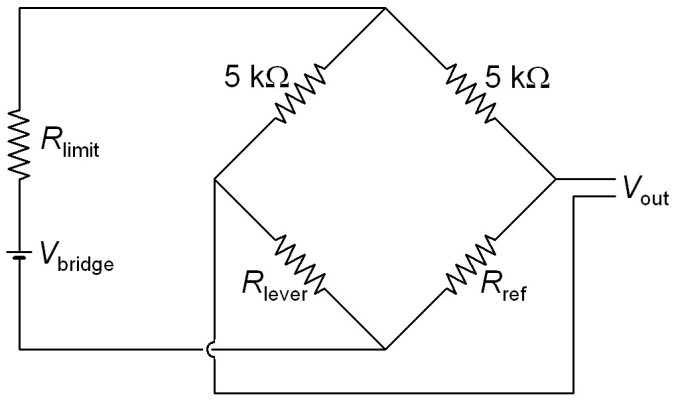

Figure 3.3: Schematic of the Wheatstone bridge detection circuit.

level through the actual bridge. For better signal-to-noise ratio, the current across the bridge should be large. At the same time, resistive heating of the cantilever requires the bridge current to be small to maintain a low temperature. The reference resistor $R_{\rm ref}$ must be matched to the cantilever resistance $R_{\rm lever}$ under experimental conditions. Note that the resistance of the piezo material changes with temperature and magnetic field[1].

The differential voltage output from the Wheatstone bridge can be amplified electronically and subsequently filtered and processed. We use coax and twin-ax (a twisted pair with a coax shield) cables throughout to shield the deflection signal from electronic noise.

The tip is metallized with a thin layer of Titanium by e-gun evaporation. We deposit 25 nm Ti at $\pm 25^\circ$ with respect to the tip normal, giving a 10-15 nm film. During evaporation a small blade acts as a shadow mask to cover the area between the two contact pads on the cantilever substrate. This prevents shorting the piezo resistor by the Ti film. To bias the tip, the entire Wheatstone bridge is lifted to a voltage $V_{\rm tip}$ above ground (GND).

3.3 Cantilever Calibration

The spring constant of the cantilever is defined as the proportionality constant between a small static force acting on the tip and the resulting cantilever deflection, Eq. (3.1). It measures the stiffness of the cantilever and can be obtained experimentally in several ways (Hutter and Bechhoefer 1993, Cleveland et al. 1993, Sader

[1] A surprise finding was that the resistance of our metal thin-film resistors increases steadily with decreasing temperature, typically by about 1% between room temperature and $T = 4.2$ K. The piezo-resistive cantilever resistance changes non-monotonically, often with a single minimum between 77 K and 4.2 K.

et al. 1995, 1999, Levy and Maaloum 2002, Burnham et al. 2003, Proksch et al. 2004).

We calibrate the spring constant from the thermal noise spectrum of the cantilever. A typical example spectrum is shown in Fig. 3.4. This technique is still applicable to our LT-AFM cantilevers operating at cryogenic temperatures, as the condition for the validity of the equipartition theorem, $k_B T \gg \hbar\omega_0$, is always met in our system, $T \gg 4\,\mu\mathrm{K}$.

An advantage of this technique is that it is non-invasive and non-destructive to the cantilever and tip. It is easy to carry out with the existing experimental setup and yields the complete set of intrinsic cantilever parameters, the spring constant k, the free resonance frequency ω_0, and the quality factor Q, simultaneously.

Briefly, at high enough temperatures the equipartition theorem mandates

$$\frac{1}{2}\,k\,\langle \Delta z(t)^2 \rangle = \frac{1}{2}\,k_B T \qquad \Rightarrow \qquad k = k_B T \,/\, \langle \Delta z(t)^2 \rangle \;. \tag{3.2}$$

The problem reduces to measuring the mean square oscillation amplitude $\langle \Delta z(t)^2 \rangle$ due to thermal excitations reliably. As there are other source of noise in the system, for example, mechanical vibrations from the environment, electronic instrument noise, and $1/f$ noise, measuring the oscillation amplitude is not a good approach. Instead, we record the spectral density of the cantilever oscillations, $S_{\Delta z}(\omega)$. Per definition, the *spectral density* or *power spectrum* is the Fourier transform of the corresponding autocorrelation function; so, inversely,

$$\langle \Delta z(t) \cdot \Delta z(t+\tau) \rangle = \int_{-\infty}^{\infty} \frac{d\omega}{2\pi}\; S_{\Delta z}(\omega)\, e^{-i\omega\tau} \;. \tag{3.3}$$

Since the cantilever deflection Δz is real-valued, $\Delta z^*(t) = \Delta z(t)$, its spectral density is real-valued and an even function of frequency, $S_{\Delta z}(-\omega) = S_{\Delta z}(\omega)$. In this case

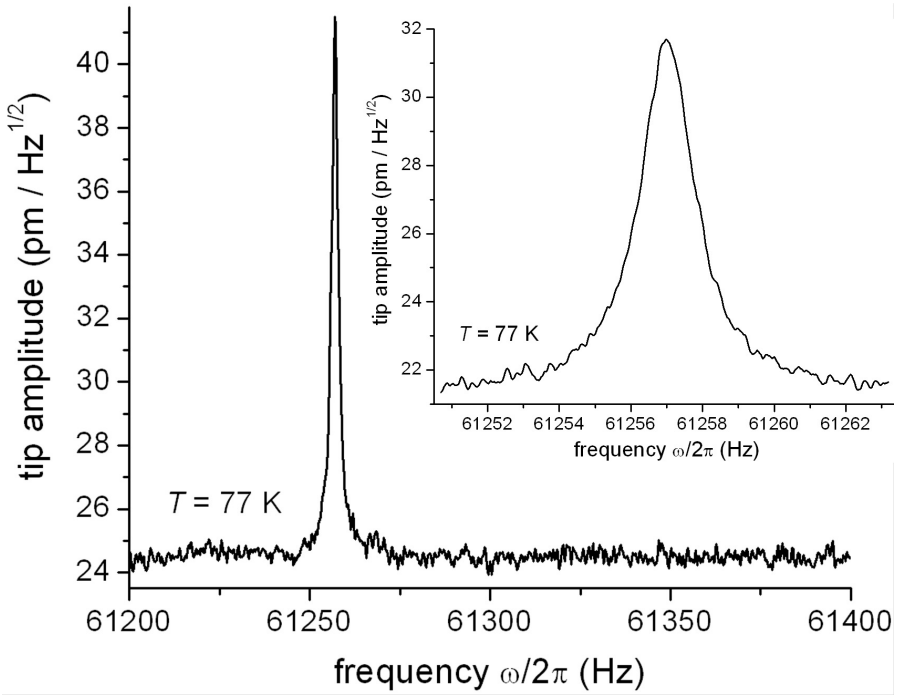

Figure 3.4: Thermal noise spectrum of the AFM cantilever, recorded at $T = 77\,\mathrm{K}$.

the integral (3.3) can be rewritten as[2]

$$\langle \Delta z(t) \cdot \Delta z(t+\tau) \rangle = 2 \int_0^\infty \frac{d\omega}{2\pi} \, S_{\Delta z}(\omega) \, \cos(\omega\tau) \qquad \text{if } \Delta z \text{ is real.} \tag{3.4}$$

Setting $\tau = 0$, we find that the desired mean square oscillation amplitude is given by twice the area under the thermal resonance peak in the spectral density, after subtracting the flat background noise. As it is unlikely that other noise sources are peaked about the resonance frequency of the cantilever, this isolates the contribution from thermal noise excitations. In combination with the equipartition theorem, Eq. (3.2), this allows us to determine the spring constant k of the cantilever.

The cantilever resonance frequency is given by the location of the peak of the spectral density. The quality factor is the ratio of the resonance frequency to the Lorentzian peak width of the spectral density, as can be seen from the following argument: The spectral density of the response is related to the spectral density of the excitation source by the Green's function $G(\omega)$ as

$$S_{\Delta z}(\omega) = |G(\omega)|^2 \, S_F(\omega) \; . \tag{3.5}$$

The Green's function for the damped harmonic oscillator is given by

$$G(\omega) = \frac{1}{k} \, \frac{\omega_0^2}{(\omega_0^2 - \omega^2) - i\,\omega\omega_0/Q} \; . \tag{3.6}$$

A thermal white noise source has the spectral density of excitation (Heer 1972)

$$\begin{aligned} S_F^{(\text{thermal})} &= 2\gamma\,\hbar\omega_0 \left(\frac{1}{e^{\hbar\omega_0/k_BT} - 1} + \frac{1}{2} \right) \\ &\xrightarrow{\hbar\omega_0 \ll k_BT} \; 2\gamma\, k_BT = 2\,\frac{k}{\omega_0}\,\frac{1}{Q}\,k_BT \; . \end{aligned} \tag{3.7}$$

[2] Experimentally, in the spirit of Eq. (3.4), the spectral density is sometimes defined as $2S_{\Delta z}(\omega)$. In our treatment, we will retain the definition (3.3) and carry along all necessary factors of 2. Having said this, one should cautiously check the definition of the output of one's spectrum analyzer. While checking the convention of our SR785, for example, we found an inconsistency in simple unit conversions.

So, the spectral density of thermal fluctuations in the cantilever deflection is

$$S_{\Delta z}^{(\text{thermal})}(\omega) = 2\,\frac{k_B T}{k}\,\frac{\omega_0}{Q}\,\frac{\omega_0^2}{(\omega_0^2-\omega^2)^2+(\omega\omega_0/Q)^2}\;. \tag{3.8}$$

Note that the spectral density is an even function of frequency, $S_{\Delta z}^{(\text{thermal})}(-\omega) = S_{\Delta z}^{(\text{thermal})}(\omega)$. Consequently, the resonance peak at ω_0 is mirrored at $-\omega_0$.

In the limit of small damping, $Q \gg 1$, the resonance is very sharp and the cantilever oscillation amplitude is only appreciable near either resonance peak; for the peak at $\omega \approx \pm\omega_0$, we approximate $\omega_0^2 - \omega^2 = (\omega_0+\omega)(\omega_0-\omega) \approx 2\omega_0\,(\omega_0 \mp \omega)$, respectively, and find that

$$S_{\Delta z,\,\pm\omega_0\text{-peak}}^{(\text{thermal})}(\omega) \approx 2\,\frac{k_B T}{k}\,\frac{\omega_0/Q}{4\,(\omega \mp \omega_0)^2+(\omega_0/Q)^2}\;. \tag{3.9}$$

The total spectral density is the sum of the contributions from the two peaks, which is an even function of ω again. Each peak has the form of a Lorentz function,

$$\mathcal{L}(x) = \mathcal{L}_0 + \frac{1}{2\pi}\left[4A\,\frac{W}{4\,(x-x_0)^2+W^2}\right]\;. \tag{3.10}$$

The factor $1/2\pi$ outside the brackets accounts for the corresponding integration factor in the inverse Fourier transform, Eq. (3.3). Extracting the center of the Lorentz peak x_0, the full-width half maximum W, the area A under either peak, and the offset $\mathcal{L}_0$ as fitting parameters on the measured spectral density gives the resonance frequency ω_0, the resonance width $\Delta\omega_{\text{FWHP}} = \omega_0/Q$, half the mean square displacement $k_B T/2k$, and the flat background noise, respectively.

When measuring the spectral density of thermal noise fluctuation of the cantilever deflection, the measurement line width should be much finer than the so-called equivalent noise bandwidth, while the frequency span of the measurement should exceed it. For a white noise source, the equivalent noise bandwidth is given

by (Ott 1988)

$$B_{\text{noise}} = \int_0^\infty \frac{d\omega}{2\pi} \left| \frac{G(\omega)}{G(\omega_0)} \right|^2 . \tag{3.11}$$

For the resonant cantilever, this equates to $B_{\text{noise}} = \omega_0/4Q$, which is typically $0.3 - 0.5\,\text{Hz}$ for our cantilevers.

To convert the spectral density of thermal tip oscillations from a spectrum analyzer output into proper units (nm^2/Hz), we need to calibrate the piezo deflection sensitivity of the cantilever. Note that it changes with temperature and the manufacturer quoted value is only roughly approximate. For this purpose, we collect force-distance curves, i.e., we record the dc-deflection of the cantilever as the scan tube extents in z until it pushes the tip slightly into the surface. This procedure in turn requires calibration of the scan tube extension, which we perform on a known height standard.

3.4 Detection Limit and Noise Considerations

Noise is always present in any experimental system and arises from different intrinsic and avoidable sources. Intrinsic noise often originates from random processes (for example, thermal fluctuations), and it is impossible to predict the exact noise amplitude at any given moment. Nonetheless, we can make reliable statistical statements and predict the average noise level. Correspondingly, the method of averaging the signal, in particular the time scales[3] involved in data taking, is relevant to the quality of data, as measured by the signal to noise ratio.

When sampling with a bandwidth B, the minimum force[4] that can be detected

[3]The leap from statistical ensemble average to time average is subtle in theory and subject to several conditions. We content ourselves with the assumption that the ergodic hypothesis is applicable.

[4]We define the limit of sensitivity as unity signal-to-noise ratio, $S/N = 1$.

by the cantilever is limited by[5] (Heer 1972)

$$F_{\text{noise}} = \sqrt{2\, S_F^{(\text{noise})}\, B} \;\geq\; \sqrt{\frac{4\, k\, k_B T\, B}{\omega_0\, Q}}\,, \tag{3.12}$$

where the last term evaluates the thermal noise contribution, Eq. (3.7). The most common strategy to reduce the force noise in the cantilever (and thereby increase the ultimate force sensitivity of the AFM) is to reduce the cantilever spring constant. Ultrasoft cantilevers with spring constants below $k \approx 10^{-5}\,\text{N/m}$ have been fabricated and force sensitivities down to $3\,\text{aN}/\sqrt{\text{Hz}}$ at $T = 4.2\,\text{K}$ have been measured (Stowe et al. 1997, Stipe et al. 2001, Jenkins et al. 2004). The corresponding noise in the cantilever rms-amplitude for our resonant measurement is given by

$$\Delta z_{\text{noise}} = \sqrt{2\, S_{\Delta z}^{(\text{noise})}(\omega_0)\, B} \;\geq\; \sqrt{\frac{4\, Q\, k_B T\, B}{\omega_0\, k}}\,. \tag{3.13}$$

Note that in the thermal noise limit, the equivalent noise bandwidth (3.11) formally reproduces the rms-amplitude (3.13) from the equipartition theorem, Eq. (3.2). Consequently, as our measurement bandwidth is larger than that, we sample most of the thermal noise response of the cantilever in our experiments.

For a typical piezo-resistive cantilever, Table 3.1, the above thermal noise limits evaluate to

$$\begin{aligned} \sqrt{2\, S_F^{(\text{thermal})}} &\approx 200\, \frac{\text{aN}}{\sqrt{\text{Hz}}} \times \sqrt{\frac{T}{4.2\,\text{K}}} \\ \sqrt{2\, S_{\Delta z}^{(\text{thermal})}(\omega_0)} &\approx 3.0\, \frac{\text{pm}}{\sqrt{\text{Hz}}} \times \sqrt{\frac{T}{4.2\,\text{K}}} \end{aligned} \tag{3.14}$$

for the cantilever force and deflection, respectively.

Equation (3.12) predicts the amount of thermal noise in the cantilever force and thereby establishes the ultimate limit of sensitivity of the AFM. The actual sensitivity, however, is determined by the cumulative effect of all noise contributions

[5]The factor of 2 in front of the noise power spectrum arises from the same factor in front of the integral (3.4) and is sometimes absorbed in the definition of the spectral density (Albrecht et al. 1991). See also footnote 2.

present in the system. As the cantilever deflection signal is detected, transferred, and processed, other sources of noise enter the signal path. To achieve the ultimate sensitivity, their cumulative effect has to remain well below the intrinsic noise of the cantilever.

An unavoidable source of noise is electronic instrument noise, whose most relevant contribution along the signal processing chain is the 1st amplification stage[6]. We use a home-made low-noise differential amplifier (McCormick 1998). The amplifier is special in several ways. To name just a few of its features: It offers a high voltage gain with a flat transfer characteristic from audio frequencies down to dc, $\mathcal{G}(\omega) \approx 6000 \;\; \forall \omega < 2\pi \times 100\,\mathrm{kHz}$. It has a large dynamic output range of $\pm 30V$ and a good common mode rejection ratio (CMRR). The amplifier operates at room temperature with a measured spectral noise density of $\sqrt{2\,S_V^{(\mathrm{ampl})}} \approx 0.7\,\mathrm{nV}/\sqrt{\mathrm{Hz}}$ at the input (McCormick 1998). Among other design criteria, to achieve such a low noise power at room temperature, we use 2×5 low-noise JFETs in parallel at the heart of the amplifier, which were hand-picked for their superior characteristics (and to match each other). In comparison, according to our detection scheme (see circuit diagram in Fig. 3.3), the thermal noise in the cantilever deflection (3.13) produces a voltage signal

$$\sqrt{2\,S_{\Delta V}^{(\mathrm{thermal})}(\omega)} = \frac{I_{\mathrm{bridge}}}{2}\,R_{\mathrm{lever}}\left(\frac{\Delta R/R}{\Delta z}\right)\sqrt{2\,S_{\Delta z}^{(\mathrm{thermal})}(\omega)} \tag{3.15}$$

at the output of the Wheatstone bridge. Under usual experimental conditions ($I_{\mathrm{bridge}} \approx 100\,\mu\mathrm{A}$), a typical cantilever (Table 3.1) produces thermal fluctuations of $\sqrt{2\,S_{\Delta V}^{(\mathrm{thermal})}(\omega_0)} \approx 0.6\,\mathrm{nV}/\sqrt{\mathrm{Hz}} \times \sqrt{T/4.2\,\mathrm{K}}$ at the input of the amplifier. Evidently, the electronic instrument noise of the 1st stage amplifier (operating at room

[6]After the signal has been amplified, the downstream noise is hopefully small in comparison and doesn't affect the signal-to-noise ratio any longer.

temperature) matches the thermal noise from the cantilever at about $T = 5.7\,\mathrm{K}$.

To be limited by thermal cantilever noise at lower temperatures, it is necessary reduce the electronic noise of the amplifier further. The main source of electronic instrument noise in our amplifier is Johnson-Nyquist noise (Johnson 1928, Nyquist 1928). It arises from thermal noise fluctuations in dissipative circuit elements. The spectral density of Johnson-Nyquist voltage noise originating from an ohmic resistance R is given by (Heer 1972, Papoulis and Pillai 2002)

$$S_{V(R)}^{(\mathrm{thermal})} = 2R\,k_B T\ . \tag{3.16}$$

Evidently, the Johnson-Nyquist noise of electronic components can be greatly reduced by operating at a lower temperature. Implementing a cold amplifier located inside the inner vacuum chamber of the cryostat for the 1$^{\mathrm{st}}$ amplification stage would decrease the electronic instrument noise notably. Further considerations need to go into the design of low-temperature electronics. In particular, many common Silicon-based electronic chips freeze out under cryogenic conditions and are not suitable for low temperature operation. A popular version of a cold amplifier is based on high-electron mobility transistors (HEMTs).

The Johnson-Nyquist noise analysis is directly applicable to our detection scheme: A cantilever deflection Δz is transduced into a resistance change ΔR by the piezo-resistive cantilever legs. The Wheatstone bridge turns this resistance change into a differential voltage readout ΔV by comparing the cantilever piezo resistance $R_{\mathrm{lever}} = R_{\mathrm{lever}}^{(0)} + \Delta R$ to a matched reference resistor $R_{\mathrm{ref}} \approx R_{\mathrm{lever}}^{(0)}$ as depicted in Fig. 3.3. From Eq. (3.16) we predict a voltage noise figure of

$$\sqrt{2\,S_{\Delta V}^{(\mathrm{bridge})}} = \sqrt{4R_{\mathrm{bridge}}\,k_B T} \approx 0.8\,\frac{\mathrm{nV}}{\sqrt{\mathrm{Hz}}} \times \sqrt{\frac{T}{4.2\,\mathrm{K}}}\ , \tag{3.17}$$

at the Wheatstone bridge output due to the detection scheme, where R_{bridge} is

the Thévenin equivalent resistance of the bridge circuit (Horowitz and Hill 1989). Hence, the electronic noise figure of our detection scheme is comparable to the noise from thermal cantilever vibrations at the same temperature and the home-built amplifier electronic noise. Notice that the thermal cantilever noise readout depends on the bridge current, Eq. (3.15), in contrast to the electronic detection and amplification noise. It can be adjusted slightly with respect to the other noise sources if needed – for example, when calibrating the cantilever by thermal noise detection, Sec. 3.3.

The above discussion considers several noise sources and evaluates their effect on the cantilever deflection and oscillation amplitude signal. A similar noise analysis can be done for the cantilever resonance frequency, as discussed in the literature (Albrecht et al. 1991).

3.5 Resonant Loop and Signal Readout

The quality factor of our cantilevers operating in (cryo-pumped) vacuum is very high. Correspondingly, our resonance peak is very narrow, $\Delta\omega_{\mathrm{FWHP}}/2\pi \approx 1\,\mathrm{Hz}$. In comparison, the overall change in resonance frequency within an image exceeds the resonance width many times. If the cantilever was driven at a fixed frequency, as common in many room temperature AFMs operating under ambient conditions or in liquids (with much lower Q-factor), the amplitude of cantilever oscillation would vanish in large parts of the image. To maintain a good amplitude response signal, the ac-driving force needs to follow the cantilever resonance frequency.

In our setup we use a phase-locked loop to keep the driving force on resonance, as schematically depicted in Fig. 3.5. The tip deflection signal is amplified (home-built low-noise amplifier) and band-pass filtered (Krohn-Hite 3382) appro-

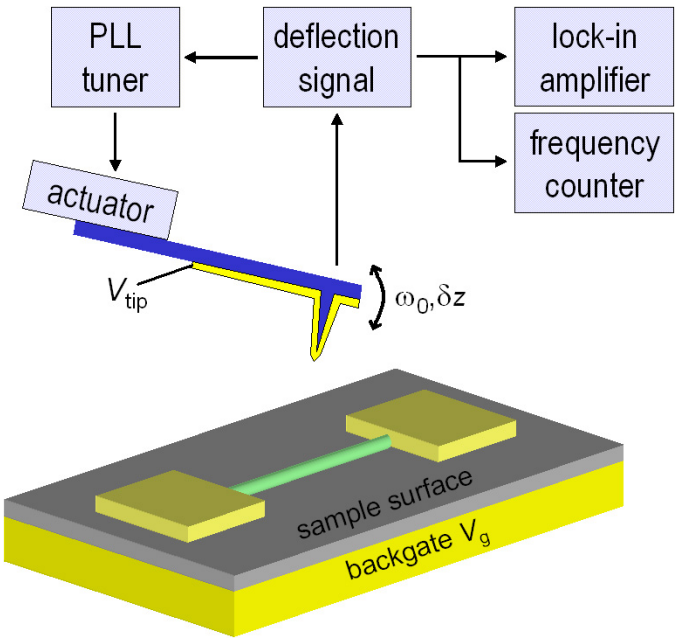

Figure 3.5: AFM resonant loop and output signal channels.

priately. After branching off the output channels for amplitude (EG&G 124A) and frequency (Agilent 53131A-010) readout, the signal is sent through a tunable phase shifter with constant amplitude output (home-built). The phase shifter's output is a TTL square wave at the same frequency as its input signal, i.e., the cantilever resonance frequency. The TTL square wave voltage is divided down to an appropriate amplitude and then used to drive a bimorph piezo actuator inside the tip holder, which mechanically sets the cantilever in motion. The cantilever can also be actuated capacitively through the sample, for example, by an ac-voltage on the extended backgate. This 2$^{\text{nd}}$ actuation scheme would not permit extracting dissipation information from the cantilever amplitude, however, as Q-degradation measurements require that the cantilever be driven at a constant ac-force amplitude. The driving force here scales with the backgate-tip capacitance derivative, though, which varies across the sample, $F_{\omega_0} = \dfrac{dC_{\text{tg}}(\vec{r})}{dz}\,\Delta V_{\text{tg}}^{(\text{dc})}\,V_{\text{g}}^{(\omega_0)}$. For resonance frequency measurements, either actuation scheme can be used.

3.6 Summary

In this chapter we have discussed several aspects of how to implement and operate an AFM at low-temperatures, with particular focus on our home-built system. Our force detection scheme using piezo-resistive cantilevers has been outlined and a common calibration procedure based on thermal noise fluctuations explained, yielding the full set of intrinsic cantilever parameters. We have addressed several sources of noise and evaluated fundamental noise limits for the cantilever deflection. Operationally, we run our AFM resonantly in a phase-locked loop. This mode offers two obvious signal channels: the tip oscillation amplitude and the cantilever resonance frequency, which are used in our experiments in Chap. 5 and 6.

CHAPTER 4

DEVICE FABRICATION

This section details several aspects of the sample fabrication. There are types of 2 samples investigated in this thesis: Carbon nanotube (CNT) electronic devices and gold nanoparticles that are chemically attached to a CNT by a linker molecule. In both samples, the CNT is embedded in a field-effect transistor (FET) geometry, where the CNT is directly contacted by two metal contacts, commonly called *source* and *drain*, and capacitively coupled to a 3rd electrode, called *gate*. A schematic of such a CNT-FET is shown in Fig. 4.1. First we discuss the fabrication of CNTs into a FET device, which mainly involves standard nanofabrication techniques and CNT growth. In the latter section we comment on how to link gold nanoparticles to a CNT and the related chemistry.

4.1 Carbon Nanotube Device Fabrication

In this section we outline the steps involved in making CNT electronic devices. Before going into specific details, we start out with an overview over the principal steps in the fabrication procedure:

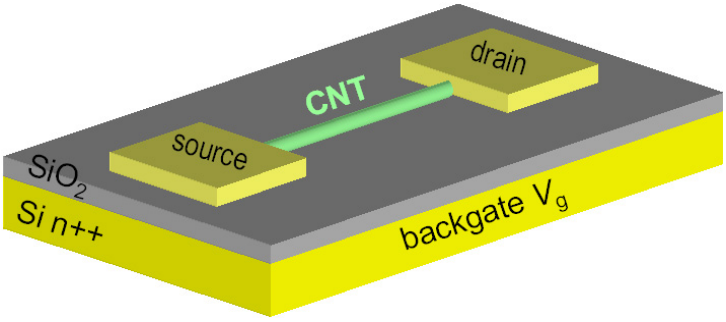

Figure 4.1: Schematic of a carbon nanotube in the field-effect transistor geometry.

1. We start from a degenerately doped silicon wafer with a thermal oxide of desired thickness. In a 1st lithographic process, we define alignment marks for later lithography steps on the wafer.

2. In a 2nd lithography step, we write the catalyst islands into a layer of resist.

3. After catalyst deposition and lift-off, we grow CNTs by chemical vapor deposition (CVD) in a furnace.

4. The source and drain contacts to the CNT devices are lithographically patterned, followed by metal evaporation and lift-off.

5. All CNT devices are probed electrically. The chip is mounted in a chip carrier and selected CNT devices are wire bonded for LT-AFM measurements.

For most processing steps, multiple tools are available to choose from and a large number of process variations exist. I first make some general remarks on several processing steps, where I frequently voice my personal opinion on some fabrication aspects. This is intended to motivate our choices at different stages in the device fabrication process. Afterwards we introduce some specific requirements for our LT-AFM samples and discuss how they can be implemented. To summarize, we give a more detailed sequence of processing steps at the end of this section, as it was employed in making the samples for Chap. 5.

Thermal oxide. Silicon wafers with a thermal oxide of any thickness are readily available commercially. Unfortunately, the thermal oxide quality of many commercial wafers varies from mediocre to poor. For higher quality thermal SiO_2, we often grow the oxide ourselves in a CMOS furnace. Particular care should be taken of cleanliness. Before the oxide growth, we subject the wafers to an RCA clean,

followed by a buffered oxide etch, which removes the native oxide from the wafers. For 100 nm or thicker SiO_2, we use a wet growth process (Pierret 1996).

The reason for our concern over the thermal oxide quality is that the SiO_2 serves as gate dielectric to the degenerately doped Si wafer, which is conducting even at cryogenic temperatures and commonly referred to as *backgate*. The backgate extends under all devices on the chip and gates all of them simultaneously. A poor thermal oxide breaks down more easily – at high applied gate voltages or during wire bonding – and causes ohmic conduction across the dielectric (called *gate leakage*) afterwards.

Alignment marks. In the first lithography step, we expose a series of alignment marks on the wafer. These include global alignment marks on the periphery of the wafer and a set of alignment marks for each chip on the wafer, which are best placed in the 4 corners of each chip. For convenience of orienting ourselves on the wafer later and finding the alignment marks in an optical or scanning electron microscope (SEM), we write along some optical locators, both globally on the wafer and within each chip. In this step we also write a local array of specific shapes on each chip, which allows us to precisely locate the CNTs on the sample surface, as explained later in the "special needs" section. Since the alignment marks must survive the high furnace temperatures during CNT growth pristinely, we etch them into the substrate. For e-beam lithography, at least 1 μm deep marks provide sufficient topographic contrast in the SEM, so that the automatic alignment algorithm of our e-beam writer works reliably, even at low beam current, as needed for the source and drain electrode exposure. For steep side walls, we use dry etches only. First we transfer the marks and locators into the thermal oxide with a standard

reactive ion etch using fluoroform (CHF_3). Once we reach the bottom of the oxide, we proceed with a Bosch deep etch process into the silicon. The shape of alignment marks is specific to the lithography tool(s) to be used later. On the Leica VB6 HR and the Leica EBMF 10.5 e-beam lithography tools, square marks with a $4\,\mu$m side have worked well for us. If applicable, bonding pads to the backgate may also conveniently be written and deep etched along in this step.

CNT synthesis. We grow our CNTs on chip by chemical vapor deposition (Kong et al. 1998). This process involves flowing some carbon-containing gas (or vapor) over the catalyst particles on the sample surface at a high temperature. The catalyst particles help decompose the carbon-containing gas, and CNTs grow out of them. There is a vast number of CVD recipes for CNT growth available today, with variations in catalyst materials and other add-on ingredients, different carbon-containing gases and vapors, carrier gas composition, flow rates, growth temperature, etc. (Dai 2000, 2001, 2002). In this research, all CNTs are grown from nonahydrate ferric nitrate ($Fe(NO_3)_3 \cdot 9\,H_2O$) as catalyst material. For our LT-AFM samples, we avoid other catalyst ingredients. Methane (CH_4) or ethylene (C_2H_4) are our preferred choice of carbon source for CNT growth. We use argon (Ar) as carrier gas and a small coflow of hydrogen (H_2). Our growth temperature varies between $T = 700 - 900\,^\circ$C, depending on the recipe. Just to mention some alternatives, CNTs can also be synthesized using other methods, for example, HiPCO or laser ablation, as discussed in the literature (Terrones 2004, Baddour and Briens 2005, Awasthi et al. 2005).

Lithography. Among the different lithography tools available, we have chosen an all e-beam process, for reasons explained later in this section. The cat-

alyst islands are designed as $2\,\mu\text{m} \times 2\,\mu\text{m}$ squares and exposed into a single thin layer of Poly(methyl methacrylate) (PMMA). In principle, this exposure could be done in photolithography, as it doesn't require precise alignment or small feature size. Some catalyst solvents (like methanol) tend to dissolve photoresist, but not PMMA, though. For the lift-off process of the source and drain contacts, we use a bilayer of e-beam resists. Over time I have come to prefer the combination of 495/950 PMMA[1] over a copolymer/495 PMMA bilayer with our e-beam writers. In the last lithography step, we skip the descum after resist development, as an oxygen plasma also etches the (partly exposed) CNTs readily.

Metal contacts. In the last lithography step of our fabrication outline above, we define the source and drain contacts to the CNTs. Palladium (Pd) is used as contact material to the CNT devices in Chap. 5. After the lithographic exposure and development of the electrode mask, a 50 nm film of Pd (without any adhesion layer) is e-gun evaporated and slowly lifted off in Acetone. No sonication is used to assist lift-off. The CNT devices in Chap. 6 are contacted by gold (Au) leads with a chromium (Cr) adhesion layer. Here we thermally evaporated 3 nm Cr followed by 35 nm Au.

Special LT-AFM sample needs. For experiments in the LT-AFM, some uncommon sample features are desirable:

- For purely operational convenience, the wire bonds to the sample should stay far away from the device regions; if possible, outside the range of the walker.

[1]The number before PMMA denotes the molecular weight of the resist in kilo Daltons (kDa). Per definition, a Dalton is the weight of a hydrogen atom. It is very similar to the weight of one atomic mass unit; sometimes they are set equal.

This way the AFM cantilever cannot break by running into wire bonds or contact wires during coarse approach of the sample surface.

- To avoid tall features in the sample topography near the scan area, we prefer a thin layer of small catalyst particles in the catalyst islands.

- A small capacitance between the AFM tip and the source and drain contacts reduces the electrostatic background signal in the measurement.

The 1st requirement is easily fulfilled: We push the bonding pads far out to the periphery of the chip. If the increasing resistance of the leads is problematic, we can increase the width and thickness of the metal strips between the bonding pads and the device contacts. To keep the catalyst islands small, we deposit catalyst particles from a very dilute solution of catalyst only, avoiding alumina particles and other add-on ingredients. Alternatively, one could also evaporate a thin layer of catalyst material (iron in our case) instead. To accommodate the last requirement, we do two things: (i) We only use relatively long CNTs for our devices[2]. This way the AFM tip gets away from the contacts. (ii) We design the source and drain contacts with a small footprint near the scan region. The correspondingly small surface area of the contacts gives a small capacitance to the AFM tip. In order to make the area of the contacts as small as possible, we need to locate every CNT to be connected and design a separate mask for each device, which is exposed in e-beam lithography. In order to locate the exact position of the CNTs on the surface, we need some unique features of known position nearby each CNT. For this purpose, we write an array of easily recognizable shapes on the surface, which

[2]All CNT devices in this research are longer than 7 μm. In the meantime, new CNT growth recipes (Huang et al. 2003a,b, Kim et al. 2002) have enabled the CVD growth of much longer CNTs.

Figure 4.2: Our choice of 4 elementary shapes for a local mark array.

has a fixed location with respect to the alignment marks. These shapes can be exposed and transferred together with the alignment marks. The details of our particular choices of shapes and their arrangement in an array are outlined in the following paragraph. With this array, we can image the grown CNTs on the sample surface, find their position relative to these shapes, and design an electrode mask for each tube.

Local mark array. The local array of easily recognizable shapes allows us to locate the CNTs on the sample surface and design an electrode mask for each CNT with small surface area near the device. We have selected 4 different elementary shapes, which are shown in Fig. 4.2. The center of each shape should be easy to find, as edges are unreliable in lithography and etching. For practical reasons, it is convenient to have at least one elementary shape that cannot be mapped onto itself or any other shape by 90° rotations. It gives a sense of (up/down and right/left) orientation of the chip within an image of the sample surface. Among our shapes in Fig. 4.2, the right-most one serves this purpose.

We arrange these 4 shapes in an array, where any square containing at least 4 shapes has a unique location within the array. Specifically, the 14×14 array we used is shown in Fig. 4.3. For clarity, the array is not drawn to scale. For our CNT devices, we make the shapes $1\,\mu$m wide and tall with a $10\,\mu$m center-to-center separation on the wafer.

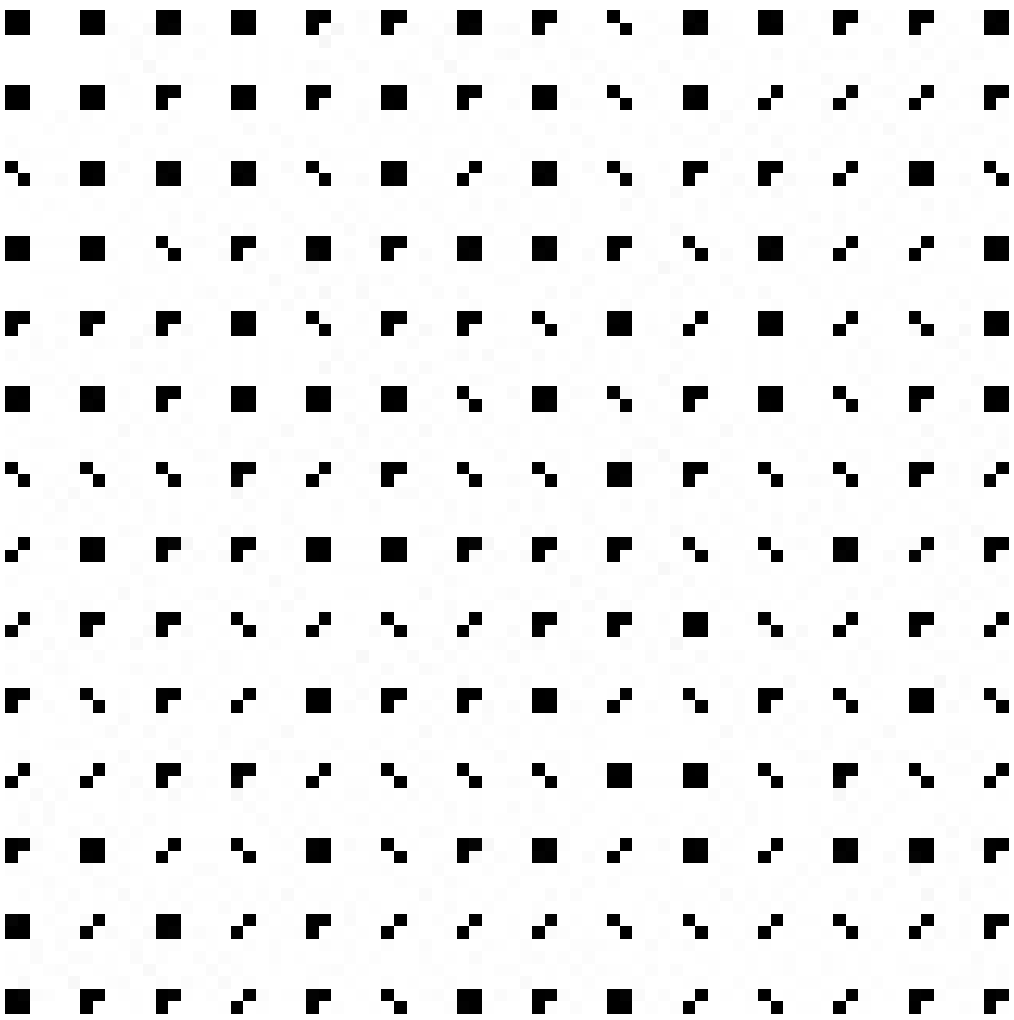

Figure 4.3: Local mark array that is used to locate the CNTs on the sample surface post growth. The 14×14 array arranges the 4 different shapes (Fig. 4.2) such that any 2×2 square is unique within the array. The array is not depicted true to scale. On the CNT chips, individual shapes are $1\,\mu$m on the side and spaced $10\,\mu$m center-to-center.

Sequence of fabrication steps. Now that we have gone into some detail on fabrication aspects and motivated our choices, we briefly run through the actual sequence of relevant steps once: We start from a degenerately doped silicon wafer terminated by a thermal oxide, which was either home-grown or bought commercially. In the first lithography step, we expose all features that give a sense of location and orientation: These are global alignment marks for the wafer, sets of alignment marks for each chip on the wafer, adequate optical locators, and a array of small shapes (local marks) on each chip, whose location is known with respect to the chip alignment marks. Additionally, we also expose the wire bonding pads to the backgate on each chip. All these features are written into a thick layer of PMMA in a single exposure, developed, and descummed, followed by a SiO_2 plasma etch (using CHF_3) and subsequent Si deep etch (Bosch process). In a second e-beam exposure, we use the global wafer alignment marks to expose $2\,\mu\text{m} \times 2\,\mu\text{m}$ squares at select locations within the local mark array into a thin resist layer. After the exposure, the wafer is cut into smaller chips ($5\,\text{mm} \times 5\,\text{mm}$) in a dicing saw. The resist is developed and descummed, then catalyst is deposited (either from solution or by evaporation) and lifted-off on each chip individually, leaving behind small islands of catalyst particles. CNTs are grown in a furnace by chemical vapor deposition. After growth, we use an AFM to locate the tubes with respect to the local mark array on the chip. Two topographic AFM images of CNTs after growth are shown in Fig. 4.4. A thin catalyst island is visible as a bright square in the middle of both images. The etched shapes of the mark array appear dark on the top and the bottom of the images. A CNT is seen as thin bright line emerging from the catalyst island. Knowing the tube's location with respect to 4 shapes in the mark array determines its location on the chip and allows

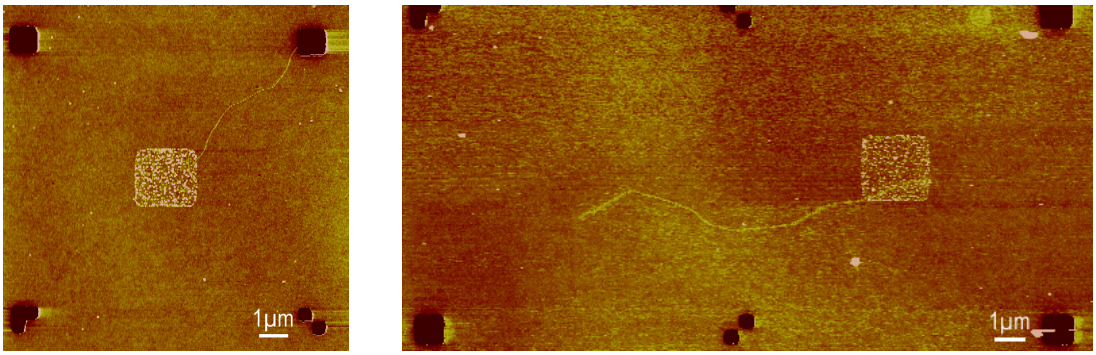

Figure 4.4: Topographic AFM images of CNTs on the patterned substrate.

us to design a mask with source and drain electrodes specifically tailored to the selected CNT. The electrode masks are written into a PMMA bilayer using e-beam lithography. After developing the electrodes, we evaporate the contact metal, followed by lift-off in Acetone. At this point the CNT is in an FET geometry. A few optical microscope images, shown in Fig. 4.5, give an impression of a typical e-beam chip made by the above fabrication sequence. The bright yellow areas are covered by gold. The Si/SiO_2 substrate appears differently colored in each image because of different microscope objectives used. In the right-most optical image, which is zoomed in furthest, the array of etched local marks is visible as black points. Some topographic AFM images of CNT devices are shown in Fig. 4.6.

Once a chip is made, we measure the conductance of each CNT device as a

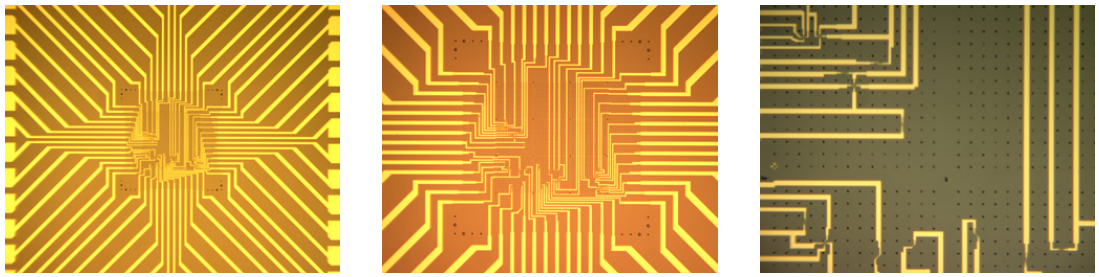

Figure 4.5: Optical microscope images of an e-beam chip.

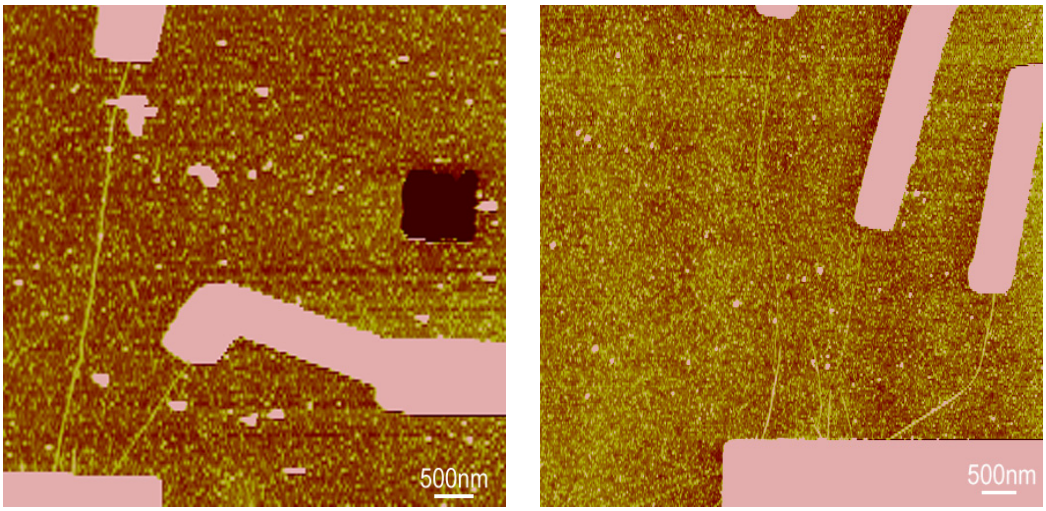

Figure 4.6: Topographic AFM images of CNTs with source and drain contacts. To make the CNT visible in the 2D color plots, we increase the image contrast by limiting the range of the height scale to a few nanometers. The much taller metal electrodes reach beyond this range, though, and seem flat in the 2D images. Their actual size ratio is illustrated in the 3D topographic AFM image in Fig. 1.2. The CNTs and the electrodes appear wider than they are due to the size and shape of the AFM tip.

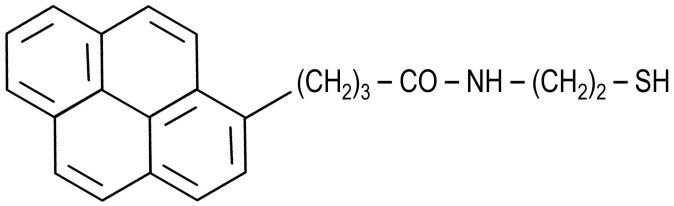

Figure 4.7: Chemical structure of the linker molecule between the CNT and a gold nanoparticle.

function of the backgate voltage at room temperature. Some exemplary transport traces are shown in Fig. 1.3 in Chap. 1. From the transport trace we determine whether the contacted CNT is metallic or semiconducting. The maximum device conductance gives us an idea about the contact resistance of each device. Promising CNT device candidates are electrically probed in a cryogenic probe station at $T \leq 10\,\mathrm{K}$. Afterwards, the chip is glued onto a home-made chip carrier with silver epoxy. Selected CNT devices (and the backgate) are wire bonded to the chip carrier. Care should be taken that the wires connecting the chip don't stick out too high, but stay low and come in at a sharp angle with respect to the substrate near the sample wire bonds. Tall wires may interfere with the AFM tip or the tip holder.

4.2 Gold Nanoparticle Attachment to a Carbon Nanotube

For the experiments described in Chap. 6, we use gold nanoparticles that are chemically linked to a CNT by an organic molecule. The chemical structure of the molecule used to link a gold nanoparticle and a CNT is depicted in Fig. 4.7. Essentially, the molecule consists of a pyrenyl group and a thiol that are connected by an organic chain. The –CO–NH– piece within the otherwise alkane chain is a remnant of the reaction chemistry in the synthesis of the molecule. The aromatic

pyrene (left end in Fig. 4.7) interacts strongly with the sidewalls of CNTs via π-stacking, as known from studies on graphite and CNTs. It adsorbs onto the surface of CNTs in organic solvents and is stable against desorption in aqueous solution (Chen et al. 2001). The thiol (right end in Fig. 4.7) is known to form a covalent bond with gold.

For the gold nanoparticle attachment, we start from a CNT device in the FET geometry, as described in Sec. 4.1. The source and drain contacts to the CNT for our samples in Chap. 6 are patterned by photolithography. We select CNTs with fairly flat backgate response in their transport characteristic. Since this is the only requirements on the CNTs, we are free to choose very long CNTs for this sample[3] so as to be able to get away from the CNT device contacts.

The CNT attachment scheme is adopted from Chen et al. (2001). It proceeds in the following three steps: (1) synthesize the linker molecule, (2) synthesize the gold nanoparticles, and (3) link the nanoparticles to the CNT. We briefly comment on each step below.

Linker molecule chemistry. The linker molecule is synthesized from two components: 1-pyrenebutanoic acid, succinimidyl ester and cysteamine. We freshly dissolve pyrenebutyric acid succinimidyl ester in dimethylformamide (DMF) to make a 0.08M solution. We also prepare a fresh 0.1M solution of cysteamine in DMF. We mix 0.3 ml of each solution in a microreactive vial and stir it in the dark for 2.5 hours. Afterwards, we dilute the product solution further with 10 ml DMF for later incubation of the CNT devices.

[3]In recent years, new CVD recipes have enabled the growth of extremely long CNTs (Huang et al. 2003a,b); up to 4 mm long CNTs have been reported (Zheng et al. 2004).

Gold nanoparticle synthesis. There are multiple ways to synthesize monodisperse gold colloids (Frens 1973, Slot and Geuze 1985, Brust et al. 1994, 1995, Bradley 1994). In principle, we reduce Au^{3+} ions using citrate: We let 25 μmol of $HAuCl_4$ and 200 μmol of Na_3-citrate react in 100 ml deionized water following Frens (1973). This ratio of reactants yields gold nanoparticles with a diameter of 12 nm. We centrifuge the gold colloid solution at 5000 rpm for 5 minutes to remove any gold aggregates. Only the clear, burgundy-colored solution is used in the following step. We infer the size distribution of the gold nanoparticles after the attachment process from their height in high-resolution topographic AFM images.

Attachment procedure. Before starting the actual attachment chemistry, we prepare the CNT-FET chip by outgassing it in a heated vacuum jar at 55 °C for 5 hours, followed by a 20-minute anneal at 400 °C under Argon flow in a furnace. Immediately afterwards, the CNT chip is soaked for 1 hour in the linker molecule solution (from step 1). The chip is thoroughly rinsed in DMF to wash off any excess molecules and dried in a pure nitrogen environment. It is then dipped for 60 seconds in the just centrifuged gold colloid solution, thoroughly rinsed in deionized water, and dried in pure nitrogen.

This linking of gold nanoparticles is highly specific, as the pyrene attaches selectively to the CNT over the substrate. Figure 4.8 shows topographic AFM images (recorded at room temperature) of CNT samples subjected to the above procedure. Clearly, the functionalized gold nanoparticles preferably link to the CNT. Only a few nanoparticles are found on the substrate away from the tube.

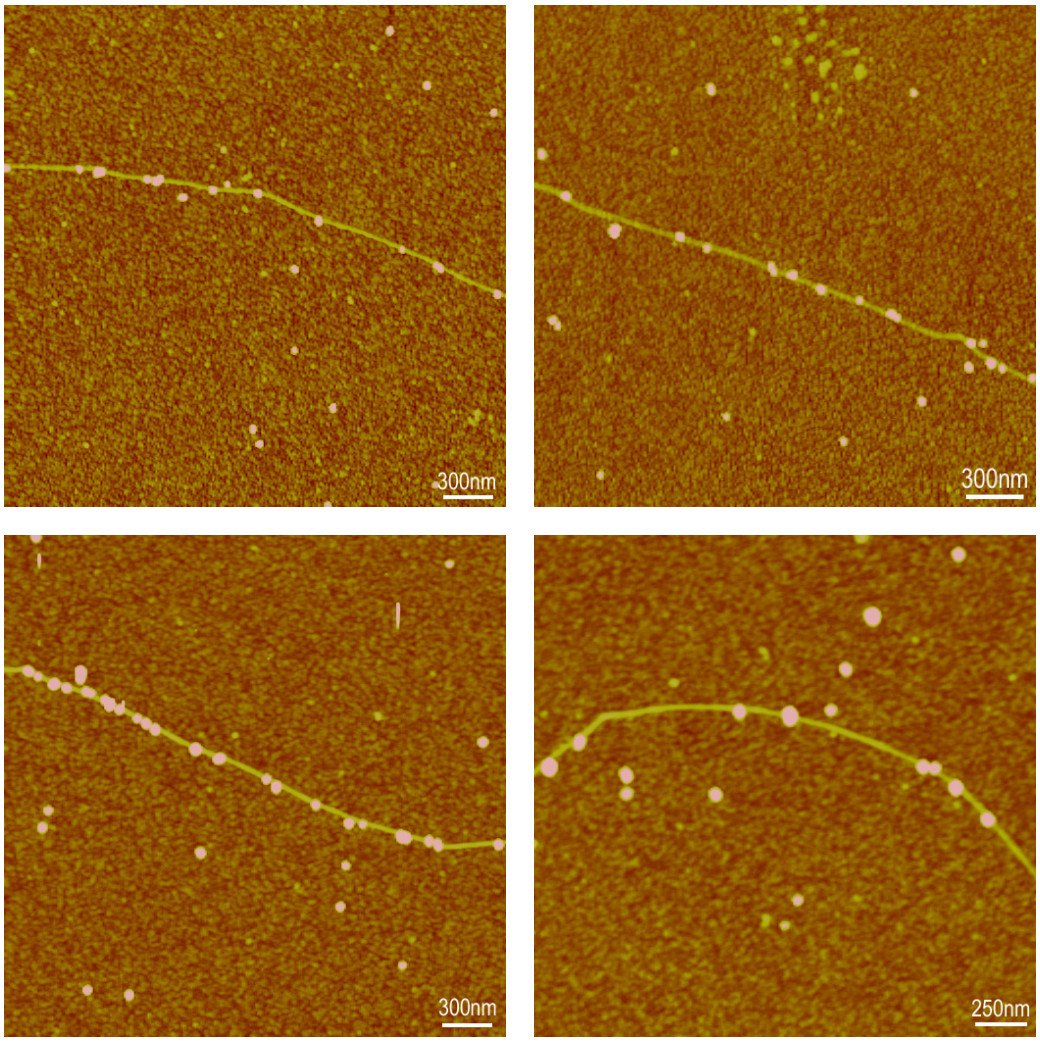

Figure 4.8: Topographic AFM images of gold nanoparticles attached to a CNT. The CNTs appear as thin bright line across the middle of each image. The gold nanoparticles (12 nm in diameter) are visible as white circles. Both the gold nanoparticles and the CNT appear wider in the images due to the size of the AFM tip. Most gold nanoparticles are located on top of or right next to the CNT. Only few of them are found on the SiO_2 substrate away from the tube.

CHAPTER 5

FREQUENCY SHIFT IMAGING OF SINGLE-ELECTRON CHARGING IN SEMICONDUCTING CARBON NANOTUBES AT $T = 4.2\,\mathrm{K}$

Carbon Nanotubes are an amazing material with unusual properties. Electronically, they are truly one-dimensional (1D) conductors or semiconductors, depending on the crystal structure. As the length of a CNT device is reduced, finite size effects are expected to occur, as the CNT enters the regime of Coulomb blockade and single-electron charging effects. This has been observed in low-temperature transport measurements (Tans et al. 1997, Bockrath et al. 1997, 1999). Figure 5.1 shows a low-temperature transport trace of a short, semiconducting CNT device. The conductance of this short device clearly shows multiple, quite evenly spaced peaks with zero conductance in between them. These so-called Coulomb oscillations in the conductance of the CNT device are a result of Coulomb blockade in an effectively zero-dimensional (0D) system. As the length of a CNT device (as measured by the distance between the source and drain contacts) increases, the separation between these Coulomb oscillations is expected to decrease. At some

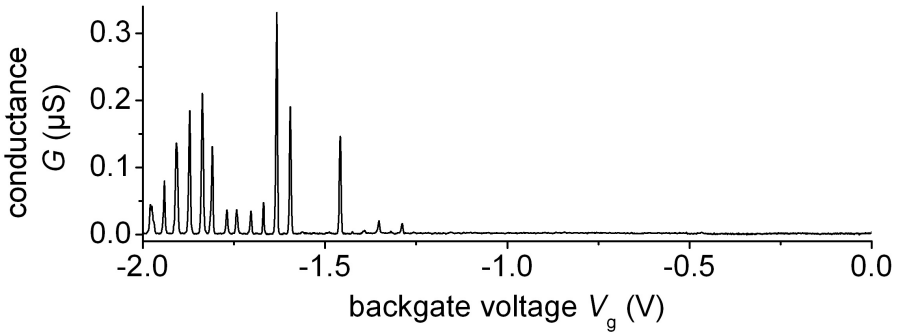

Figure 5.1: Coulomb oscillations in the low-temperature conductance of a short CNT device.

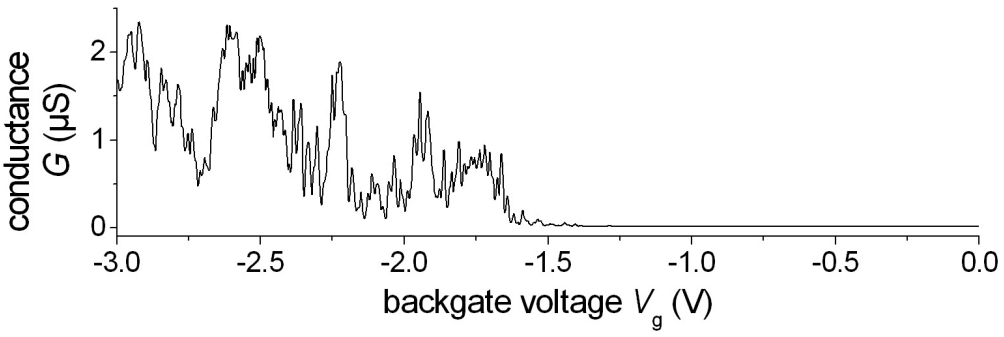

Figure 5.2: Electronic transport trace of a $8\,\mu$m long semiconducting CNT at $T = 4.2\,\mathrm{K}$.

tube length the peaks overlap, and ultimately (once $k_B T \gg E_C \propto 1/L_{\mathrm{CNT}}$) the 1D character of a long CNT device should become apparent in the transport trace.

Experimentally, however, we find a different situation realized. Figure 5.2 shows a transport trace of a $8\,\mu$m long, semiconducting CNT device at $T = 4.2\,\mathrm{K}$. Overall, this electron transport characteristic looks rather messy. While we observe non-zero conductance at backgate voltages $V\mathrm{g} \leq -1.8\,\mathrm{V}$, the device does not turn on monotonically. We still observe many peaks in the conductance. The peaks appear not quite evenly spaced, and we could make out several periods. In short, this is not the transport signal we expect from a clean 1D system.

This type of transport characteristic is expected, though, if there is disorder in the system. The term disorder summarizes a variety of unpredictable and random potential fluctuations that are caused by the environment of the device and will be present in most real systems. For example, disorder in our CNT device can be due to imperfections and defects in the substrate, fixed charges on the sample surface, adsorbates on the CNT, etc. In effect, disorder creates a non-uniform potential energy landscape that is felt by the charge carriers on the CNT and superimposes itself on the band structure of the nanotube. This is illustrated

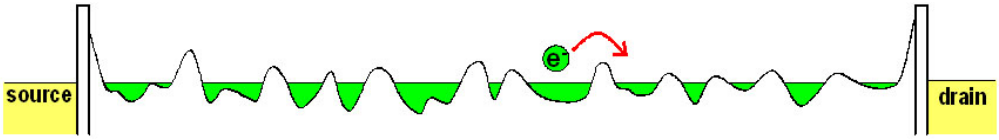

Figure 5.3: Non-flat conduction band edge of a CNT due to the disorder potential. At low temperature and low carrier density the CNT acts like a chain of quantum dots.

schematically in Fig. 5.3. The cartoon depicts the electrostatic potential seen by electrons on the CNT along the length of the tube. The shaded areas represent filled electron states in the conduction band of the tube. To move across the device, a conduction electrons has to overcome the barriers in the potential energy landscape along the conduction band bottom. As suggested by Fig. 5.3, disorder tends to be particularly visible at low carrier density, where the free electrons on the tube cannot collectively compensate for the effects of disorder.

To investigate these non-uniform potential variations and its effects on the electronic properties of a CNT, we need a spatially sensitive tool, such as a scanning probe microscope. Previous scanning probe studies of the electronic properties of CNTs at cryogenic temperatures include Scanning Gate Microscopy on metallic CNTs (Woodside 2001, Woodside and McEuen 2002), where single-electron charging effects were observed. Using the same technique, Coulomb blockade phenomena have also been observed in another 1D conductor, silicon nanowires (Bleszynski 2006). Quantum dots in two-dimensional electron gases (2DEGs) that were defined electrostatically or by etching have also been investigated by the scanning gate technique (Pioda et al. 2004, Fallahi et al. 2005, Kicin et al. 2005).

In this chapter we make use of the local force probe capabilities of the AFM cantilever to explore single-electron charging effects in semiconducting CNTs at low

carrier density. In particular, we use the resonance frequency ω_0 of the cantilever as a sensitive measure of the electrostatic interactions between the AFM tip and the sample. We start by estimating the size of the resonance frequency shift that we can expect from single-electron tunneling on and off a quantum dot in the CNT. Summarizing Eqs. (2.81) and (2.82), the relative shift of the cantilever resonance frequency due to single-electron tunneling on and off a quantum dot in response to the nearby oscillating AFM tip is given by

$$\frac{\delta\omega_0}{\omega_0} = \frac{1}{2k}\left(\frac{dq_\mathrm{c}}{dz}\,\frac{e}{C_\mathrm{dot}}\right)^2 \frac{f'(\Delta E_\mathrm{dc})}{1+(\omega/\Gamma)^2}\,. \tag{5.1}$$

From a rough estimate, $-\dfrac{dq_\mathrm{c}}{dz} \approx \dfrac{dC_\mathrm{td}}{dz}\,V_\mathrm{tip} \approx \epsilon_0\,V_\mathrm{tip}$, $C_\mathrm{dot} \approx 10\,\mathrm{aF}$, $\omega = \omega_0 < \Gamma$, and $f'(0) = \dfrac{-1}{4k_BT}$, we expect at $T = 4.2\,\mathrm{K}$ a resonance frequency shift on the order of $\delta\omega_0/2\pi \approx -1\,\mathrm{Hz}$ for our cantilevers (Table 3.1). This shift is easily resolved by a commercial frequency counter[1]. To validate this prediction experimentally, we record several traces of the cantilever resonance frequency as the AFM tip oscillates above a semiconducting CNT and the backgate voltage induces carriers on the tube. A few example traces are shown in Fig. 5.4. A single trace collected at a tip height of $z_0 = 100\,\mathrm{nm}$ is seen in Fig. 5.4(a). There are 4 distinct dips in the cantilever resonance frequency below the otherwise slowly varying background. Their size is, indeed, as estimated from Eq. (5.1). We attribute these dips to single-electron charging events of a quantum dot that is in close proximity of the AFM tip. The background envelope of the cantilever resonance frequency arises from the capacitive backgate-tip interaction. In Fig. 5.4(b) we show several traces of the cantilever resonance frequency at different tip heights. In each trace, 12 dips are visible in the cantilever resonance frequency due to different single-electron

[1]We typically achieve a frequency resolution of about $\Delta\omega_\mathrm{noise}/2\pi \approx 0.05\,\mathrm{Hz}$ in our measurements.

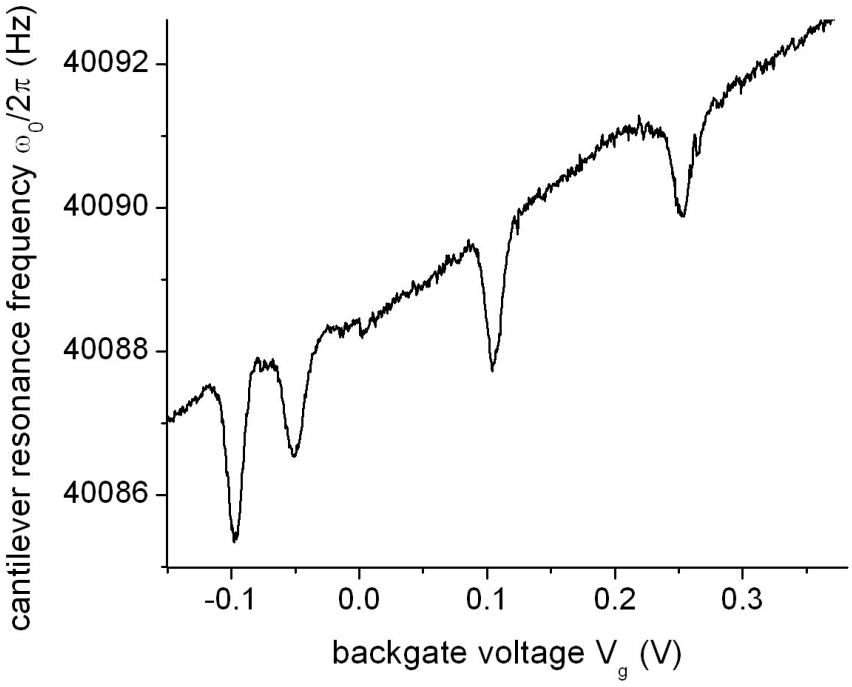

(a) Cantilever resonance frequency at $z_0 = 100\,\mathrm{nm}$ and $T = 4.2\,\mathrm{K}$.

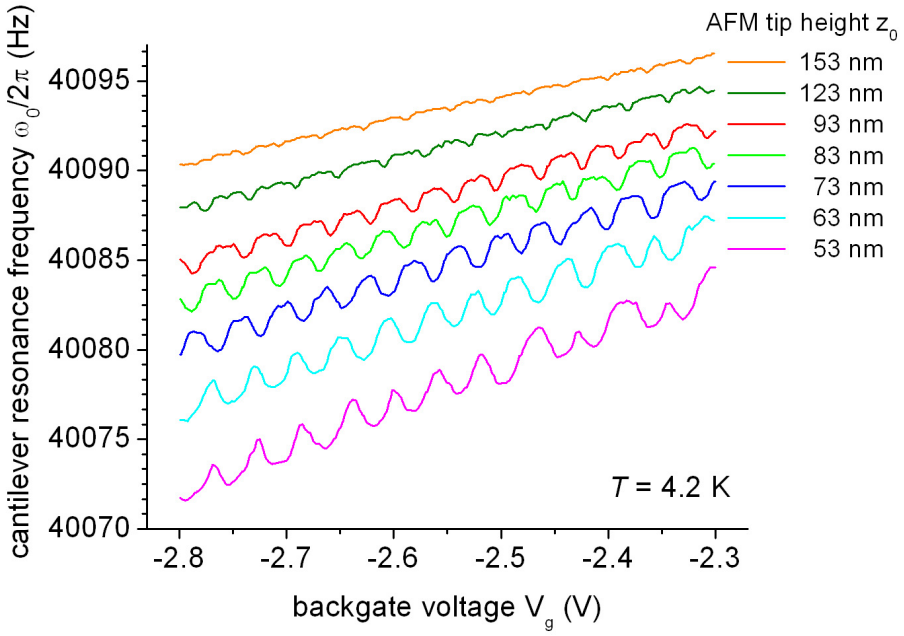

(b) Cantilever resonance frequency traces at $T = 4.2\,\mathrm{K}$.

Figure 5.4: Cantilever resonance frequency shift due to single-electron tunneling.

charging events. At the largest tip height, $z_0 = 153\,\mathrm{nm}$, the dips are barely visible. As the tip gets closer to the CNT, the dips in the cantilever resonance frequency get first deeper and ultimately also broader. The peak broadening can be reduced by decreasing the cantilever oscillation amplitude, which we intentionally kept constant for all tip heights in this plot.

Evidently, single-electron charging events of quantum dots in CNTs are clearly resolved in the cantilever resonance frequency. Now we can use the versatile capabilities of the AFM to image these single-electron charging events in various ways and examine the properties of the underlying quantum dots. This chapter takes the following path:

We first track the dips seen in Fig. 5.4 in space (Sec. 5.1). To do so, we record the cantilever resonance frequency as a function of tip position on a square grid, where the AFM tip has the same height above the sample surface at each point on the grid. We call such a 2D map of the cantilever resonance frequency a *spatial frequency shift image*. Such spatial images allow us to locate individual quantum dots on the CNT. We can also count the number of quantum dots along the CNT and get an idea about their size. Once we know where the quantum dots are located, we can address and study them individually, one at a time.

In Sec. 5.2 we combine the spatial resolution of the AFM with the gating capabilities of the backgate or tip voltage. Any 2D map of single-electron charging events in the cantilever resonance frequency as a function of a gate voltage and the tip position (along some fixed direction) we call a *spectroscopic frequency shift image* or just *frequency shift spectrum* of one or multiple quantum dots.

Replacing the one remaining spatial dimension of a spectrum, we track the single-electron charging events as a function of the voltages applied to our two gates –

the extended backgate and the AFM tip – as exemplified at the end of Sec. 5.2. To distinguish between the different images involving gate voltage, we sometimes label them intuitively V_g-x spectra and V_g-V_{tip} spectra of quantum dots.

Multi-dot V_g-x spectra enable us to extract the backgate coupling and the size of quantum dots (Sec. 5.3). We find that the mutual capacitance between the extended backgate and a CNT quantum dot scales linearly with the length of the quantum dot section of the CNT.

In the V_g-x spectra we observe the systematic charging of the quantum dots along the CNT over a large range of gate voltage (Sec. 5.4). Effectively, a quantum dot spectrum encodes the charge addition spectrum. The evolution of the spectrum in gate voltage reflects the underlying potential energy landscape as experienced by the carriers on the CNT. As a consequence, the charging spectrum mirrors the band structure of the semiconducting CNT (Sec. 5.6). Furthermore, the disorder potential is encoded in the evolution of each charging spectrum (Sec. 5.5).

At the intersection between the charging lines from neighboring quantum dots we frequently observe avoided crossings. These are analyzed in Sec. 5.7.

Up to this point, the size of the dips in the cantilever resonance frequency has not been used, only their positions in space and gate voltage. In Sec. 5.8 we analyze the information contained in the magnitude of frequency shift and extract the charging energy of a quantum dot from it.

The advantages of the frequency shift technique have been apparent throughout this chapter, but were rarely mentioned explicitly. In the last section of this chapter (Sec. 5.9) we explore some distinct benefits of the technique. We analyze spatial images collected from a CNT without source or drain contact and draw conclusions on the number of contacts needed for our measurement.

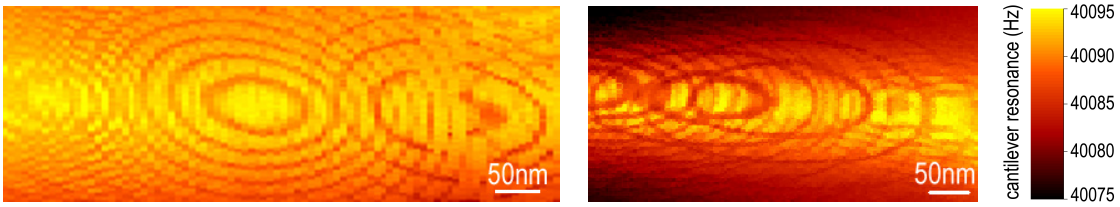

Figure 5.5: Spatial frequency shift images of quantum dots in semiconducting carbon nanotubes.

5.1 Spatial frequency shift images

A spatial frequency shift image is a map of the cantilever resonance frequency as a function of the biased tip position in the (x, y)-plane parallel to the sample surface. Spatial frequency shift images of quantum dots in CNTs are very useful. They allow us to find the quantum dots along the CNT, which we need in order to study them individually. When locating a quantum dot, we rely on the signature of single-electron tunneling on and off the quantum dot in the resonance frequency of the AFM cantilever, as described by Eq. (5.1).

Figure 5.5 shows two spatial frequency shift images of sections of a semiconducting CNT. The resonance frequency of the cantilever is encoded in the color scale, as shown on the right. A semiconducting CNT runs horizontally across each image. It is responsible for the wide, bright (yellow) line in the smooth electrostatic background. Single-electron charging events of quantum dots are visible as closed dark contours. A quantum dot is located at the center of each set of concentric contours. Small quantum dots have (almost) circular single-electron charging rings. Larger dots extend over a longer 1D segment of the CNT and have more oval single-electron charging contours. Since their charging energy is less, larger quantum dots also have more finely spaced single-electron charging contours than

small quantum dots.

Since it is not immediately obvious, we explicitly establish the relationship between the dark concentric contours in the spatial frequency shift images (Fig. 5.5) and the dips in the resonance frequency as a function of backgate voltage (Fig. 5.4). Both figures show a reduced cantilever resonance frequency at single-electron charging events of a quantum dot. The way charge is induced on the quantum dot, however, is different. In the 1D traces, we induce charges on the quantum dot by means of the voltage V_{g} on the backgate. In the spatial images, we use the biased AFM tip as a mobile, local gate. Changing the tip position $\vec{r}$ modifies the tip-dot capacitance $C_{\mathrm{td}}(\vec{r})$ and thereby induces charge on the quantum dot.

A unified description of both mechanisms is available in terms of a cumulative gate charge of the quantum dot, as defined in Eq. (2.5) or (2.51). The gate charge accounts for all electrostatic gating mechanisms of the quantum dot. Experimentally, the only two gates in the system[2] are the extended backgate and the mobile AFM tip, so

$$-q_{\mathrm{c}} = C_{\mathrm{gd}}\, V_{\mathrm{g}} + C_{\mathrm{td}}(\vec{r})\, V_{\mathrm{tip}} \; . \tag{5.2}$$

C_{gd} is the backgate-dot capacitance and V_{tip} is the voltage applied to the AFM tip. The voltages on the extended backgate and the AFM tip are V_{g} and V_{tip}, respectively. Clearly, the gate charge is a function of the backgate voltage, the tip voltage, and the tip location as externally adjustable parameters, $q_{\mathrm{c}} = q_{\mathrm{c}}(V_{\mathrm{g}}, V_{\mathrm{tip}}, \vec{r})$.

When the tip moves along a concentric contour in the spatial image, the gate

[2]The source and drain contacts also have some capacitance to the dots on the CNT, particularly for dots near the contact. Their contribution does not appear in Eq. (5.2), as we use the device contacts as our reference potential, $V_{\mathrm{s}} = V_{\mathrm{d}} = 0$. Even during scanning gate images, where we put a small bias across the CNT, their contribution is negligible. Gating by single-electron charging of other nearby quantum dots through interdot capacitive coupling is discussed separately in Sec. 5.7.

charge is maintained constant. When the tip moves perpendicular to these contours, the gate charge changes. As a consequence, the electrostatic potential of the quantum dot also changes, Eq. (2.5). At each dark ring the gate charge is such that two charge states of the quantum dot are degenerate. When the tip crosses a dark line, it causes an electron to tunnel on or off the quantum dot, depending on the sign of the tip voltage and the direction of tip motion (towards or away from the dot). Correspondingly, we could count the number of electrons on the dot (up to some fixed offset), which is unchanged in between the dark rings.

Besides locating the center of quantum dots, the information in a spatial image can give us an estimate of the size of our quantum dots. A simple upper bound is established from twice the center-to-center distance between neighboring dots. More elaborate algorithms can yield tighter bounds on the dot sizes from the spatial images. We won't expand on details here, as a different kind of scan allows us to calculate the exact size of our quantum dots. This scan is introduced in the following section. A method to extract the size of quantum dots from it is discussed in Sec. 5.3.

5.2 Spectroscopic frequency shift images

With the notion of a gate charge (5.2), there are clearly other 2D maps of the cantilever resonance frequency that exhibit single-electron charging. Instead of adjusting the gate charge (5.2) by means of the tip location, we can also use a gate voltage as an alternative experimental knob. There are some advantages to using a gate voltage: It can cover a large range of gate charges, and the gate charge varies linearly with gate voltage, which makes the quantitative analysis of the data simpler.

In this section we introduce 2D scans with variable gate voltage. For the 2 scan variables, we may choose to increment a gate voltage on one image axis and scan the tip location (along some fixed curve, for example, along the CNT) on the other image axis, retaining one spatial dimension in the image. Alternatively, we can independently vary the voltages on 2 gates, in our case the extended backgate and the AFM tip, to create a 2D scan of the cantilever resonance frequency. We call either such 2D image on one or more quantum dots a *spectroscopic image* or in short *spectrum* of the dot(s). Both types of spectra provide useful information about the quantum dot(s), and we explore them separately below.

V_g-x spectra of quantum dots. We start with spectra of mixed variables, i.e., a spatial dimension and a gate voltage (or energetic dimension). Figure 5.6 shows a V_g-x frequency shift spectrum of a relatively small quantum dot in a semiconducting CNT. The backgate voltage increases along the y-axis, ranging from $V_g = 1.4\,\mathrm{V}$ at the bottom to $V_g = 5.8\,\mathrm{V}$ at the top. Along the x-axis the tip scans 100 nm above a short section of the CNT. The cantilever resonance frequency is shown in color. A number of separate scans was stitched together in this figure.

Many single-electron charging events are visible as humps[3] in this 2D image. Along these humps, the gate charge (5.2) is constant and fixes the state of the underlying quantum dot at a transition between two charge states, N and $N+1$, so that an electron can repeatedly tunnel on and off the quantum dot. Here N and $N+1$ denote the number of electrons on the quantum dot. In between these charging humps, the dot is in Coulomb blockade and the number of electrons on

[3]The humps indicate a negative voltage on the AFM tip, $V_{\mathrm{tip}} < 0V$. With a positive tip voltage we would observe single-electron charging lines in the shape of slumps.

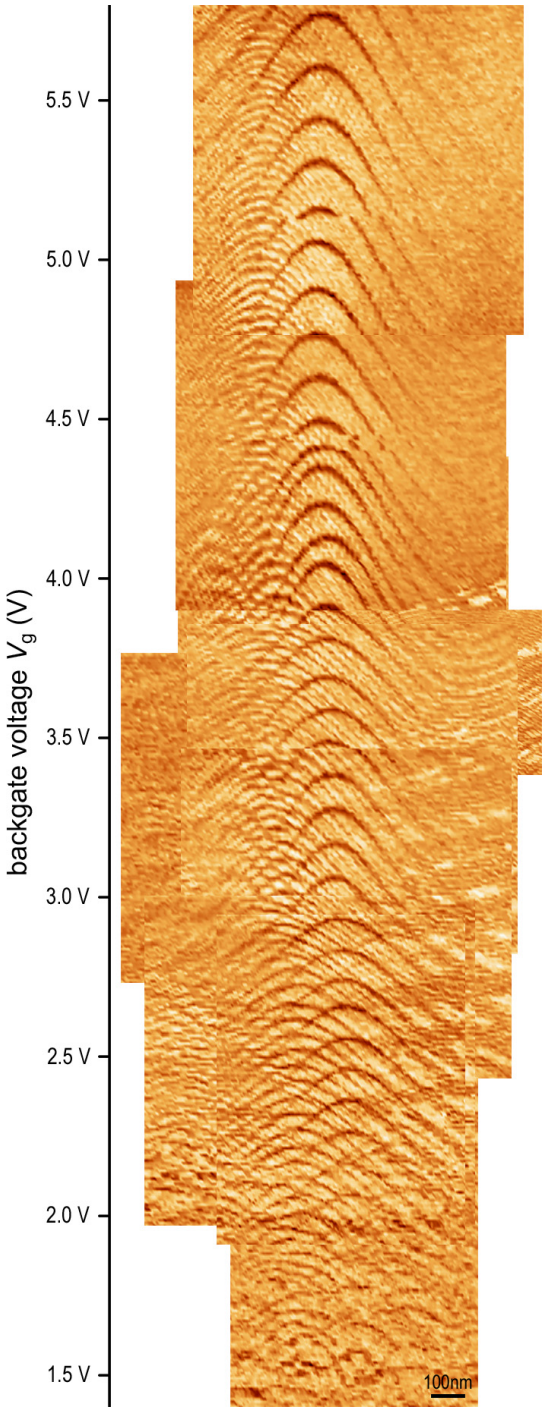

Figure 5.6: Large charge addition spectrum of a small quantum dot in a CNT. The gate voltage increases along the y-axis from $V_g = 1.4\,\mathrm{V}$ at the bottom to $V_g = 5.8\,\mathrm{V}$ at the top. Along the x-axis, the tip scans above a short section of a CNT at a height of $z_0 = 100\,\mathrm{nm}$. The top edge of the image is $1\,\mu\mathrm{m}$.

the quantum dot is constant. At the apex of each hump the tip is closest to the dot, i.e., right above the dot in our scan.

Besides the center of the quantum dot along the spatial scan axis, we can readout the separation between two charging events along the gate voltage axis in a spectrum. We call the difference in gate voltage between two consecutive single-electron charging events the single-electron *addition gate voltage* of the corresponding gate and dot. The addition gate voltage was already introduced in Sec. 2.1.5 and evaluated in Eq. (2.8). With this notion in mind, we can think of our quantum dot spectrum as an addition energy diagram. To readout actual addition energies that are intrinsic to the quantum dot, the y-axis still needs to be scaled by the gate efficiency $\alpha_\mathrm{g} = C_\mathrm{gd}/C_\mathrm{dot}$. We will discuss later in this chapter how we can measure the backgate-dot capacitance C_gd (Sec. 5.3) and the total dot capacitance C_dot (Sec. 5.8). For the time being, we accept arbitrary units on our addition energy axis.

The first obvious question to be asked about a spectrum is how the addition gate voltage of the quantum dot evolves as we induce electrons one by one on the dot. Figure 5.7 shows the evolution of the addition backgate voltage of the small quantum dot in Fig. 5.6, whose charging humps are conspicuously visible in the spectrum. (There is another, larger quantum dot visible in the same spectrum, just left of this dot.) For the first 25 electrons resolved on this dot, the addition backgate voltage evolves with a fairly constant average of $\Delta V_\mathrm{g}^{(\mathrm{add})} = 98\,\mathrm{mV}$ and a standard deviation of 10 mV. At high electron number, $N - N_\mathrm{offset} > 30$, corresponding to backgate voltages $V_\mathrm{g} > 4.2\,\mathrm{V}$, the average moves to higher addition backgate voltages, for unknown reasons. The variations in the addition backgate voltage are an indication of the limits of the constant interaction model, which was introduced

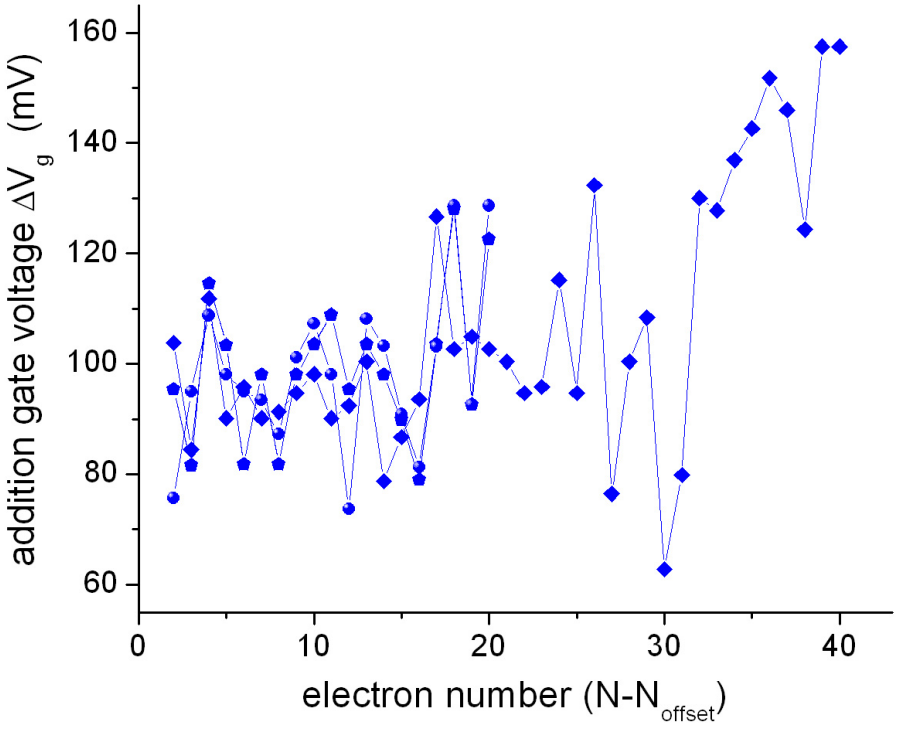

Figure 5.7: Evolution of the addition backgate voltage of a quantum dot in a semiconducting CNT. A charging spectrum of this quantum dot is shown in Fig. 5.6. Multiple overlapping lines are readouts from different images. The electron count N along the x-axis is only accurate up to an offset N_{offset}.

in Sec. 2.1.5. The data in Fig. 5.7 illustrates that the charging process of our quantum dot is a complex many-particle problem, and the assumption of a constant total capacitance is a simplification of the real situation.

It is also worth noting that we don't observe any systematic, repeating pattern in the addition backgate voltage. In particular, we don't find 4-fold shell filling, as has been seen in open CNT quantum dots (Liang et al. 2002, Moriyama et al. 2005, Sapmaz et al. 2005), or an even-odd symmetry, as has been seen in closed CNT quantum dots (Cobden and Nygard 2002, Jarillo-Herrero et al. 2004). This is not too surprising in a long semiconducting CNT. In fact, the absence of a regular charging pattern is more common than not in most experiments. Its presence and absence has even been observed in different sections of the same CNT (Sapmaz et al. 2006).

V_g-V_{tip} frequency shift spectra of quantum dots. In this paragraph we go one step further and replace the one remaining spatial dimension in the 2D scan by a second gate voltage. Figure 5.8 shows the single-electron charging of a quantum dot as a function of the backgate voltage and the tip voltage. In this scan the AFM tip is resonating at a height of $z_0 = 100\,\mathrm{nm}$ above the center of a quantum dot. The single-electron charging events appear as straight dark lines in the image, along which the gate charge (5.2) is constant. The slope of this line determines the ratio of gate capacitances, which is identical to the ratio of their gate efficiencies,

$$-\frac{dV_{\mathrm{tip}}}{dV_{\mathrm{g}}} = \frac{C_{\mathrm{gd}}}{C_{\mathrm{td}}(\vec{r})} = \frac{\alpha_{\mathrm{gd}}}{\alpha_{\mathrm{td}}(\vec{r})}\ . \tag{5.3}$$

The gate efficiency of gate i on dot d is defined as $\alpha_{\mathrm{id}} = C_{\mathrm{id}}/C_{\mathrm{dot}}$. It is important to remember that the tip-dot capacitance (and thereby the tip's gate efficiency) depends on the the tip location $\vec{r}$ (including the tip height), and so does this

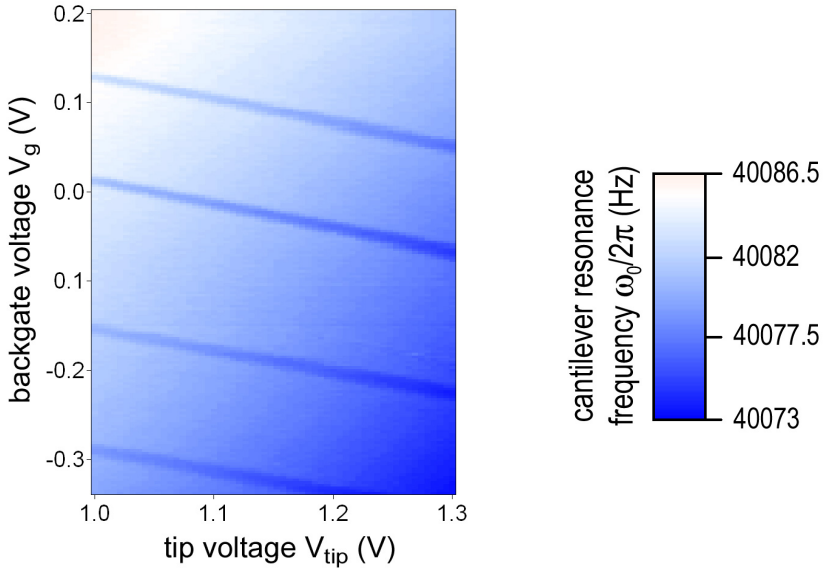

Figure 5.8: Frequency shift charging spectrum of a quantum dot in a semiconducting CNT as a function of the voltages applied to two gates, the extended backgate and the AFM tip. The tip is parked 100 nm above the center of the quantum dot. The cold plate temperature is $T = 1\,\mathrm{K}$ during this scan. Four single-electron charging events are visible as parallel dark lines, whose slope determines the ratio of the gate-dot capacitances of the two gates, Eq. (5.3). At this tip height, the AFM tip is clearly a weaker gate than the extended backgate.

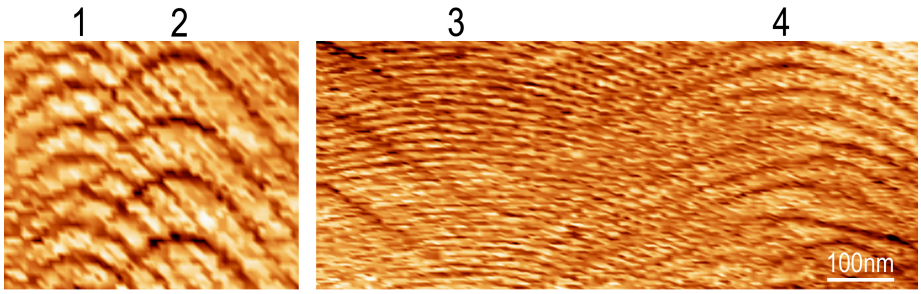

Figure 5.9: Frequency shift spectra of a chain of 4 quantum dots.

ratio. From the slope of the lines in Fig. 5.8 we find a ratio $C_{\rm gd}/C_{\rm td} = 4$ at a tip height $z_0 = 100\,\text{nm}$ above the dot. This measurement confirms the general observation that the extended backgate underneath the thermal oxide is more efficient at inducing charges on the quantum dot than the AFM tip, at least at our typical tip heights.

5.3 Capacitance Scaling

By increasing the spatial scan range of the AFM tip along the CNT, we extend the single-electron charging spectra to multiple quantum dots. In this section we analyze such multi-dot spectra quantitatively and characterize the backgate coupling and size of the quantum dots.

Figure 5.9 shows the spectra of 4 neighboring quantum dots along a section of a semiconducting CNT. Each quantum dot is labeled by a number above the image. From a multi-dot spectrum of quantum dots in a CNT, like Fig. 5.9, we can infer two pieces of information about the quantum dots:

1. The separation of single-electron charging lines for each dot along the gate voltage axis. This is the addition gate voltage $\Delta V_{\rm g}^{\rm (add)}$, which was introduced in Sec. 2.1.5 and 5.2. In the classical limit, the addition backgate voltage is

inversely proportional to the electrostatic capacitance between the backgate and the quantum dot, Eq. (2.8), and $e = C_{\rm gd}\,\Delta V_{\rm g}^{\rm (add)}$. This relation allows us to extract the backgate-dot capacitance $C_{\rm gd}$ for each dot.

2. The center-to-center distance between neighboring dots along the x-axis, which contains information about the size of the quantum dots.

The separation between neighboring dots alone is not enough to extract the size of the quantum dots, for the following reason: If we have a chain of n quantum dots and denote their size by L_i, there are $(n-1)$ center-to-center distances $\frac{1}{2}(L_i + L_{i+1})$ of neighboring dots. These $(n-1)$ quantities are not enough to determine the n quantum dot sizes. We always end up one necessary piece of information short.

More information about the dot size can be obtained in the following way: Modeling the extended backgate and the CNT as a plane and a cylinder (Dresselhaus et al. 1996, Yao et al. 2001), the capacitance $C_{\rm gd}$ between the backgate and a CNT piece of length L is predicted to follow the relation

$$\frac{C_{\rm gd}}{L} = \frac{2\pi\epsilon\epsilon_0}{\ln(4t/d)}\,, \tag{5.4}$$

where d is the diameter of the CNT, t is the distance between the backgate and the CNT, i.e., the thermal oxide thickness, $\epsilon_0 = 8.854 \times 10^{-12}\,\mathrm{F/m}$ is the permittivity of free space, ϵ is the relative dielectric constant of the medium they are placed in.

By assuming capacitance scaling between 2 out of the n dots, we obtain the additional piece of information needed to calculate the size of all quantum dots. Afterwards, we can verify our assumption of capacitance scaling on the remaining $(n-2)$ center-to-center distances.

This procedure is carried out on the 4 quantum dots in Fig. 5.9. The results of the analysis are summarized in Table 5.1. The capacitance of these 4 quantum

Table 5.1: Backgate-dot capacitance scaling from a chain of 4 quantum dots in a semiconducting CNT, as shown in Fig. 5.9.

Quantity	dot 1	dot 2	dot 3	dot 4
addition backgate voltage $\Delta V_{\rm g}^{\rm (add)}$	50 mV	98 mV	14 mV	36 mV
backgate-dot capacitance $C_{\rm gd}$	3.2 aF	1.6 aF	11.4 aF	4.4 aF
dot size L	210 nm	105 nm	750 nm	290 nm

dots indeed scales with the dot size. We find a common scaling law of $C_{\rm gd}/L = 1.5\,{\rm aF}/100{\rm nm}$.

To compare our experimental result with theory, Eq. (5.4), we note that the diameter of our CNT is $d = 1.4\,{\rm nm}$. The thermal SiO_2 is $t = 200\,{\rm nm}$ thick in our device. To account for the thermal oxide ($\epsilon \approx 3.9$) underneath the CNT and vacuum ($\epsilon = 1$) above the CNT, we assume an average dielectric constant of $\epsilon \approx 2$, as used in the literature (Yao et al. 2001). From these parameters we predict a scaling law of $C_{\rm gd}/L = 1.75\,{\rm aF}/100{\rm nm}$, in good agreement with the experimental finding.

From the confirmed scaling law and the agreement between the experiment and the simple model, we are confident that we resolve all the quantum dots along the CNT.

5.4 Large spectra of multiple nanotube quantum dots

In this section we investigate a multi-dot spectrum of a larger section of a semiconducting CNT with a sizeable backgate voltage range and analyze common features of the single-electron charging events. Figure 5.10 shows the frequency shift spec-

trum of a $3\,\mu$m section of a semiconducting CNT at $T = 4.2\,\mathrm{K}$. The entire CNT device is $8\,\mu$m long. The end of the right metal contact to the CNT is located at $x \approx 0\,\mu$m, near the right edge of the plot.

Several features are prominently visible in this CNT spectrum: Many single-electron charging humps appear in the top half of the image, at backgate voltages $V_\mathrm{g} \geq 2\,\mathrm{V}$. In the bottom half, certainly below $V_\mathrm{g} = 1\,\mathrm{V}$, no charging events are visible in the spectrum, except at the far right of the scan, near the contact. This arrangement of charging events mirrors the band structure of our semiconducting CNT: At the bottom of the image, the electrochemical potential of the CNT is in the band gap of the tube. Since our Palladium metal contacts have a larger work function than the CNT, a p-type quantum dot forms near the contact (Park and McEuen 2001). The last few holes on this p-dot are visible at the bottom right of the spectrum. This work function difference is also responsible for the formation of a Schottky-barrier at the contact on the n-side of the band gap (Martel et al. 2001, Heinze et al. 2002). The Schottky-barrier can limit the charge injection into the conduction band. This is thought to be the major reason for the often poor conduction of semiconducting CNTs in the n-regime. A transport plot of the CNT device conductance vs. the backgate voltage at $T = 4.2\,\mathrm{K}$, Fig. 5.11, indeed shows no n-type conduction on this semiconducting CNT. Up to the maximum backgate voltage of $V_\mathrm{g} = 6.5\,\mathrm{V}$ that we have applied, we don't measure an electron current between the source and drain contact of the tube, certainly not within the gate range of our n-type spectrum, Fig. 5.10. Observing single-electron charging along the CNT nonetheless underlines one benefit of our local force detection scheme: It enables us to measure electron transport phenomena even in the absence of long-range device conductance. We will expand on this point in Sec. 5.9.

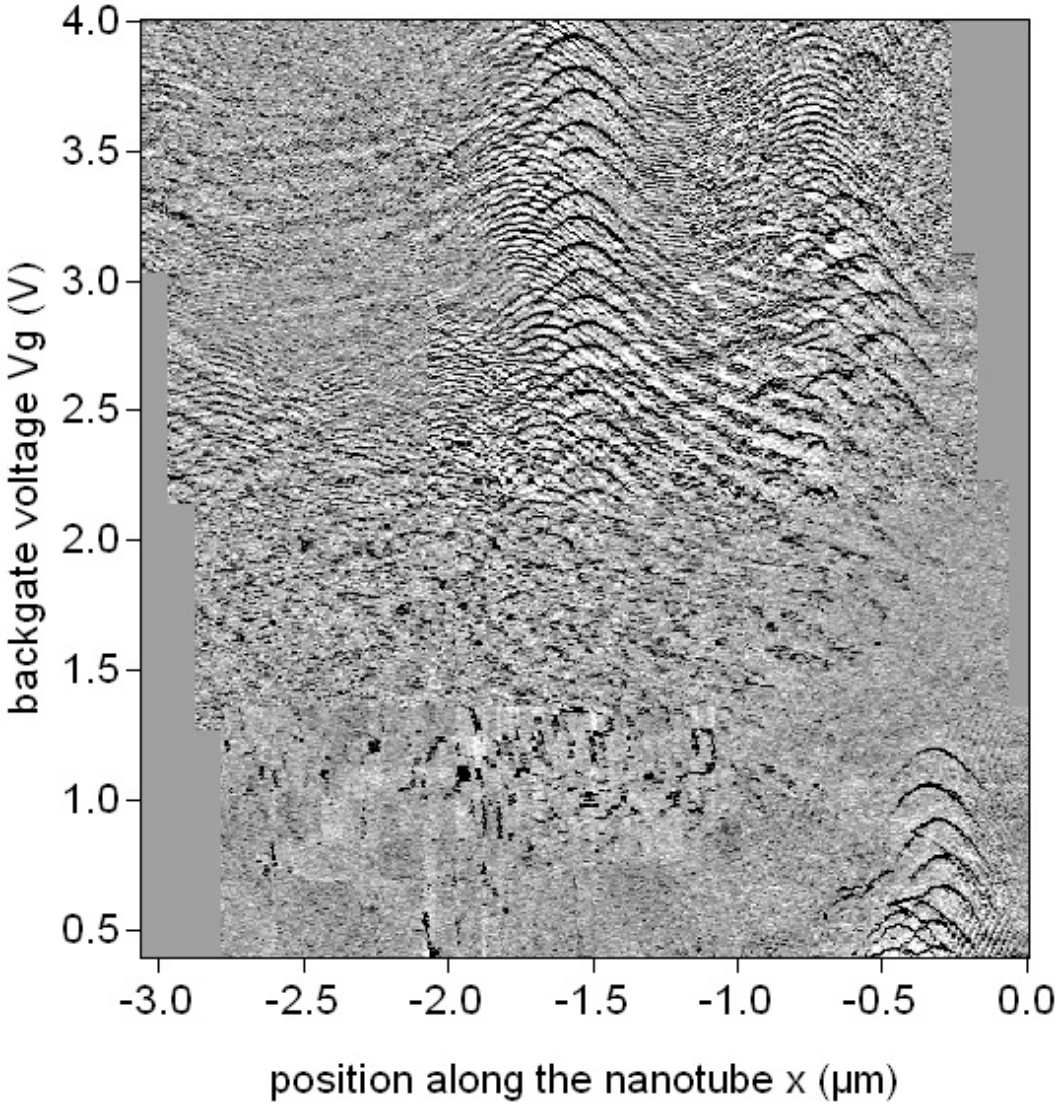

Figure 5.10: Charge addition spectrum of a $3\,\mu$m section of a semiconducting CNT. One metal contact starts at the right edge of the image, at about $x=0$. The left contact to the CNT is several microns away.

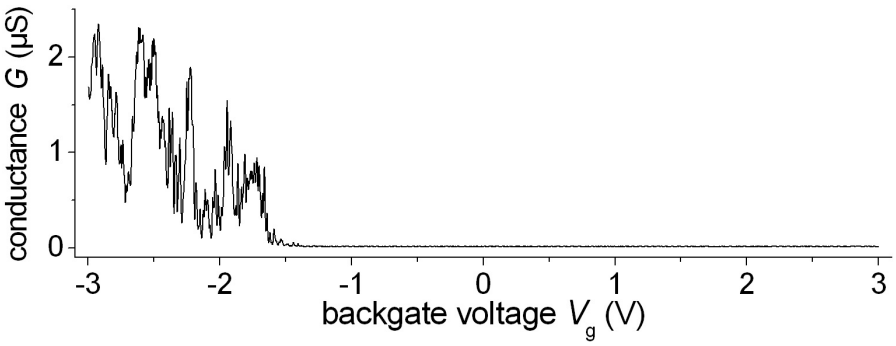

Figure 5.11: Electronic transport trace of the CNT in Fig. 5.10 at $T = 4.2\,\mathrm{K}$.

5.5 Disorder potential

As we have just discussed, the spectrum of the semiconducting CNT maps out the tube's band structure. Naturally, the question arises why we observe quantum dots, as opposed to electrons delocalized in the conduction band.

To offer an answer to this question, we need to consider the entire sample, which includes the CNT and its vicinity. The substrate and other surroundings can have a visible influence on the carrier distribution on the CNT near the band gap: As the electrochemical potential of the CNT enters the conduction band, the first few conduction electrons are induced on the tube. In this regime of low carrier density, the electron distribution on the CNT is very sensitive to the electrostatic environment of the tube. Spatial variations of the external potential superimpose themselves on the CNT's band structure and modify the flat bottom of the conduction band non-uniformly. Effectively, they may create a rough potential energy landscape for the electrons on the CNT. As a result, the tube electronically breaks up into segments, which act as a chain of quantum dots. This situation is illustrated in Fig. 5.3. To move across the CNT device, a conduction electrons has to overcome the barriers in the potential energy landscape.

Local variations in the potential energy landscape can arise from many sources: Imperfections of the substrate are an obvious candidate. It is well known that there are many charge traps in SiO_2, particularly near the SiO_2/Si interface (Kooi 1967, Nishi 1971). Depending on whether these traps are occupied or not, they can create local variations of the electrostatic potential. Another source can be charged residues on the surface that are left behind from the device fabrication. They modify the electrostatic environment of the CNT similarly to the charge traps in the oxide. If the biased AFM tip comes into contact with the surface, charges may be left behind that don't diffuse away at cryogenic temperatures. To make a long story short, there are numerous sources in the environment of our CNT devices that can create a non-uniform electrostatic potential landscape in unpredictable ways. All possible such contributions are commonly summarized in the term *disorder potential*.

At every backgate voltage, the distribution of quantum dots in our CNT charging spectrum shows a snapshot of the disorder potential at the given electrochemical potential of the CNT. Looking at the evolution of single-electron charging events with backgate voltage can give us clues about the underlying potential energy landscape, i.e., how the disorder potential develops in energy. We can indeed extract such information from our CNT spectrum, Fig. 5.10. First we examine the evolution of single-electron charging events qualitatively, before we comment on a quantitative analysis.

Qualitative evolution of the disorder potential. Starting from the right in Fig. 5.10 (nearest the contact), we see many charging humps near the band gap. A high-resolution image of this region is shown in Fig. 5.12. The apexes of

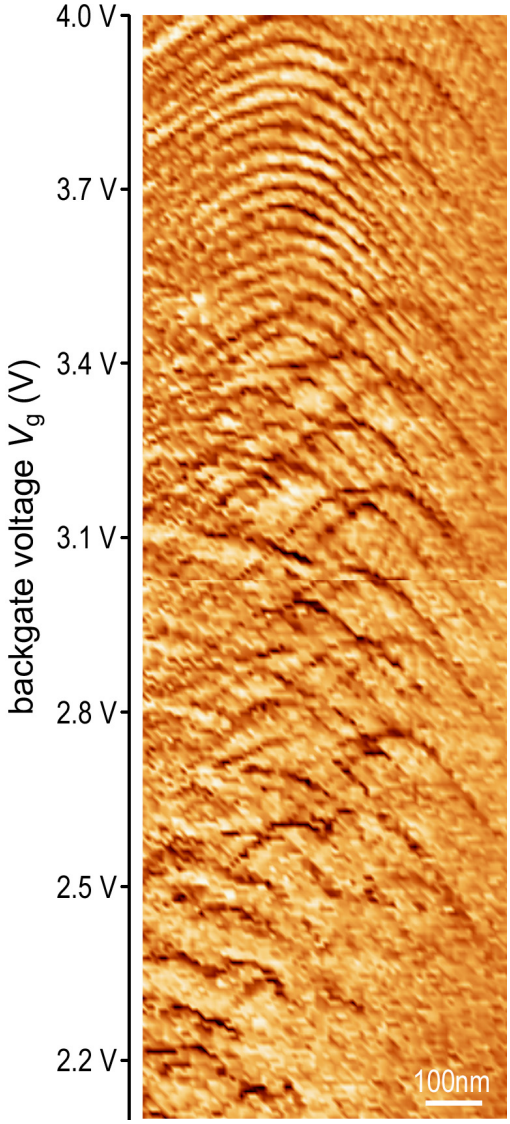

Figure 5.12: Spectrum of quantum dots near the lead in n-regime.

these charging events near the conduction band bottom don't align exactly, which indicates that there are multiple very small quantum dots present in this area, with correspondingly large addition backgate voltages. At $V_g \approx 3.3\,\mathrm{V}$ a regular set of single-electron charging humps emerges. Apparently, at this backgate voltage several tiny dots join into one larger dot. The apexes of its charging humps align and their spacing is quite constant.

The conspicuous quantum dot at $x \approx -1.5\,\mu\mathrm{m}$ with a large addition backgate voltage is quite stable. Its tunnel barriers on both sides appear to be fairly tall, as the extended spectrum of this dot over a larger backgate voltage range in Fig. 5.6 proves.

In between these two dots, nothing particular seems discernible in our CNT spectrum, Fig. 5.10. A careful scan, as seen in Fig. 5.13(a), however, reveals a large quantum dot with very fine addition backgate voltage[4]. Figure 5.13(b) explicitly overlays the single-electron addition spectra of the 3 quantum dots visible in Fig. 5.13(a). This dot is so large that we count ~ 8 electrons tunneling onto the dot for every electron tunneling onto the small dot on its left, in total at least 134 electrons on the dot by the time the backgate voltage reaches $V_g = 4\,\mathrm{V}$.

Neighboring on the left of the small dot is a medium-sized quantum dot with an interesting evolution of its single-electron charging humps. As seen in the big CNT spectrum, Fig. 5.10, and more clearly in Fig. 5.14, the charging events of this quantum dot are regularly spaced and their apexes line up well, until the backgate voltage reaches $V_g = 3\,\mathrm{V}$. At this point, the apex of the charging events moves about 65 nm to the left and the spacing between the charging events decreases by approximately 18 mV. Apparently, this quantum dot increases in size by expanding

[4]Note that a careful scan at lower backgate voltages, where we indicated the band gap of the CNT, does not reveal single-electron charging events.

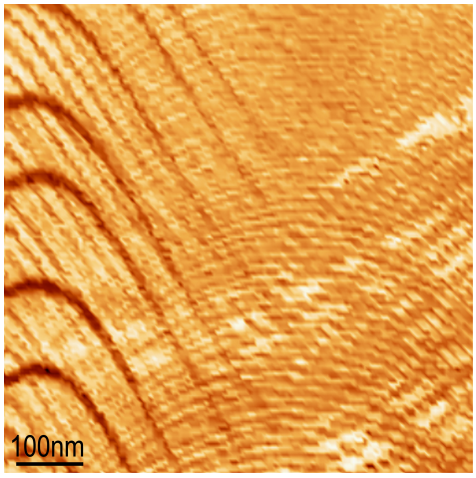

(a) High-resolution spectrum of quantum dots in a semiconducting CNT. V_g ranges from 3.5 V to 4 V.

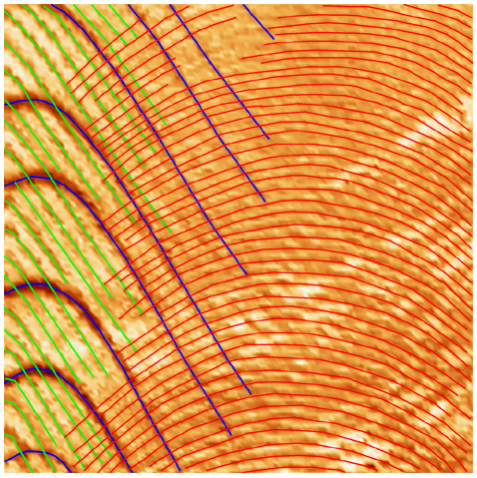

(b) Spectrum of Fig. 5.13(a) with single-electron charging lines from 3 dots overlayed (green, blue, red).

Figure 5.13: High-resolution spectrum of large CNT quantum dot.

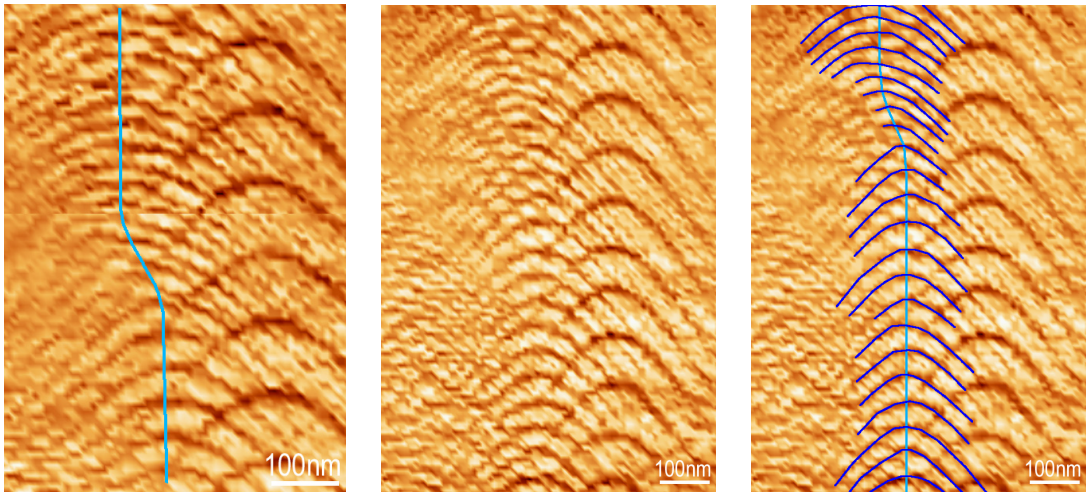

Figure 5.14: Spectrum of a CNT quantum dot expanding in size. The left and the middle image are 2 different scans that capture this growth in size. The right image overlays the interesting charging spectrum on the middle image. A center line of the dot is shown in the left and the right image. See also Fig. 5.15(a).

to the left at $V_g = 3\,\mathrm{V}$. The high-resolution spectrum below, Fig. 5.15(a), also shows this change very clearly.

Further left in the spectrum we find a number of similarly sized quantum dots near the conduction band bottom, which unify into a very large joint dot quite quickly. Figure 5.15 shows two high-resolution spectra of this area.

A plot of the single-electron addition backgate voltages from the 4 quantum dots discussed above is shown in Fig. 5.16. The colors are consistent with with the overlayed spectra in Fig. 5.13(b). The right-most quantum dot, which was discussed first above, is not visible in Fig. 5.13(a). We only plot its addition backgate voltage once the many small dots have unified into a larger quantum dot with aligned apexes of charging humps. None of the 4 quantum dots exhibits a repeating pattern in its addition backgate voltage, in particular no 4-fold or alternating pattern. The increase in size of the left-most quantum dot of these 4 is visible in Fig. 5.16 as a jump of its addition backgate voltage to a lower value at $V_g = 3\,\mathrm{V}$.

Quantitative bounds on the disorder potential. The qualitative analysis of the evolution of the single-electron charging events with backgate voltage above gave considerable information about the potential energy landscape, as it is experienced by the first few electrons in the conduction band of the CNT. There is also a quantitative relationship, which we explore in the following. An alternative derivation of the relevant relation, Eq. (5.7), and some additional details are given in Appendix A.2.

Reading out the single-electron addition backgate voltages of quantum dots continuously, as shown for 4 dots in Fig. 5.16, is essentially an electron counting

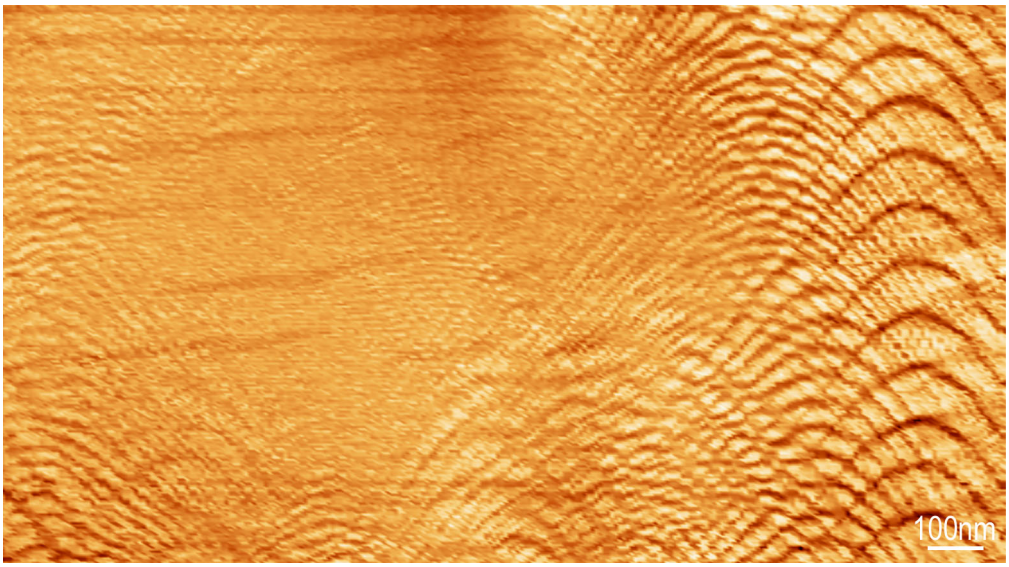

(a) 1.8 μm, 2.5 V $\leq V_g \leq$ 3.5 V.

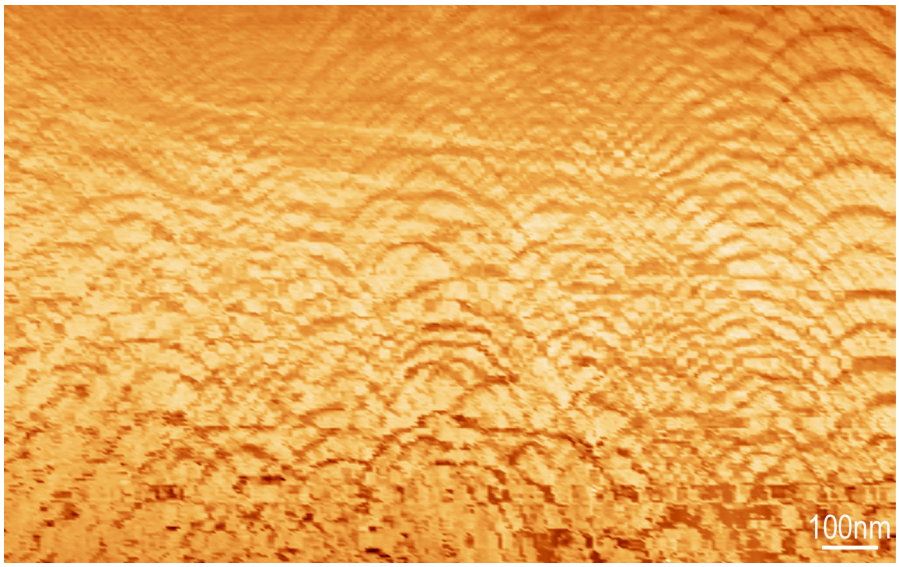

(b) 1.6 μm, 1.7 V $\leq V_g \leq$ 2.7 V.

Figure 5.15: High-resolution CNT spectra in the n-regime. The spectra cover part of the top of Fig. 5.10. The conspicuous charging spectrum on the right of the images can serve as a feature to align the spectra along the x-axis. In the lower image, Fig. 5.15(b), instrument drift (piezo creep) caused the charging spectra to slowly bend to the left with increasing backgate voltage. A more patient operator than myself could have easily avoided this artifact.

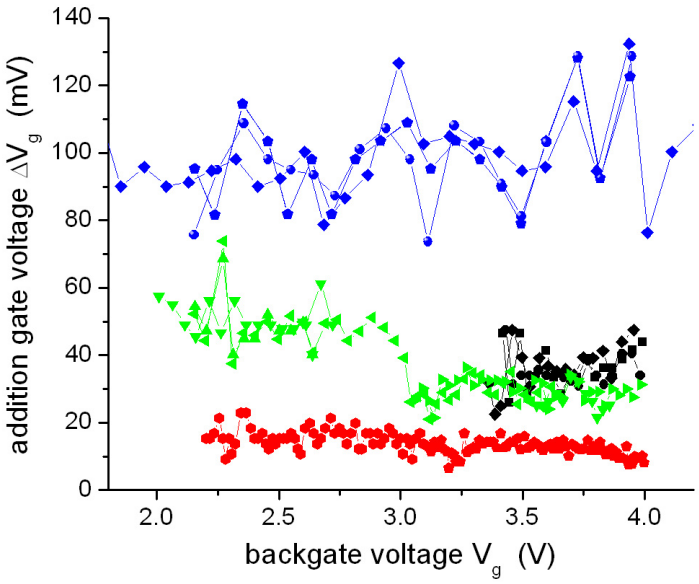

Figure 5.16: Evolution of the addition backgate voltage of 4 neighboring quantum dots in a semiconducting CNT. The data originates from the same dots as in Fig. 5.9 and Table 5.1. Multiple lines of the same color indicate readouts from different images on the same dot.

experiment on each dot. Figure 5.17 replots the data in Fig. 5.16 as the number of single-electron charging events that was counted at or below a given backgate voltage. Due to the Pauli exclusion principle, the number of electrons is intimately related to the energy of the highest occupied single-particle state. In other words, the electron density can tell us what range of single-particle levels is occupied above the conduction band bottom. Fixing the electrochemical potential, which is constant along the CNT, we can resolve the bottom of the conduction band and its spatial variations, as depicted in the above cartoon, Fig. 5.3. The bottom of the conduction band gives a direct image of the underlying disorder potential. In the following, we first outline the relationship between the electron density and the electrochemical potential for CNTs in the classical limit. This relationship is then applied to the data from the 4 quantum dots shown in Fig. 5.17.

The low-energy electronic dispersion relation of a CNT (Ajiki and Ando 1993) is given by[5]

$$\begin{aligned} E_{\mathrm{CNT}}(k) &= \pm\sqrt{\left(\frac{E_{\mathrm{gap}}}{2}\right)^2 + (\hbar k\, v_F)^2} \\ &\approx \pm\left(\frac{E_{\mathrm{gap}}}{2} + \frac{(\hbar k\, v_F)^2}{E_{\mathrm{gap}}} + o(k^4)\right) . \end{aligned} \tag{5.5}$$

E_{gap} is the band gap of the semiconducting CNT[6], as calculated in Eq. (A.15), v_F is the Fermi velocity of the charge carriers, Eq. (A.16), and $2\pi\hbar$ is Planck's constant. $E_{\mathrm{CNT}} = 0$ is fixed in the middle of the band gap; the conduction band of the CNT is located at single-particle energies $E_{\mathrm{CNT}} \geq \frac{1}{2}E_{\mathrm{gap}}$, the valence band at $E_{\mathrm{CNT}} \leq -\frac{1}{2}E_{\mathrm{gap}}$. The carrier momentum k is offset such that $k = 0$ gives the minimum of the conduction band and the maximum of the valence band. The

[5]Notice that the functional form of this dispersion relation is the same as the dispersion of a relativistic particle, $E(p) = \sqrt{(m_0c^2)^2 + (pc)^2}$. This is the origin of the analogy between Dirac-Fermions and electrons in CNTs.

[6]$E_{\mathrm{gap}} = 0$ gives the dispersion relation of the lowest subband of a metallic CNT. Its electrons are equivalent to massless Dirac-Fermions.

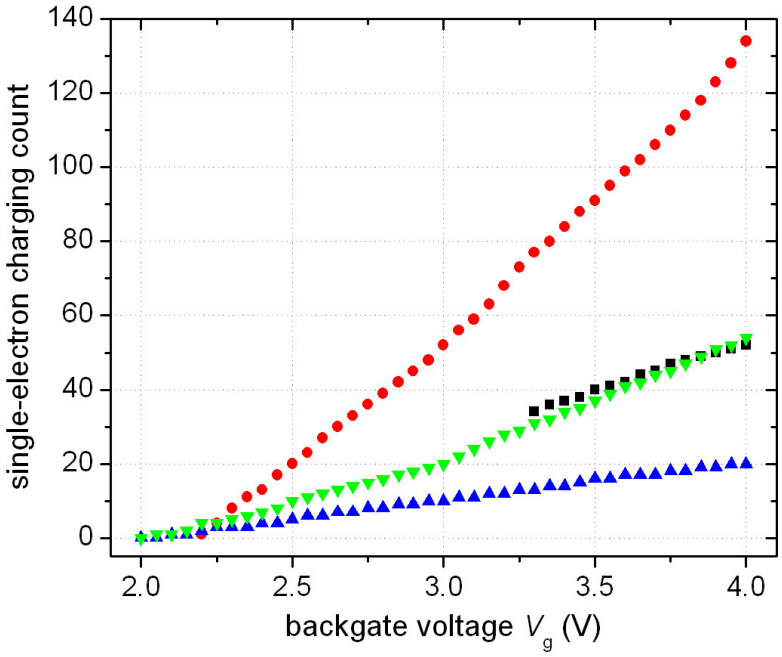

Figure 5.17: Single-electron counting experiment. The y-axis plots the number of single-electron charging events below the backgate voltage on the x-axis. The data was obtained from the n-type spectrum, Fig. 5.10, but it really is a different representation of the data in Fig. 5.16. The color of data points in this plot and Fig. 5.16 corresponds to the same quantum dot. Notice the change of slope in the green trace at $V_g = 3\,\mathrm{V}$, where the single-electron addition backgate voltage of this dot jumps to a lower value.

expansion makes is clear that the dispersion relation is quadratic near the bottom of the conduction band and the top of the valence band (Saito et al. 1998), just like for free particles. This permits us to use the free electron approximation at low carrier density, where the carriers in the CNT have an effective mass

$$m^* = \hbar^2 \left| \frac{\partial^2 E}{\partial k^2} \right|^{-1}_{k=0} = \frac{E_{\mathrm{gap}}}{2 v_F^2} \; . \tag{5.6}$$

We only need to account for the 4-fold shell structure in CNTs (Liang et al. 2002, Moriyama et al. 2005, Sapmaz et al. 2005), which arises from the spin degeneracy and the 2-fold orbital degeneracy of electronic states in CNTs.

Spin-degenerate particles that can move freely in one direction but are tightly confined in the other two spatial dimensions (1D conductor) obey the relation $n_{\mathrm{1D}} = 2k_F/\pi$ (Kittel 2005) between the particle density n_{1D} and the Fermi momentum k_F at $T = 0$. Including the additional 2-fold orbital degeneracy, we find for semiconducting CNTs at low carrier density n_{scCNT}

$$n_{\mathrm{scCNT}} = \frac{4k_F}{\pi} = \frac{4}{\pi\hbar} \sqrt{2m^*(E_F - E_0)} \qquad \text{for} \quad E_F \geq E_0 \; , \tag{5.7}$$

where the right-hand side results from the quadratic dispersion relation. E_F is the electrochemical potential of the CNT, E_0 is the energy of the conduction band bottom. An alternative derivation of this formula is given in Appendix A.2. The only free parameter in this equation is the effective electron mass m^*. For our semiconducting CNT of diameter $d_{\mathrm{CNT}} = 1.4\,\mathrm{nm}$, we predict $m^* = 0.067\,m_e$ from theory, Eq. (A.17).

To make Eq. (5.7) useful for our analysis of quantum dots in semiconducting CNTs, we assume that the electrons on a quantum dot are delocalized over the size of the dot. Then the carrier density is uniform along each dot and given by the number of conduction electrons on the quantum dot divided by the length of

the CNT section where the quantum dot forms, $n_{\mathrm{scCNT}}^{(\mathrm{dot})} = N_{\mathrm{dot}}/L_{\mathrm{dot}}$. The size L_{dot} of each dot is calculated in Sec. 5.3 below for our 4 quantum dots, see Table 5.1. The number of electrons on each dot N_{dot} is taken as the number of single electron charging humps in the spectrum below the given gate voltage. With this information, Eq. (5.7) allows us to calculate the energy range of occupied single-particle levels, $E_F - E_0$.

An example readout from our 4 dots at $V_{\mathrm{g}} = 3.95\,\mathrm{V}$ is shown in Fig. 5.18. This plot puts our experimental observations well into context: Despite the reasonably high backgate voltage, the single-particle energy is only little above the conduction band bottom of the CNT. Clearly, we are still very near the conduction band bottom, which explains the sensitivity to the electrostatic environment and the persistence of the quantum dots at the applied backgate voltages. The variations of the conduction band bottom are also not huge, but all within a few meV.

Unfortunately, our data that provides Fig. 5.18 can only give lower bounds on $E_F - E_0$ for the following reason: While we are confident that we count electrons without missing any charging events on the way, we cannot guarantee that we resolve the very first electron or even the first few electrons on each dot. In fact, as the electrochemical potential of the CNT gets close to the band gap, the frequency shift signal loses contrast[7]. Consequently, our count of single-electron charging events is only a lower bound to the actual number of electrons on each dot. This lower bound propagates to a lower bound on the electron density $n_{\mathrm{scCNT}}^{(\mathrm{dot})}$ and a lower bound on the energy range $E_F - E_0$ of occupied single-particle states.

[7]We attribute this loss of contrast to a lack of charge injection from the leads due to the Schottky barriers at the CNT contacts, whose size increases near the band gap. As illustrated in Fig. 2.9, the frequency shift signal due to single-electron tunneling is greatly reduced as the quantum dot turns opaque and gets isolated from its charge reservoir.

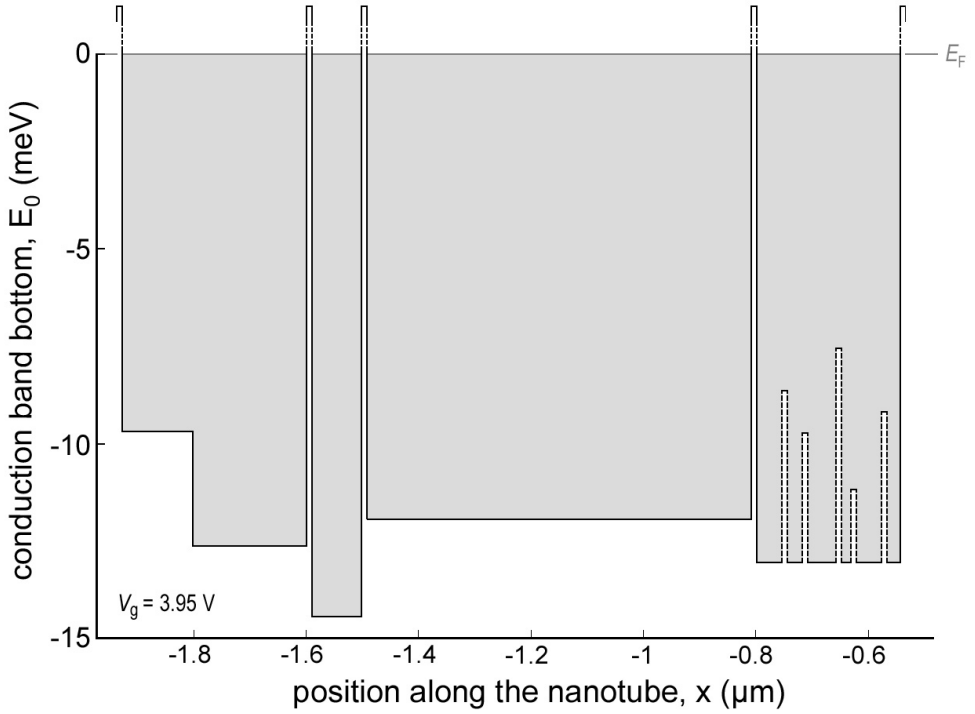

Figure 5.18: Lower bound on the range $E_F - E_0$ of occupied single-particle states in the conduction band, calculated classically from the counted number of single-electron charging events on the quantum dots. The energy of the highest occupied single-particle state is set to 0. The shaded area shows the filled conduction electron states at $V_\mathrm{g} = 3.95\,\mathrm{V}$. The bottom of the conduction band may actually be lower than shown, as the number of electrons can exceed the count of single-electron charging events if we didn't resolve the first electron tunneling onto each quantum dot. The width of the tunnel barriers is unknown from our measurement and depicted as 10 nm wide. The dashed tunnel barriers inside the right-most quantum dot, centered at $x \approx -0.67\,\mu\mathrm{m}$, illustrate symbolically that there appear to be several not-too-high barriers near the band bottom, as seen in the spectrum, Fig. 5.10. The location and number of these (dashed) barriers is arbitrary and not a result of the calculation. The height of the tallest barrier among them reaches the energy where we see a single dot emerge in the data.

Consequently, the bottom of the CNT's conduction band may be further below the Fermi energy than depicted in Fig. 5.18.

With a more complete quantum dot spectrum that includes the entire band gap and parts of the conduction and valence band of the CNT, as shown in Fig. 5.20 below, we can also establish an upper bound on $E_F - E_0$, in the following way: Since the addition backgate voltage is quite constant (at $V_g < 3\,\mathrm{V}$) for all 4 dots, we can project the number of electrons on the dot, assuming that the electrochemical potential emerges from the band gap into the conduction band at lower backgate voltages than where we resolve the first charging events. Once this projection of the conduction band bottom reaches backgate voltages where we resolve hole charging on the quantum dots (in the valence band), we certainly project an upper bound to the number of electrons on the quantum dots in the conduction band. Since Eq. (5.7) is monotonic, this upper bound on the electron carrier density gives an upper bound to $E_F - E_0$ for filled electron states in the conduction band.

5.6 Combined n- and p-type spectrum

Similarly to the n-type spectrum of single-electron charging when the electrochemical potential of the CNT moves into the tube's conduction band, we can also pull the CNT's electrochemical potential to the p-side of the band gap by means of negative backgate voltages and take a spectrum of single-hole charging in the CNT valence band, Fig. 5.19.

When comparing the n- and p-type spectra, a slight subtlety arises, though, that needs to be addressed: To maintain good signal contrast, we have to avoid the region of similar backgate and tip voltage. In other words, we need to use a

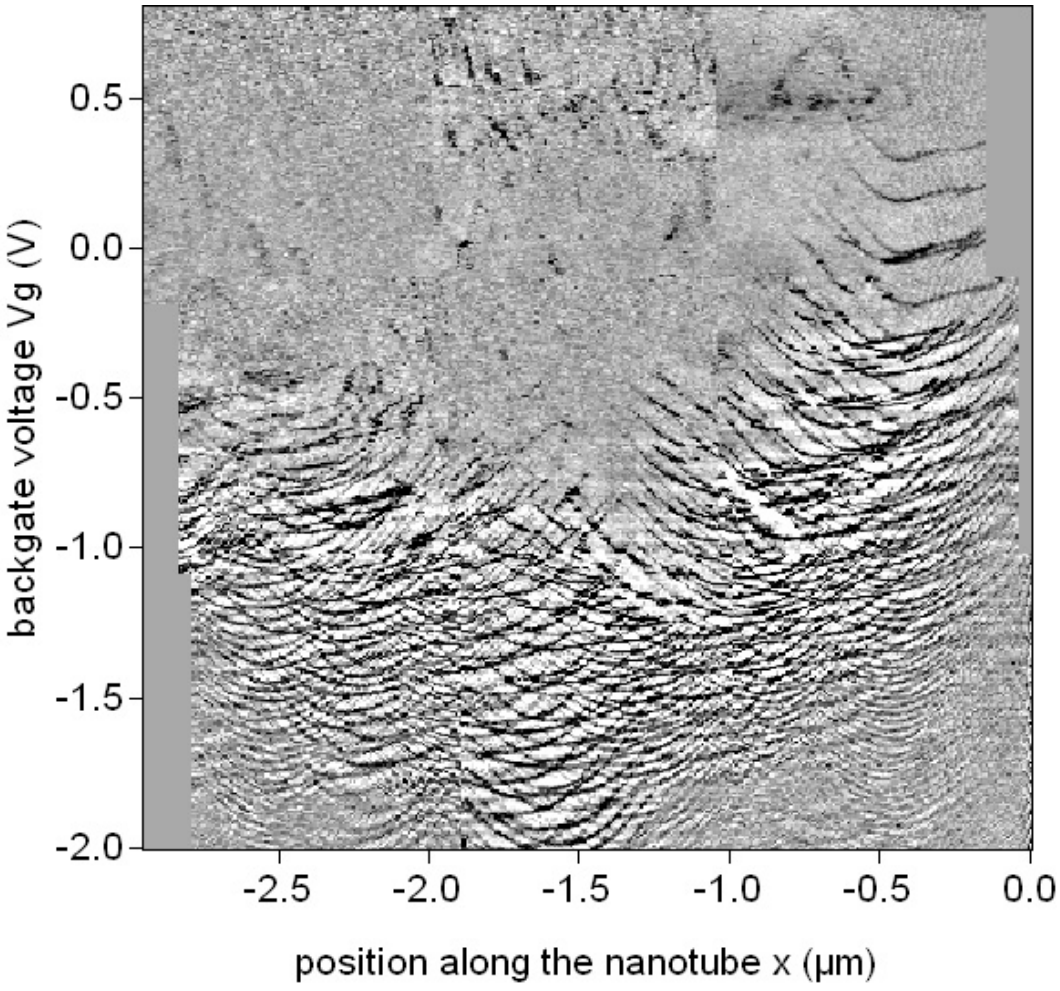

Figure 5.19: *p*-type charge addition spectrum of CNT quantum dots.

different tip voltage on either side of the band gap[8]. The tip, however, gates the CNT, too, and the same backgate voltage doesn't reproduce the same dot state as before if the tip voltage has changed. A suitable quantity to describe the effective gating, particularly when both tip and backgate voltage are changed, is the gate charge (5.2). To stay with gate voltage units, we define an effective gate voltage by dividing the gate charge by the backgate-dot capacitance,

$$V_{\mathrm{g}}^{(\mathrm{eff})} = -\frac{q_c}{C_{\mathrm{gd}}} = V_{\mathrm{g}} + \frac{C_{\mathrm{td}}}{C_{\mathrm{gd}}} V_{\mathrm{tip}} \,. \tag{5.8}$$

Practically, this means that the backgate voltage is offset by some amount to account for a change in tip voltage. The exact amount, however, scales with the tip-dot capacitance and depends on the tip position and the dot. As we are most interested in the charge addition spectra, i.e., comparison between the apex of the charging humps or dips, we really care mostly about the tip-dot capacitances when the tip is nearest each dot, i.e., right above its center. For a rough estimate and comparison between the two spectra or with the transport plot, the capacitance ratio can be approximated by a constant, $C_{\mathrm{td}}/C_{\mathrm{gd}} \approx 0.25$ for our tip height of $z_0 = 100\,\mathrm{nm}$, as obtained from Fig. 5.8. Since both the tip-dot capacitance and backgate-dot capacitance scale roughly linearly with the size of the dot (see Sec. 5.3), their ratio is expected to be constant. For the two large spectra shown above, the n-type spectrum, Fig. 5.10, was taken at $V_{\mathrm{tip}} = -1.5\,\mathrm{V}$, so we need to subtract $0.375\,\mathrm{V}$ from its back gate voltage scale. The p-type spectrum, Fig. 5.19, was recorded at $V_{\mathrm{tip}} = +1.5\,\mathrm{V}$, and adding $0.375\,\mathrm{V}$ to the back gate voltage scale makes it comparable to similarly treated spectra and transport traces (in the

[8]The fact that our tip voltage changes sign is also visible in the spectra. In our n-type spectra, recorded at a negative tip voltage, the single-electron charging lines appear as humps. The positive tip voltage in the p-type spectra turns the charging lines into slumps instead.

absence of the tip). At the end of this procedure, the single-electron charging lines of the p-dot near the contact, which are visible in both images, fall almost on top of each other. Figure 5.20 shows the combined spectrum of Figs. 5.10 and 5.19.

Now we can accurately compare the spectra of different regions with each other and with electronic transport data, Fig. 5.11. The CNT device conducts only at the very bottom of the spectrum, at backgate voltages of $V_{\mathrm{g}}^{(\mathrm{eff})} < -1.3\,\mathrm{V}$ in Fig. 5.20. At this voltage, the quantum dots on the CNT have already acquired quite a few charges. There are also signs of quantum dots merging into larger ones, even though some dots appear still quite distinctly. Most of the spectrum, though, is taken under conditions where the tube does not conduct. This is a great benefit of our local force probe technique, which is further explored in Sec. 5.9.

Tracking the charging lines in this combined spectrum carefully, the size of the bandgap appears to be $\Delta V_{\mathrm{g}}^{(\mathrm{gap})} \approx 1\,\mathrm{V}$ in backgate voltage. In the simplest version, this gate voltage difference should reproduce the bandgap of the semiconducting CNT[9]. There are a number of effects that can make the bandgap appear larger in backgate voltage, though. Even away from the metal leads, the backgate efficiency is still smaller than 1. We may also not resolve all single-electron charging events close to the band edge. The loss of contrast in the single-electron frequency shift signal near the bandgap on the n-side was already addressed in Sec. 5.5 on the disorder potential. A potential cause might be the increasing size of the Schottky barriers and correspondingly insufficient charge injection from the leads as the CNT's electrochemical potential approaches the conduction band edge. From theory we predict $E_{\mathrm{gap}} = 0.51\,\mathrm{eV}$ for this $d_{\mathrm{CNT}} = 1.4\,\mathrm{nm}$ nanotube by Eq. (A.15).

[9]Away from the contacts, the backgate is the most efficient gate, $C_{\mathrm{gd}}/C_{\mathrm{dot}} \lessapprox 1$. Furthermore, only the chemical potential of the CNT is relevant as the electron gas is incompressible while the CNT's electrochemical potential μ is in the bandgap, $dn/d\mu = 0$. This justifies the relation $E_{\mathrm{gap}} = eC_{\mathrm{gd}}\Delta V_{\mathrm{g}}^{(\mathrm{gap})}/C_{\mathrm{dot}} \lessapprox e\Delta V_{\mathrm{g}}^{(\mathrm{gap})}$.

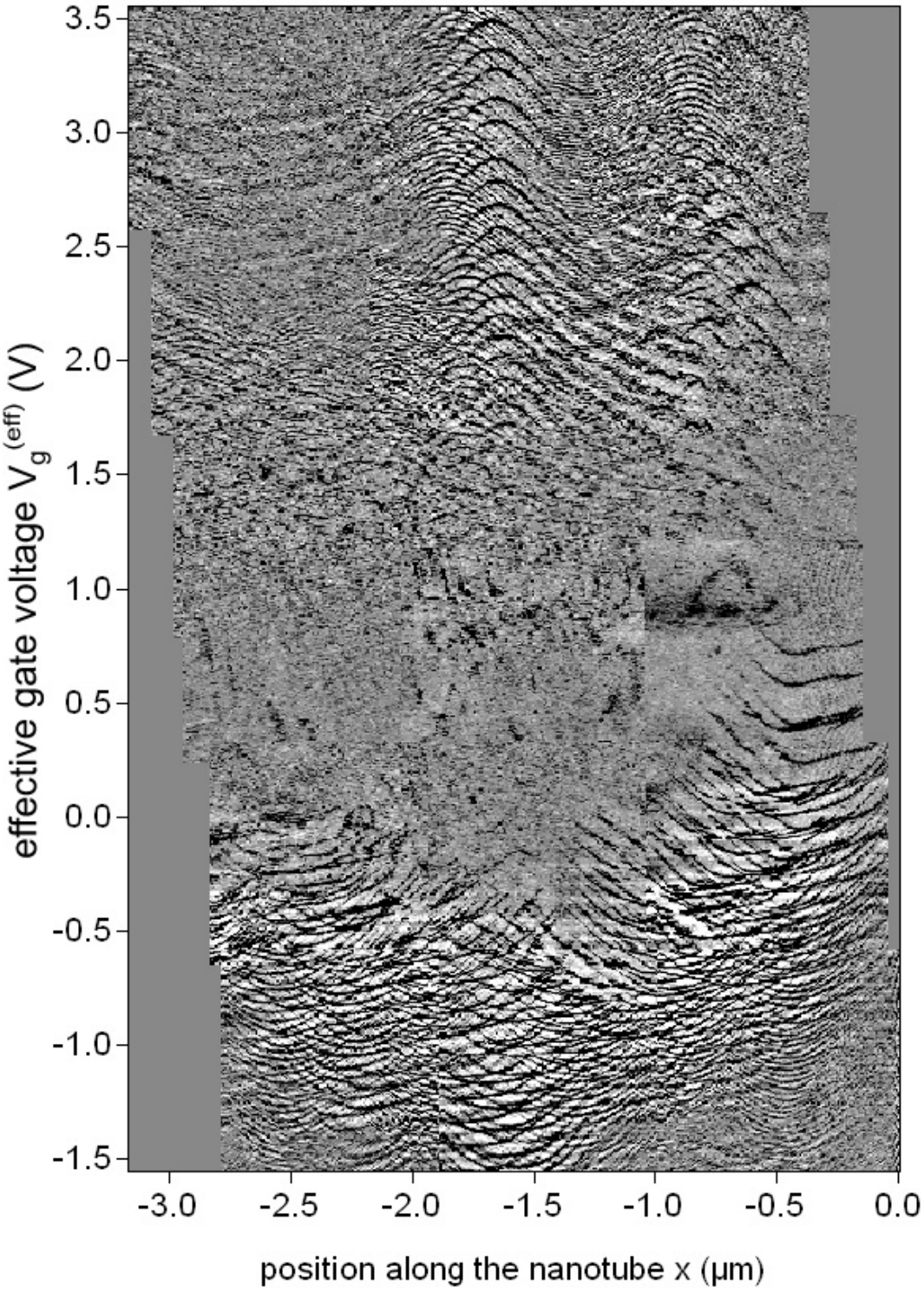

Figure 5.20: Combined n-type & p-type spectrum of a long semiconducting CNT.

5.7 Interdot Coupling

In this section we zoom into the frequency shift images of quantum dots in semiconducting CNTs and examine the degeneracy points, where the charging lines from two quantum dots intersect.

In natural systems, ground state degeneracies (other than spin degeneracy) are a rare occurrence. Nature finds many ways to break such degeneracies[10]. Often only small perturbations are needed to lift the degeneracy and create an avoided crossing at the degeneracy point. These small perturbations typically arise from interactions between the many-body constituents of the system. In the spirit of this general trend, we will look for avoided crossings at the intersection of single-electron charging lines from different quantum dots and attribute the splitting to interactions between the two dots.

5.7.1 Avoided crossings in multi-dot spectra

Figure 5.21 shows a spatial frequency shift image of a part of a semiconducting CNT and two careful scans of smaller areas within this image. In these smaller images, many avoided crossings are clearly visible at the intersection of single-electron charging rings of neighboring quantum dots. Instead of following their usual round or elliptical shape, the charging lines pick up another line at an intersection and divert from their contour. While we frequently observe avoided crossings in fine

[10]The Jahn-Teller theorem (Jahn and Teller 1937) is a prominent formulation of this observation in the context of (natural) atoms forming molecules. It proves group-theoretically that *all molecular configurations are unstable to an orbitally degenerate electronic ground state, except for the linear chain of atoms.* In other words, any molecule with a degenerate electronic ground state (except the linear chain of atoms) will undergo conformational changes (for example, distortions) to form a configuration of lower symmetry. Thereby, it will break the degeneracy and lower its ground state energy.

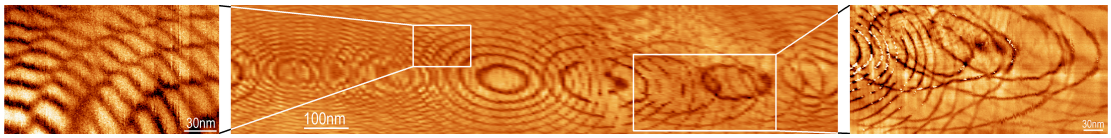

Figure 5.21: Spatial frequency shift images with avoided crossings.

scans over small areas, the ones shown are on the extreme side. The same avoided crossings are also visible in the charge addition spectra of these dots, as shown in Fig. 5.22. In the two zoomed-in charging spectra shown, the usually smooth single-electron charging humps conspicuously display a zig-zag pattern.

These avoided crossings are a sign of coupling between the two quantum dots whose single-electron charging lines intersect. In the metaphor of artificial atoms, we could say that the two quantum dots show signs of forming a molecule. As discussed in Sec. 2.1.8, the splitting of the charging lines can be either due to an elevated interdot tunnel coupling Γ_{m} (covalent molecular bond) or a large mutual capacitance C_{m} (ionic molecular bond) between the quantum dots (Waugh et al. 1996, Livermore et al. 1996). Both possibilities are described by a coupling impedance Z_{m} between the two dots, Eq. (2.26). First we discuss a model of two coupled quantum dots in the LT-AFM so as to clarify our measurement. Afterwards we quantitatively extract the coupling from the observed line splitting in the spectra.

5.7.2 Description of the avoided crossings in V_{g}-x spectra

From the splitting of the charging lines we can extract quantitative information about the interdot coupling strength. Our spectral images, Fig. 5.22, are essentially an unusual representation of the stability diagram (Pothier et al. 1992) of a coupled double dot system. The double dot stability diagram was introduced and discussed

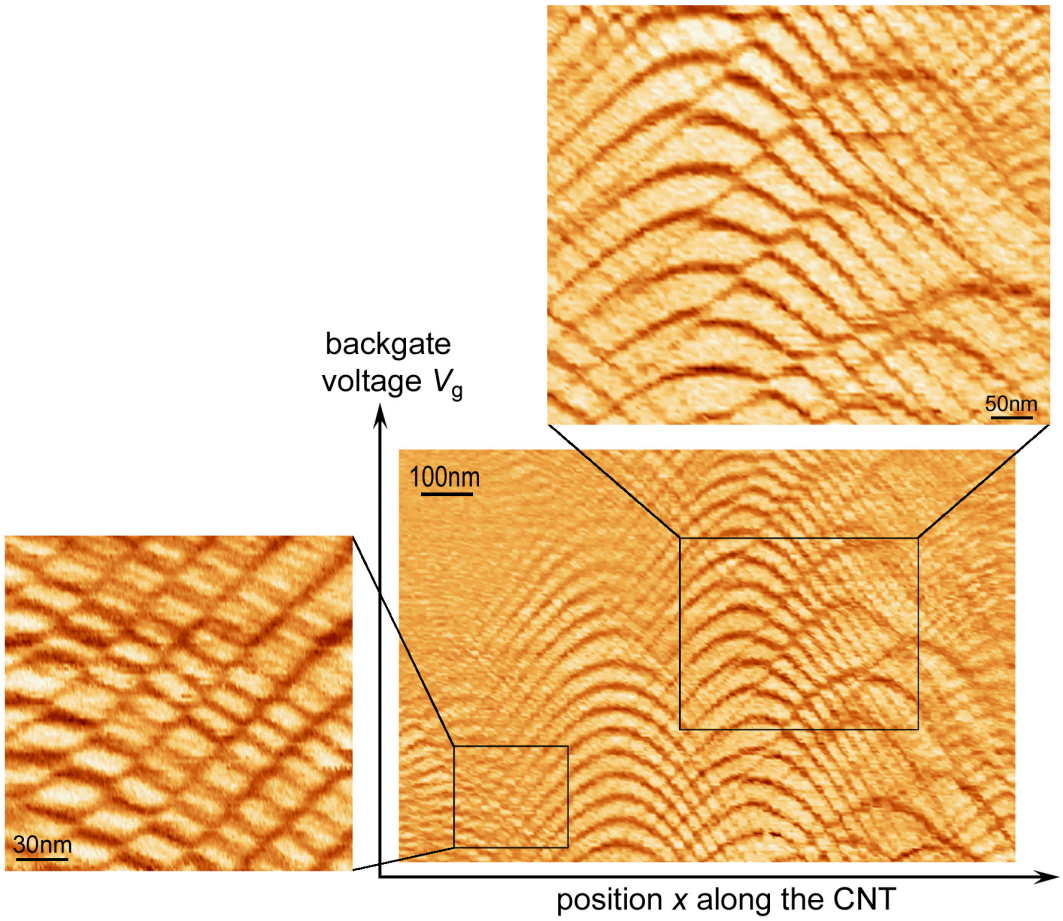

Figure 5.22: Frequency shift spectra with avoided crossings.

in Sec. 2.1.8. An example is shown in Fig. 2.6(a), where the charge state of the double dot is displayed as a function of two gate voltages, V_{g1} and V_{g2}. We could collect a similar stability diagram in our system by sweeping the backgate and tip voltage (as in Fig. 5.8) with the tip placed near a degeneracy point of two coupled quantum dots. Since our backgate couples well to all quantum dots, however, and since the AFM tip must couple reasonably to both dots so as to resolve charging on both dots in its resonance frequency shift, this measurement scheme is unfavorable for our setup.

In our unusual stability diagram, Fig. 5.22, in contrast, we use a spatial dimension, the tip location, along the x-axis to tune the relative strength of the two tip-dot capacitances. Along the y-axis we vary the voltage on the extended backgate, which couples to both quantum dots simultaneously. The situation in our experiment is depicted schematically in Fig. 5.23. The two quantum dots #1 and #2 are mutually coupled by the tunnel barrier between them. The two contacts (labeled "source" and "drain") are grounded and act as tunnel-coupled charge reservoirs for the dots. Their sole purpose in this model is to set an electrochemical reference potential for the two quantum dots and to permit tunneling of electrons onto or off each dot. Both gates, the backgate and the AFM tip, couple to both quantum dots via the capacitances C_{gd1}, C_{gd2} and $C_{\mathrm{td1}}(\vec{r})$, $C_{\mathrm{td2}}(\vec{r})$, respectively. The backgate-dot capacitances C_{gd1} and C_{gd2} vary only weakly with tip position and can be regarded as fixed. At our typical tip heights, the AFM tip is a much less efficient gate than the extended backgate, $C_{\mathrm{gd}} > C_{\mathrm{td}}$. Hence, we use the backgate voltage to sweep the electrochemical potential of the dots. But since the backgate couples to both dots simultaneously, a sweep of the backgate voltage alone could only record a 1-dimensional cut of a large phase space of the double

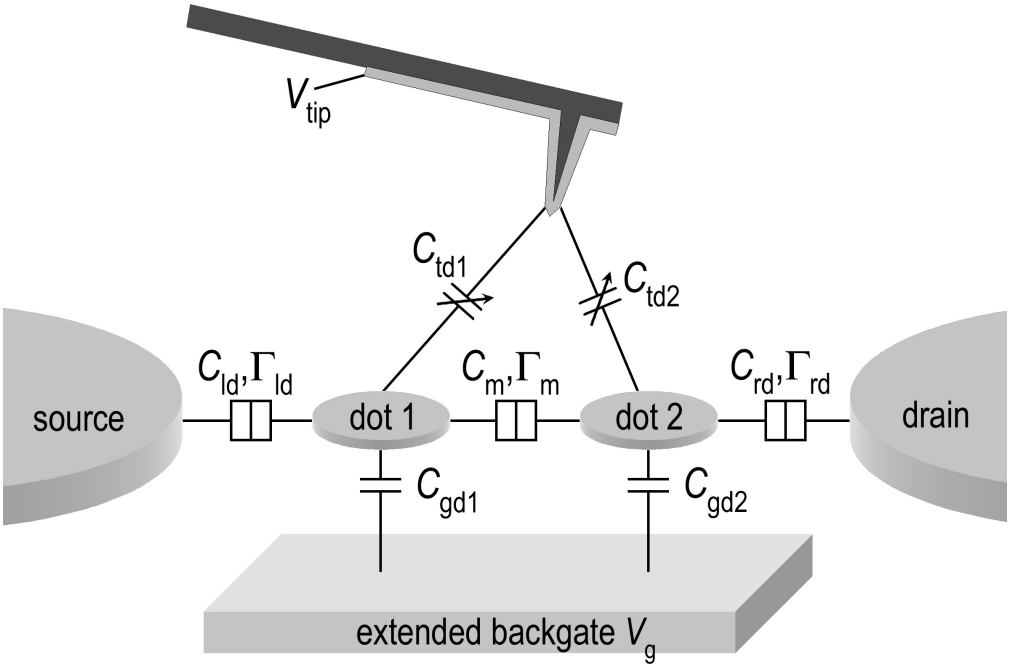

Figure 5.23: Model of two mutually coupled quantum dots in the LT-AFM. Each quantum dot is tunnel-coupled to a charge reservoir, labeled source and drain. The extended backgate and the AFM tip act as gates on both dots. The two tip-dot capacitances vary with tip position.

dot system. For this reason the tip serves an important function: By moving the tip over a little, we can change the gating conditions slightly – gate one dot a little more and the other a little less than before (as measured by their respective gate charges (5.2)) – and allow the backgate to sweep the electrochemical potentials of the dots under slightly different electrostatic conditions. This way we can access a 2-dimensional plot of the coupled double dot phase space. This 2-dimensional $V_{\rm g}$-x scan of the coupled double dot phase space gives our tilted version of the double dot stability diagram. A schematic adaptation is shown in Fig. 5.24(a).

5.7.3 Quantitative analysis of the line splitting

For the quantitative analysis of the line splitting we assume that the two quantum dots are capacitively coupled, but it is implicitly understood that this coupling could be due to capacitive and/or tunnel coupling. In this sense, the mutual dot capacitance extracted below really quantifies the magnitude of the coupling impedance, $|Z_{\rm m}|$.

From the $V_{\rm g}$-x stability diagram, as schematically shown in Fig. 5.24(a), we can extract 4 relevant quantities:

- The addition gate voltage for each dot, $\Delta V_{\rm g1}$ and $\Delta V_{\rm g2}$, defined as the amount of gate voltage needed to promote one more electron onto one dot without changing the charge on the other dot. This is the same quantity we have already evaluated for several dots previously in Sec. 5.3 in the absence of interdot coupling.

- The amount of gate voltage needed to compensate for the induced gate charge when the other (coupled) dot has acquired one more electron. In general,

it may be different for each of the two coupled dots, depending on its gate efficiency and its charging energy. We will call them $\Delta V_{\mathrm{g1}}^{(\mathrm{m})}$ and $\Delta V_{\mathrm{g2}}^{(\mathrm{m})}$ for dot #1 and #2, respectively. This quantity describes how well the two dots are coupled and is related to the interdot coupling strength.

Figure 5.24(b) shows how all 4 voltages are extracted from a double dot spectrum. A definition of these voltages in terms of the electrochemical potentials of the dots is given in Eq. (A.4) in Appendix A.1.

In the classical limit, $k_B T \gg \Delta E_{\mathrm{level}}$, we can calculate the interdot gating efficiencies $C_{\mathrm{m}}/C_{\mathrm{dot}\,\#1}$ and $C_{\mathrm{m}}/C_{\mathrm{dot}\,\#2}$ of capacitively coupled dots from these 4 backgate voltage differences, using the formula

$$C_{\mathrm{m}} = \frac{\Delta V_{\mathrm{g2}}^{(\mathrm{m})}}{\Delta V_{\mathrm{g2}}}\, C_{\mathrm{dot}\,\#1} = \frac{\Delta V_{\mathrm{g1}}^{(\mathrm{m})}}{\Delta V_{\mathrm{g1}}}\, C_{\mathrm{dot}\,\#2}\ . \tag{5.9}$$

A derivation of this relation is given in Appendix A.1. This equation also produces the ratio of the charging energies of the two capacitively coupled dots.

As an example analysis, we take a readout of the 4 voltage differences needed from the spectrum in Fig. 5.24(c) and find $\Delta V_{\mathrm{g1}} = 25.4\,\mathrm{mV}$ and $\Delta V_{\mathrm{g2}} = 29.3\,\mathrm{mV}$ for the direct addition backgate voltages of the two dots. Within the image resolution of $1.95\,\mathrm{mV/pixel}$ for the backgate voltage in Fig. 5.24(c), the amount of splitting is the same for both dots, $\Delta V_{\mathrm{g1}}^{(\mathrm{m})} = \Delta V_{\mathrm{g2}}^{(\mathrm{m})} = 7.8\,\mathrm{mV}$. Under the assumption of weak interdot tunnel coupling, these values correspond to interdot gating efficiencies of $C_{\mathrm{m}}/C_{\mathrm{dot}\,\#1} = 0.27$ and $C_{\mathrm{m}}/C_{\mathrm{dot}\,\#2} = 0.31$.

Although we have analyzed the line splitting under the hypothesis of dominant capacitive coupling, we stress that the coupling could be either due to tunnel or capacitive coupling (or both). A convenient quantity that accounts for both possibilities is the coupling impedance Z_{m} that was proposed in Sec. 2.1.8. From

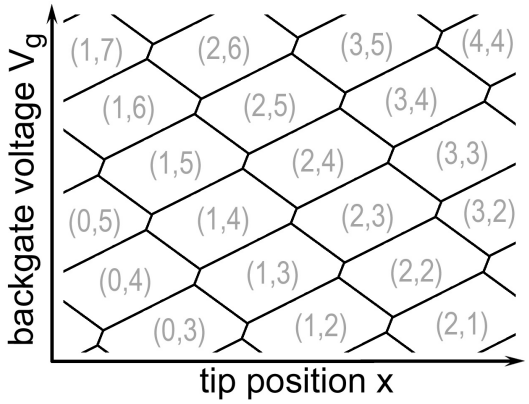

(a) Schematic charge stability diagram in the V_g-x spectrum form. The labels (N_l, N_r) denote the equilibrium occupation of electrons on the left and right dot, each up to an offset.

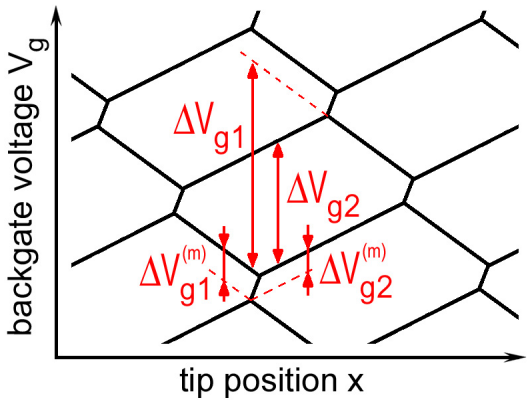

(b) How to determine ΔV_{g1}, ΔV_{g2}, $\Delta V_{g1}^{(m)}$, and $\Delta V_{g2}^{(m)}$ from the charge stability diagram.

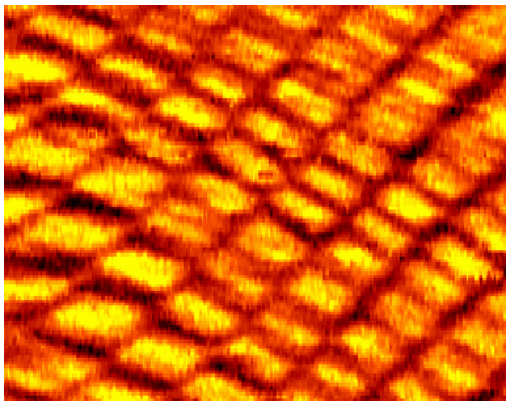

(c) Experimental charge stability diagram in the V_g-x spectrum form.

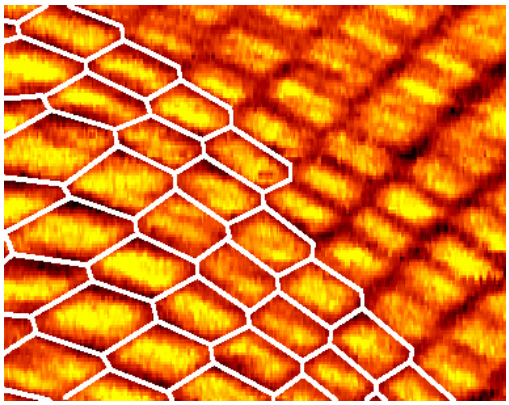

(d) Same spectrum as Fig. 5.24(c), but with charge stability diagram partly overlaid (to guide the eye).

Figure 5.24: Charge stability diagram in the V_g-x spectrum of two coupled quantum dots in a CNT.

the numerical analysis above we can infer its magnitude. In the capacitive coupling limit, the magnitude of the coupling impedance is the reciprocal of Eq. (2.27),

$$|Z_{\mathrm{m}}| = \frac{h}{e^2}\,\frac{1}{2\pi}\left(\frac{C_{\mathrm{dot\#1}}\,C_{\mathrm{dot\#2}}}{C_{\mathrm{m}}^2} - 1\right)\ . \tag{5.10}$$

Hence, we reexpress the coupling as $|Z_{\mathrm{m}}| = 1.75\,\dfrac{h}{e^2}$ for the dot analyzed above.

Not every pair of quantum dots that we have taken images of shows as strong avoided crossings at the intersection of their charging lines. The calculated numbers above are among the strongest coupling we have observed and are not typical. In some cases, the splitting (if present) is below our resolution. To estimate our resolution limit for this measurement, we take Fig. 5.24(c) as an example and consider the following information: Our step size in backgate voltage is 1.95 mV per pixel along the y-axis. With the above backgate addition energies of the two dots in the spectrum we reach the digitization limit of the image at $C_{\mathrm{m}}^{(\mathrm{min})}/C_{\mathrm{dot}} \approx 0.07$. Correspondingly, any coupling impedance $|Z_{\mathrm{m}}| > 30\,\dfrac{h}{e^2}$ cannot be resolved in this image even under optimum conditions. For the sharpest charging lines in the image we could confidently resolve a splitting of only one pixel. On average the single-electron charging lines in Fig. 5.24(c) are 2 points wide along the V_{g}-axis. In our experience, an avoided crossing similar to the width of the lines in an image is well visible and sufficient to measure the line splitting. With this standard, the minimum detectable gating efficiency in Fig. 5.24(c) is typically $C_{\mathrm{m}}/C_{\mathrm{dot}} \approx 0.13$, corresponding to a coupling impedance $|Z_{\mathrm{m}}| \approx 10\,\dfrac{h}{e^2}$. Clearly, the lower detection limit on the capacitance ratio also depend on the charging energy of the dots in the image. Taking Fig. 5.13(a) as another example, the small dot (with the smallest total dot capacitance) on the left of the image has an addition backgate voltage of $\Delta V_{\mathrm{g}}^{(\mathrm{add})} = 98\,\mathrm{mV}$. On the scale of the width of its charging lines (about 6 mV) we don't observe any splitting in the image. By Eq. (5.9), the image resolution

bounds $C_{\rm m}/C_{\rm dot} < 0.06$ for the large dot to the right of the small dot and its coupling capacitance to the small dot. For these two dots we infer $|Z_{\rm m}| > 10\,\frac{h}{e^2}$ from Eq. (5.10).

5.8 Charging Energy from the Frequency Shift Amplitude[11]

Summarizing our approach in all previous sections of this chapter, we have used the signature of single-electron tunneling in the cantilever resonance frequency to identify where charging events occur in space and gate voltage. Some features of these charging curves or the relation between several such curves enabled us to extract qualitative and quantitative information about the quantum dots and their electrostatic environment. In this section we return to our starting equation (5.1) for frequency shift microscopy and analyze the information contained in the actual amount of frequency shift due to single-electron tunneling. Our goal is to extract the charging energy E_C of a quantum dot, or equivalently its total capacitance $C_{\rm dot}$.

To extract the charging energy of a quantum dot from the resonance frequency shift due to single-electron tunneling, we return to the individual traces of the cantilever resonance frequency vs. backgate voltage. Figure 5.25 shows several such traces, where the AFM tip is resonating at different tip heights above the same quantum dot. These traces are equivalent to cuts through a $V_{\rm g}$-x charging spectrum (Fig. 5.6) at fixed tip location or cuts at constant tip voltage in a $V_{\rm g}$-$V_{\rm tip}$ spectrum (Fig. 5.8). Instead of encoding it in the color scale of a 2D scan, these 1D traces make the actual amount of resonance frequency shift clearly visible. Each

[11] Part of this section was published in Zhu, Brink, and McEuen, *Appl. Phys. Lett.* 87, 242102 (2005).

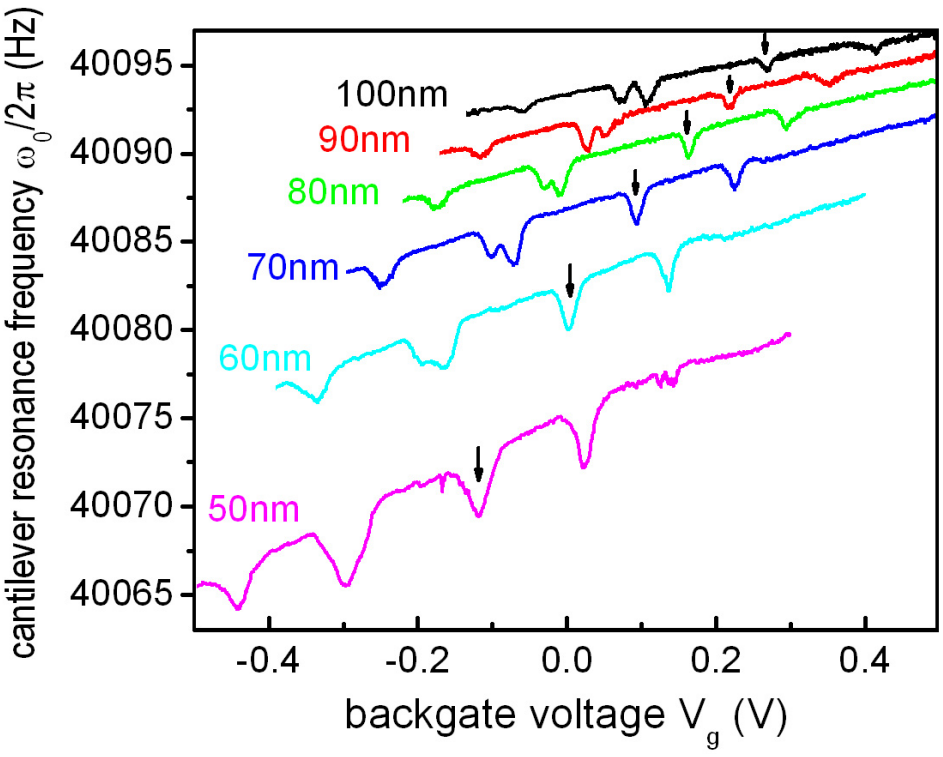

Figure 5.25: Frequency shift traces of the AFM cantilever from a CNT quantum dot versus backgate voltage. In each trace the AFM tip is resonating at a different height above the center of the same dot. The tip height is labeled in the same color next to each trace. Single-electron charging events in the frequency shift signal are observed as dips on the smooth background. The sequence of black arrows marks the same charging event $N \rightarrow N+1$ of the quantum dot at different tip heights.

dip in the cantilever resonance frequency below the smooth background is due to single-electron charging of the quantum dot underneath the resonating AFM tip.

To isolate the charging energy from any of the dips in the resonance frequency, we need to evaluate two terms that appear in Eq. (5.1): The spatial derivative of the gate charge with respect to tip height, $\frac{dq_c}{dz}$, and the factor $\frac{f'(E_{dc})}{1+(\omega/\Gamma)^2}$ that carries the dependence on the backgate voltage and the electron life time on the quantum dot. We address these two terms in this order in the following.

Spatial derivative of the gate charge, dq_c/dz. To evaluate how the gate charge q_c varies with the tip height z_0 above the quantum dot, we look at the evolution of the single-electron charging dips with tip height. In Fig. 5.25 we see that the dips corresponding to the same charging event (as marked by arrows) move towards lower backgate voltage as the height of the (positively biased) AFM tip is reduced. For small changes Δz_0 in tip height, their shift $\Delta V_g^{(\Delta z_0)}$ in backgate voltage follows from[12]

$$\frac{dq_c}{dz_0} = C_{gd}\,\frac{dV_g}{dz_0}\,. \tag{5.12}$$

From the sequence of charging dips in Fig. 5.25 we obtain the ratio $\frac{\Delta V_g^{(z_0)}}{\Delta z_0} \approx \frac{dV_g}{dz_0}$ on the right hand side in Eq. (5.12). The backgate-dot capacitance is obtained from the separation of charging dips at constant tip height. In the classical limit, the gate charge of neighboring charging events differs by e, so that $e = C_{gd}\,\Delta V_g^{(add)}$,

[12]This relation is an application of the general equation

$$-\left(\frac{\partial q_c}{\partial z_0}\right)_{V_g,V_{tip}} = \left(\frac{\partial q_c}{\partial V_g}\right)_{z_0,V_{tip}} \left(\frac{\partial V_g}{\partial z_0}\right)_{q_c,V_{tip}} \tag{5.11}$$

for a function $q_c = q_c(V_g, V_{tip}, z_0)$ and its inverse $V_g = V_g(q_c, V_{tip}, z_0)$. In this notation the subscripts outside the parentheses are kept constant during the derivative inside.

where $\Delta V_{\rm g}^{\rm (add)}$ is the backgate voltage difference between the two neighboring charging events at constant tip height. From the data in Fig. 5.25, we extract a backgate-dot capacitance $C_{\rm gd} = 1.02\,{\rm aF}$ with a standard deviation of 1% across the different tip heights and no systematic trend within $z_0 = 50-100\,{\rm nm}$. This justifies experimentally the assumption that $C_{\rm gd}$ is independent of tip position under our operating conditions, as required for some measurements in this chapter[13]. A plot of $dq_{\rm c}/dz$ obtained in this way is shown in Fig. 5.26. The red line fits a power law to the extracted $dq_{\rm c}/dz$ data points.

Charging energy from the frequency shift signal in the transparent limit, $\omega \ll \Gamma$. In the limit of a transparent quantum dot, the electron tunneling time on and off the dot is irrelevant. Electrons tunnel instantly on the time scale of the cantilever resonance, and the factor $\dfrac{1}{1+(\omega/\Gamma)^2}$ drops out of Eq. (5.1). In this limit we simply integrate out the derivative of the Fermi-Dirac distribution on the right-hand side of Eq. (5.1), which describes the shape of the single-electron tunneling dip. The area in the single-electron charging dip of the relative cantilever frequency shift is determined by

$$-\,e\frac{C_{\rm gd}}{C_{\rm dot}}\int\limits_{-\infty}^{\infty}\frac{\delta\omega_0}{\omega_0}\,dV_{\rm g} = \frac{1}{2k}\left(\frac{dq_c}{dz}\,\frac{e}{C_{\rm dot}}\right)^2 \qquad \text{if} \quad \omega \ll \Gamma\,. \tag{5.13}$$

The factor in front of the integral converts backgate voltage to electrostatic energy of the dot, $d(\Delta E_{\rm dc}) = e\,dq_{\rm c}/C_{\rm dot} = -eC_{\rm gd}\,dV_{\rm g}/C_{\rm dot}$. The area of the single-electron charging dip in the frequency shift signal allows us to determine the charging energy

[13] We implicitly assume this condition in the following paragraph, for example: When integrating out the right-hand side of Eq. (5.1) to obtain Eqs. (5.13) and (5.14), $dq_{\rm c}/dz$ is assumed to be independent of the backgate voltage, which requires that $C_{\rm gd}$ is independent of the tip height, see Eq. (5.2). Another example is the analysis of coupled quantum dots in Sec. 5.7 – see footnote 1 in Appendix A.1.

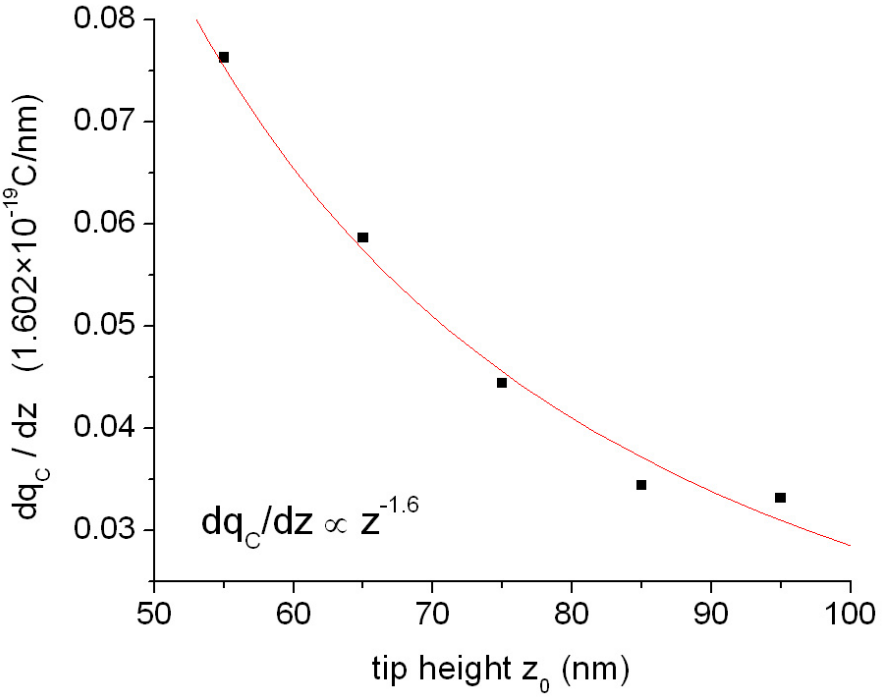

Figure 5.26: Spatial derivative of the gate charge, dq_c/dz, extracted from tip height dependent frequency shift vs. backgate traces on a quantum dot (Fig. 5.25).

of the dot,

$$E_C = \frac{e^2}{C_{\rm dot}} = -2k \left(\frac{dq_c}{dz}\right)^{-2} eC_{\rm gd} \int_{-\infty}^{\infty} \frac{\delta\omega_0}{\omega_0}\, dV_{\rm g} \qquad \text{if} \quad \omega \ll \Gamma\ . \tag{5.14}$$

Knowing the cantilever spring constant $k = 1.7\,\mathrm{N/m}$ (from cantilever calibration, Sec. 3.3), the gate charge derivative $dq_{\rm c}/dz$ at different tip heights, Fig. 5.26, and the backgate-dot capacitance $C_{\rm gd} = 1.02\,\mathrm{aF}$ from above, we can numerically integrate the area in any of the arrowed single-electron dips in Fig. 5.25. This gives a charging energy of $E_C = 47\,\mathrm{meV}$ from Eq. (5.14), which corresponds to a total dot capacitance of $C_{\rm dot} = 3.4\,\mathrm{aF}$. The charging energies that we calculate from the marked dips in different traces in Fig. 5.25 are all identical, as is shown in Fig. 5.27. Here we plot the area in the single-electron charging dip at different tip heights versus the square of the gate charge derivative at the same tip height. According to Eq. (5.14), they are related linearly with a slope of $\dfrac{E_C}{2k\, eC_{\rm gd}}$. Clearly, the data points in Fig. 5.27 indeed lie on a line that goes through the origin of the coordinate system, confirming the prediction of Eq. (5.14) and the value of the charging energy from the marked dip in all traces in Fig. 5.25.

We remark that the quantum dot we have chosen for the above analysis is the *p*-dot that forms at the metal contact as the CNT's electrochemical potential enters the bandgap from the valence band. This dot is visible in the bottom right corner of the spectrum in Fig. 5.10. It allows us to estimate how big the capacitance to the lead can become if the dot is placed right next to it. We find an upper bound of $C_{\rm lead} \leq C_{\rm dot} - C_{\rm gd} - C_{\rm td} \approx 2\,\mathrm{aF}$ for this dot. Given the very close proximity to the lead, this coupling seems reasonable.

We are confident that our disorder-induced quantum dots in semiconducting CNTs are fairly transparent on the scale of our driving frequency at the cantilever

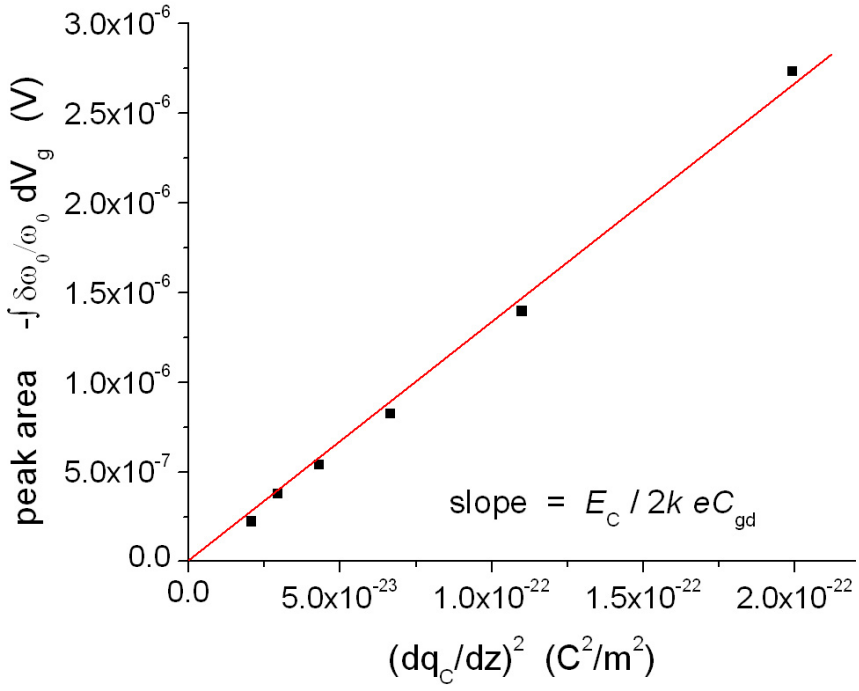

Figure 5.27: Charging energy of a quantum dot derived from the amount of cantilever frequency shift due to single-electron charging. The data points (black squares) obtained from different tip heights predict the same charging energy E_C and confirm the linear relationship between the area in the single-electron charging dips of the cantilever resonance frequency and the square of the spatial derivative of the gate charge, as predicted by Eq. (5.14).

resonance, as we observe a strong frequency shift signal in our measurements. As graphed in Fig. 2.9, the amount of frequency shift due to single-electron tunneling is greatly reduced when the tunneling rate of the quantum dot gets larger than the driving frequency. For the sake of completeness of the described method of extracting the charging energy, we extend the analysis to non-transparent dots in Appendix A.3.

5.9 Isolated Carbon Nanotubes

Not all CNTs on the chip were connected by source and drain contacts. In this section we explore spatial images from an isolated CNT with no leads attached. This particular CNT was attractive for the measurement as there was no catalyst island near either end of the tube; it was just lying on its own on the SiO_2 surface[14]. With the lack of source and drain contacts, we were unable to perform transport measurements on this CNT and could not determine whether it was a metallic or semiconducting CNT. Despite this uncertainty, the data from the isolated CNT illustrates some benefits of frequency shift microscopy as an experimental technique very clearly. These results are also relevant to contacted CNTs and other samples.

Figure 5.28 shows spatial frequency shift images of an isolated CNT at different backgate voltages. The tip height above the substrate is $z_0 = 83\,\mathrm{nm}$ in all images. The scans in Fig. 5.28 cover almost the full length of the isolated CNT. Although this CNT does not have any leads attached, we clearly observe single-electron charging rings from quantum dots on the tube. At first sight, this observation might seem surprising: Since the isolated CNT doesn't couple to any charge reser-

[14]This CNT may still have grown from an Fe nanoparticle that was left on the surface during catalyst lift-off.

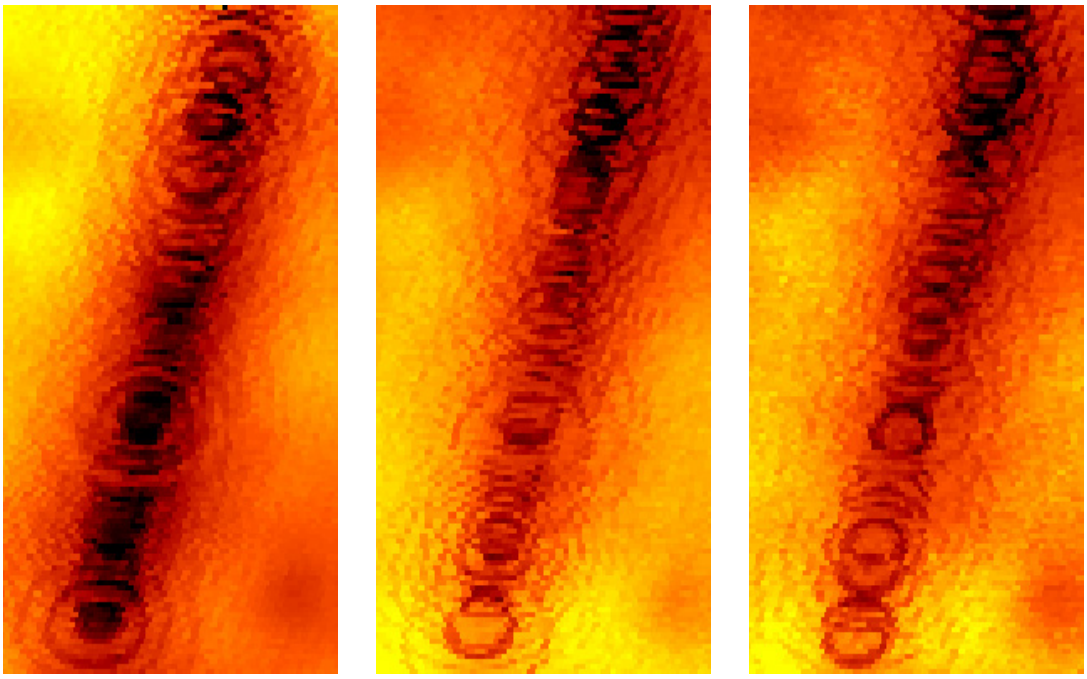

(a) $V_g = -2.3\,\mathrm{V}$. (b) $V_g = -1.7\,\mathrm{V}$. (c) $V_g = -1.1\,\mathrm{V}$.

Figure 5.28: Spatial frequency shift images of a CNT without contacts. The voltage on the extended backgate is shown under each figure. All images scan the same $0.5\,\mu\mathrm{m} \times 1\,\mu\mathrm{m}$ area.

voirs, a gate voltage cannot induce charges on the CNT, and the total number of electrons on the CNT is fixed. At a second thought, the underlying mechanism for the observation becomes clear: Single-electron charging of quantum dots on an isolated tube is possible by changing the charge density locally underneath the tip at the cost of other tube locations. In other words, the electrons on the CNT are redistributed between different quantum dots depending on the tip location. This observation conveys a useful feature of our frequency shift measurements: Our measurement requires only local electron motion, i.e., a local current, to detect single-electron charging. For CNTs with leads this implies that the charge of a tunneling electron does not necessarily have to come all the way from the source or drain contact. In fact, this aspect of frequency shift microscopy has enabled us to study semiconducting CNTs when transport across the CNT device was absent, for example, in the n-regime.

Even though single-electron tunneling is possible without any contact if the CNT is not too short, rearranging a fixed total number of electrons on the tube can only access a limited range of charge states on the quantum dots. To record a large charge addition spectrum such as Fig. 5.6, the CNT must couple to an infinite charge reservoir. At the same time it is also clear that a single charge reservoir – i.e., a single metal contact – is sufficient for the frequency shift measurement. A second lead, as we had available in our CNT-FETs and necessary for transport measurements or scanning gate microscopy, is not required to perform frequency shift measurements.

The need for none or only one contact expands the range of interesting samples to investigate with frequency shift microscopy greatly. It can also significantly simplify the fabrication process for many samples. As an example, Chap. 6 explores

gold nanoparticles that are chemically linked to a single charge reservoir. This is just one sample that benefits from the single contact geometry.

5.10 Conclusions

In the experiments presented in this chapter, we have visualized the formation of quantum dots in a long semiconducting CNT. We have attributed these quantum dots to the effects of disorder on the nanotube at low carrier density. Spatially addressing one quantum dot at a time by our low-temperature atomic force microscope, we have extracted their size and backgate coupling and found a common scaling law among them. We have demonstrated how to extract the charging energy of a quantum dot from the resonance frequency shift of the AFM cantilever. Interaction between neighboring quantum dots has been observed and analyzed. Monitoring spatially how charge is induced on the semiconducting CNT by the backgate voltage, we found the bandstructure of the CNT imposed on the potential energy landscape seen by carriers on the CNT. Relying on measurements by our local force probe, we have resolved charging events even in the absence of device conduction. We have furthermore extracted information about the underlying disorder from the charging pattern of the quantum dots in backgate voltage and space.

These measurements have demonstrated the power of our local force probe technique. In particular, we have found that only local electron motion is needed to resolve and characterize the quantum dots. This observation has enabled us to resolve the charging properties also on the n-side, where no device conduction was observed and opens the door to a variety of other samples, one of which is discussed in the following chapter.

CHAPTER 6

SINGLE-ELECTRON CHARGING OF GOLD NANOPARTICLES LINKED TO A CARBON NANOTUBE AT $T = 77\,\mathrm{K}$

In this chapter we investigate single-electron charging of gold nanoparticles that are attached to a CNT by a linker molecule (Fig. 4.7). The gold nanoparticles are 12 nm in diameter and expected to show Coulomb blockade behavior even at liquid nitrogen temperature, $T = 77\,\mathrm{K}$, as predicted by numerical finite element simulations. The CNT serves as a lead or charge reservoir for the gold nanoparticle. CNTs are an obvious choice for this purpose, because they are small and don't interfere with the scanning probe measurement topographically. Furthermore, their small size implies that the mutual capacitance between the CNT and the gold nanoparticle is relatively small, certainly in comparison to microfabricated metal leads. This last consideration is important as we retain the ability to gate the gold nanoparticles by the backgate and the AFM tip with good efficiency.

Using our force-sensing AFM cantilever as a a mobile, local detector allows us to investigate the gold nanoparticles in a single-contact geometry. The independence of our scanning force probe measurement from transport across the quantum dot, which would require two contacts to each nanoparticle, was discussed in some detail in Sec. 5.9. This single-contact geometry alleviates many fabrication issues with wiring up nanoscale objects with two contacts. Very innovative methods have been devised to make two leads with nanometer separation (Reed et al. 1997, Morpurgo et al. 1999, Park et al. 1999, Zhang et al. 2003, Tomfohr et al. 2005, De Poortere et al. 2006, Guo et al. 2006, for example). Nonetheless, the fabrication in any of these clever schemes is challenging. Furthermore, it is impossible to make truly identical junctions on the nanometer scale, at least at this point in time. The single-

contact geometry may be advantageous in these respects: Their fabrication is much simpler and requiring only one contact improves the chances for reproducibility.

Lastly, this chapter also introduces another signal channel of our scanning force technique: The tip oscillation amplitude. As illustrated in the schematic of our experimental setup, Fig. 3.5, the tip oscillation amplitude can be recorded simultaneously with the cantilever resonance frequency. Single-electron charging events can also be visible in the tip amplitude signal. A reduction of the tip oscillation amplitude z_ω during single-electron charging events is due to dissipation in the tunneling process. At the cantilever resonance frequency ω_0 it is given by

$$\delta z_{\omega_0} = \frac{F_{\omega_0}}{k}\,\delta Q\ , \tag{6.1}$$

where F_{ω_0} is the (constant) amplitude of the resonant ac-driving force, k is the spring constant of the cantilever, and Q its quality factor. Changes in the spring constant due to single-electron charging are too small to be observed in the tip oscillation amplitude. Operationally, we fix the ac-force amplitude by driving the cantilever mechanically through a bimorph piezo element underneath the cantilever substrate in the AFM tip holder[1]. The instrument setup for this measurement mode is depicted in Fig. 3.5.

We start this chapter with electron transport and scanning gate measurements on the CNT device, so as to exclude the possibility of quantum dots on the CNT (Sec. 6.1). Spatial images of a CNT device that has gold nanoparticles linked to it are shown in Sec. 6.2. We use these spatial images to locate gold nanoparticles that are coupled to the CNT for the following experiments. In Sec. 6.3 we quantitatively

[1]This mode of operation is different from some setups for electrostatic force microscopy (EFM), where the cantilever is excited capacitively via the sample. The frequency shift signal is the same in either setup, but the amplitude signal can be different.

extract the capacitive couplings and the charging energy of the gold nanoparticles from the tip amplitude data, using mostly similar methods as discussed in Chap. 5. The predictions of Eq. (6.1) for the tip oscillation amplitude signal are experimentally validated in Sec. 6.4. This measurement confirms that the tip oscillation amplitude measures the dissipation in the single-electron tunneling process. We analyze the tip amplitude data quantitatively in Sec. 6.5. With the aid of the capacitive couplings (Sec. 6.3), we extract the tunnel resistance of the junction between the gold nanoparticle and the CNT. Complementing the amplitude signal with resonance frequency shift data provides a more straight-forward path to the tunnel coupling of the gold nanoparticles, as discussed and employed in Sec. 6.6. In Sec. 6.7 we turn the tables and use the gold nanoparticles to interrogate the CNT. We discuss how to measure the voltage profile of a CNT by means of the linked gold nanoparticles and apply this technique to looped CNT. In a time-tested fashion, the chapter concludes with conclusions.

6.1 Transport and Scanning Gate Measurements of the CNT devices

In the light of Chap. 5 and the existence of quantum dots in CNTs at $T = 4.2\,\mathrm{K}$, we first validate experimentally that the CNT used here doesn't show any signs of Coulomb blockade at $T = 77\,\mathrm{K}$. Figure 6.1 shows the $T = 77\,\mathrm{K}$ transport trace of the CNT device imaged in Fig. 6.2. Clearly, the source-drain conductance of the CNT shows no sign of Coulomb oscillations – for comparison, see Figs. 5.1 and 5.2. This proves that the CNT is acting as a metal lead for the gold nanoparticles.

To further exclude the possibility of quantum dots on the CNT, we do extensive Scanning Gate Microscopy (SGM) measurements on each CNT device, where we record the source-drain conductance as a function of the biased tip position. Each

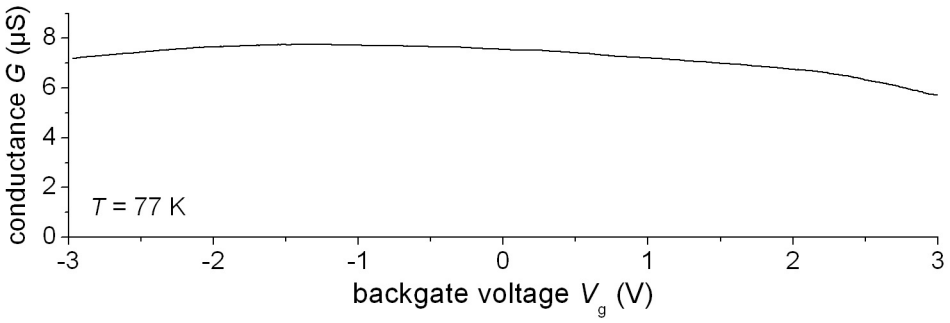

Figure 6.1: Electron transport trace of a CNT device functionalized with gold nanoparticles, recorded at $T = 77\,\mathrm{K}$.

SGM image is recorded together with an amplitude image during the same scan. While the amplitude images exhibit single-electron charging rings abundantly (see Sec. 6.2), the simultaneous SGM images are completely featureless. This characterization of the CNT is carried out fully on all devices used in this chapter. None of the CNTs shows any sign of Coulomb blockade.

We conclude that any single-electron charging events observed under our operational conditions cannot be due to the CNT. This finding is consistent with previous studies of charging effects in CNTs (Tans et al. 1997, Bockrath et al. 1999, Woodside 2001, for example).

6.2 Spatial amplitude images of gold nanoparticles

As mentioned in the introduction and touched upon at the end of Sec. 2.2.2, single-electron charging events can alter the tip oscillation amplitude. In this section we take the experimental approach and look for signs of tunneling events in spatial amplitude images. A spatial amplitude image records the tip oscillation amplitude as a function of the biased AFM tip position on a square grid of fixed tip height above the sample surface.

Figure 6.2 shows several spatial images of a CNT with gold nanoparticles linked to it. Each of the 17 high-resolution images in the stitched sequence is recorded at a tip height of $z_0 = 60\text{nm}$ and $T = 77\,\text{K}$. The sequence covers the entire length of the CNT between its source and drain contact. The color scale in these images encodes the tip oscillation amplitude at the cantilever resonance frequency. For comparison, the three AFM images in the inset show large area scans of the entire CNT device. The CNT appears as a dark line in the frequency shift (top) and amplitude (middle) inset images, which were also taken at liquid-nitrogen temperature. The tube is bright in the topographic height image (bottom inset), which was recorded in tapping mode at room temperature. This topographic image also clearly shows the gold nanoparticles as even brighter dots and the metal contacts at the left and right edge of the scan.

Looking at the sequence of low-temperature high-resolution images, there are many sets of concentric rings (and some single rings) visible along the CNT. It is noteworthy that

- all rings are circular (without elliptical distortions),
- there are gaps along the CNT without any rings, i.e., some sets of concentric rings don't have an immediate neighbor to the left and to the right,
- sometimes the centers of two nearby sets of concentric rings (or just individual non-concentric rings) are at the same location along the CNT, but offset perpendicular to the tube, and
- at a few spots, the centers of three nearby (non-concentric) rings don't lie on a line but at the corners of a small triangle.

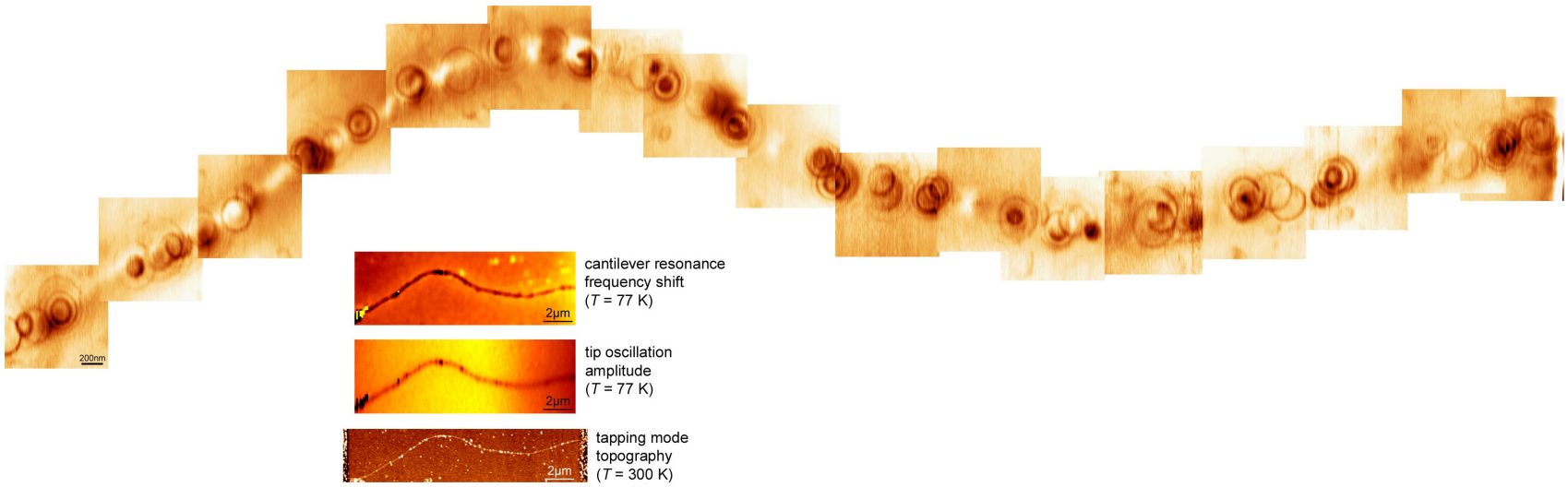

Figure 6.2: Spatial images of gold nanoparticles attached to a CNT. The sequence of stitched images depicts the tip oscillation amplitude along the CNT at $T = 77\,\mathrm{K}$. In all constituent images, the voltage on the backgate is $V_\mathrm{g} = -2\,\mathrm{V}$, the tip voltage is $V_\mathrm{tip} = +3\,\mathrm{V}$, and the tip scans at a height of $z_0 = 60\,\mathrm{nm}$ above the surface. Sets of concentric dark rings are well visible at many locations in close proximity of the CNT. The three inset images show large area scans of the same CNT device. The top two insets are low-temperature, non-contact images of the cantilever resonance frequency shift and the tip oscillation amplitude, as labeled. The bottom inset image is a tapping mode topographic AFM image recorded at room temperature. The device contacts are clearly visible on the left and right of this image.

We attribute each dark ring to a single-electron charging event of a gold nanoparticle (or a cluster of nanoparticles) at the center of the ring. The fact that these rings appear dark shows that the amplitude change is due to energy dissipation in the single-electron tunneling process, as analyzed in Appendix A.4. We also remark that the 4 observations made above stand in contrast to the concentric contours that were observed in spatial images of CNT devices in Chap. 5. Compare to the images in Fig. 5.5, for example. Even though we have already excluded charging effects on the CNT in Sec. 6.1 these findings provides further evidence that the charging events don't occur on the CNT.

The main benefit of visualizing single-electron tunneling in spatial images, however, is to locate gold nanoparticles that are coupled to the CNT. Once we know their location, we can move the AFM tip near them and investigate their properties one at a time. The following sections illustrate different such measurements on individual gold nanoparticles.

6.3 Capacitive couplings of the gold nanoparticles

We first characterize the electrostatic properties of the gold nanoparticles. In particular, we extract the gate-nanoparticle capacitances and the charging energy of the nanoparticles. These capacitances allow us to bound the mutual CNT-nanoparticle capacitance of the tunnel barrier created by the linker molecule between the two. The procedure here is very similar to the steps followed for quantum dots in CNTs, as discussed in Chap. 5. Only the charging energy is measured differently.

To extract its capacitances, we park the biased AFM tip above the gold nanoparticle to be characterized. We sweep the backgate voltage while monitoring the

amplitude of the resonating cantilever. A few such amplitude traces, recorded at different tip voltages, are shown in Fig. 6.3. Single-electron charging of the gold nanoparticle is visible as dips in the resonant amplitude below the smooth background. The single-electron tunneling dips move to lower gate voltages when the tip voltage is increased, as shown by the set of arrows, which tracks one charging event of the gold nanoparticle. The other dips move over by the same amount. Effectively, the traces taken at different tip voltages are translated horizontally with respect to each other. The vertical offset between traces is added manually for clarity.

From the separation of two subsequent charging dips within one trace, which we introduced as *addition backgate voltage* $\Delta V_{\mathrm{g}}^{(\mathrm{add})}$ in Chap. 5, we find the backgate-nanoparticle mutual capacitance by

$$C_{\mathrm{g-Au}} = e/\Delta V_{\mathrm{g}}^{(\mathrm{add})} \; . \tag{6.2}$$

This relation follows from Eq. (2.8) in the classical limit. From the traces in Fig. 6.3 we find $C_{\mathrm{g-Au}} = 0.33\mathrm{aF}$, independent of the tip voltage.

To measure the mutual capacitance between the gold nanoparticle and the AFM tip, $C_{\mathrm{tip-Au}}$, we can sweep the tip voltage and determine the separation between neighboring charging events, as we've just done for the backgate. Instead, we will compute the tip-nanoparticle capacitance from the shift of a charging event in backgate voltage that results from changing the tip voltage. As detailed for CNT quantum dots in Eq. (5.3), the same charging event moves by

$$\Delta V_{\mathrm{g}}^{(\Delta V_{\mathrm{tip}})} = -\frac{C_{\mathrm{tip-Au}}}{C_{\mathrm{g-Au}}}\,\Delta V_{\mathrm{tip}} \tag{6.3}$$

in backgate voltage if the tip voltage is changed by ΔV_{tip}. From the shift between traces of different tip voltage in Fig. 6.3 we find $C_{\mathrm{tip-Au}} = 0.18\,\mathrm{aF}$.

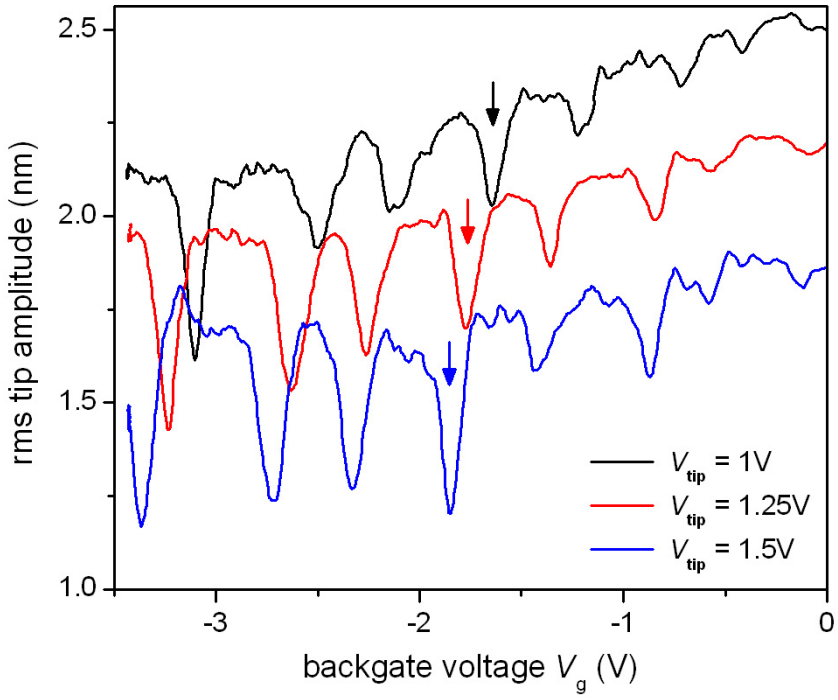

Figure 6.3: Tip oscillation amplitude vs. backgate voltage while the tip is parked straight above a gold nanoparticle at a height $z_0 = 60\,\text{nm}$. The three traces correspond to different voltages on the AFM tip, as labeled. For clarity, the traces are offset vertically with respect to each other. For one single-electron charging event, the corresponding dips are marked by an arrow on each trace.

At $T = 77\,\mathrm{K}$ we extract the charging energy $E_C = e^2/C_{\mathrm{Au}}$ of a gold nanoparticle from the width of the charging dips, which is thermally limited and determined by (Grabert and Devoret 1992)

$$\frac{C_{\mathrm{g-Au}}}{C_{\mathrm{Au}}}\, e\Delta V_{\mathrm{g}}^{(\mathrm{width})} = 4k_B T\ . \tag{6.4}$$

From the width of dips in Fig. 6.3 we find a charging energy $E_C = 106\,\mathrm{meV}$ or equivalently a total nanoparticle capacitance $C_{\mathrm{Au}} = 1.5\,\mathrm{aF}$.

We would also like to characterize the coupling between the gold nanoparticle and the CNT. Their mutual capacitance is difficult to measure on our samples. We can, however, calculate an upper bound on their coupling capacitance $C_{\mathrm{CNT-Au}}$ from the other capacitances extracted above. Since the total nanoparticle capacitance is the sum of the mutual capacitance to all other conductors, Eq. (2.53), we obtain an upper bound from

$$C_{\mathrm{CNT-Au}} \leq C_{\mathrm{Au}} - C_{\mathrm{g-Au}} - C_{\mathrm{tip-Au}}\ . \tag{6.5}$$

If the nanoparticle is far away from both CNT contacts, we think that this bound is close to the actual value of $C_{\mathrm{CNT-Au}}$. From the previously calculated capacitances, we find $C_{\mathrm{CNT-Au}} \leq 1\,\mathrm{aF}$ for the capacitance of the tunnel barrier to the CNT of this gold nanoparticle.

By recording multiple tip oscillation amplitude traces as a function of backgate voltage at different AFM tip heights z_0 above the dot (not shown), we can measure the change of gate charge q_{c} on the gold nanoparticle as a function of tip height. This method was discussed and used in Sec. 5.8, as illustrated in Figs. 5.25 and 5.26. For small changes in tip height, Δz_0, the single-electron charging event moves by

$$\Delta V_{\mathrm{g}}^{(\Delta z_0)} = \frac{1}{C_{\mathrm{g-Au}}}\,\frac{dq_{\mathrm{c}}}{dz_0}\,\Delta z_0 \tag{6.6}$$

in backgate voltage. This relation is a reformulation of Eq. (5.12) and derived from Eq. (5.11). At $z_0 = 60\,\mathrm{nm}$ and $V_{\mathrm{tip}} = 1\,\mathrm{V}$, we find for the above gold nanoparticle a gate charge derivative of $-\dfrac{dq_{\mathrm{c}}}{dz} = 7.3 \times 10^{-12}\,\dfrac{\mathrm{C}}{\mathrm{m}} = 0.045\,\dfrac{e}{\mathrm{nm}}$.

Comparing the above capacitances with measurements of other gold nanoparticles on the same and another CNT on the same chip, we find that the above couplings are a little on the small side, but still typical. The ratios of capacitances are representative. Table 6.1 summarizes the capacitances measured on other gold nanoparticles on the same chip.

6.4 Measuring energy dissipation due to single-electron tunneling

As mentioned in the introduction, the tip amplitude change due to single-electron charging arises from energy dissipation in the tunneling process. Before analyzing the amplitude signal based on this assumption, as encoded in Eq. (6.1), we validate it experimentally.

For this purpose, we compare the tip oscillation amplitude (and its change) to direct measurements of the cantilever quality factor. Specifically, we do the following experiment: We select a gold nanoparticle from a spatial image and park the biased AFM tip right above it. First, we record the tip oscillation amplitude z_{ω_0} as we sweep the backgate voltage and induce charges on the nanoparticle. In this part the ac-driving force follows the cantilever resonance frequency. Then we fix the backgate voltage and sweep the frequency of the ac-driving force. By monitoring the tip oscillation amplitude, we record a resonance curve of the cantilever. The width of the resonance curve $\Delta\omega_{\mathrm{FWHP}} = \omega_0/Q$ is a direct measure of the quality factor Q, where the resonance frequency ω_0 is the location of the maximum of the resonance curve. We record such a resonance curve at several different backgate

Table 6.1: Electrostatic capacitances of gold nanoparticles that are chemically linked to a CNT by an organic molecule. All measurements were performed at a tip height of $z_0 = 60\,\mathrm{nm}$. The first three data columns were obtained by Eqs. (6.2), (6.3), (6.4), respectively; the remaining three columns were inferred from the previous three.

particle No.	$C_{\mathrm{g-Au}}$	$\frac{C_{\mathrm{tip-Au}}}{C_{\mathrm{g-Au}}}$	$\frac{C_{\mathrm{g-Au}}}{C_{\mathrm{Au}}}$	$C_{\mathrm{tip-Au}}$	C_{Au}	$E_C = \frac{e^2}{C_{\mathrm{Au}}}$
particle #04	0.46 aF	0.50	0.22	0.23 aF	2.1 aF	76 meV
particle #06	0.40 aF	0.56	0.26	0.22 aF	1.52 aF	105 meV
particle #12	0.46 aF	0.54		0.25 aF		
particle #20	0.33 aF	0.55	0.22	0.18 aF	1.5 aF	106 meV
particle #22	0.39 aF	0.59	0.23	0.23 aF	1.69 aF	95 meV
particle #23	0.46 aF	0.50	> 0.22	0.23 aF	< 2.1 aF	> 76 meV

voltages and extract the quality factor.

The result of this experiment on two gold nanoparticles is shown in Fig. 6.4. The red trace in both graphs shows the tip oscillation amplitude as a function of backgate voltage. Multiple single-electron charging events are visible as dips in the amplitude signal. The independently measured quality factors are shown as blue squares in both graphs and connected by straight lines. In each graph, we use one data point to divide the measured tip amplitude by the quality factor so as to extract the proportionality factor $\frac{F_{\omega_0}}{k}$ between the two. This fixes the relation between the scales on the left and the right coordinate axes in Fig. 6.4.

The tip oscillation amplitude and the cantilever quality factor clearly track each other closely. We have collected similar tip amplitude traces and direct Q measurements on a total of 5 gold nanoparticles that are linked to a CNT. All of them confirm the proportionality between the reduced tip amplitude and the change in the cantilever quality factor.

This measurement verifies the origin of the single-electron charging signal in the top oscillation amplitude experimentally and confirms the validity of Eq. (6.1). In the following two sections we analyze this dissipation signal in the tip amplitude to extract the tunnel coupling between the gold nanoparticle and the CNT quantitatively.

6.5 Electron Tunneling Rate across the Junction

In this section we investigate the information contained in the dissipation signal due to single-electron tunneling. In particular, we extract the tunneling rate Γ of the tunnel junction between the gold nanoparticle and the CNT from the relative change of the tip oscillation amplitude. For the analysis in this section we also

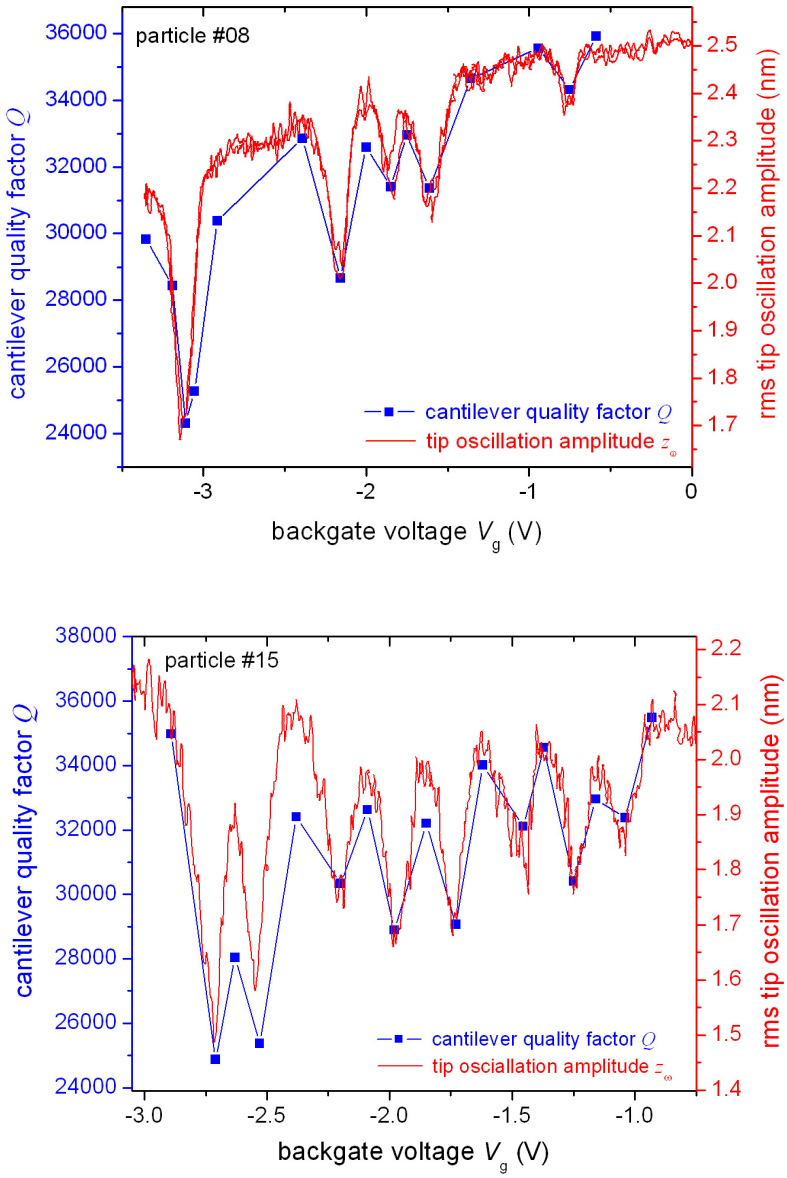

Figure 6.4: Tip oscillation amplitude z_{ω_0} and cantilever quality Q factor in comparison. The data in these two plots was collected on different gold nanoparticles. The quality factor was directly measured from the width of the cantilever resonance curve at each data point. The resonant tip amplitude clearly follows the cantilever quality factor, as predicted by Eq. (6.1).

rely on the capacitive couplings of the gold nanoparticle from Sec. 6.3 and the cantilever parameters as calibrated in Sec. 3.3.

Accounting for the dissipation term $\delta\gamma$ and neglecting the in-phase component of the single-electron force, the relative amplitude change from electron tunneling (2.84) is given by

$$\begin{aligned} \frac{\delta z_{\omega_0}}{z_{\omega_0}} \;\approx\; -\frac{\delta\gamma}{\gamma} \;&=\; \frac{\delta k}{k}\, Q\, \frac{\omega_0}{\Gamma} \\ &=\; \frac{Q}{k}\left(\frac{dq_\mathrm{c}}{dz}\,\frac{e}{C_\mathrm{dot}}\right)^2 f'(\Delta E_\mathrm{dc})\,\frac{\omega_0/\Gamma}{1+(\omega_0/\Gamma)^2}\;, \end{aligned} \tag{6.7}$$

where we used $\delta\gamma$ and δk from Eqs. (2.82) and (2.81). Not surprisingly, the amount of dissipation measured in the tip amplitude is influenced by the following three factors: (1) the intrinsic cantilever parameters k, Q, and ω_0, (2) the electrostatic properties of the gold nanoparticles, which we abbreviate by

$$\delta k^{(\omega_0 \ll \Gamma)} = \left(\frac{dq_\mathrm{c}}{dz}\,\frac{e}{C_\mathrm{dot}}\right)^2 f'(\Delta E_\mathrm{dc})\;, \tag{6.8}$$

and (3) the tunneling rate Γ between the gold nanoparticle and its charge reservoir, the CNT. We evaluate the first two from separate measurements so as to infer the tunneling rate from $\dfrac{\delta z_{\omega_0}}{z_{\omega_0}}$. If we know the cantilever parameters and $\delta k^{(\omega_0 \ll \Gamma)}$, we invert the quadratic equation (6.7) in ω_0/Γ and find

$$\frac{\omega_0}{\Gamma} = \frac{Q}{2c} \pm \sqrt{\left(\frac{Q}{2c}\right)^2 - 1} \;\xrightarrow{Q \gg 2c}\; \left(\frac{Q}{c}\right)^{\pm 1} \quad \text{with } \; c = \frac{\delta z_{\omega_0}/z_{\omega_0}}{\delta k^{(\omega_0 \ll \Gamma)}/k}\;. \tag{6.9}$$

In taking the limit in Eq. (6.9) we caution that the condition $Q \gg 2c$ is not always satisfied; in particular, it is violated near $\omega_0 \approx \Gamma$. The two solutions correspond to the more transparent ($\omega_0 < \Gamma$) and the more opaque ($\omega_0 > \Gamma$) side of tunnel coupling. The dissipation measurement by itself cannot distinguish between the two roots, as illustrated in Fig. 2.9.

As an example, we demonstrate the above procedure on some typical measurements on our gold nanoparticles. For the dissipation in the tip oscillation

Table 6.2: Relative amplitude drop due to single-electron charging of gold nanoparticles on resonance with the CNT. The data from particle #08 is shown in the top graph of Fig. 6.4; data recorded on particle #15 is shown at the bottom.

particle	dip at lowest V_g $\longrightarrow$ dip at highest V_g							
#08	-22%	-14.5%	-7%	-10%	-5%			
#15	-29%	-24%	-14.5%	-17.5%	-16.5%	-10%	-13%	-9.5%

amplitude, we analyze particle #08 and #15 as typical examples, whose data is depicted in Fig. 6.4. Our readout of the relative change on all single-electron charging dips seen in the two plots are listed in Table 6.2. All amplitudes are evaluated at the minimum of each single-electron tunneling dip. We find an average amplitude change of -12% for particle #08 and -17% for particle #15. These values are typical compared to all gold nanoparticles we have measured. Generally, most single-electron charging events of gold nanoparticles that we have observed reduce the amplitude by 10% to 20%. For the remaining analysis we assume a typical amplitude reduction of $\delta z_{\omega_0}/z_{\omega_0} \approx -15\%$.

From the capacitance and gate charge measurements described in Sec. 6.3, we find typically $C_{\mathrm{Au}} \approx 2\,\mathrm{aF}$ and $-dq_c/dz = 0.045\,e/\mathrm{nm}$. To calculate the prefactor $\delta k^{(\omega_0 \ll \Gamma)}$ from Eq. (6.8), we note that at the minimum of any single-electron charging dip the electrochemical potentials of gold nanoparticle and the CNT lead are in resonance at the minimum of each single-electron charging dip, $\Delta E_{\mathrm{dc}} = 0$. Correspondingly, the derivative of the Fermi-Dirac distribution is $f'(0) = \dfrac{-1}{4k_BT}$. With this information we find $\delta k^{(\omega_0 \ll \Gamma)} = -7.8 \times 10^{-5}\,\mathrm{N/m}$ for the electrostatics of our gold nanoparticles. The spring constant k is measured by the cantilever

calibration procedure, as explained in Sec. 3.3, and found to be $k = 2.5\,\mathrm{N/m}$ at $T = 77\,\mathrm{K}$ for the lever used.

All together, we calculate a typical tunnel coupling of $\frac{\omega_0}{\Gamma} = 0.14$ or 7.0 for our gold nanoparticles. From the expression for the tunneling rate in the classical limit, Eq. (2.16), we reexpress the tunnel coupling ω_0/Γ in terms of the tunneling resistance R_T of the tunnel barrier and find $R_T = 31\,\mathrm{G\Omega}$ and $R_T = 1.5\,\mathrm{T\Omega}$ for the transparent ($\omega_0 < \Gamma$) and the opaque ($\omega_0 > \Gamma$) solution, respectively. Unfortunately, the dissipation measurement by itself cannot tell us which of the two tunnel couplings is accurate. For an unambiguous measurement of Γ or R_T, we need to combine the amplitude measurement with frequency shift data. This treatment is discussed in the following section.

Out of curiosity, we evaluate the power that is dissipated by single-electron tunneling from Eq. (2.102) or (2.103),

$$\mathcal{P} = -\frac{1}{2} k z_{\omega_0}^2 \, \frac{\omega_0}{Q} \, \frac{\delta z_{\omega_0}}{z_{\omega_0}} \, . \tag{6.10}$$

From the data of particles #08 and #15 in Fig. 6.4 and Table 6.2 we separately find $\mathcal{P} = 20\,\mathrm{aW}$ for both of them[2]. It is remarkable that such a small energy dissipation is easily resolvable, which underlines the sensitivity of this local force probe technique.

6.6 Combination of Dissipation and Frequency Shift Measurements

The analysis of the tunnel coupling between the gold nanoparticles and the CNT, as presented in the previous section, has a few weaknesses:

[2]The difference in $\delta z_{\omega_0}/z_{\omega_0}$ between the two nanoparticles is compensated for by the different total tip oscillation amplitudes z_{ω_0}, see Fig. 6.4, which enters the expression (6.10) for dissipated power quadratically.

- In order to calculate the tunneling rate Γ from the reduced tip amplitude alone, we rely on separate measurements of the charging energy and gate charge derivative (Sec. 6.3), whose values enter the calculation quadratically, Eq. (6.7).

- The cantilever spring constant k is also needed for the above calculation. Since its value changes with temperature, there is some uncertainty in it.

- The solution for ω_0/Γ is obtained from a quadratic equation, which varies sensitively with the number input near $\omega_0 \approx \Gamma$.

- From the quadratic equation in ω_0/Γ we obtain two roots, and the dissipation signal alone cannot distinguish which one is the correct solution.

In this section we complement the tip amplitude measurements with resonance frequency shift measurements. The combination of both overcomes these problems. We won't introduce frequency shift measurements separately here, as they were discussed extensively on quantum dots in CNTs (Chap. 5). The measurements in this chapter are carried out in just the same way.

The frequency shift measurement overcomes the above problems, because it measures $\delta k/k$ in Eq. (6.7) directly. This measurement contains the quadratic dependence on ω_0/Γ, the capacitive couplings of the quantum dot, and the cantilever spring constant. Combining Eqs. (2.84) and (2.82), we find

$$\frac{\delta z_{\omega_0}}{z_{\omega_0}} = \frac{\delta\omega_0}{\omega_0}\left(2Q\,\frac{\omega_0}{\Gamma} - 1\right) \approx 2Q\,\frac{\delta\omega_0}{\Gamma} \tag{6.11}$$

Clearly, the ratio between the relative change in tip amplitude and cantilever resonance frequency is a direct measure of the tunneling rate of the quantum dot under investigation.

Figure 6.5 shows the amplitude and frequency shift measurement from a gold nanoparticle that is attached to a CNT. The two traces are measured simultaneously. Both the tip oscillation amplitude and the shift of the cantilever resonance frequency show 5 dips over this gate voltage range, corresponding to single-electron charging events of the gold nanoparticle underneath the AFM tip. The dips occur at the same backgate voltages in both traces.

To illustrate the analysis, we readout the relative amplitude change and the frequency shift from the traces in Fig. 6.5, as summarized in Table 6.3. The cantilever resonance frequency during the measurement was $\omega_0/2\pi \approx 61200\,\mathrm{Hz}$, varying quadratically with backgate voltage from 61180 Hz to 61230 Hz over the domain of the graph. The precise cantilever resonance frequency at the single-electron charging dips are also listed in Table 6.3. From these numbers we calculate the tunneling rates of the gold nanoparticle according to Eq. (6.11). The results are shown in the last line of Table 6.3. These tunneling rates correspond to an electron life time of $\tau = 1/\Gamma \approx 1\,\mu\mathrm{s}$ on the gold nanoparticle.

The combined tip amplitude and cantilever frequency shift measurements show unambiguously that $\omega_0 < \Gamma$ in our sample. We feel that the variations of the tunneling rate are larger than the uncertainties in this measurement. Correspondingly, we attribute the fluctuations to actual changes of the tunneling rate from one charging event to another.

Lastly, we compare the values of the tunneling rate obtained in this section, where we combined amplitude and frequency shift measurements, to the ones in the previous section, where we calculated ω_0/Γ from the tip amplitude measurement, the electrostatics of the quantum dot, and the cantilever parameters. From all gold nanoparticles measured in both ways, we consistently derive larger values for

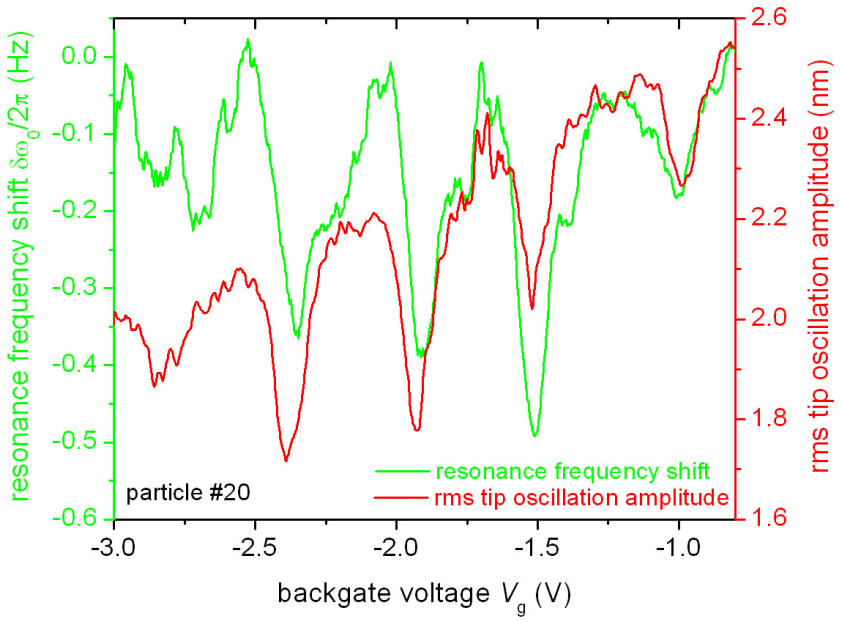

Figure 6.5: Combined amplitude and frequency shift measurement on a gold nanoparticle (particle #20). The tip is biased at $V_{\mathrm{tip}} = 1\,\mathrm{V}$ and resonating at a height of $z_0 = 60\,\mathrm{nm}$ above the gold nanoparticle. The two traces are recorded simultaneously. On the frequency shift trace, the quadratic background has been removed. Over the depicted domain, the cantilever resonance frequency varies monotonically between $\omega_0/2\pi = 61180\,\mathrm{Hz}$ at $V_{\mathrm{g}} = -3\,\mathrm{V}$ and $\omega_0/2\pi = 61230\,\mathrm{Hz}$ at $V_{\mathrm{g}} = -0.8\,\mathrm{V}$. Dips due to single-electron tunneling are clearly visible in both traces and appear well aligned between the two traces.

Table 6.3: Combined dissipation and frequency shift measurement on a gold nanoparticle. The relative amplitude change $\delta z_{\omega_0}/z_{\omega_0}$ and the absolute frequency shift $\delta\omega_0/2\pi$ are obtained from Fig. 6.5. The cantilever resonance frequency $\omega_0/2\pi$ is taken from the quadratic fit that has been subtracted from the measured cantilever resonance frequency to give the frequency shift trace in Fig. 6.5. We assume a quality factor of $Q = 34000$ in the absence of single-electron tunneling, which is a typical value for this cantilever (see Fig. 6.4).

particle #20	dip at lowest V_g	$\longrightarrow$			dip at highest V_g
$\delta z_{\omega_0}/z_{\omega_0}$	-6%	-19%	-20%	-13.5%	-9.5%
$\delta\omega_0/2\pi$	-0.16 Hz	-0.36 Hz	-0.36 Hz	-0.43 Hz	-0.15 Hz
$\omega_0/2\pi$	61186 Hz	61199 Hz	61209 Hz	61218 Hz	61227 Hz
ω_0/Γ	0.34	0.47	0.5	0.29	0.56

ω_0/Γ from the combination of frequency shift and dissipation measurements. A factor of 2 or 3 between the two results is not untypical. At the moment, we are carefully investigating potential sources of systematic error.

As a final remark we note that combined frequency shift and dissipation measurements of single-electron charging are only possible in a certain range of tunnel couplings. While frequency shift measurements show strongest contrast in the transparent coupling regime, $\omega_0 \ll \Gamma$, there is no dissipation signal in this limit, as discussed at the end of Sec. 2.2.3. The strongest dissipation signal is observed at $\omega_0 = \Gamma$, see Eq. (2.102), where the frequency shift has lost already half its contrast. This situation is illustrated in Fig. 2.9. As a necessary (but not sufficient) condition for reasonable contrast in both signal channels, the dissipation in the tip amplitude and the cantilever resonance frequency shift, the tunnel coupling must fall into the regime

$$\omega_0 \leq \Gamma \ll 2Q\omega_0 \; . \tag{6.12}$$

The upper bound is derived in Appendix A.4, Eq. (A.24). Depending also on the operating temperature, the experimentally useful range is even smaller.

6.7 Gold nanoparticles as local potentiometers

The sensitivity of the single-electron tunneling signals to several external parameters suggests that the gold nanoparticles can be used as sensing devices. In this section, we discuss the use of gold nanoparticles as potentiometers on a metallic CNT[3]. By measuring the electrostatic potential of the CNT from several gold

[3]To name another potential sensing application that is not explored in this thesis: Once the charging energy and the gate coupling of a nanoparticle have been extracted (Sec. 6.3), the width of the single-electron charging peak can thereafter serve as a thermometer of the electron temperature in the CNT.

nanoparticles along the length of the tube, we record the voltage profile of a biased CNT. This profile also yields the contact resistance to either lead independently.

The idea of the measurement is to use the the electrochemical potential of the gold nanoparticle to probe the Fermi energy of the CNT. This measurement relies on the linear dependence of the gold nanoparticle's electrochemical potential on the gate voltage, as given in Eq. (2.6). The proportionality constant is easily extracted by a simple calibration procedure, as described below.

We first discuss the measurements necessary to extract the voltage of the CNT at the attachment point of the gold nanoparticle from the single-electron charging signal. Then we apply this sequence to a CNT that makes a loop and crosses itself. This particular sample also permits comparison between the tube-to-tube electron tunneling at the self-crossing point of the CNT and the resistance of the looped section.

Measurement protocol. To measure the voltage drop at a particular location of the CNT, we first take a spatial image of the vicinity and find a gold nanoparticle on the CNT to be used as a potentiometer. Once we have selected a nanoparticle, the experiment proceeds in the following steps:

1. **Reference trace.** After parking the AFM tip at a height z_0 straight above the chosen nanoparticle, we ground the source and drain contact of the CNT, sweep the backgate voltage, and watch the single-electron charging events as dips in the cantilever oscillation amplitude. We select a suitable reference dip and note the location of its minimum as $V_{\mathrm{g}}^{(\mathrm{ref})}$.

2. **Calibration trace.** To calibrate the potentiometer, we raise both contacts, source and drain, to a voltage V_0 above ground (GND), sweep the backgate

voltage again, and record how far the reference dip has moved in backgate voltage. We call the location of its minimum $V_{\mathrm{g}}^{(\mathrm{cal})}$.

3. **Measurement trace.** For the actual measurement of the voltage drop, we leave the source contact at V_0 and ground the drain contact. Now the CNT is biased. We sweep the backgate voltage again and readout the position of the reference charging dip in backgate voltage, $V_{\mathrm{g}}^{(\mathrm{sd})}$.

4. **Consistency trace.** As a consistency test, we ground the source contact and bias the drain contact at V_0. Now the CNT device has the opposite bias. We sweep the backgate voltage and measure location of the reference charging dip one last time, which we call $V_{\mathrm{g}}^{(\mathrm{ds})}$.

We repeat the reference and calibration traces afterwards to guarantee stability. Another spatial image ensures that the tip and the gold nanoparticle are still aligned at the end of the measurement.

Figure 6.6 illustrates the measurement protocol schematically. In the measurement trace (step 3), the voltage of the CNT at the location of the gold nanoparticle attachment is given by

$$V_{\mathrm{CNT-Au}}^{(\mathrm{step\,3})} = V_0 \, \frac{V_{\mathrm{g}}^{(\mathrm{sd})} - V_{\mathrm{g}}^{(\mathrm{ref})}}{V_{\mathrm{g}}^{(\mathrm{cal})} - V_{\mathrm{g}}^{(\mathrm{ref})}} \, . \tag{6.13}$$

Similarly, the voltage of the CNT at the location of the gold nanoparticle attachment during the consistency trace (step 4) is

$$V_{\mathrm{CNT-Au}}^{(\mathrm{step\,4})} = V_0 \, \frac{V_{\mathrm{g}}^{(\mathrm{ds})} - V_{\mathrm{g}}^{(\mathrm{ref})}}{V_{\mathrm{g}}^{(\mathrm{cal})} - V_{\mathrm{g}}^{(\mathrm{ref})}} \, . \tag{6.14}$$

Because of the highly symmetric way of biasing the source and drain contacts in the 4 backgate voltage sweeps, the extracted gate voltages are related by

$$V_{\mathrm{g}}^{(\mathrm{sd})} - V_{\mathrm{g}}^{(\mathrm{ref})} + V_{\mathrm{g}}^{(\mathrm{ds})} - V_{\mathrm{g}}^{(\mathrm{cal})} = 0 \, . \tag{6.15}$$

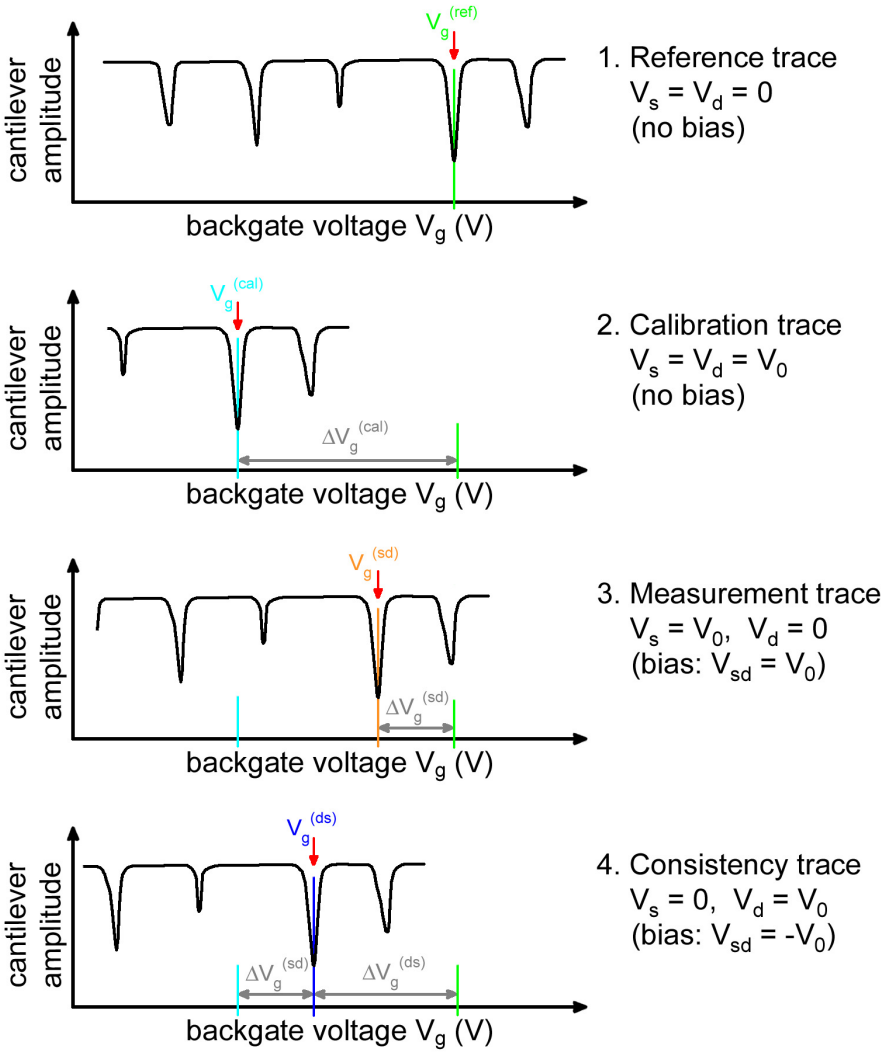

Figure 6.6: Measurement protocol for using gold nanoparticles as potentiometers on the CNT at the location of their attachment. The traces are hand-drawn for illustration and not a result of a measurement. In each trace, the source and drain contacts are biased as noted on the right. As a result, the single-electron charging dips in the cantilever oscillation amplitude are translated horizontally. The charging dip that was selected for the measurement is marked by a red arrow in all 4 traces. By bias symmetry, the translation of the dip in the last trace can be predicted by the previous 3 traces as $\Delta V_g^{(ds)} = \Delta V_g^{(cal)} - \Delta V_g^{(sd)}$, as indicated by the grey arrows and reformulated in Eq. (6.15).

In other words, this relation expresses that the minimum of the charging dip in the measurement trace should be as far away from the minimum in the reference trace as the minimum in the consistency trace is from the minimum in the calibration trace. This is illustrated in the bottom trace of Fig. 6.6. As a result, the information contained in the last trace (step 4) is redundant and serves as a consistency check.

Voltage profile of a looped CNT. We apply the above measurement sequence to several gold nanoparticles along a CNT to map out the voltage profile along the tube. Figure 6.7 (top) shows a topographic AFM image (collected at room temperature) of a CNT that has gold nanoparticles linked to it. The CNT is $35\,\mu$m long and contains a $17\,\mu$m long loop. The overlayed arrows in the image point towards the gold nanoparticles that we use to create a voltage profile. For each gold nanoparticle, we collect the 4 backgate voltage sweeps discussed above. Using Eqs. (6.13) and (6.14), we extract the magnitude of the voltage drop from the CNT at the location of the gold nanoparticle attachment to the respectively grounded lead. We normalize the voltage drop by our bias voltage $V_0 = 200\,\mathrm{mV}$. Figure 6.7 (bottom) shows these normalized voltages plotted as a function of the location of the gold nanoparticle along the CNT. The location of the gold nanoparticle is measured from the topographic AFM image (Fig. 6.7 top) as the length of the CNT section from the nanoparticle to one contact. Measured CNT voltages are shown as black triangle for the measurement trace (step 3) and red squares for the consistency trace (step 4). The two straight lines are fitted to the correspondingly colored data points.

We measure a roughly linear decrease in voltage (from the bias point) with

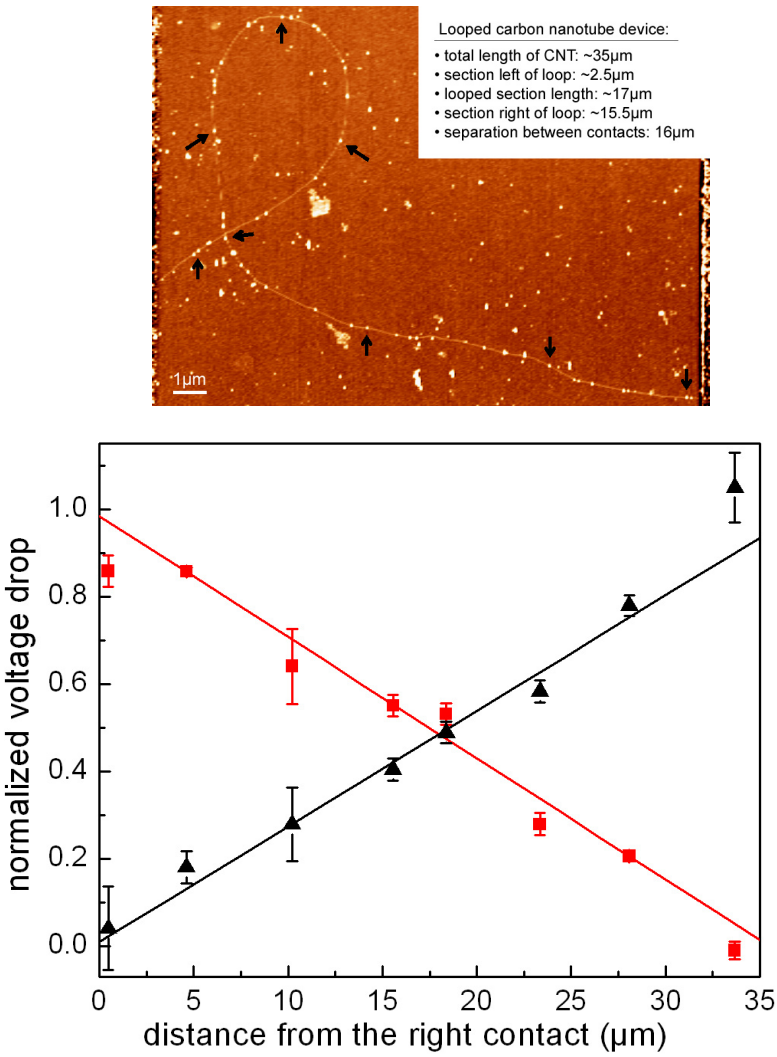

Figure 6.7: Gold nanoparticles as potentiometers on a looped CNT. The arrows in the topographic AFM image (top figure) point towards gold nanoparticles that are used as potentiometers on the CNT to measure the voltage profile (bottom figure). The plotted CNT voltages are normalized by the bias voltage. The black data points show the measured CNT voltage when the left contact is biased and the right contact is grounded. The red data points show the CNT voltage measured at opposite bias, when the right contact is biased and the left contact is grounded. The two lines are fitted to the respectively colored data points.

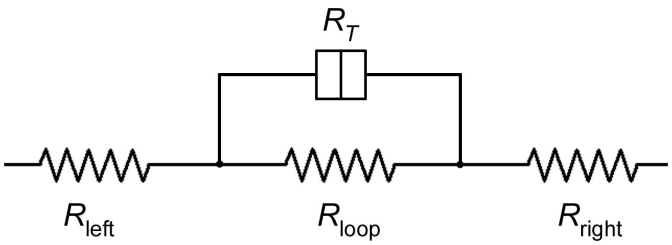

Figure 6.8: Circuit model of a looped CNT. R_{left}, R_{loop}, and R_{right} are the resistances of the respective CNT sections and proportional to the length of the section. R_T is the tunnel resistance of the CNT-CNT junction at the self-contact point.

the length of the tube. Evidently, the CNT is conducing ohmically. This is not surprising given the length of 35μm, which expectedly exceeds the electron mean free path in the CNT at $T = 77\,\text{K}$. Both contact resistances are found to be small compared to the total CNT resistance, as the fitted lines cross the location of the CNT-lead contact points ($x = 0$ and $x = 35\,\mu\text{m}$) close to 0 and 1. We also don't observe significant contributions to the device transport from CNT-CNT tunneling: We model the self-looped CNT by an equivalent circuit shown in Fig. 6.8. The CNT is represented by 3 resistors in series, corresponding to the section between the left contact and the loop, the looped section, and the section between the loop and the right contact. The two contact resistances are not explicitly accounted for in Fig. 6.8, but they are easy to append as an additional resistance on either end of the CNT. The coupling of the CNT to itself at the touching location is included in this model as a tunnel junction. Electron tunneling at the self-contact point of the CNT would bypass the looped section and thereby reduce the effective resistivity of the looped section, as compared to the sections to the left and right of the loop. Since we don't measure a deviation from the straight line along the loop (spanning $x = 15.5\,\mu\text{m}$ to $32.5\,\mu\text{m}$), we conclude that the resistance of the

loop is small compared to the tunnel resistance, $R_{\text{loop}} \ll R_T$.

Other experimental methods have been used to spatially probe the voltage profile of CNTs, including scanning probe techniques. We briefly comment on three: Kelvin Probe Force Microscopy (KFM), Electrostatic Force Microscopy (EFM), and Scanning Voltage Probe Microscopy. In KFM (Nonnenmacher et al. 1991, 1992) the tip bias is adjusted until the tip-sample force is zeroed out. In plotting this tip bias as a function of tip position one obtains a surface potential map. This technique is useful, but can be challenging to implement and operate stably (Jacobs et al. 1999). EFM is technically and operationally easier to perform. As the name suggests, it spatially maps the electrostatic force between the tip and the sample. Extracting voltages quantitatively requires post-processing of images, though, with a separate procedure to remove the background signal (Bachtold et al. 2000). Scanning Voltage Probe (Yaish et al. 2004) employs the AFM tip as movable ohmic probe in a three-terminal transport measurement. It requires physical contact with the device and can be mechanically invasive. Each of these techniques has its own advantages and challenges. The downside of the voltage profile measurement by gold nanoparticle is that it is slow – we collect a spatial image and 4 backgate voltage sweeps for each point along the CNT. It also requires low temperatures for our gold nanoparticles to be in the Coulomb blockade regime. On the bright side, though, it is nice in its simplicity and ease of measurement. The CNT voltage at the location of the nanoparticle is obtained straight-forwardly from the shifts in single-electron charging events without complex data processing. In some sense, the gold nanoparticles are quantum dot probes that are integrated into the CNT sample.

6.8 Conclusions

We have measured single-electron charging of gold nanoparticles that are chemically linked to a CNT by an organic molecule at $T = 77\,\mathrm{K}$. Transport measurements, scanning gate microscopy, and the shape and spatial distribution of the single-electron charging events in spatial images have shown unambiguously that these charging events are not due to quantum dots in the CNT. We have used our LT-AFM to address the gold nanoparticles individually and extracted their electrostatic gate couplings and charging energy. Analyzing the tip oscillation amplitude as a signal channel, we have experimentally verified that it measures the power dissipation associated with single-electron tunneling. We have extracted the tunnel coupling of the gold nanoparticles to the nanotube, both from (1) the electrostatic and the dissipation measurements and (2) the dissipation and frequency shift measurements. Comparing both methods, we have obtained similar, but not identical results. At the end we have demonstrated how the gold nanoparticles can be used as sensing devices to obtain information about the CNT. We have used them as potentiometers on the CNT and measured a voltage profile of a looped CNT, where we have found a roughly linear increase in the voltage drop from the biased contact, small contact resistance on both ends of the nanotube, and negligible tube-to-tube tunneling at the self-contact point in comparison to the resistance of the $17\,\mu\mathrm{m}$ long CNT loop at $T = 77\,\mathrm{K}$.

The combination of dissipation and frequency shift measurements has proven very fruitful. The two signals are in many ways complementary, as they relate to the out-of-phase and in-phase component of the single-electron tunneling force (2.79). As a result, we have been able to characterize the static properties of the quantum dots and the dynamic process of electron tunneling.

From a broader viewpoint, all these measurements have demonstrated the utility of our local force probe technique on a sample in a single-contact geometry. The need for only one charge reservoir makes this kind of measurement interesting for many other nanoscale samples. In fact, most non-designed nanoscale structures would benefit from the local nature of our measurement, combined with the spatial resolution of the AFM.

CHAPTER 7

CONCLUSIONS

We have measured Coulomb blockade phenomena and single-electron charging effects by low-temperature scanning force microscopy in two samples: Long semiconducting carbon nanotubes and gold nanoparticles attached to a carbon nanotube by an organic linker molecule.

We have observed disorder-induced quantum dots along long semiconducting carbon nanotubes at low carrier density. Addressing these quantum dots spatially one by one using the force microscope, we have characterized their electrostatic properties, including their gate couplings, charging energy, and interdot coupling. Resolving spatially how charge is induced on the nanotube by a gate, we have observed an imprint of the carbon nanotube's band structure on our single-electron charge addition spectra and drawn conclusions about the underlying disorder potential.

In our gold nanoparticle sample, we have combined frequency shift and dissipation measurements of our local force probe and thereby accessed the in-phase and the out-of-phase component of the single-electron tunneling force. Beyond the electrostatic properties of the gold nanoparticles, this combination has allow us to extract their tunnel coupling to the carbon nanotube. We have also demonstrated how the gold linked nanoparticles can be used as potentiometer on the carbon nanotube and measured the voltage profile of a carbon nanotube with a loop.

The success of the the scanning probe measurements presented and the large amount of information inferred about our nanoscale samples points towards many exciting opportunities for the technique.

Many nanoscale samples would benefit from the simplicity of the single-contact geometry in our measurement. An simple extension of our gold nanoparticle experiments is to reduce the quantum dot size further, for example, with a single-molecule metal coordination complex. At this size scale, the charging energy may be large enough so that the measurement could even become room-temperature compatible.

The idea of imaging the electron density within a quantum dot has been discussion for a while. Even thoughts of locally perturbing the electron wavefunction in a few-electron quantum dot and spatially resolving its consequences, such as a change in the probability distribution, have been brought forward. This proposal is interesting, and our force probe scheme – being truly local – would have much to contribute. At the same time, the requirements on the instrument sensitivity, resolution, and stability are beyond our team's current capabilities.

While scanning gate measurements require device conduction and frequency shift measurements are most suitable for quantum dots with fast tunneling, dissipation measurements extend much further into the resistive regime and might give a better direct view into charge motion in poor conductors, such as some organic or biomolecules.

New materials could also profit from the versatility and spatial resolution of the AFM. For example, resolving magnetotransport in single sheets (or very thin layers) of graphite, where the biased AFM tip can also be used to locally perturb the system, would be an interesting project.

APPENDIX A

EXTENDED ANALYSES, DERIVATIONS, AND CALCULATION DETAILS

A.1 Mutual Capacitance of Coupled Quantum Dots

In this section, we derive the relation between the mutual capacitance of two coupled quantum dots and the total dot capacitances, Eq. (5.9). This equation was used to extract interdot gating efficiencies from the coupled dot spectra assuming weak tunnel coupling. We restrict ourselves to the classical limit, $k_B T \gg \Delta E_{\mathrm{level}}$, where the density of single-particle states of the dots is continuous.

The electrochemical potentials of the two coupled (classical) dots in the presence of the extended backgate is given by

$$\begin{aligned}
\mu_1(N_1, N_2, V_{\mathrm{g}}) &= \left(N_1 - \frac{1}{2}\right) E_{C_1} + N_2\, E_{C_{\mathrm{m}}} - \frac{V_{\mathrm{g}}}{e}\left(C_{\mathrm{gd1}}\, E_{C_1} + C_{\mathrm{gd2}}\, E_{C_{\mathrm{m}}}\right) \\
\mu_2(N_1, N_2, V_{\mathrm{g}}) &= \left(N_2 - \frac{1}{2}\right) E_{C_2} + N_1\, E_{C_{\mathrm{m}}} - \frac{V_{\mathrm{g}}}{e}\left(C_{\mathrm{gd2}}\, E_{C_2} + C_{\mathrm{gd1}}\, E_{C_{\mathrm{m}}}\right) \ ,
\end{aligned} \tag{A.1}$$

where N_1 and N_2 are the number of electrons on dot #1 and dot #2, respectively. The backgate is biased at a voltage V_{g}, which couples to the dots by the backgate-dot capacitances C_{gd1} and C_{gd2}. The interdot coupling capacitance of the tunnel barrier between the two dots is C_{m}. E_{C_1} and E_{C_2} are the charging energies of dot #1 and #2, respectively. $E_{C_{\mathrm{m}}}$ is the so-called electrostatic coupling energy of the two dots.

A derivation of the electrochemical potentials can be found in the literature (Ruzin et al. 1992, Dixon 1998, van der Wiel et al. 2003). Note that we use a single extended gate that couples to both dots simultaneously; so we simplified $V_{\mathrm{g1}} = V_{\mathrm{g2}} \equiv V_{\mathrm{g}}$ in (van der Wiel et al. 2003, Eqs. (5) and (6)). The charging

energies of the two dots are given by

$$E_{C_1} = \frac{e^2}{C_1}\left(\frac{1}{1-\frac{C_{\rm m}^2}{C_1\,C_2}}\right) \qquad \text{and} \qquad E_{C_2} = \frac{e^2}{C_2}\left(\frac{1}{1-\frac{C_{\rm m}^2}{C_1\,C_2}}\right)\,, \tag{A.2}$$

where we used the shorthand notation $C_1 = C_{\rm dot\,\#1}$ and $C_2 = C_{\rm dot\,\#2}$ for the total dot capacitances. The electrostatic coupling energy is given by

$$E_{C_{\rm m}} = \frac{e^2}{C_{\rm m}}\left(\frac{1}{\frac{C_1\,C_2}{C_{\rm m}^2}-1}\right) = \frac{e^2}{C_1\,C_2}\,C_{\rm m}\left(\frac{1}{1-\frac{C_{\rm m}^2}{C_1\,C_2}}\right)\,. \tag{A.3}$$

The quantities $\Delta V_{\rm g1}$, $\Delta V_{\rm g2}$ and $\Delta V_{\rm g1}^{\rm (m)}$, $\Delta V_{\rm g2}^{\rm (m)}$ as described in Fig. 5.24(b) are defined by the equations

$$\begin{aligned}
&\text{(1a)} \qquad \mu_1(N_1,N_2,V_{\rm g}) = \mu_1(N_1{+}1,N_2,V_{\rm g}{+}\Delta V_{\rm g1})\\
&\text{(1b)} \qquad \mu_1(N_1,N_2,V_{\rm g}) = \mu_1(N_1,N_2{+}1,V_{\rm g}{+}\Delta V_{\rm g1}^{\rm (m)})\\
&\text{(2a)} \qquad \mu_2(N_1,N_2,V_{\rm g}) = \mu_2(N_1,N_2{+}1,V_{\rm g}{+}\Delta V_{\rm g2})\\
&\text{(2b)} \qquad \mu_2(N_1,N_2,V_{\rm g}) = \mu_2(N_1{+}1,N_2,V_{\rm g}{+}\Delta V_{\rm g2}^{\rm (m)})\,.
\end{aligned} \tag{A.4}$$

Using the expressions for the electrochemical potentials, Eq. (A.1), these definitions are rewritten as

$$\begin{aligned}
&\text{(1a)} \qquad E_{C_1} = \tfrac{1}{e}\,\Delta V_{\rm g1}\,(C_{\rm gd1}\,E_{C_1} + C_{\rm gd2}\,E_{C_{\rm m}})\\
&\text{(1b)} \qquad E_{C_{\rm m}} = \tfrac{1}{e}\,\Delta V_{\rm g1}^{\rm (m)}\,(C_{\rm gd1}\,E_{C_1} + C_{\rm gd2}\,E_{C_{\rm m}})\\
&\text{(2a)} \qquad E_{C_2} = \tfrac{1}{e}\Delta V_{\rm g2}\,(C_{\rm gd2}\,E_{C_2} + C_{\rm gd1}\,E_{C_{\rm m}})\\
&\text{(2b)} \qquad E_{C_{\rm m}} = \tfrac{1}{e}\,\Delta V_{\rm g2}^{\rm (m)}\,(C_{\rm gd2}\,E_{C_2} + C_{\rm gd1}\,E_{C_{\rm m}})\,.
\end{aligned} \tag{A.5}$$

Notice that the terms in parentheses are identical in lines (1a) and (1b); the same is true for lines (2a) and (2b). Taking the ratio of each pair of equations gives

$$E_{C_{\rm m}} = \frac{\Delta V_{\rm g1}^{\rm (m)}}{\Delta V_{\rm g1}}\,E_{C_1} = \frac{\Delta V_{\rm g2}^{\rm (m)}}{\Delta V_{\rm g2}}\,E_{C_2}\,. \tag{A.6}$$

Using the expressions for the charging energies, Eq. (A.2), and the electrostatic coupling energy, Eq. (A.3), in Eq. (A.6) gives the relation between the mutual and

the total dot capacitances

$$C_{\mathrm{m}} = \frac{\Delta V_{\mathrm{g1}}^{(\mathrm{m})}}{\Delta V_{\mathrm{g1}}}\, C_2 = \frac{\Delta V_{\mathrm{g2}}^{(\mathrm{m})}}{\Delta V_{\mathrm{g2}}}\, C_1 \ . \tag{A.7}$$

The above derivation is also valid in the presence of the AFM tip as an additional gate, as depicted in Fig. 5.23. Formally, the electrochemical potentials of the quantum dots (A.1) have two additional terms due to the tip (from direct and indirect gating). But all 4 relevant quantities ΔV_{g1}, ΔV_{g2}, $\Delta V_{\mathrm{g1}}^{(\mathrm{m})}$, and $\Delta V_{\mathrm{g2}}^{(\mathrm{m})}$ for the analysis are pure backgate voltage differences, each read out at a fixed tip location (parallel to the y-axis in the spectrum) and at the same tip voltage. Under these conditions, the tip contribution to the electrochemical potentials is the same on the left and right hand side in all Eqs. (A.4). Consequently, Eqs. (A.5) remain as stated in the presence of the tip, and all results are preserved[1].

[1] A more subtle requirement for the claim that the above derivation remains unchanged in the presence of the tip is that the backgate-dot capacitances C_{gd1} and C_{gd2} must be independent of the tip location. In fact, the backgate-dot capacitances do have a weak dependence on the tip-dot separation, which can become appreciable as the tip height is reduced. Within our CNT spectra, which are collected at a constant tip height of typically $z_0 \approx 100\,\mathrm{nm}$ above the substrate, we find that this effect is negligible. Furthermore, we extract the 4 backgate voltage differences from the spectra at the same tip position or at least in close proximity, within a narrow band of tip positions.

A.2 Density of States and Carrier Density of Carbon Nanotube Bands

In this section, we take another look at the density of states of semiconducting CNTs and provide an alternative derivation of the relation between the carrier density on a CNT and the energy of the highest filled single-particle state, Eq. 5.7. To put everything into context, we start with the general framework that applies to all crystalline solids, before we evaluate the relations specific to CNTs.

In general, the density of states $D(E)$ can have contributions from multiple bands, which add cumulatively,

$$D(E) = \sum_m D_m(E) \; . \tag{A.8}$$

Here m is an index that labels the contributions from the different bands. The density of states of a band $D_m(E)$ depends on the band's dispersion relation $E_m(k)$ and the dimensionality d of the system. Since the density of states is an extensive quantity, it is commonly normalized by the system volume,

$$D_m(E) = \; (\#\text{degeneracies}) \int\limits_{\text{FBZ}} \frac{d^d k}{(2\pi)^d} \, \delta(E - E_m(\vec{k})) \; . \tag{A.9}$$

The integral extends over the first Brillouin zone (FBZ) of the crystal lattice. The spin-degeneracy of electronic states is the most typical degeneracy included in the prefactor. In semiconducting CNTs, all bands are 4-fold degenerate (from spin- and 2-fold orbital degeneracy). With our normalization, the number density of carriers n is related to the density of states by

$$n = \int\limits_{-\infty}^{\infty} dE \, D(E) \, f(E) \quad \xrightarrow{T \to 0} \quad \int\limits_{-\infty}^{E_F} dE \, D(E) \; , \tag{A.10}$$

where E_F is the electrochemical potential of the system and f is the Fermi-Dirac distribution. The contribution from any given band is isolated by replacing the density of states under the integral by the density of states of that band.

At low excitation energies, the density of states of the CNT bands that contribute to conduction is universally given by (Mintmire and White 1998, White and Mintmire 2005)[2]

$$D_m^{(\mathrm{CNT})}(E) = \begin{cases} \dfrac{16}{3\pi}\dfrac{1}{d_{\mathrm{CNT}}}\dfrac{1}{E_{\mathrm{gap}}}\sqrt{\dfrac{E^2}{E^2-(\frac{1}{2}E_{\mathrm{gap}}^{(m)})^2}} & \text{if} \quad |E| > \frac{1}{2}E_{\mathrm{gap}}^{(m)} \\ 0 & \text{otherwise.} \end{cases} \tag{A.11}$$

d_{CNT} denotes the diameter of the CNT. For semiconducting CNTs, E_{gap} is the band gap of the tube and $E_{\mathrm{gap}}^{(m)} = |3m{+}1|\, E_{\mathrm{gap}}$ the energy gap of the subband with index m. The energy is fixed such that $E = 0$ is in the middle of the band gap. At $E > \frac{1}{2}E_{\mathrm{gap}}^{(m)}$ is the conduction subband, at $E < -\frac{1}{2}E_{\mathrm{gap}}^{(m)}$ the valence subband. The band index $m \in \{0, \pm1, \pm2, \pm3, ...\}$ can be any integer. $m = 0$ gives the lowest subband and the band gap of the semiconducting tube, $E_{\mathrm{gap}} = E_{\mathrm{gap}}^{(m=0)}$. The electron density in the conduction band of this 1st subband is

$$n_{\mathrm{scCNT},\,e^-}^{(m=0)} = \frac{16}{3\pi}\frac{1}{d_{\mathrm{CNT}}}\sqrt{\frac{E_F^2-(\frac{1}{2}E_{\mathrm{gap}})^2}{E_{\mathrm{gap}}^2}} \qquad \text{for} \quad E_F \geq \tfrac{1}{2}E_{\mathrm{gap}}\,. \tag{A.12}$$

When the CNT's electrochemical potential is near the band edge, $E_F \approx \frac{1}{2}E_{\mathrm{gap}}$, we can approximate $E_F^2 - (\frac{1}{2}E_{\mathrm{gap}})^2 = (E_F - \frac{1}{2}E_{\mathrm{gap}})(E_F + \frac{1}{2}E_{\mathrm{gap}}) \approx (E_F - \frac{1}{2}E_{\mathrm{gap}})E_{\mathrm{gap}}$ to simplify the term under the square root,

$$n_{\mathrm{scCNT},\,e^-}^{(m=0)} = \frac{16}{3\pi}\frac{1}{d_{\mathrm{CNT}}}\sqrt{\frac{E_F-\frac{1}{2}E_{\mathrm{gap}}}{E_{\mathrm{gap}}}} \qquad \text{for} \quad E_F \gtrapprox \tfrac{1}{2}E_{\mathrm{gap}}\,. \tag{A.13}$$

In this regime of low carrier density, we reproduce the free electron approximation, as used in Eq. 5.7,

$$n_{\mathrm{1D}} = \frac{4}{\pi\hbar}\sqrt{2m^*(E_F - E_0)}\,, \tag{A.14}$$

[2]In contrast to our definition in Eq. (A.9), Mintmire and White normalize the density of states by the volume of the first Brillouin zone. In 1D we return to our normalization by multiplying their expression for the density of states by the factor $\ell_{\mathrm{FBZ}}/2\pi$. For CNTs, the first Brillouin zone has a volume $\ell_{\mathrm{FBZ}} = \frac{4\pi^2}{3\sqrt{3}}\, d_{\mathrm{CNT}}/a_{\mathrm{C-C}}^2$.

where we used the common free electron notation: m^* is the effective mass of electrons in the CNT, and E_0 is the energy of the conduction band bottom (if $E = 0$ goes through the middle of the band gap, then $E_0 = \frac{1}{2}E_{\text{gap}}$).

The band gap of a semiconducting CNT is inversely proportional to the nanotube diameter d_{CNT} (White et al. 1993, Dresselhaus et al. 1996) as

$$E_{\text{gap}} = 2\,V_{pp\pi}\,\frac{a_{\text{C-C}}}{d_{\text{CNT}}} = \frac{4\hbar v_F}{3d_{\text{CNT}}} \approx \frac{0.72\,\text{eV}\cdot\text{nm}}{d_{\text{CNT}}}\,, \tag{A.15}$$

where $V_{pp\pi} \approx 2.5\,\text{eV}$ is the tight-binding interaction integral (also called Slater-Koster parameter) between the unsaturated p-orbitals from nearest neighbor carbon atoms[3] that form the delocalized π-bonds, along which conduction occurs. $a_{\text{C-C}} \approx 0.144\,\text{nm}$ is the covalent bond length between two carbon atoms. For our $d_{\text{CNT}} = 1.4\,\text{nm}$ semiconducting CNT we predict a band gap of $E_{\text{gap}} = 0.51\,\text{eV}$. The magnitude of the Fermi velocity v_F of carriers in a CNT is given by (White and Mintmire 2005)

$$v_F = \frac{3}{2\hbar}\,V_{pp\pi}\,a_{\text{C-C}} \approx 8.2\times10^5\,\text{m/s}\,. \tag{A.16}$$

The effective mass or band mass of the low-energy charge carriers in a semiconducting CNT, as derived in Eq. (5.6), is given by

$$m^* = \frac{E_{\text{gap}}}{2v_F^2} = \frac{2\hbar}{3v_F\,d_{\text{CNT}}} \approx \frac{0.094\,m_e}{d_{\text{CNT}}/\text{nm}}\,. \tag{A.17}$$

For our semiconducting CNT of $d_{\text{CNT}} = 1.4\,\text{nm}$, we predict an effective electron mass of $m^* = 0.067\,m_e$.

[3]In the graphite community, this tight-binding interaction integral is typically denoted by γ_0 and has a slightly larger value, $\gamma_0 = 3.13\,\text{eV}$. Its value for CNTs varies among publications, typically in the range of $2.4 - 2.8\,\text{eV}$.

A.3 Charging Energy from Frequency Shift on Non-Transparent Dots

In this section we explore the effects of a finite tunneling rate Γ of a quantum dot on the calculation of the charging energy, when it is derived from the amount of cantilever frequency shift due to single-electron tunneling. This analysis was already done for transparent quantum dots in Sec. 5.8, which resulted in Eq. (5.14). For the sake of completeness of the introduced method, we extend the analysis to non-transparent quantum dots here and discuss corrections to Eq. (5.14) that arise from a non-zero electron life time $\tau \propto 1/\Gamma$ on the quantum dot.

Restating our starting point for extracting the charging energy E_C, the relative shift of the cantilever resonance frequency due to single-electron tunneling was given by

$$\frac{\delta\omega_0}{\omega_0} = \frac{1}{2k}\left(\frac{dq_\mathrm{c}}{dz}\,\frac{e}{C_\mathrm{dot}}\right)^2 \frac{f'(\Delta E_\mathrm{dc})}{1+(\omega/\Gamma)^2}\,. \tag{A.18}$$

The difference between quantum dots in the classical and the quantum limit is encoded in the tunneling rate Γ, as given in Tab. 2.1. This relation was derived in the theory chapter in Sec. 2.2.2. In the non-transparent case, $\omega \not\ll \Gamma$, where electrons have a non-zero life time on the quantum dot and don't tunnel instantly on the time scale of the driving frequency, the factor $\dfrac{1}{1+(\omega/\Gamma)^2}$ in Eq. A.18 becomes relevant. The calculation that accounts for its influence is different in the quantum and classical limit (due to the different gate dependencies of the tunneling rates Γ, see Tab. 2.1), so we treat them separately below.

Quantum limit, $\Delta E_\mathrm{level} \gg k_B T$. In the quantum limit, the correction to the charging energy (5.14) due to a finite tunneling rate are straight-forward, as Γ is a constant that is set by the properties of the tunnel barrier and independent of the applied gate voltage. In comparison to our previous analysis in Sec. 5.8, we

retain the constant factor $\dfrac{1}{1+(\omega/\Gamma_{\rm qdot})^2}$ on the right-hand side of Eq. (5.13). The analysis proceeds exactly as outlined in Sec. 5.8, resulting in

$$\frac{E_C}{1+(\omega/\Gamma_{\rm qdot})^2} = -2k\left(\frac{dq_c}{dz}\right)^{-2} eC_{\rm gd}\int\limits_{-\infty}^{\infty}\frac{\delta\omega_0}{\omega_0}\,dV_{\rm g} \tag{A.19}$$

instead of Eq. (5.14). Clearly, the true charging energy is larger than the one calculated from Eq. (5.14) if the tunneling rate of the quantum dot does not exceed the cantilever resonance frequency significantly.

Classical limit, $\Delta E_{\rm level} \ll k_B T$. In the classical limit, the calculation away from the transparent limit is slightly more involved, as Γ is a function of the alignment between the electrochemical potentials of the quantum dot and the charge reservoir, $\Delta E_{\rm dc}$. Since $\Gamma = \tilde{g}_{\rm dc}\,\Gamma_{\rm cdot}$ varies with backgate voltage, the peak shape of the single-electron tunneling dip is modified compared to its shape in the transparent limit (and the quantum limit), which is described by the derivative of the Fermi-Dirac distribution alone. In this case we have to redo the integration over backgate voltages in order to obtain the area in the frequency shift dips, Eq. (5.13). Numerical integration allows us to calculate the correction factor $\displaystyle\int\limits_{-\infty}^{\infty}\frac{-f'(\Delta E_{\rm dc})}{1+(\omega/\tilde{g}_{\rm dc}\Gamma_{\rm cdot})^2}\,d(\Delta E_{\rm dc})$, at different tunneling rates of the dot. This correction factor needs to be multiplied to the right-hand side of Eq. (5.13) and the left-hand sides of Eq. (5.14),

$$E_C\int\limits_{-\infty}^{\infty}\frac{-f'(\Delta E_{\rm dc})}{1+(\omega/\tilde{g}_{\rm dc}\Gamma_{\rm cdot})^2}\,d(\Delta E_{\rm dc}) = -2k\left(\frac{dq_c}{dz}\right)^{-2} eC_{\rm gd}\int\limits_{-\infty}^{\infty}\frac{\delta\omega_0}{\omega_0}\,dV_{\rm g}\,. \tag{A.20}$$

Both correction factors, applicable to the classical and the quantum limit, are plotted in Fig. A.1 as a function of the ratio of the driving frequency to the tunneling rate, ω/Γ. In our experiments, the driving frequency is fixed at the cantilever resonance frequency, $\omega = \omega_0$.

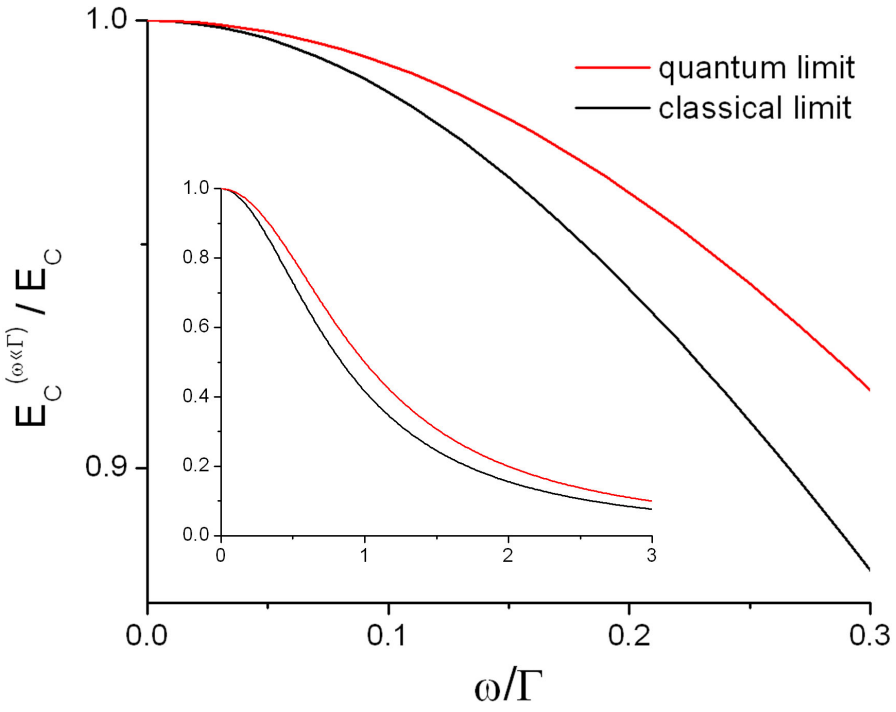

Figure A.1: Corrections to the charging energy due to a finite tunneling rate Γ of a quantum dot. The correction factor plotted along the y-axis gives the ratio of the charging energy when calculated assuming the transparent limit ($\omega \ll \Gamma$) to the actual charging energy, $\dfrac{E_C^{(\omega\ll\Gamma)}}{E_C}$. Consequently, the charging energy obtained from Eq. (5.14) needs to be divided by this factor in order to account for a finite tunneling rate. In the quantum limit, $\Delta E_{\rm level} \gg k_B T$, the correction factor is given by $\dfrac{1}{1+(\omega/\Gamma_{\rm qdot})^2}$. In the classical limit, $\Delta E_{\rm level} \ll k_B T$, the correction factor departs from 1 slightly sooner. Its value is given by $\displaystyle\int_{-\infty}^{\infty} \frac{-f'(\Delta E_{\rm dc})}{1+(\omega/\tilde{g}_{\rm dc}\Gamma_{\rm cdot})^2}\, d(\Delta E_{\rm dc})$, where $\tilde{g}_{\rm dc} = \dfrac{1}{2}\dfrac{\Delta E_{\rm dc}}{k_B T} \coth\left(\dfrac{1}{2}\dfrac{\Delta E_{\rm dc}}{k_B T}\right)$ is the dimensionless parameter defined in Eq. (2.73). In either limit, Eq. (5.14) underestimates the true charging energy if electrons don't tunnel on and off the dot instantaneously. The inset plot shows the correction factors over a larger domain of ω/Γ.

A.4 Effects of single-electron tunneling on the tip amplitude

This section of the appendix revisits the tip oscillation amplitude and its change due to single-electron tunneling with a more detailed theoretical analysis. In Sec. 6.4 we validated experimentally that the tip amplitude change during single-electron charging events of our gold nanoparticles linked to a CNT is due to dissipation in the electron tunneling process. As evaluated in Eq. (2.84), though, the tip amplitude is also affected by the in-phase component of the single-electron tunneling force (2.79), which we neglected previously based on the experimental evidence. In this section we sketch a more theoretically minded approach to the tip oscillation amplitude, where we include the (small) in-phase component in all expressions.

Restating Eq. (2.43), the tip oscillation amplitude at the cantilever resonance frequency ω_0 is given by

$$z_{\omega_0} = \frac{F_{\omega_0}}{k}\, Q = \frac{F_{\omega_0}}{\gamma\omega_0}\,, \tag{A.21}$$

where F_{ω_0} is the amplitude of the resonant ac-driving force, k is the cantilever spring constant, γ is the damping coefficient of the cantilever, and Q its quality factor. When the cantilever is driven with a constant ac-force amplitude, $F_{\omega_0} =$ const, any change in the tip amplitude correlates with a resonance frequency shift $\delta\omega_0$ or some additional energy dissipation mechanism $\delta\gamma$,

$$\frac{\delta z_{\omega_0}}{z_{\omega_0}} = -\frac{\delta\gamma}{\gamma} - \frac{\delta\omega_0}{\omega_0}\,. \tag{A.22}$$

The single-electron tunneling force (2.79) and (2.80) can cause both, a resonance frequency shift and increased dissipation, as given in Eq. (2.82). The dissipation term $\delta\gamma$ is solely due to the out-of-phase component of the single-electron force, and the resonance frequency shift $\delta\omega_0$ is only due to its in-phase compo-

nent. Rephrasing Eq. (2.82), which relates both components to the change in the cantilever spring constant,

$$\frac{\delta\omega_0}{\omega_0} = \frac{\delta k}{2k} \qquad \text{and} \qquad \frac{\delta\gamma}{\gamma} = -\frac{\delta k}{k}\, Q\, \frac{\omega_0}{\Gamma}\,, \tag{A.23}$$

we realize that the two contributions have opposite sign[4]. As can be verified from Eq. (2.81), the change in spring constant due to single-electron tunneling is always negative, $\delta k \leq 0$. This reduces the cantilever resonance frequency, $\delta\omega_0 \leq 0$, as observed in Chap. 5, and increases the energy dissipation, $\delta\gamma \geq 0$. Experimentally, we find that the tip oscillation amplitude (at constant ac-driving force) is reduced during single-electron tunneling, which provides theoretical evidence that the tip amplitude resolves energy dissipation in the single-electron charging process.

We quickly evaluate numerically how large the in-phase contribution to our tip amplitude is expected to be on the gold nanoparticles in Chap. 6. A back-of-the-envelope estimate of the resonance frequency shift due to single-electron tunneling, Eq. (5.1), using $-\dfrac{dq_\mathrm{c}}{dz} \approx \dfrac{dC_\mathrm{td}}{dz}\, V_\mathrm{tip} \approx \epsilon_0\, V_\mathrm{tip}$, $C_\mathrm{dot} \approx 2\,\mathrm{aF}$, $\omega = \omega_0 \approx \Gamma$, and $f'(0) = \dfrac{-1}{4k_B T}$, predicts $\dfrac{\delta\omega_0}{\omega_0} \approx -10^{-5}$ for gold nanoparticles at $T = 77\,\mathrm{K}$. This change can be resolved in a resonance frequency measurement, but is impossible to observe in our oscillation amplitude measurement. In fact, under typical operational conditions, this amplitude change is $\delta z_{\omega_0} < 1\,\mathrm{pm}$ and below the thermal noise level even at the base temperature of our cryostat, $T = 0.3\,\mathrm{K}$. Consequently, we are unable to measure the in-phase contribution of the single-electron force in the tip amplitude.

The fact that we do observe the energy dissipation due to single-electron charging has already consequences on the tunneling rate Γ. In a fully transparent quantum dot, $\Gamma \to \infty$, electrons tunnel instantly as soon as it is energetically favorable,

[4]The constants in both expressions, $\{k,\, \omega_0,\, \gamma,\, Q,\, \Gamma,\, z_{\omega_0},\, F_{\omega_0}\}$, are all positive.

and no energy is dissipated, as seen in Fig. 2.9. This realization is implicitly already expressed in the above discussion, and we make it explicit here. Since the in-phase and out-of-phase component of the tunneling force affect the oscillation amplitude with opposite sign, the magnitude of the dissipation term due to single-electron tunneling must far exceed the corresponding magnitude of the frequency shift term to be able to reduce the tip's oscillation amplitude measurably. By Eqs. (A.22) and (A.23), this requires

$$\frac{\delta\gamma}{\gamma} \gg -\frac{\delta\omega_0}{\omega_0} \qquad \Leftrightarrow \qquad \frac{\omega_0}{\Gamma} \gg \frac{1}{2Q} \tag{A.24}$$

as a necessary condition for observing energy dissipation due to single-electron tunneling in the amplitude signal. We check this relation on our measured data in Chap. 6 and find it well obeyed, $2Q\omega_0/\Gamma \approx 10^4 \gg 1$.

An alternative quantity that is related to dissipation is the cantilever quality factor $Q = m\omega_0/\gamma$. Its reciprocal measures the relative energy loss per oscillation cycle and thereby has a contribution from the in-phase and out-of-phase component of the single-electron tunneling force[5],

$$\frac{\delta Q}{Q} = -\frac{\delta\gamma}{\gamma} + \frac{\delta\omega_0}{\omega_0} \, . \tag{A.25}$$

Under the condition discussed above, Eq. (A.24), the change in the cantilever quality factor due to single-electron tunneling is dominated by the dissipation term. This implies that the reduction in the amplitude measurement is directly proportional to the change in quality factor,

$$\delta z_{\omega_0} \xrightarrow{\Gamma \ll 2Q\omega_0} \frac{F_{\omega_0}}{k} \, \delta Q \, . \tag{A.26}$$

[5]The in-phase component of the single-electron force reduces the total energy stored in the cantilever; the out-of-phase component increases the amount of energy dissipated. The cantilever quality factor, which measures their ratio (up to a factor of 2π), is modified by both, as expressed in Eq. (A.25).

In other words, the change in tip oscillation amplitude is a direct measure of the modification of the quality factor. This explains theoretically our observation in Sec. 6.4 and derives Eq. (6.1). This relation provides a convenient means of measuring the additional energy dissipation due to single-electron tunneling.

Even though the in-phase component has only negligible effect on the tip amplitude in our experiments on the gold nanoparticles, we provide a set of exact equations below. Summarizing Eqs. (A.22) and (A.23), the relative change of the tip oscillation amplitude due to single-electron tunneling is given by

$$\begin{aligned} \frac{\delta z_{\omega_0}}{z_{\omega_0}} &= \frac{\delta k}{k}\left(Q\frac{\omega_0}{\Gamma}-\frac{1}{2}\right) \\ &= \frac{1}{k}\left(\frac{dq_c}{dz}\,\frac{e}{C_{\rm dot}}\right)^2 \frac{f'(\Delta E_{\rm dc})}{1+(\omega_0/\Gamma)^2}\left(Q\frac{\omega_0}{\Gamma}-\frac{1}{2}\right)\,, \end{aligned} \tag{A.27}$$

where δk is given in Eq. (2.81). In the limit (A.24), this relation reduces to Eq. (6.7) as used in Sec. 6.5. In solving the quadratic equation (A.27) for ω_0/Γ, we find

$$\frac{\omega_0}{\Gamma} = \frac{Q}{2c} \pm \sqrt{\left(\frac{Q}{2c}\right)^2 - 1 - \frac{1}{2c}} \xrightarrow{Q\gg 2c\gg 1} \left(\frac{Q}{c}\right)^{\pm 1} \quad \text{with} \;\; c = \frac{\delta z_{\omega_0}/z_{\omega_0}}{\delta k^{(\omega_0\ll\Gamma)}/k}\,. \tag{A.28}$$

The quantity $\delta k^{(\omega_0\ll\Gamma)}$ is defined in Eq. (6.8). The in-phase component of the single-electron force makes the term $\dfrac{1}{2c}$ appear under the square root, as seen in comparison to Eq. (6.9). While the condition $2c \gg 1$ is always fulfilled experimentally by Eq. (A.24) if we observe an amplitude reduction at tunneling events, the second condition $Q \gg 2c$ for the limiting expansion is violated near $\omega_0 \approx \Gamma$.

The power dissipation by single-electron tunneling can be calculated from Eq. (2.102) or (2.103) and gives

$$\mathcal{P}_{\omega_0} = \frac{1}{2}\, z_{\omega_0}^2\, \omega_0^2\, \delta\gamma \quad \xrightarrow{2Q\omega_0\gg\Gamma} \quad -\frac{1}{2} k z_{\omega_0}^2\, \frac{\omega_0}{Q}\, \frac{\delta z_{\omega_0}}{z_{\omega_0}}\,. \tag{A.29}$$

The condition (A.24) for the limiting approximation is always satisfied if we observe dissipation in the amplitude signal.

The value of $\delta k/k$ in Eq. (A.27) can be measured directly by the cantilever resonance frequency shift, as seen from Eq. (A.23) or (2.82). It contains the quadratic dependence on ω_0/Γ and the capacitive couplings of the quantum dot. This is most obviously expressed in the ratio of the dissipation and the frequency shift due to single-electron tunneling,

$$\frac{\delta\gamma}{\gamma} = \frac{\delta\omega_0}{\omega_0}\left(-2Q\,\frac{\omega_0}{\Gamma}\right) . \tag{A.30}$$

For the relation between the amplitude reduction and the frequency shift due to single-electron tunneling this implies

$$\frac{\delta z_{\omega_0}}{z_{\omega_0}} = \frac{\delta\omega_0}{\omega_0}\left(2Q\,\frac{\omega_0}{\Gamma} - 1\right) \xrightarrow{2Q\omega_0 \gg \Gamma} 2Q\,\frac{\delta\omega_0}{\Gamma} , \tag{A.31}$$

as can be seen from Eq. (A.22) and (A.30). Clearly, the ratio between the relative change in tip amplitude and cantilever resonance frequency is a direct measure of the tunneling rate of the quantum dot under investigation, as analyzed on our gold nanoparticles linked to a CNT in Sec. 6.6.

APPENDIX B

MORE IMAGES

This appendix presents a few more low-temperature scanning probe images. The purpose of this image gallery is to give a few more examples and illustrations. We also show some data that didn't find its space earlier in the experimental chapters.

We start with a spatial frequency shift image that shows a 'conventional' electrostatic potential map of a CNT device, Fig. B.1. This image was taken at a large tip height and high scan speed, in contrast to the frequency shift images that show single-electron charging of quantum dots in a CNT, Fig. B.2.

By applying a small source-drain bias across the CNT device and monitoring the device conductance as a function of tip location, we collect a so-called Scanning Gate Microscopy (SGM) image. When the CNT device is conducting, simultaneous frequency shift and SGM images show single-electron charging at the same tip location, as seen in Fig. B.3. The frequency shift image shows the electrostatic sample features, such as the CNT and fixed charges on the sample surface, in addition to the charging rings. Figures B.3a,b depict a single CNT quantum dot, while Figs. B.3c,d show the signal from two neighboring dots.

Two high-resolution frequency shift spectra of a sizeable section of a CNT that are stitched together are shown in Fig. B.4.

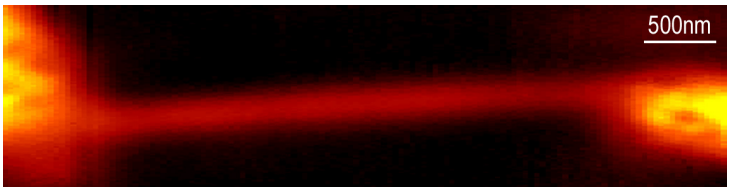

Figure B.1: Low temperature frequency shift image of a CNT device. The CNT goes horizontally across the image with metal contacts at either end.

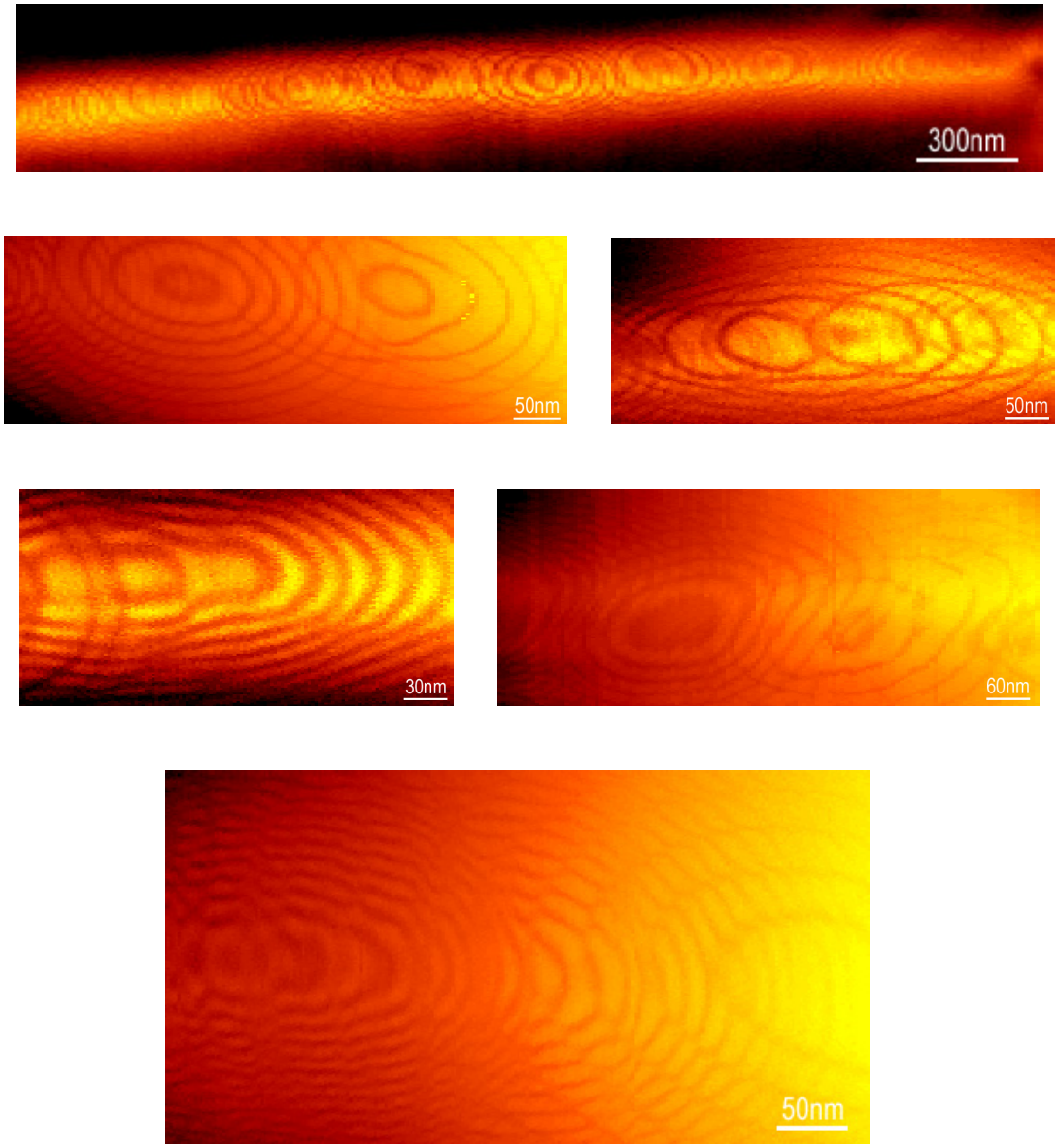

Figure B.2: Spatial frequency shift images of quantum dots in semiconducting carbon nanotubes.

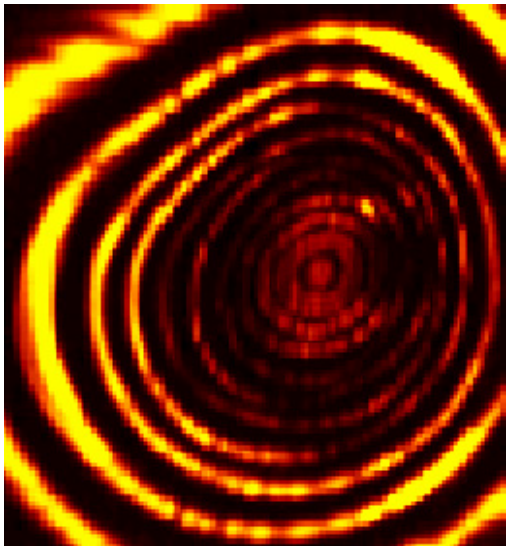

(a) Scanning gate image.

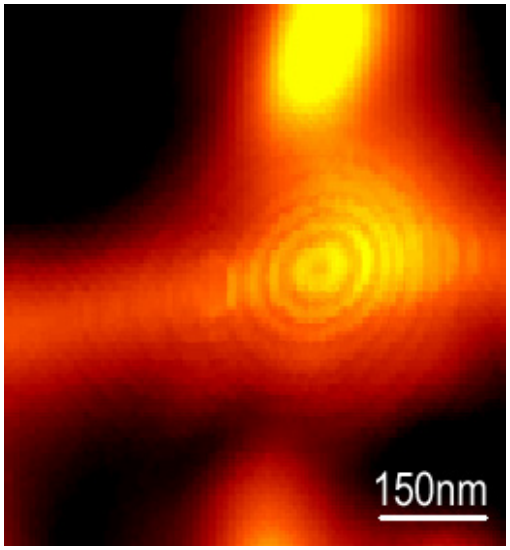

(b) Frequency shift image.

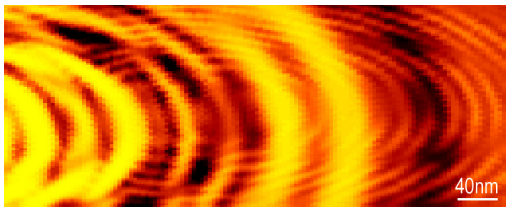

(c) Scanning gate image.

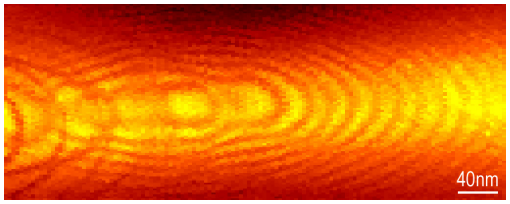

(d) Frequency shift image.

Figure B.3: Simultaneous scanning gate and frequency shift images of quantum dots in a CNT. In the top two images, the scale bar applies to both images. The sets of concentric rings in the conductance of the CNT device (SGM image) and in the cantilever resonance frequency overlay perfectly between the left and right images. The frequency shift image exhibits additional electrostatic features, such as the CNT and fixed charges on the sample surface (bright spots at the top and bottom of the image).

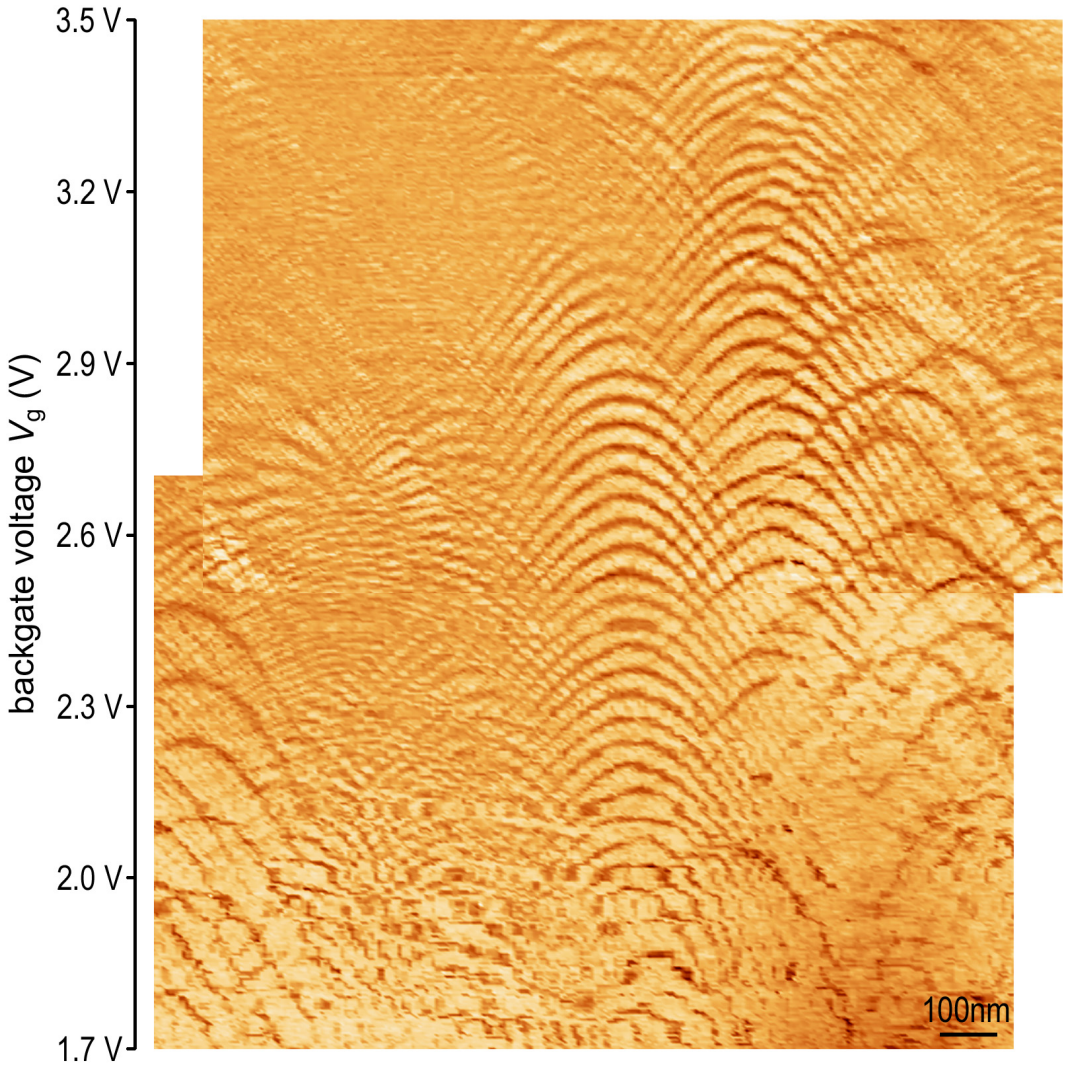

Figure B.4: Multi-dot frequency shift spectra from a semiconducting CNT. The tip voltage is $V_{\text{tip}} = 1\,\text{V}$ and the tip height is $z_0 = 100\,\text{nm}$ in both scans.

REFERENCES

Aharonov, Y. and Bohm, D. (1959). Significance of electromagnetic potentials in the quantum theory. *Physical Review*, 115(3):485.

Ajiki, H. and Ando, T. (1993). Electronic states of carbon nanotubes. *Journal of the Physical Society of Japan*, 62(4):1255–1266.

Albrecht, T. R., Grutter, P., Horne, D., and Rugar, D. (1991). Frequency-modulation detection using high-Q cantilevers for enhanced force microscope sensitivity. *Journal of Applied Physics*, 69(2):668–673.

Albrecht, T. R., Grutter, P., Rugar, D., and Smith, D. P. E. (1992). Low-temperature force microscope with all-fiber interferometer. *Ultramicroscopy*, 42:1638–1646.

Altshuler, B. L. (1985). Fluctuations in the extrinsic conductivity of disordered conductors. *JETP Letters*, 41(12):648–651.

Averin, D. V., Korotkov, A. N., and Likharev, K. K. (1991). Theory of single-electron charging of quantum-wells and dots. *Physical Review B*, 44(12):6199–6211.

Averin, D. V. and Likharev, K. K. (1991). Single electronics: A correlated transfer of single electrons and cooper pairs in systems of small tunnel junctions. In Altshuler, B. L., Lee, P. A., and Webb, R. A., editors, *Mesoscopic phenomena in solids*, Modern problems in condensed matter sciences, vol 30, pages 173–271. North-Holland; Elsevier Science, Amsterdam; New York.

Awasthi, K., Srivastava, A., and Srivastava, O. N. (2005). Synthesis of carbon nanotubes. *Journal of Nanoscience and Nanotechnology*, 5(10):1616–1636.

Bachtold, A., Fuhrer, M. S., Plyasunov, S., Forero, M., Anderson, E. H., Zettl, A., and McEuen, P. L. (2000). Scanned probe microscopy of electronic transport in carbon nanotubes. *Physical Review Letters*, 84(26):6082–6085.

Baddour, C. and Briens, C. (2005). Carbon nanotube synthesis: A review. *International Journal of Chemical Reactor Engineering*, 3:R3.

Bardeen, J., Cooper, L. N., and Schrieffer, J. R. (1957). Theory of superconductivity. *Physical Review*, 108(5):1175–1204.

Beenakker, C. W. J. (1991). Theory of coulomb-blockade oscillations in the conductance of a quantum dot. *Physical Review B*, 44(4):1646–1656.

Beenakker, C. W. J. and van Houten, H. (1991). Quantum transport in semiconductor nanostructures. *Solid State Physics-Advances in Research and Applications*, 44:1–228.

Besocke, K. (1987). An easily operable scanning tunneling microscope. *Surface Science*, 181(1-2):145–153.

Bharucha-Reid, A. T. (1997). *Elements of the theory of Markov processes and their applications*. Dover Publications, Mineola, N.Y.

Binnig, G., Quate, C. F., and Gerber, C. (1986). Atomic force microscope. *Physical Review Letters*, 56(9):930–933.

Binnig, G., Rohrer, H., Gerber, C., and Weibel, E. (1982). Surface studies by scanning tunneling microscopy. *Physical Review Letters*, 49(1):57–61.

Bleszynski, A. C. (2006). *Imaging Electrons in Semiconductor Nanostructures*. PhD thesis, Harvard University.

Bockrath, M., Cobden, D. H., Lu, J., Rinzler, A. G., Smalley, R. E., Balents, T., and McEuen, P. L. (1999). Luttinger-liquid behaviour in carbon nanotubes. *Nature*, 397(6720):598–601.

Bockrath, M., Cobden, D. H., McEuen, P. L., Chopra, N. G., Zettl, A., Thess, A., and Smalley, R. E. (1997). Single-electron transport in ropes of carbon nanotubes. *Science*, 275(5308):1922–1925.

Bradley, J. S. (1994). The chemistry of transition metal colloids. In Schmid, G., editor, *Clusters and colloids: from theory to applications*, pages 459–505. VCH, Weinheim; New York.

Brust, M., Fink, J., Bethell, D., Schiffrin, D. J., and Kiely, C. (1995). Synthesis and reactions of functionalized gold nanoparticles. *Journal of the Chemical Society-Chemical Communications*, (16):1655–1656.

Brust, M., Walker, M., Bethell, D., Schiffrin, D. J., and Whyman, R. (1994). Synthesis of thiol-derivatized gold nanoparticles in a 2-phase liquid-liquid system. *Journal of the Chemical Society-Chemical Communications*, (7):801–802.

Burnham, N. A., Chen, X., Hodges, C. S., Matei, G. A., Thoreson, E. J., Roberts, C. J., Davies, M. C., and Tendler, S. J. B. (2003). Comparison of calibration methods for atomic-force microscopy cantilevers. *Nanotechnology*, 14(1):1–6.

Chen, R. J., Zhan, Y. G., Wang, D. W., and Dai, H. J. (2001). Noncovalent sidewall functionalization of single-walled carbon nanotubes for protein immobilization. *Journal of the American Chemical Society*, 123(16):3838–3839.

Cleveland, J. P., Manne, S., Bocek, D., and Hansma, P. K. (1993). A nondestruc-

tive method for determining the spring constant of cantilevers for scanning force microscopy. *Review of Scientific Instruments*, 64(2):403–405.

Cobden, D. H. and Nygard, J. (2002). Shell filling in closed single-wall carbon nanotube quantum dots. *Physical Review Letters*, 89(4):046803.

Dai, H. J. (2000). Controlling nanotube growth. *Physics World*, 13(6):43–47.

Dai, H. J. (2001). Nanotube growth and characterization. In *Carbon Nanotubes*, volume 80 of *Topics in Applied Physics*, pages 29–53.

Dai, H. J. (2002). Carbon nanotubes: opportunities and challenges. *Surface Science*, 500(1-3):218–241.

De Poortere, E. P., Stormer, H. L., Huang, L. M., Wind, S. J., O'Brien, S., Huang, M., and Hone, J. (2006). Single-walled carbon nanotubes as shadow masks for nanogap fabrication. *Applied Physics Letters*, 88(14):143124.

Dixon, D. C. (1998). *Dots, Diodes and DNP: Electronic and Nuclear Interactions in Two-Dimensional Electron Gases*. PhD thesis, University of California, Berkeley.

Dresselhaus, M. S., Dresselhaus, G., and Avouris, P. (2001). *Carbon Nanotubes: Synthesis, Structure, Properties, and Applications*, volume 80 of *Topics in applied physics*. Springer, Berlin; New York.

Dresselhaus, M. S., Dresselhaus, G., and Eklund, P. C. (1996). *Science of fullerenes and carbon nanotubes*. Academic Press, San Diego.

Drude, P. (1900). On the electron theory of metals. *Annalen Der Physik*, 1(3):566–613.

Fallahi, P., Bleszynski, A. C., Westervelt, R. M., Huang, J., Walls, J. D., Heller, E. J., Hanson, M., and Gossard, A. C. (2005). Imaging a single-electron quantum dot. *Nano Letters*, 5(2):223–226.

Frens, G. (1973). Controlled nucleation for regulation of particle-size in monodisperse gold suspensions. *Nature-Physical Science*, 241(105):20–22.

Grabert, H. and Devoret, M. H. (1992). *Single charge tunneling: Coulomb blockade phenomena in nanostructures*. NATO ASI series B: Physics; vol. 294. Plenum Press, New York.

Grabert, H. and Horner, H. (1991). Special issue on single charge tunneling. *Zeitschrift für Physik B-Condensed Matter*, 85(3):317.

Guo, X. F., Small, J. P., Klare, J. E., Wang, Y. L., Purewal, M. S., Tam, I. W., Hong, B. H., Caldwell, R., Huang, L. M., O'Brien, S., Yan, J. M., Breslow, R., Wind, S. J., Hone, J., Kim, P., and Nuckolls, C. (2006). Covalently bridging gaps in single-walled carbon nanotubes with conducting molecules. *Science*, 311(5759):356–359.

Hagedorn, P. and Stadler, W. (1988). *Non-linear oscillations*. Oxford engineering science series. Clarendon Press, Oxford University Press, Oxford, New York, 2nd edition.

Hayashi, C. (1985). *Nonlinear oscillations in physical systems*. Princeton University Press, Princeton, NJ.

Heer, C. V. (1972). *Statistical mechanics, kinetic theory, and stochastic processes*. Academic Press, New York.

Heinze, S., Tersoff, J., Martel, R., Derycke, V., Appenzeller, J., and Avouris, P. (2002). Carbon nanotubes as schottky barrier transistors. *Physical Review Letters*, 89(10):106801.

Horowitz, P. and Hill, W. (1989). *The art of electronics*. Cambridge University Press, Cambridge, New York, 2nd edition.

Huang, S. M., Cai, X. Y., and Liu, J. (2003a). Growth of millimeter-long and horizontally aligned single-walled carbon nanotubes on flat substrates. *Journal of the American Chemical Society*, 125(19):5636–5637.

Huang, S. M., Maynor, B., Cai, X. Y., and Liu, J. (2003b). Ultralong, well-aligned single-walled carbon nanotube architectures on surfaces. *Advanced Materials*, 15(19):1651.

Hutter, J. L. and Bechhoefer, J. (1993). Calibration of atomic-force microscope tips. *Review of Scientific Instruments*, 64(7):1868–1873.

Iijima, S. (1991). Helical microtubules of graphitic carbon. *Nature*, 354(6348):56–58.

Ingold, G.-L. and Nazarov, Y. V. (1992). Charge tunneling rates in ultrasmall junctions. In Grabert, H. and Devoret, M. H., editors, *Single Charge Tunneling*, NATO ASI series, vol. B294, pages 21–107. Plenum Press, New York, London.

Jackson, J. D. (1999). *Classical electrodynamics*. Wiley, New York, 3rd edition.

Jacobs, H. O., Knapp, H. F., and Stemmer, A. (1999). Practical aspects of kelvin probe force microscopy. *Review of Scientific Instruments*, 70(3):1756–1760.

Jahn, H. A. and Teller, E. (1937). Stability of polyatomic molecules in degenerate electronic states: I. orbital degeneracy. *Proceedings of the Royal Society of London Series a-Mathematical and Physical Sciences*, 161(A905):220–235.

Jarillo-Herrero, P., Sapmaz, S., Dekker, C., Kouwenhoven, L. P., and van der Zant, H. S. J. (2004). Electron-hole symmetry in a semiconducting carbon nanotube quantum dot. *Nature*, 429(6990):389–392.

Jenkins, N. E., DeFlores, L. P., Allen, J., Ng, T. N., Garner, S. R., Kuehn, S., Dawlaty, J. M., and Marohn, J. A. (2004). Batch fabrication and characterization of ultrasensitive cantilevers with submicron magnetic tips. *Journal of Vacuum Science and Technology B*, 22(3):909–915.

Johnson, J. B. (1928). Thermal agitation of electricity in conductors. *Physical Review*, 32(1):97–109.

Keller, M. W., Eichenberger, A. L., Martinis, J. M., and Zimmerman, N. M. (1999). A capacitance standard based on counting electrons. *Science*, 285(5434):1706–1709.

Kicin, S., Pioda, A., Ihn, T., Sigrist, M., Fuhrer, A., Ensslin, K., Reinwald, M., and Wegscheider, W. (2005). Spatially highly resolved study of afm scanning tip-quantum dot local interaction. *New Journal of Physics*, 7:185.

Kim, W., Choi, H. C., Shim, M., Li, Y. M., Wang, D. W., and Dai, H. J. (2002). Synthesis of ultralong and high percentage of semiconducting single-walled carbon nanotubes. *Nano Letters*, 2(7):703–708.

Kittel, C. (2005). *Introduction to solid state physics*. Wiley, Hoboken, NJ, 8th edition.

Kong, J., Soh, H. T., Cassell, A. M., Quate, C. F., and Dai, H. J. (1998). Synthesis of individual single-walled carbon nanotubes on patterned silicon wafers. *Nature*, 395(6705):878–881.

Kooi, E. (1967). *The surface properties of oxidized silicon*. PhD thesis, Technische Hogeschool Eindhoven.

Kouwenhoven, L. P., Austing, D. G., and Tarucha, S. (2001). Few-electron quantum dots. *Reports on Progress in Physics*, 64(6):701–736.

Kouwenhoven, L. P., Johnson, A. T., Vandervaart, N. C., and Harmans, K. J. P. M. (1992). Single-electron pump and turnstile in semiconductor nanostructures. *Institute of Physics Conference Series*, (127):229–234.

Kouwenhoven, L. P., Johnson, A. T., Vandervaart, N. C., Vanderenden, A., Harmans, C. J. P. M., and Foxon, C. T. (1991). Quantized current in a quantum dot turnstile. *Zeitschrift für Physik B-Condensed Matter*, 85(3):381–388.

Kouwenhoven, L. P., Marcus, C. M., McEuen, P. L., Tarucha, S., Westervelt, R. M., and Wingreen, N. S. (1997). Electron transport in quantum dots. In Sohn, L. L., Kouwenhoven, L. P., and Schön, G., editors, *Mesoscopic Electron Transport*, NATO ASI series, vol. E345, pages 105–213. Kluwer Academic Publishers, Dordrecht, Boston.

Lee, P. A. and Stone, A. D. (1985). Universal conductance fluctuations in metals. *Physical Review Letters*, 55(15):1622–1625.

Levy, R. and Maaloum, M. (2002). Measuring the spring constant of atomic force microscope cantilevers: thermal fluctuations and other methods. *Nanotechnology*, 13(1):33–37.

Liang, W. J., Bockrath, M., and Park, H. (2002). Shell filling and exchange coupling in metallic single-walled carbon nanotubes. *Physical Review Letters*, 88(12):126801.

Likharev, K. K. (1988). Correlated discrete transfer of single electrons in ultrasmall tunnel-junctions. *IBM Journal of Research and Development*, 32(1):144–158.

Livermore, C., Crouch, C. H., Westervelt, R. M., Campman, K. L., and Gossard, A. C. (1996). The coulomb blockade in coupled quantum dots. *Science*, 274(5291):1332–1335.

Martel, R., Derycke, V., Lavoie, C., Appenzeller, J., Chan, K. K., Tersoff, J., and Avouris, P. (2001). Ambipolar electrical transport in semiconducting single-wall carbon nanotubes. *Physical Review Letters*, 87(25):256805.

McCormick, K. L. (1998). *Electrical Probes of Mesoscopic Systems with a Low Temperature Atomic Force Microscope*. PhD thesis, University of California, Berkeley.

Minorsky, N. (1962). *Nonlinear oscillations*. Van Nostrand, Princeton, NJ.

Mintmire, J. W. and White, C. T. (1998). Universal density of states for carbon nanotubes. *Physical Review Letters*, 81(12):2506–2509.

Morita, S., Wiesendanger, R., and Meyer, E. (2002). *Noncontact atomic force microscopy*. NanoScience and Technology. Springer, Berlin, New York.

Moriyama, S., Fuse, T., Suzuki, M., Aoyagi, Y., and Ishibashi, K. (2005). Four-electron shell structures and an interacting two-electron system in carbon-nanotube quantum dots. *Physical Review Letters*, 94(18):186806.

Morpurgo, A. F., Marcus, C. M., and Robinson, D. B. (1999). Controlled fabrication of metallic electrodes with atomic separation. *Applied Physics Letters*, 74(14):2084–2086.

Nayfeh, A. H. and Mook, D. T. (1979). *Nonlinear oscillations*. Wiley, New York.

Nishi, Y. (1971). Study of silicon-silicon dioxide structure by electron spin resonance .1. *Japanese Journal of Applied Physics*, 10(1):52–62.

Nonnenmacher, M., Oboyle, M. P., and Wickramasinghe, H. K. (1991). Kelvin probe force microscopy. *Applied Physics Letters*, 58(25):2921–2923.

Nonnenmacher, M., Oboyle, M. P., and Wickramasinghe, H. K. (1992). Surface investigations with a kelvin probe force microscope. *Ultramicroscopy*, 42:268–273.

Nyquist, H. (1928). Thermal agitation of electric charge in conductors. *Physical Review*, 32(1):110–113.

Odom, T. W., Hafner, J. H., and Lieber, C. M. (2001). Scanning probe microscopy studies of carbon nanotubes. In *Carbon Nanotubes*, volume 80 of *Topics in Applied Physics*, pages 173–211.

Oreg, Y., Byczuk, K., and Halperin, B. I. (2000). Spin configurations of a carbon nanotube in a nonuniform external potential. *Physical Review Letters*, 85(2):365–368.

Ott, H. W. (1988). *Noise reduction techniques in electronic systems*. Wiley, New York, 2nd edition.

Papoulis, A. and Pillai, S. U. (2002). *Probability, random variables, and stochastic processes*. McGraw-Hill, Boston, 4th edition.

Park, H., Lim, A. K. L., Alivisatos, A. P., Park, J. W., and McEuen, P. L. (1999). Fabrication of metallic electrodes with nanometer separation by electromigration. *Applied Physics Letters*, 75(2):301–303.

Park, J. W. and McEuen, P. L. (2001). Formation of a p-type quantum dot at the end of an n-type carbon nanotube. *Applied Physics Letters*, 79(9):1363–1365.

Pierret, R. F. (1996). *Semiconductor device fundamentals*. Addison-Wesley, Reading, Mass.

Pioda, A., Kicin, S., Ihn, T., Sigrist, M., Fuhrer, A., Ensslin, K., Weichselbaum, A., Ulloa, S. E., Reinwald, M., and Wegscheider, W. (2004). Spatially resolved manipulation of single electrons in quantum dots using a scanned probe. *Physical Review Letters*, 93(21):216801.

Pobell, F. (1996). *Matter and methods at low temperatures*. Springer-Verlag, Berlin, New York, 2nd edition.

Pothier, H., Lafarge, P., Orfila, P. F., Urbina, C., Esteve, D., and Devoret, M. H. (1991). Single electron pump fabricated with ultrasmall normal tunnel-junctions. *Physica B*, 169(1-4):573–574.

Pothier, H., Lafarge, P., Urbina, C., Esteve, D., and Devoret, M. H. (1992). Single-electron pump based on charging effects. *Europhysics Letters*, 17(3):249–254.

Proksch, R., Schaffer, T. E., Cleveland, J. P., Callahan, R. C., and Viani, M. B. (2004). Finite optical spot size and position corrections in thermal spring constant calibration. *Nanotechnology*, 15(9):1344–1350.

Reed, M. A., Zhou, C., Muller, C. J., Burgin, T. P., and Tour, J. M. (1997). Conductance of a molecular junction. *Science*, 278(5336):252–254.

Richardson, R. C. and Smith, E. N. (1988). *Experimental techniques in condensed matter physics at low temperatures*. Addison-Wesley, Redwood City, Calif.

Rugar, D., Mamin, H. J., Erlandsson, R., Stern, J. E., and Terris, B. D. (1988). Force microscope using a fiber-optic displacement sensor. *Review of Scientific Instruments*, 59(11):2337–2340.

Rugar, D., Mamin, H. J., and Guethner, P. (1989). Improved fiber-optic interferometer for atomic force microscopy. *Applied Physics Letters*, 55(25):2588–2590.

Ruzin, I. M., Chandrasekhar, V., Levin, E. I., and Glazman, L. I. (1992). Stochastic coulomb blockade in a double-dot system. *Physical Review B*, 45(23):13469–13478.

Sader, J. E., Chon, J. W. M., and Mulvaney, P. (1999). Calibration of rectangular atomic force microscope cantilevers. *Review of Scientific Instruments*, 70(10):3967–3969.

Sader, J. E., Larson, I., Mulvaney, P., and White, L. R. (1995). Method for the calibration of atomic-force microscope cantilevers. *Review of Scientific Instruments*, 66(7):3789–3798.

Saito, R., Dresselhaus, G., and Dresselhaus, M. S. (1998). *Physical properties of carbon nanotubes*. Imperial College Press, London.

Sapmaz, S., Jarillo-Herrero, P., Kong, J., Dekker, C., Kouwenhoven, L. P., and van der Zant, H. S. J. (2005). Electronic excitation spectrum of metallic carbon nanotubes. *Physical Review B*, 71(15):153402.

Sapmaz, S., Meyer, C., Beliczynski, P., Jarillo-Herrero, P., and Kouwenhoven, L. P. (2006). Excited state spectroscopy in carbon nanotube double quantum dots. *Nano Letters*, 6(7):1350–1355.

Sarid, D. (1994). *Scanning Force Microscopy: With Applications to Electric, Magnetic, and Atomic Forces*. Oxford series in optical and imaging sciences. Oxford University Press, New York, revised edition.

Slot, J. W. and Geuze, H. J. (1985). A new method of preparing gold probes for multiple-labeling cyto-chemistry. *European Journal of Cell Biology*, 38(1):87–93.

Sohn, L. L., Kouwenhoven, L. P., and Schön, G. (1997). *Mesoscopic Electron Transport*. NATO ASI series E: Applied Sciences; vol. 345. Kluwer Academic Publishers, Dordrecht, Boston.

Stipe, B. C., Mamin, H. J., Stowe, T. D., Kenny, T. W., and Rugar, D. (2001). Magnetic dissipation and fluctuations in individual nanomagnets measured by ultrasensitive cantilever magnetometry. *Physical Review Letters*, 86(13):2874–2877.

Stowe, T. D., Yasumura, K., Kenny, T. W., Botkin, D., Wago, K., and Rugar, D. (1997). Attonewton force detection using ultrathin silicon cantilevers. *Applied Physics Letters*, 71(2):288–290.

Tans, S. J., Devoret, M. H., Dai, H. J., Thess, A., Smalley, R. E., Geerligs, L. J., and Dekker, C. (1997). Individual single-wall carbon nanotubes as quantum wires. *Nature*, 386(6624):474–477.

Terrones, M. (2004). Carbon nanotubes: synthesis and properties, electronic

devices and other emerging applications. *International Materials Reviews*, 49(6):325–377.

Thune, E. and Strunk, C. (2005). Quantum transport in carbon nanotubes. In Cuniberti, G., Richter, K., and Fagas, G., editors, *Introducing Molecular Electronics*, volume 680 of *Lecture Notes in Physics*, pages 351–380. Springer, Berlin, Heidelberg.

Tomfohr, J., Ramachandran, G. K., Sankey, O. F., and Lindsay, S. M. (2005). Making contacts to single molecules: Are we there yet? In Cuniberti, G., Richter, K., and Fagas, G., editors, *Introducing Molecular Electronics*, volume 680 of *Lecture Notes in Physics*, pages 301–312. Springer, Berlin, Heidelberg.

Treacy, M. M. J., Ebbesen, T. W., and Gibson, J. M. (1996). Exceptionally high young's modulus observed for individual carbon nanotubes. *Nature*, 381(6584):678–680.

van der Wiel, W. G., De Franceschi, S., Elzerman, J. M., Fujisawa, T., Tarucha, S., and Kouwenhoven, L. P. (2003). Electron transport through double quantum dots. *Reviews of Modern Physics*, 75(1):1–22.

van Houten, H., Staring, A. A. M., and Beenakker, C. W. J. (1992). Coulomb-blockade oscillations in a quantum dot. In Grabert, H. and Devoret, M. H., editors, *Single Charge Tunneling*, NATO ASI series, vol. B294, pages 167–216. Plenum Press, New York, London.

van Houten, H., Staring, A. A. M., and Beenakker, C. W. J. (2005). Coulomb-blockade oscillations in a quantum dot. *COND-MAT*, 0508545.

Waugh, F. R., Berry, M. J., Crouch, C. H., Livermore, C., Mar, D. J., Westervelt, R. M., Campman, K. L., and Gossard, A. C. (1996). Measuring interactions between tunnel-coupled quantum dots. *Physical Review B*, 53(3):1413–1420.

Waugh, F. R., Berry, M. J., Mar, D. J., Westervelt, R. M., Campman, K. L., and Gossard, A. C. (1995). Single-electron charging in double and triple quantum dots with tunable coupling. *Physical Review Letters*, 75(4):705–708.

White, C. T. and Mintmire, J. W. (2005). Fundamental properties of single-wall carbon nanotubes. *Journal of Physical Chemistry B*, 109(1):52–65.

White, C. T., Robertson, D. H., and Mintmire, J. W. (1993). Helical and rotational symmetries of nanoscale graphitic tubules. *Physical Review B*, 47(9):5485–5488.

Wiesendanger, R. (1994). *Scanning Probe Microscopy and Spectroscopy: Methods and Applications*. Cambridge University Press, Cambridge, New York.

Woodside, M. T. (2001). *Scanned Probe Microscopy of the Electronic Properties of Low-Dimensional Systems*. PhD thesis, University of California, Berkeley.

Woodside, M. T. and McEuen, P. L. (2002). Scanned probe imaging of single-electron charge states in nanotube quantum dots. *Science*, 296(5570):1098–1101.

Yaish, Y., Park, J. Y., Rosenblatt, S., Sazonova, V., Brink, M., and McEuen, P. L. (2004). Electrical nanoprobing of semiconducting carbon nanotubes using an atomic force microscope. *Physical Review Letters*, 92(4):046401.

Yao, Z., Dekker, C., and Avouris, P. (2001). Electrical transport through single-wall carbon nanotubes. In Dresselhaus, M. S., Dresselhaus, G., and Avouris, P., editors, *Carbon Nanotubes: Synthesis, Structure, Properties, and Applications*, volume 80 of *Topics in Applied Physics*, pages 147–171. Springer.

Zhang, Y. J., Petta, J. R., Ambily, S., Shen, Y. L., Ralph, D. C., and Malliaras, G. G. (2003). 30 nm channel length pentacene transistors. *Advanced Materials*, 15(19):1632.

Zheng, L. X., O'Connell, M. J., Doorn, S. K., Liao, X. Z., Zhao, Y. H., Akhadov, E. A., Hoffbauer, M. A., Roop, B. J., Jia, Q. X., Dye, R. C., Peterson, D. E., Huang, S. M., Liu, J., and Zhu, Y. T. (2004). Ultralong single-wall carbon nanotubes. *Nature Materials*, 3(10):673–676.

Zhu, J., Brink, M., and McEuen, P. L. (2005). Frequency shift imaging of quantum dots with single-electron resolution. *Applied Physics Letters*, 87(24):242102.